Application of Reconstructed Layered Materials for Environmental Energy Harvesting

A dissertation submitted to the
Indian Institute of Technology Guwahati as
partial fulfilment of the Degree of

DOCTOR of PHILOSOPHY

Submitted by

Jumi Deka
Roll No: 156122042

Department of Chemistry
Indian Institute of Technology Guwahati
Guwahati-781039 Assam, India
February 2021

TH-2654_156122042

TH-2654_156122042

Dedicated to My Family

TH-2654_156122042

TH-2654_156122042

INDIAN INSTITUTE OF TECHNOLOGY

GUWAHATI

Department of Chemistry

STATEMENT

I hereby declare that the matter embodied in this thesis entitled **"*Application of Reconstructed Layered Materials for Environmental Energy Harvesting*"** is the results of the investigations carried out by me at the Department of Chemistry, Indian Institute of Technology Guwahati, Assam, India under the guidance of Associate Professor, Dr. Kalyan Raidongia.

In keeping with the general practice in reporting scientific observations, due acknowledgement has been made whenever the work described is based on the findings of other investigators.

Date: February, 2021

IIT Guwahati

Jumi Deka

TH-2654_156122042

TH-2654_156122042

INDIAN INSTITUTE OF TECHNOLOGY

GUWAHATI

Department of Chemistry

CERTIFICATE

This is to certify that the matter embodied in this thesis entitled "***Application of Reconstructed Layered Materials for Environmental Energy Harvesting***" has been carried out by **Miss Jumi Deka** at the Department of Chemistry, Indian Institute of Technology Guwahati, Assam, India. It has not been submitted elsewhere for the award of any degree or diploma.

Date: February, 2021
IIT Guwahati

Dr. Kalyan Raidongia
(Thesis Supervisor)
Department of Chemistry
Indian Institute of Technology Guwahati
Guwahati-781039
Assam, India

TH-2654_156122042

TH-2654_156122042

PREFACE

The present thesis, entitled as "Application of Reconstructed Layered Materials for Environmental Energy harvesting" is divided into six chapters based on detailed investigation of various layered materials and their application to harvest environmental energy. Chapter 1 contains a general overview of 2D materials, exfoliation techniques and their application in energy harvesting systems.

Chapter 2 elaborates the fabrication of multifunctional soil membranes by tuning the structure of ubiquitous soil components, viz. clay and humic acids. Crosslinking of exfoliated clay layers with purified humic acids not only conferred mechanical strength but also enhanced chemical robustness of the membranes. The percolated network of molecularly sized channels of the soil membranes exhibits characteristic nanofluidic phenomena which is exploited to harvest energy from salinity gradient. Electrical conductivity is induced to otherwise insulating soil membranes by heating in an inert atmosphere, without affecting their nanofluidic ionic conductivity. The soil membranes also provided a new platform to prepare and study mixed conducting materials. Strips of heated membranes shown to exhibit excellent sensitivity towards NH_3 gas under atmospheric conditions.

In chapter 3, the complementary charge transfer activities of boron (B-r-GO) and nitrogen (N-r-GO) doped reduced graphene oxide (r-GO) flakes are exploited to extract energy from serene water resources. B-r-GO and N-r-GO samples prepared by annealing graphene oxide sheets with boric acid and urea were individually coated on cellulose membranes to fabricate B-r-GO/N-r-GO devices. DFT calculations were carried out which indicate that compared to N-r-GO, the B-r-GO structure is more stable and has considerably higher charge transfer activity with water molecules.

TH-2654_156122042

In chapter 4, we demonstrate the fabrication of a highly robust, inflammable, and pressure-responsive energy device. The energy device was prepared by pressing a polydiallyldimethylammonium chloride (PDDA) doped nanofluidic membrane of natural vermiculite clay (PDDA-VM) on kitchen-grade aluminium foil (PDDA-VM/Al) consumes atmospheric water molecules as the cathode reagent and aluminium atoms at the anodic reaction. Remarkably, the clay-based energy devices exhibit excellent resistance to fire. The PDDA-VM/Al membrane recovered ~ 70 % of its output power after being exposed to an open flame for more than 2 minutes. Moreover, multiple devices can be assembled to add up the output current and voltage generated by the individual devices to power electronic equipment.

In Chapter 5, the principles of metal-water batteries were applied to develop a sustainable pressure-responsive energy delivery system. Application of a humble pressure of 56 kPa on agar and glycerol-based hydrogel membrane sandwiched between aluminum foil and nanofluidic V_2O_5 membrane (Al-gel-VO device) generate open-circuit voltage up to 1.3 V accompanied by an output current of 85 µA (power density = 0.45 Wm^{-2}). Unlike typical humidity powered energy systems, the energy output of the current device is resistant towards the diurnal variations in environmental conditions. Remarkably, both gel and V_2O_5 membrane can be completely regenerated after damage caused by prolong use or accidents without any deterioration in the energy-efficiencies.

Chapter 6 consist of an overall conclusion of the work done during my PhD tenure and the future perspective of the work.

TH-2654_156122042

ACKNOWLEDGEMENTS

I would like to take the opportunity here to thank all the wonderful people who stood beside me throughout my doctoral journey. It would have been impossible to achieve my goals without all the helping hands.

Foremost, I wish to express my deepest gratitude to my supervisor, Dr. Kalyan Raidongia, for believing in me and giving me this great opportunity to work under his supervision. He has persuasively guided and encouraged me to be an independent professional as I am today and cheered me to do the right thing even when the road got tough. His motivation and patience in solving the unknown challenges is truly inspiring. I will remain forever obliged for his considerable aid in the creation of this thesis. I and my work have immensely benefited from his proficient guidance and mentorship.

Besides my supervisor, my sincere gratitude goes out to my doctoral committee members: Prof. Anil Kumar Saikia, Dr. Debapratim Das and Dr. Sunanda Chatterjee, for their insightful comments and encouragement throughout the evaluation process of my annual progress and synopsis seminars.

My sincere acknowledgement to Dr. Hemant Kumar Srivastava for extending his kind support to carry out DFT calculations and guiding us with the theoretical results. My special thanks to Dr. Gitish K Dutta for his kind help and valuable inputs with electrochemical analysis.

I am thankful to the Indian Institute of Technology Guwahati for providing me the fellowship and to the Department of Chemistry and Central Instruments Facilities (CIF) for

TH-2654_156122042

providing the research and instrumental facilities. I extend my sincere gratitude to the staff members of the chemistry office and student affairs. Thank you for providing all the assistance and reminders during five years of my PhD. Furthermore, I am thankful to all the FESEM, FETEM, RAMAN, AFM, and pXRD operators for their help. I would like to express honest appreciation to Dr. Babulal Das for his kind assistance in teaching various scientific instruments.

My deepest gratitude to my fellow labmates Kundan Saha and Dr. Raj Kumar Gogoi for welcoming me into the group with so much affection and warmth, and ever since their constant support and help throughout my PhD period. I would like to extend my heartfelt thanks to all my lab juniors Tukhar Jyoti Konch, Arindom Bikash Neog, Trisha Dutta, Madhurjya Buraguhain, Priyamjeet Deka and Raktim Gogoi for their kind and helping hands in every aspect during these five years and creating a fun and homely atmosphere in lab, moments which I will cherish for the lifetime. My heartiest appreciation to few of my project students Anish, Neelam, Kushadeep, Priyamvada, and Himan for their helping hands in my research work.

My acknowledgement column would remain incomplete without the mention of the most special group of people whom I met in IIT Guwahati and eventually turned into a family for lifetime. My Special thanks to Megha Balha, Prerona Baruah, Kundan Saha, Raj Kumar Gogoi, Indrajit Das, Nimisha Bania, Shreya Singh, Subhasmita Saikia, and Duborima Kashyap for being a constant source of love, positivity and support throughout my stay at IIT Guwahati. I would also like to thank Namami Goswami, Abhilasha Bora, Angana Bhattacharya, and Puja Hazarika for all the wonderful times we shared. I would like to

TH-2654_156122042

extend my thankfulness to my childhood friends Chimi, Titli, Partha and Abhishek for their constant encouragement and uplifting me in my hard times.

Finally, most importantly, my deep and honest gratefulness to my family for their constant and unparalleled love and support throughout my journey so far. Firstly, I would like to thank my mother Santana Deka and father Kailash Chandra Deka for educating me with the moral values of life which helped me to grow as a better person. I am forever indebted to my parents for believing in me and giving me every opportunity which helped me to reach to a position where I am today. I am extremely grateful to my elder sister Rimjim Deka Kakati for being my biggest pillar of strength. She has been my role model who taught me to be confident, strong, hard- working, determined and kind. Thanks for taking the best care of me in every aspect of my life. My heartfelt gratitude to my brother-in-law Partha Kakati whose advice and wisdom inspired me for new endeavors.

At last, my heartfelt gratitude to my best friend and companion, Kundan, for his unconditional help and support throughout my PhD journey. Starting from problem solving to calming me down during PhD hurdles, without him by my side the journey would have been a difficult road.

TH-2654_156122042

Synopsis Report

Chapter I: Introduction to two dimensional nanomaterials.

The introduction of coal as a source of energy, in the 18th century, can be marked as the beginning of the industrial revolution. Similar to coal, petroleum and natural gas also paved their way into the industrial revolution, and set-up the platform for the modern age of technological developments. The discovery of fossils fuels can be considered as one of the primary milestones towards the luxury of modern life. Though the burning of fossil fuels fulfills most of the energy need of the society, over the years, it has created new issues like global warming and energy crisis. The burning of fossil fuels not only emits carbon dioxide but also releases other harmful gases like mercury, sulfur dioxide, and toxic soot. Over the years, the rate of energy consumption has increased drastically, and the ever-increasing population is demanding more and more power to meet their energy-expensive livelihood. At present, ~ 84 % of the world energy requirements are fulfilled by non-renewable resources like petroleum, natural gas, and coal. The rest 16 % is supported collectively by nuclear power, renewable sources such as solar, hydro, tidal energy. Based on the limited-availability, high rate of consumption, and environmental impact, a switch to sustainable energy sources is an urgent need of the hour. A drift towards the non-conventional sources of energy through the creation of new technologies that can exploit ambient energy sources is a necessity for the survival of mankind. In recent years, the unique characteristics of atomically thin 2D materials are drawing significant attention in developing efficient energy devices to harvest cleaner and greener electricity from otherwise futile energy sources.

Layered materials are comprised of nanometer-thick two-dimensional (2D) layers of crystals stacked together by weak van der Waals, electrostatic, or hydrogen bonding interactions. Upon exfoliation, the portion of atoms exposed to the surface becomes several

times higher than that of the inner volume of the materials. This extraordinary enhancement in the surface to volume ratio imbues many unique characteristics to the exfoliated sheets. With plenty of phenomenon taking place at the surface such as efficient heat transfer or properties that involves an exchange between the interfaces, 2D nanomaterials provide a promising platform for energy conversion, and energy storage applications.

Chapter-II: Reconstruction of Soil Components into Multifunctional Freestanding Membranes

In this chapter, we have demonstrated the fabrication of freestanding composite membranes by tuning the structure of ubiquitous soil components, viz. clay and humic acids with application possibilities in the areas like nanofluidic energy harvesting, water purification and sensing of toxic chemicals. Humic acids, the mixtures of acidic organic polymers that are believed to be a product of the natural break-down process of plant- and animal-based materials, were extracted and purified following the standard alkaline-acid treatment-based procedure. Natural vermiculite $(Al,Mg,Fe^{3+})_4(Si,Al)_8O_{20}(OH)_4$, a smectite group 2:1 clay, is used here as the model clay system. Two-steps ion exchange method was employed to obtain homogeneous aqueous dispersion of the clay sample. Aqueous dispersions of exfoliated clay layers and purified humic acids were mixed at different ratios and their colloidal stability was monitored over a period of three months. Pure humic acids and vermiculite dispersions started settling down after around 24 undisturbed hours; in contrast, humic acids-vermiculite dispersions remain stable up to three months indicating favorable interactions between the two. Such augmentations of colloidal stability of bulk clay particles induced by humic acids are already documented in the relevant literature. Humic acids bind to clay particles through following modes of

TH-2654_156122042

interactions- (a) anion-exchange to clay edges, (b) cation- or water-bridges to clay surfaces (c) H-bonding to the surface Si–OH groups, and (d) van der Waals forces.

Seeking the advantage of the diverse crosslinking possibilities of humic acids and exfoliated clay layers, freestanding composite membranes were prepared by vacuum filtration of dispersions of humic acids and exfoliated vermiculite layers were mixed in different weight ratios (20 %, 30 %, 50 % and 70 % humic acids). Study of bending stiffness and tensile strength revealed enhanced mechanical properties of the soil membranes as compared to that of pure vermiculite membranes which is attributed to the cross linking effect of humic acids. Soil membranes with well-defined interlayer spacing exhibited unique molecular and/or ionic transport properties. Percolated network of nanofluidic channels across the soil membrane were confirmed by the surface charge governed ionic transport by the membranes. Soil-based nanofluidic membranes are also employed to harvest green energy from concentration differences. The molecularly thin nanofluidic channels of soil membranes enriched with surface charges also enable the selective-cation-transport behavior and could effectively remove cationic dye from aqueous solution. Further, electrical conductivity is induced to otherwise insulating soil membranes by heating in an inert atmosphere, without affecting their nanofluidic ionic conductivity. The soil membranes also provided a new platform to prepare and study mixed conducting materials. Strips of heated soil membrane were found to exhibit excellent sensitivity towards NH_3 gas under atmospheric conditions. The high sensitivity of heated soil membrane toward ammonia vapors can be attributed to smaller flake sizes, higher defect density and larger interlayer spacing.

Chapter-III: Electrical power Generation from the Contrasting Interfacial Activities of Boron- and Nitrogen-Doped Reduced Oxide Membranes

TH-2654_156122042

Water, the medium of life has also served as a sustainable source of energy for hundreds of years. However, most of the water-based energy harvesting techniques relies either on rapid flow or on the fast evaporation rate of the molecules. In this chapter, we are employing boron and nitrogen doped reduced graphene oxide (r-GO) films to harvest electricity from calm water. As boron and nitrogen atoms manipulate the electron density of r-GO flakes in the opposite directions producing p-type and n-type semiconductors, they attract the opposite poles of the water molecules leading to a charge separation process and hence breaks the electrical neutrality. Graphene oxide prepared by Hummer's method was independently mixed with urea and boric acid, and heated under argon atmosphere at different temperature (550, 650, 750 and 900 °C) to prepare N-doped (N-r-GO) and B-doped (B-r-GO) r-GO samples respectively. In order to harvest energy from calm water, both B-r GO and N-r-GO samples were independently dispersed on N-methyl-2-pyrrolidone with the help of an ultra-sonic bath and coated on ashless cellulose filtration membranes through vacuum filtration. Typically, the B-r-GO and N-r-GO coated filter papers connected to Cu wires were mounted on the opposite sides of a glass slide, the Cu wires were then connected to a source meter instrument to measure the open-circuit potential. An open-circuit potential difference of around 280 mV and a current output of 9 µA was generated as soon as the B-r-GO/N-r-GO device was dipped into water. The power-output were found to be tunable by varying parameters like coating area, dopant amounts, annealing temperature, and ionic conductivity. The potential-drops due to the prolong soaking of B-r-GO/N-r-GO devices (for a few days) can be completely recovered up to 78 % of potential difference produced by the pristine device through vacuum drying. In order to open-up the possibility of fabricating wearable energy devices the B-r-GO/N-r-GO samples are also coated on arbitrary substances like jeans cloths. To demonstrate the applicability of energy derived from calm water nine B-r-GO/N-r-GO devices were

TH-2654_156122042

connected in series to light up a Light emitting device (LED) of 3 V. The DFT calculations indicate that compared to N-r-GO, the B-r-GO structure is more stable and has considerably higher charge transfer activity with water molecules.

Chapter-IV: Clay-Based Nanofluidic Membrane Derived from Vermiculite Nanoflakes for Pressure-Responsive Power Generation

In the recent years, the vast amount of gaseous water molecules omnipresent in our atmospheric has been recognized as one of the most readily available sources of electrical energy. In this chapter, we have developed an energy delivering systems based on the principle of metal-moisture batteries using PDDA Poly diallyldimethylammonium chloride) coated nanofluidic membranes of vermiculite clay. PDDA-VM films showed exceptional water holding capacity under humid conditions, which is evident from the existence of nanofluidic conductivity even in the absence of direct contact with liquid water sources. Even at extremely low humidity conditions (RH = 15 %), PDDA-VM films display water-based ionic conductivity up to 4 hours. In order to fabricate the energy harvesting device, the PDDA coated side of the VM stripe was connected to a Cu wire with the help of conductive silver paste, and the other side of the VM stripe was pressed against an aluminium sheet of similar dimension to generate electrical currents of magnitude around 100 µA accompanied by an open circuit potential of 0.8 V. The output current generated by the interfacial interaction of Al and VM is attributed to the movements of interlayer cations through the interconnected nanochannel network of the freestanding VM. The output current values can be tuned from sub-micro ampere range to milliampere (mA) range by varying parameters like intercalating cations, device geometry (or device size), thickness and nature of the polymer coating, and applied pressure. The PDDA-VM/Al devices yield a stable potential of ~ 0.8 V for more than 48 hours upon subjected to a humble pressure of 56 kPa. The natural clay-based energy devices are highly robust, various chemical and

TH-2654_156122042

thermal shocks like exposure to liquid nitrogen (-195 °C), heat pulse (450 °C), steam, and mechanical stress (100 N) did not deteriorate its performance. Moreover, multiple devices can be assembled in series or parallel add up the output current and voltages generated by individual devices to power electronic equipment.

Chapter-V: Fabrication of Pressure Responsive Energy Device from Nanofluidic Vanadium Pentoxide and Polymeric Hydrogel

Among the various power management devices, chemical potential based systems are considered to be the most reliable, convenient, and energy-efficient systems. Metal water batteries are gaining a great deal of attention owing to its unique advantages like environmental compatibility, low cost, and high energy density. In this work, we exploited the principles of metal-water batteries to fabricate a pressure-responsive energy delivery system. In the metal-water (or moisture) batteries, metal atoms are consumed at the anode, but instead of oxygen here ubiquitous atmospheric water molecules are utilized as the cathode reagent. Therefore, less expensive metals such as Mg and Al are the most attractive options of anode for these kind of batteries. In this work, we have developed a pressure responsive power delivery system by exploiting the hygroscopic nature of agar and glycerol based hydrogel and outstanding nanofluidic conductivity of freestanding V_2O_5 membrane as the solid state electrolyte and spacer. The percolated network of the molecularly sized nanochannels formed by the interlayer spaces of reconstructed V_2O_5 membrane known to exhibit high stability and proton conductivity, and hence provide an ideal platform to fabricate chemically robust, thermally stable, and environment friendly power delivering systems. A gel membrane was prepared by microwave assisted heating of an aqueous solution of agar and glycerol followed by casting on a petri-dish to form uniform 2D hydrogel films. Whereas the reconstructed membranes of V_2O_5 were prepared by lamellar stacking of V_2O_5 nanosheets exfoliated by H_2O_2 oxidation of V_2O_5 powder. In order to

TH-2654_156122042

fabricate pressure responsive energy delivering systems, a 2D film of gel was sandwiched between a pair of aluminium (Al) and reconstructed V_2O_5 membrane. Both V_2O_5 membrane and Al-foil were connected to a copper wire through conducting silver paste. When the exposed surface of the agar film was pressed (~56 kPa) on to an Al foil of similar size, it generated an open circuit potential of 1.3 V and a short circuit current of 85 µA, yielding a power density of 0.45 Wm^{-2}. The output power of the Al-gel-VO can be controlled by varying applied pressure, device dimension, and nature and concentration of electrolyte dopants. Moreover, the Al-gel-VO devices can be connected in series (or parallel) to add-up the voltage (or current) values of the individual devices. Remarkably, under ambient conditions, the Al-gel-VO devices can provide a constant potential difference up to five conjugative days. Unlike typical humidity powered energy systems, the energy output of the current device is resistant towards diurnal variations in the environmental conditions. Remarkably, both gel and V_2O_5 membrane can be completely regenerated after damage caused by prolong use or accidents without any deterioration in the energy-efficiencies Additionally, the Al-gel-VO device could open up new possibilities for environmentally friendly routes of hydrogen production and electrochemical batteries.

Conclusions:

In conclusion, restacked membranes of exfoliated layered materials such as clay minerals, graphene oxide, and vanadium pentoxide were employed for development of various environment friendly energy harvesting systems. Chapter-I describes a general overview of layered materials with special emphasis on various exfoliation techniques and application on energy harvesting techniques. Chapter-II demonstrates fabrication of mechanically robust multifunctional composite membranes using naturally abundant soil components such as vermiculite clay and humic acids. The percolated network of ultra-thin nanochannel exhibiting fascinating transport properties could find applications in the

TH-2654_156122042

areas of selective molecular/ionic transport, catalysis, energy harvesting, and storage. Such materials could be ideal in the areas like the solid state fuel cell, battery, and supercapacitor, gas sensing and separation. Chapter-III reveals that the complementary charge transfer activities of p-type and n-type semiconductor properties of r-GO flakes with water molecules can be exploited to extract energy from serene water resources. Such devices open up possibilities of fabricating wearable energy harvesting devices for applications in remote areas. Chapter-IV demonstrates a responsive and robust power delivery system based on the principles of metal-water batteries. The pressure responsive power delivery system described here exploit the hygroscopic nature of the vermiculite layers and Poly(diallyldimethylammonium chloride) based nanofluidic membrane, both as the solid state electrolyte and spacer. Chapter-V unveils a moisture based pressure responsive energy delivering system by exploiting the principles of metal water batteries. The hygroscopic nature of the gel membrane used in the Al-gel-VO devices can hold the water molecules even under extreme low humidity conditions, making it an ideal candidate for challenging applications. Additionally, the Al-gel-VO device open up new possibilities for environmentally friendly routes of hydrogen production and electrochemical batteries.

TH-2654_156122042

Table of contents

TH-2654_156122042

TH-2654_156122042

TH-2654_156122042

Chapter 1

Introduction: Two-dimensional Layered Materials for Energy Harvesting Applications

TH-2654_156122042

1. INTRODUCTION

1.1.Energy from fossils

The skill to store and harness energy from environmental resources had played a vital role in the rise of human civilization. For example, the art of controlling fire distinguished them from other animals in the early Stone Age, around a million years ago. Similarly, the agricultural revolution (started around 12000 years ago) blessed humans with the power to harvest and store energy for longer durations. The introduction of coal as the new source of energy in the 18th century marked the beginning of the industrial revolution, and eventually, petroleum and natural gas have paved their way into the industries and grew as the companion of coal towards the development the modern society. The discovery of fossils fuels has steered the ever-growing luxury of modern life. The term “fossil” represents fossilized and repressed residuals of organisms that survived millions of years ago, and the word “fuel” signifies that they are being burned to generate power. Because of the origin, fossil fuels are rich in carbon content and their burning emits carbon dioxide into the atmosphere. Carbon emissions entrap heat in the atmosphere and it eventually increases the atmospheric temperature. Therefore, though the burning of fossil fuels meets the majority of society’s energy needs, over the years it has created the issue of global warming. Along with carbon dioxide, the burning also emits other harmful gases like mercury, sulfur dioxide, and a massive amount of soot into the atmosphere. The machinery powered by fossil fuels also emits poisonous gases like carbon monoxide and nitrogen oxide. These gases end up in acid rain and smog, which imposes hazardous effects on the health of humans, animals, and plants. Along with the burning of fossil fuels, massive amounts of climate-changing emissions also occur during the extraction and transportation of fossil fuels. Similarly, the extraction and mining processes of coal, natural gas, and oil take an enormous toll on our landscapes and ecosystem. For example, in the case of strip

TH-2654_156122042

mining, vast stretches of land including forests and entire mountaintops are blasted away to access the underground reserves of coal or oil. After the operation, the sites are left with nutrient leached soil, which hardly supports the growth of plants and vegetation. Drilling and mining activities also produce huge volumes of wastewater consisting of heavy metals, radioactive materials, and other pollutants. Even though the toxic wastewaters are stored in underground wells or pits they runoff into the waterways and contaminate nearby aquatic ecosystems. Oil spills during extraction and transportation is another major cause of water pollution. Historically, the technological development of human society can be directly correlated to the amount of energy consumption. As society demands more and more power to meet the requirement of the ever-growing human population and living standards, over the years, the consumption of energy has raised to skyrocket. It is very evident from the data that until 2017, the non-renewable resources that are fossil fuels - petroleum, natural gas, and coal, fulfilled 84 % of the world's energy requirements. The rest 16 % is supported collectively by nuclear power, renewable sources such as solar, hydro, tidal energy.

Due to the severe shortage and detrimental environmental impacts of fossil fuels, a switch to sustainable energy sources is the need of the hour. Currently, energy from renewable sources meet ~ 16 % of the world's energy need, but it is significantly more expensive than fossil fuels. Thus adopting them as mainstream power sources can lead to economic disparity and hardship among societies. Therefore, the focus of energy research is shifting towards the development of an affordable mechanism to generate zero-emission clean energy from sustainable resources. Thus technological innovations to extract energy from the ambient energy sources to meet the energy-requirement are a necessity for mankind. In recent years, the superior properties of atomically thin two-dimensional materials have invited the scientific community to adventure them into energy devices towards harvesting cleaner and greener energy from otherwise futile environmental resources.

TH-2654_156122042

1.2: Two-dimensional layered materials

Materials composed of weakly bound stacks of crystalline sheets are known as layered or two-dimensional (2D) materials. The layers of 2D materials are typically held together by weak interactions such as weak-electrostatic attractions, van der Waals interactions, or hydrogen bonding. The discovery of the remarkable properties of graphene by Novoselov and Geim [1], revolutionized the ongoing research and developments of layered materials. Graphene, the isolated monolayer of graphite is a network of sp^2-hybridized carbon atoms arranged in a hexagonal honeycomb structure. Immediately after the discovery, the single-atom-thick graphene sheet has emerged as the material of superlative properties. Some of the excellent properties of graphene include the exceptional mechanical strength with a young's modulus of 1.0 TPa, remarkable conductor of heat (5000 $Wm^{-1}K^{-1}$), and electricity (10^6 Scm^{-1}) with carrier mobility exceeding 2.6 × 10^6 $cm^2/V.s$, and brilliant optical transparency of ~ 97.7 % .[2-3]

Once the size of a material is reduced to the nanometer length scale, the number of atoms at the surface becomes comparable or higher than the total number of atoms present in the interior of the material. Due to this drastic enhancement in the surface to volume ratio, the characteristics of surface atoms play dominating rules in determining the overall properties of the material, which is insignificant in the bulk state. This surface-dominated property of the material opens-up plenty of new avenues of applications. With plenty of exposed surfaces, 2D nanomaterials are providing promising platforms for numerous applications such as energy conversion,[4-6] energy storage,[7] microelectronic components,[8] water treatments,[9-12] and catalysis.[13-15]

The discovery of outstanding properties of graphene also drove the attention of the scientific community towards the exploration of other 2D materials. Within a short period

TH-2654_156122042

(in 2005), Noveselov et al. demonstrated the existence of similar unique properties on exfoliated layers of boron nitride.[16] Hexagonal boron nitride (h-BN) also known as "white graphene" is a structural isomorph of graphene with alternate B and N atoms forming the honeycomb structure. Nanosheets of h-BN exhibit excellent transparency (~ 99 %) with an optical band gap of 6.07 eV ,[17] and hence, possess remarkable potentials of applications in optoelectronic devices.[18-19] Possessing a wide range of unique properties like ultrafast thermal conductivity, excellent mechanical and chemical robustness, high BET surface area, and wide band-gap, h-BN has attracted widespread attention towards the fabrication of electronic devices,[20-22] ultraviolet light-emitting devices ,[23-24] actuators,[25] and energy harvesting devices.[26-28]

Clay minerals are another class of naturally abundant layered material that belongs to the phyllosilicate family. The individual layers of clay are comprised of tetrahedral silicate sheets attached to octahedral aluminate sheets in different ratios such as 1:1, 2:1, and 2:2. Based on the arrangement of tetrahedral and octahedral layers, clay minerals are further classified into various types such as kaolinite, vermiculite, smectite, illite, chlorite, and so on. [29-30]

Clay minerals have gained significant attention in the research community because of their unique properties such as high cation exchange capacity, high aspect ratio, high surface area, excellent thermal and chemical robustness, water holding capacity, and capability of hosting organic molecules and nontoxicity. [31-33]

Transition metal dichalcogenides (TMDs) (MoS_2, $MoSe_2$, WS_2, NbS_2, WTe_2, etc) are a diverse class of naturally abundant layered materials with a monolayer formula of MX_2, where M is a transition metal from group IV to group VII and X is a chalcogen of S, Se, or, Te held together by weak van der Waals interaction. TMDs possess an assorted range

TH-2654_156122042

of electronic properties from semiconducting to metallic relying on their geometry, electron density, and composition.[34-35] MX_2 nanosheets are a direct bandgap semiconductor with a bandgap energy of 1.0-1.4 eV,[36] which makes them a potential candidate for a wide range of application such as in the energy harvesting and conversion devices ,[37-38] optoelectronics ,[39] field-effect transistors[40] and so on. Some other classes of 2D materials that have been extensively studied for energy harvesting and energy storage devices are layered double hydroxides,[41-42] carbon nitride,[43] Mxene,[44-45] and 2D metal oxides.[46] It is noteworthy that the isolation process of 2D nanosheets from their bulk counterparts is critically important for achieving superior properties, and hence, exfoliation/synthesis of the layered materials is gaining more and more importance in this research community.

1.3: PREPARATION OF 2-D MATERIALS

1.3.1: Top down methods

The top-down methodology involves exfoliation of bulk crystals into isolated 2D flakes, which were held together by weak interactions such as van der Waals forces. The top-down approach can be further categorized into mechanical and chemical processes.

The mechanical exfoliation process is known to yield high-quality mono- or few-layer nanocrystals from their bulk counterpart. It typically involves peeling/tearing of interfaces of adjacent layers. Mechanical exfoliation can also be broadly classified into techniques such as micromechanical cleavage, ball milling, and sonication. The micromechanical cleavage process is popularly known as the “Scotch tape method” is the first-ever mechanical exfoliation process applied to peel off graphene flakes from graphite in 2004.[1] This involves the application of adhesive tapes to mechanically cleave the bulk crystals repeatedly to obtain monolayer or few-layer 2D materials. Through this technique one can

TH-2654_156122042

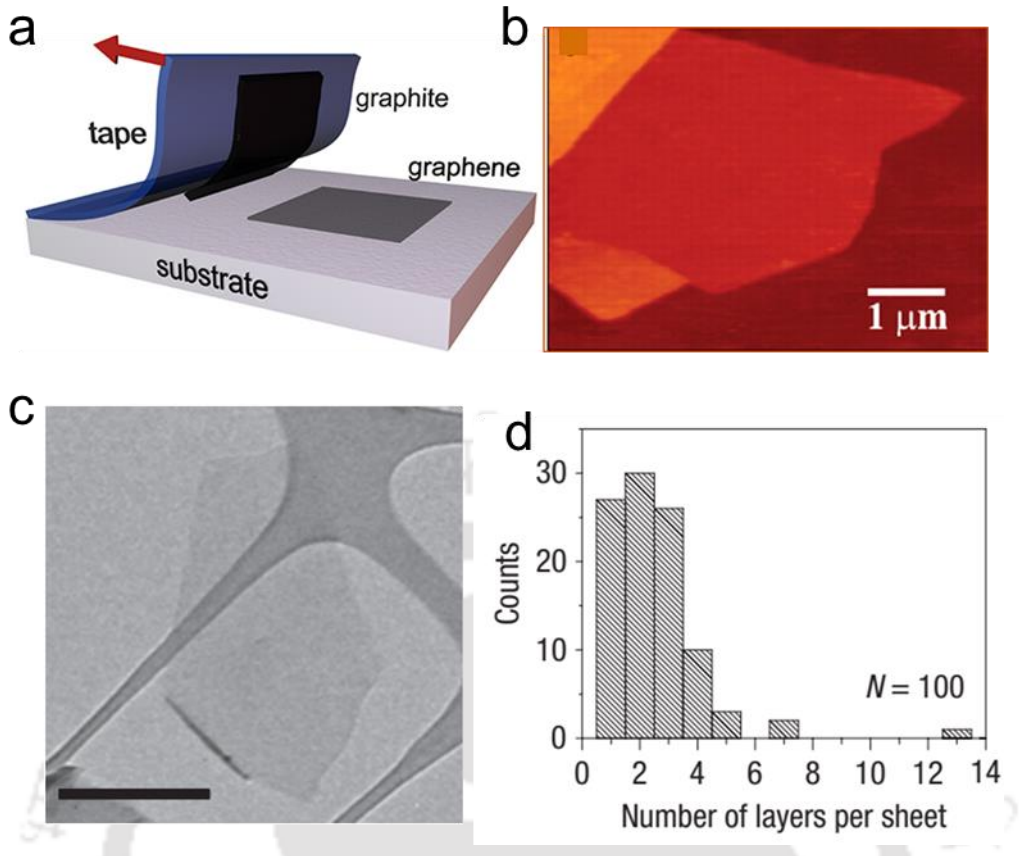

Figure 1.1: Bottom up methods of exfoliation: (a) Schematic showing scotch tape exfoliation of graphite to graphene, (b) AFM image of a single layer graphene sheet. Dark Brown color is the SiO_2 surface; brown-red (central region) is of height 0.8 nm ; yellow-brown (bottom left) is of height 1.2 nm; orange (top left) is of height 2.5 nm. (c) Bright-field TEM image of a single layer graphene sheet deposited from NMP (scale 500 nm). (d) Histogram showing number of visual observations of graphene flakes as a function of number of monolayers per flake for NMP dispersions. (Images copied from (b) Science, 2004, 206, 666-669. (c)-(d) Nat. Nanotechnol. 2008, 3, 563-568)

produce very high-quality monolayer samples but unsuitable for large-scale production, thus restricting its application only to fundamental and prototype research. Sonication is a solvent-assisted exfoliation technique that aims to exfoliate the bulk layered materials into their two-dimensional counterparts via sonication in organic solvents such as N-methyl pyrrolidone (NMP) and isopropanol. For example, in 2008, Colman et al. demonstrated a solvent (NMP) assisted exfoliation process of graphite, that has the potential of achieving large-scale production .[47] This method was further extended to obtain nanoflakes of controlled lateral dimension by tuning the sonication and centrifugation conditions.[48] Over the past years, a similar solvent-assisted exfoliation process has been applied to a wide range of other layered materials such as MoS_2, $MoSe_2$, $MoTe_2$, WS_2, BN, and Bi_2Te_3.[49]

TH-2654_156122042

Ball milling or mechanical alloying is another important technique applied for the synthesis of nanomaterials. The ball milling process involves grinding the crystals into nanometer-sized fine powders. The collisions between rigid balls in the sealed container generate the

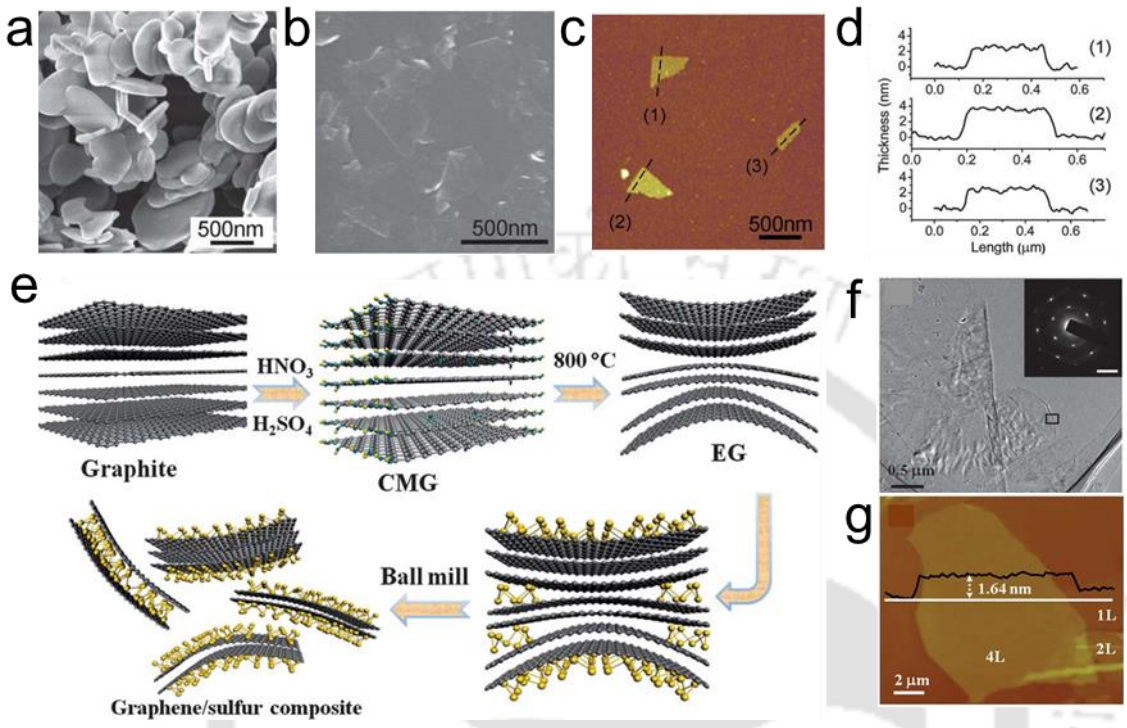

Figure 1.2: Ball milling as an exfoliation technique: (a) SEM image of the hBN particles before exfoliation. (b) SEM image of BN nanosheets exfoliated by ball milling. (c) AFM image of exfoliated BN nanosheets. (d) Height profiles of the BN nanosheets. (e) Schematic showing the exfoliation of graphite to graphene by dry ball milling. (f) TEM image and corresponding SAED pattern of exfoliated graphene/sulfur composite. (g) AFM image along with the height profile of the exfoliated nanosheets. (Images copied from (a)-(d) J. Mater. Chem. 2011, 21, 11862–11866. (e)-(f) Energy Environ. Sci., 2013,6, 1283-1290

shear force required for the exfoliation process. A wet ball milling process was adopted by Zhao et al. (in 2010) to exfoliate graphite into graphene flakes by using N, N-dimethylformamide (DMF) as the solvent medium, a planetary mill for 30 hours with a rotatory speed of 300 rpm. The choice of the solvent is crucial for the ball milling process. For example, Zhao et al. exploited the strong graphene-DMF interaction to overcome the weak van der Waals interaction between graphite layers, which leads to successful exfoliation of graphene sheets.[50] In 2011, Li et al. performed controlled ball milling of h-BN crystals to obtain 2D nanosheets of h-BN in high yield.[51] Besides wet milling, dry

TH-2654_156122042

milling has also been applied for the exfoliation of nanomaterials. Lin et al., exploited the favorable interaction between graphene and sulfur atoms to cleave the graphene layers. This process simultaneously functionalizes the edges and surface of graphene flakes with Sulphur molecules.[52] Though ball milling evolved as an effective method for large-scale production of 2D nanomaterials, control over the milling parameters such as milling speed, size of the balls, milling agent, ratio of ball-to-powder are obligatory for optimum production.

Ion intercalation is a prominent chemical exfoliation process, in which the van der Waals interactions between the layers are weakened through the intercalation of appropriate ions. Transition metal dichalcogenides with moderately large interlayer distance and weak interaction between the layers are an easy candidate for alkali metal intercalation into the spacious layers. This technique was first demonstrated by Joensen et al. in 1986, to isolate single-layer MoS_2 using n-butyl lithium (in hexane) as intercalating agent.[53] Li insertion morphs the local crystal structure in MoS_2 to transform the 2H phase to metallic 1T phase with desired optical and electronic properties for futuristic applications. Shortcomings of ion intercalation technique include high operational temperature along with longer reaction time, typically up to several days. Another major drawback is disproportionate lithiation resulting MoS_2 decomposition or LiS_2 precipitation due to over lithiation while incomplete Li insertion leading to a lower yield of single-layer sheets. A separate technique based on an electrochemical process was developed by the Zhang group to achieve a high yield of single-layer 2D materials, with controllability over the extent of Li insertion .[54] In this method, bulk layered materials (such as MoS_2, WS_2, TiS_2, TaS_2, ZrS_2, and graphene) is used as the cathode material while a Li foil is used as the anode of an electrochemical test cell. Controlled insertion of Li is carried out during a galvanostatic discharge process followed by subsequent exfoliation in water or ethanol. The same group also studied the

TH-2654_156122042

effect of cut off voltages and discharge current to produce high-quality inorganic nanosheets such as BN, $NbSe_2$, WSe_2, Sb_2Se_3, and Bi_2Te_3. [55]

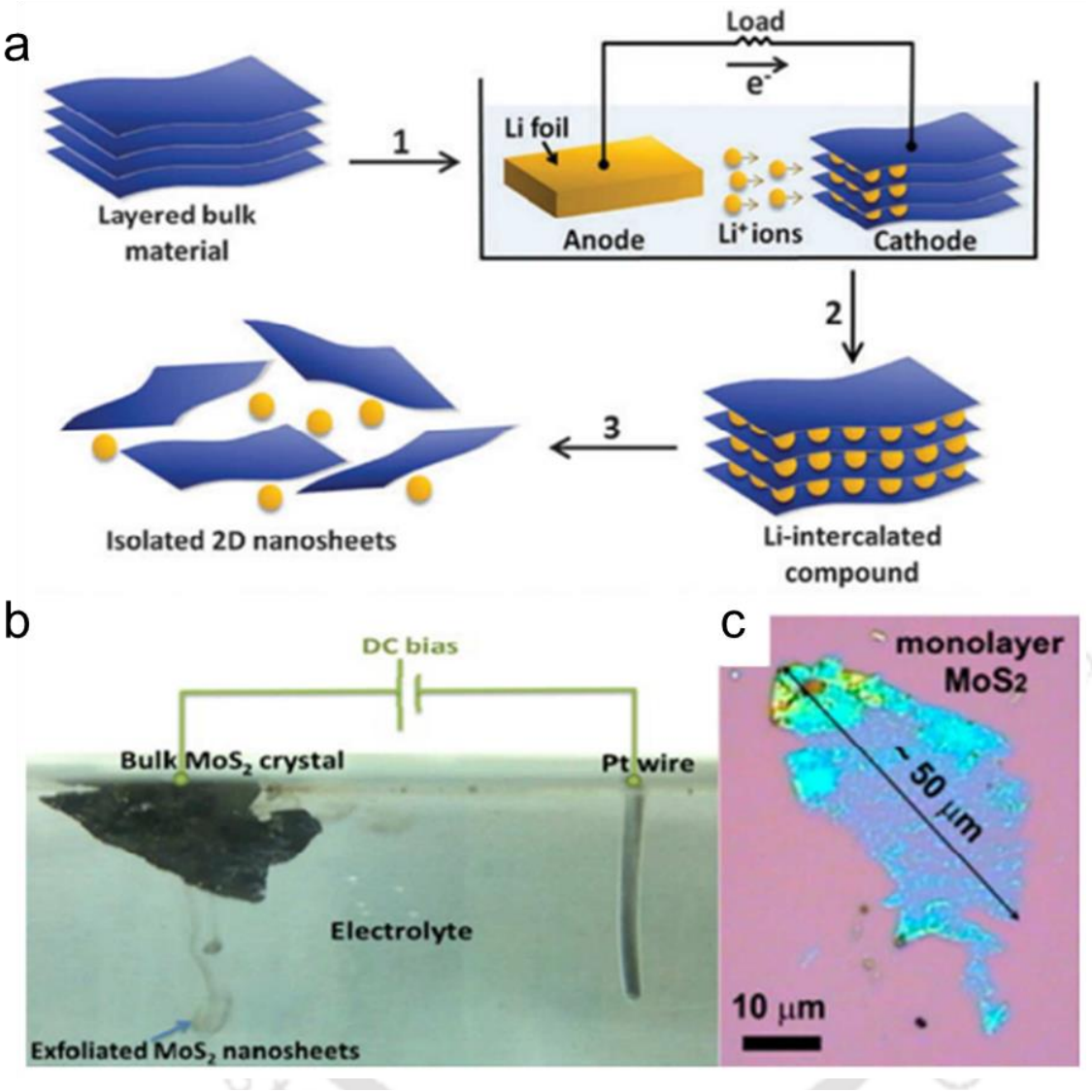

Figure 1.3: Ion intercalation as an exfoliation technique: (a) Schematic showing exfoliation of layered bulk crystals to obtain 2D nanosheets by electrochemical lithiation. (b) Experimental setup for electrochemical exfoliation of bulk MoS_2. (c) Optical microscope image of monolayer MoS_2 nanosheet obtained by electrochemical exfoliation process. (Images copied from Nanoscale 2015,7, 19358-19376)

A similar genre of liquid exfoliation is the ion-exchange method, where intercalated ions of smaller size are exchanged with ones of a relatively bigger size. Intercalation of larger ions expands the space between the layers thus weakens the interaction between the neighboring layers. Layered materials with weaker attractions between the neighboring layers can be exfoliated into 2D nanostructures through mechanical shaking or sonication.

TH-2654_156122042

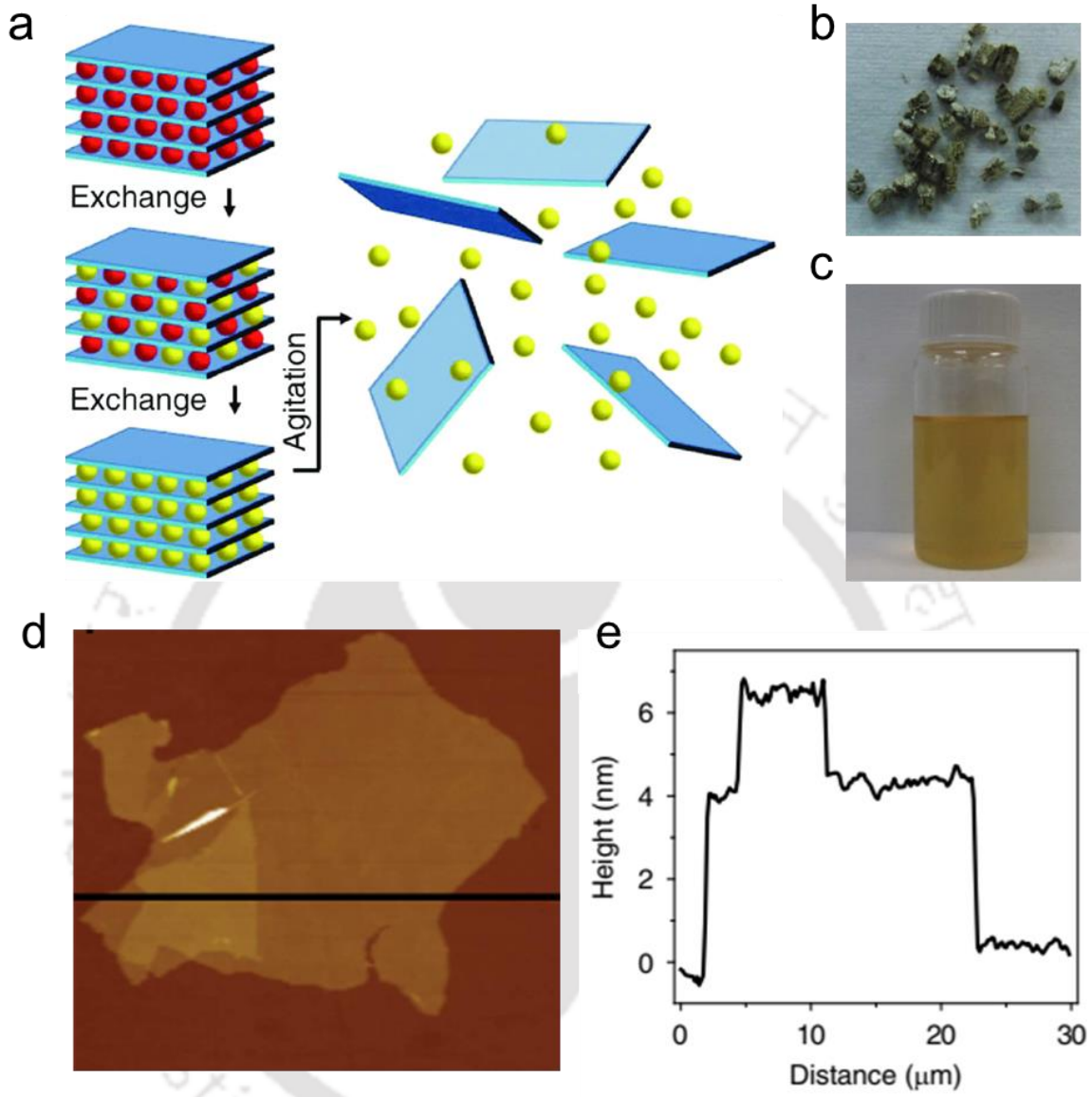

Figure 1.4: Ion exchange exfoliation of vermiculite clay: (a) Schematic showing exfoliation of clay layers by two step ion-exchange method. (b) Photo of raw vermiculite crystals. (c) Aqueous dispersion of exfoliated clay nanosheets. (c) AFM image of exfoliated vermiculite nanosheets. (d) AFM height profile of the exfoliated nanosheets. (Images copied from (b)-(e) Nat. Commun. 2015, 6, 7602-7609)

1.3.2: Bottom up methods

The bottom-up approach involves self-assembling of atomic or molecular precursors into more complex structures with nanometer dimension. Building up a nanoscale system from its smallest units can establish a thoroughgoing control over the morphology, dimension, and properties. For example, Nag et al. demonstrated the preparation of few-layer BN

TH-2654_156122042

flakes by the reaction between boric acid and urea at 900 °C in the N_2 atmosphere.[56] Controlling the ratio of urea and boric acid in the precursor mixture could tune the number of BN layers in the flakes. For example, the number of BN layers varied from 8-14 for a sample prepared by boric acid:urea ratio of 1:12 to 1-4 layers for precursor ratio of 1:48.

Chemical vapor deposition is the most recognized technique used for the bottom-up synthesis of 2D materials with superior qualities. Numerous methodologies have been developed to extend the CVD technique to a wide range of 2D materials.

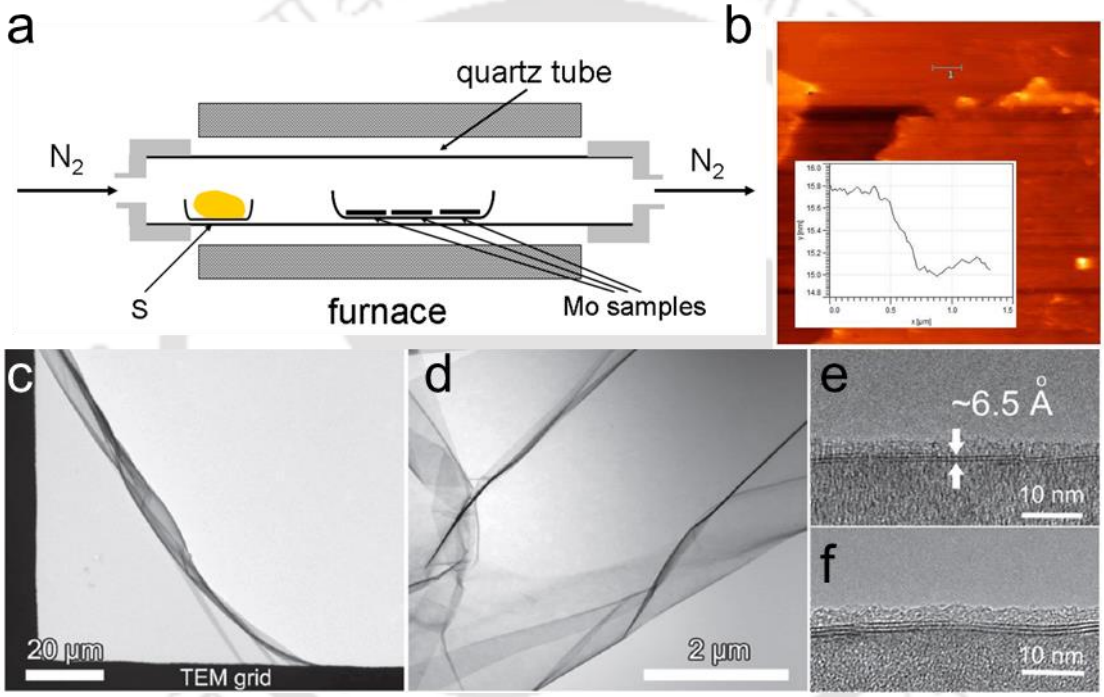

Figure 1.5: Chemical vapor deposition for exfoliation of MoS_2: (a) CVD set-up for synthesis of MoS_2 nanosheets. (b) AFM image and corresponding height profile of a single layer MoS_2 of thichness 0.7 nm. (c) TEM image of a mono layer MoS_2 nanosheet covering a TEM grid. (d) TEM image of the single layer MoS_2 magnified at the edge area. (e) and (f) are the HRTEM image of two and three layer MoS_2 respectively. (Images copied from Small 2012, 8, 966-971)

The growth of large-area graphene films (in the order of centimeters) on copper foil achieved through the CVD process is considered to be a critical breakthrough towards the fabrication of large-scale devices.[57] In the past decade, a number of CVD-based techniques were developed to grow atomically thin films of MoS_2. For example, a two-step thermal annealing process involving thermal decomposition (at 500 °C) of ammonium thiomolybdate layer dip-coated to an insulating substrate followed by high-temperature

TH-2654_156122042

annealing (1000 °C, in the presence of sulfur) has been reported to produce large-area MoS_2 films with superior electrical properties.[58] Zhan et al. reported another methodology for the direct transformation of Mo metal into MoS_2 layers of a large area by a CVD-induced sulfurization process.[59] Typically, SiO_2 substrate coated with a thin layer of Mo was reacted with sulfur gas at 750 °C to form thin films MoS_2 ranging from single to few layers. In another report, Lee and coworkers demonstrated an alternative CVD method to yield thin films of MoS_2 by the gas-phase reaction of MoO_3 and S powders on Si substrate.[60]

The application of wet or chemical methodologies for the synthesis of 2D materials is another promising bottom-up approach with a number of practical advantages like simplicity and low-cost instrumentation. Some of the well-known strategies under this category include hydrothermal or solvothermal synthesis, electrodeposition, sol-gel method, and microwave-based synthesis. In the hydrothermal method, autoclaves or reactors containing the suitable chemical precursors in liquid medium are subjected to an appropriate temperature range (100-250 °C), and a self-generated high pressure. In 2001, Peng et al. synthesized single-layer MoS_2 and $MoSe_2$ with the large surface area through hydrothermal treatment at 150- 180 °C.[61] A wide range of 2D nanosheets of transition metal oxides such as MnO_2, TiO_2, Fe_3O_4, ZnO, V_2O_5, and Co_3O_4 was prepared by the hydrothermal treatment.[62] In the hydrothermal process, the particle size can be regulated by various parameters such as temperature, reaction time, solvent type, and precursor concentration. [63]

Microwave-assisted exfoliation is another potential and versatile technique with clear advantages such as dielectric loss instead of heat transfer, which in turn facilitates fast and homogenous heating, eco-friendliness, and higher energy efficiency. Thus, atomically thick nanosheets of layered materials such as graphite, TMDs, h-BN, g-C_3N_4, and $Ti_3C_2T_x$

TH-2654_156122042

have been successfully obtained by microwave-assisted heating.[64-65] In a report by Matsumoto et al., single-layer graphene nanosheets (thickness <1 nm) with high efficiency of exfoliation (93 % yield) were obtained through microwave irradiation of graphite in ionic liquids. [66]

Electrochemical deposition emerged as an attractive synthesis approach for the preparation of nanostructured metallic materials in the form of laminar coatings or freestanding foil. Usually, a metallic coating is formed by the reduction of precursor ions in an aqueous or organic solution. A cathodic substrate reduces the charged ions in the solution, and a metallic coating is deposited on the substrate. Electrodeposition has also been applied for the fabrication of a wide range of metal chalcogenides nanostructures.[67] In 2001, Prieto et al. electrodeposited Bi_2Te_3 nanowires into porous alumina templates with a uniform pore diameter of 40 nm.[68]

1.4: ENERGY HARVESTING APPLICATIONS

1.4.1: Mechanical energy harvesting

(A) Piezoelectric nanogenerators: Piezoelectricity defines as the building-up of electric charges in solid materials (typically with a non-centrosymmetric structure) in response to an externally applied mechanical deformation. Though the piezoelectric effect was first established in 1880, the advent of energy harvesting through piezoelectric nanogenerators (PENGs) started only after the advancement of low dimensional piezoelectric materials with an excellent electromechanical response. The vertically aligned dipoles in a piezoelectric material get deformed by the external mechanical disturbance, and the potential generated by the mechanical disturbance of dipoles is balanced by the movement of electrons through the external circuit. Wang et al. introduced the first PENG in 2006 by taking aligned ZnO nanowires as an example.[69] A charge separation was created

TH-2654_156122042

across the ZnO NW through bending, which generates a pulsing electric current with an efficiency of 17- 30 %. Despite the low output voltage (9 mV), demonstration with the ZnO NW created a precedent among the scientific community to use piezoelectric materials to convert mechanical energy into electrical energy.

In recent years, the 2D semiconductor TMDs emerged as excellent piezoelectric materials

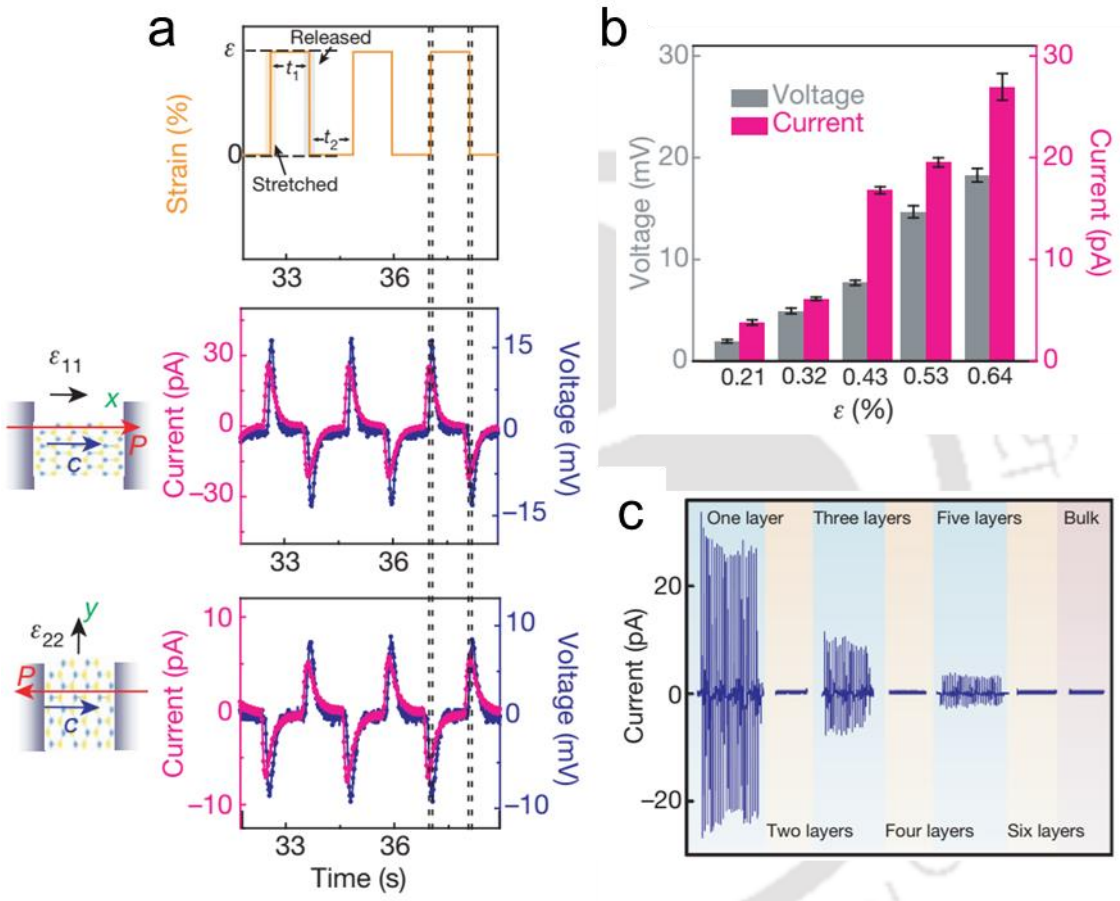

Figure 1.6: Piezoelectric nanogenerators based on mono-layer and few layer MoS_2: (a) Demonstration of output voltage and current responses of a mono-layer MoS_2 device under the influence of periodic strain in armchair and zigzag direction. (b) Piezoelectric outputs as a function of applied strain in a mono-layer MoS_2 device. (c) Output current as a function of number of atomic layers of MoS_2. (Images copied from Nature 2014, 54, 470-474)

with high piezoelectric constant and flexibility. Based on a theoretical prediction of monolayer MoS_2 exhibiting strong piezoelectricity,[70] Wang et al. developed the first experimental piezoelectric nanogenerators with exfoliated 2D nanomaterial.[71] Upon application of 0.64 % strain, the flexible and transparent nanogenerator fabricated by using monolayer MoS_2 generated an output voltage of 18 mV (current ~ 27 pA). The output

TH-2654_156122042

performance of the devices was also studied as a function of atomic layers of MoS_2. It was found that the devices with an even number of MoS_2 layers did not show any output voltage or current whereas the devices with odd numbers of MoS_2 layers displayed a positive output power, which decreased with an increasing number of layers. These results suggested that the monolayer MoS_2 has intrinsic piezoelectric characteristics whereas bulk MoS_2 with centrosymmetric bilayers is nonpiezoelectric.

(B) Triboelectric nanogenerators: Triboelectric nanogenerators (TENGs) work on the principle of the triboelectric effect and electrostatic effect to harness electricity from mechanical energy. The basic mechanism involves contact electrification at the interface of two triboelectric materials with opposite polarity followed by electron transfer to develop electrostatic charges of opposite polarities on the surface of triboelectric materials. The first-ever design of triboelectric nanogenerator was accomplished by the Zhong Lin Wang group in 2012 by rubbing two polymers with different triboelectric characteristics.[72] Ample of sources of mechanical energy is available in our surroundings in the form of human/animal movements such as walking, running, flowing water, and wind, which is getting wasted otherwise. An appropriate combination of triboelectric materials can be applied to harvest the waste mechanical energy into electrical energy.[73-76] Meanwhile, 2D materials with triboelectric characteristics possess several advantages over traditional triboelectric materials like large surface to volume ratio, transparency, stackable layers, flexibility, and ultrathin film feasibility, and came into the forefront for futuristic applications in TENG-based devices.

Graphene as a triboelectric material was first reported by Kim et al. in 2014, based on its combined ability to store electric charge induced by triboelectrification as well as its

TH-2654_156122042

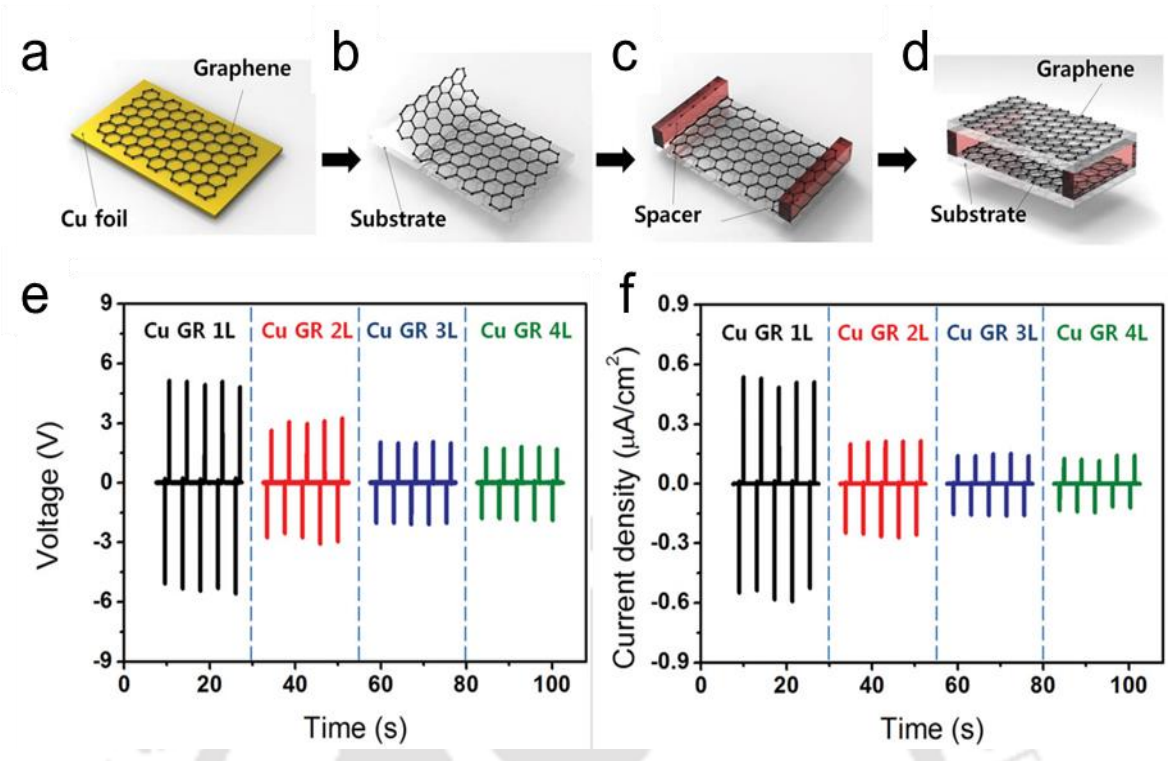

Figure 1.7: Triboelectric nanogenerators based on transparent and flexible graphene: Schematic illustration of (a) CVD grown 1 later graphene on Cu foil, (b) transferred to PET substrate, (c) incorporation of plastic spacer, and (d) integration of 1 layer graphene with PET/graphene as top electrode. (e) Output voltage and (f) current density as a function of time for 1 layer, 2 layer, 3 layer and 4 layer graphene grown on Cu foil. (Images copied from Adv. Mater. 2014, 26, 3918–3925)

conductive nature to be used as electrode for flow of electricity in the outer circuit.[77] Flexible and transparent TENGs were constructed by employing monolayer, bilayer, trilayer, and quad-layer graphene flakes, and a maximum output voltage of 3 V was recorded for monolayer graphene. These results were followed up by several other graphene-based TENGs.[78-82]

Recently, Seol et al. carried out elaborate studies on triboelectric behavior of various 2D materials such as MoS_2, WS_2, $MoSe_2$, WSe_2, graphene, and graphene oxide (GO) and subsequently arranged them in a triboelectric series.[83] The position of various 2D materials was determined by employing nylon (the most positive material) as the complimentary reference material in a simple pushing type TENG device. The output performances of the devices were also studied by using PTFE, PDMS, polycarbonate (PC), PET, and mica as complementary to various 2D materials. While MoS_2 and $MoSe_2$ were found to be

TH-2654_156122042

relatively negative with a position set between PTFE and PDMS, the other materials such as WS_2, WSe_2, graphene and GO were found to be slightly positive and placed between PDMS and PC. The device comprised of MoS_2 yielded the highest output current and voltage indicating that MoS_2 possesses the most negative triboelectricity in the 2D triboelectric series. This study provided a clear vision of the triboelectrification in 2D materials for futuristic TENG devices.

1.4.2: Photovoltaics: Photovoltaic refers to the technology that directly converts sunlight into electricity. Being the most abundant source of renewable energy on earth, solar energy can be easily exploited as a replacement for conventional energy sources. 2D materials with fascinating electronic and optical properties offer a promising platform for the next generation photovoltaic devices. The formation of strongly bound excitons offered by quantum and dielectric confinement in 2D materials is vital for photovoltaic applications.[84] For example, Yang et al. introduced a graphene oxide interface to design graphene/GO/Si Schottky junction solar cells with a power conversion efficiency of 6.18 %.[85] In a separate report, Liu et al. used monolayer graphene as the top electrode in a semitransparent organic solar cell high power efficiency of 2.7 %, much higher than the conventional ITO electrodes, which was attributed to the better transmittance of graphene electrodes.[86] Apart from graphene, TMDs (mostly MoS_2, WS_2, and $MoSe_2$) are also considered to excellent candidates for the photovoltaic applications, mainly because of their optical response and strong absorption (up to 5- 10 %) of the incident sunlight.[87-88] For instance, Tsai et al. designed photovoltaic devices based on monolayer MoS_2 on Si substrate with a photocurrent density of 22.36 mA cm^{-2} (efficiency ~ 5.2 %).[89] In another report, Pospischil et al. demonstrated a monolayer WSe_2 based photovoltaic solar cell with a power output of 9 pW with an efficiency of 0.5 %.[90]

TH-2654_156122042

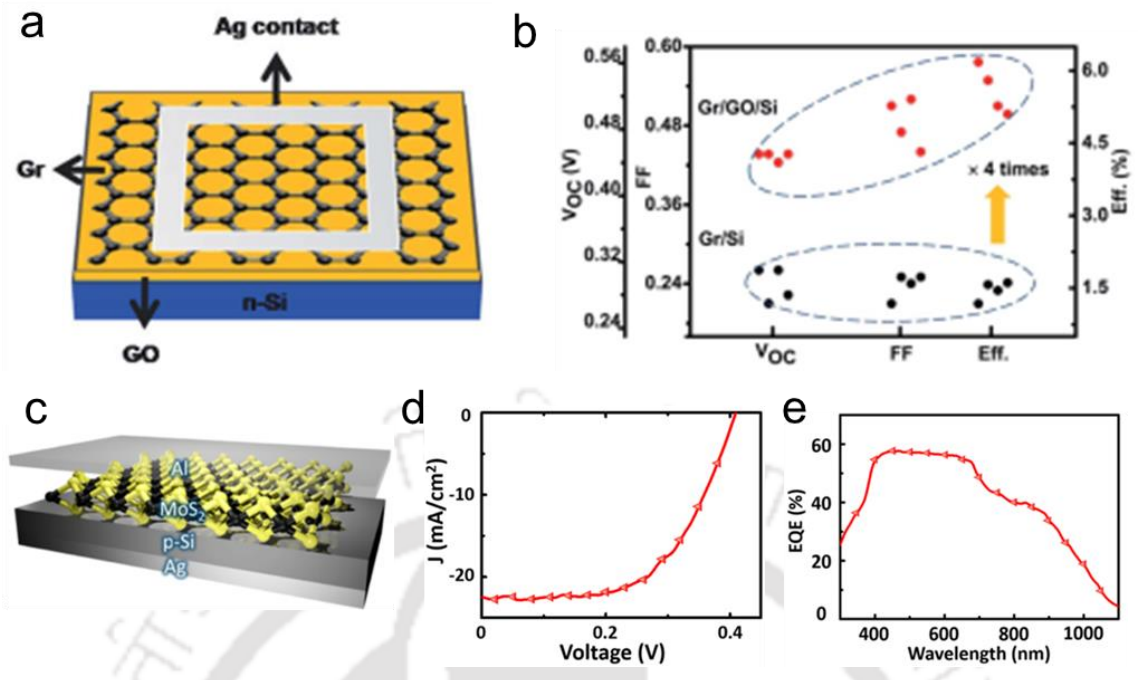

Figure 1.8: Two dimensional nanomaterials for photovoltaic applications: (a) Schematic demonstration of device configuration of a Gr/GO/Si solar cell. (b) Graphical distribution of open-circuit voltage, fill factor and efficiency of Gr/GO/Si solar cell. (c) Device configuration of MoS_2/p/Si solar cell. (d) Characteristic J-V plots and (e) EQ spectra of MoS_2/p/Si solar cell. (Images copied from (a)-(b) J. Mater. Chem. A, 2014, 2, 16877–16883. (c)-(e) ACS Nano 2015, 8, 8317-8322)

1.4.3: Hydrovoltaics: Water being the most abundant and widely available resource on earth, store a colossal amount of energy in various forms, but till date, only a little fraction of the same is being harnessed. While hydroelectric stations extensively harness the kinetic energy of the flowing water, the water-splitting process is being explored for harnessing the chemical energy stored in the individual water molecules.[91] Extraction of water-energy through these strategies requires large infrastructures, the backing of electricity, and efficient photocatalysts. [92-93]

Supported by the recent developments in nanotechnology, a new class of water-based energy harvesting strategy known as “hydrovoltaics” has been demonstrated; where the interaction of water molecules with nanostructured materials is exploited for the generation of electrical energy.

TH-2654_156122042

1.4.3.1: Streaming Potential: Streaming potential is an electrokinetic phenomenon that occurs during the relative motion between fluid and charged solid surfaces. Typically, at the solid/liquid interface, an electrical double layer (EDL) is formed to balance the excess charges present in the solid surface. EDL is composed of an immobile stern layer of counterions and a diffused layer of mobile co-ions known as the Gouy diffuse layer. When fluid is driven through the channel of charged walls by applying external pressure, a streaming current is generated due to the unipolar motion of the diffuse layer, which eventually breaks the electroneutrality of the flowing liquid.

In 2003, Ghosh et al. developed a hydrovoltaic nanogenerator by flowing water over a bundle of carbon nanotubes.[94] A potential of 2.1 mV was generated by flowing water with a flow velocity of 6×10^{-4} m/s, which was substantially decreased to 0.2 mV upon flowing non-polar solvents such as methanol. The flow-induced voltage was also found to be dependent on the ionic strength of the flowing liquid; As compared to that of DI water, a five-fold enhancement in the potential value was reported with an electrolyte of 1.2 M HCl. The streaming potential value was also reported to be varying linearly with the varying flow velocity, with excellent sensitivity for a velocity as low as 5×10^{-6} m/s.

In 2011, Dhiman et al. reported the generation of power by flowing hydrochloric acid (HCL) of different molarities over few-layered graphene films grown on silicon substrate by using the CVD process.[95] Power density up to 175 W/m^2 was reported to be achieved by flowing 0.6 M HCl over 30 ×16 μm graphene film with a flow velocity of 0.01 m/s. The flow of current was attributed to the drifting of Cl^- ions along the flow direction. Combining with water molecules, the H^+ ions form stable hydronium ions and flows along with the water molecules without interfering with surface hoping Cl^- ions.

TH-2654_156122042

In 2013, Guo et al. demonstrated the first pressure-driven nanofluidic generator based on the restacked membrane of chemically converted graphene hydrogel.[96] Flowing an ionic solution (0.1 M NaCl) through negatively charged nano capillaries of graphene by applying a gas pressure (5 kPa) generated a streaming current of around 2 nA.

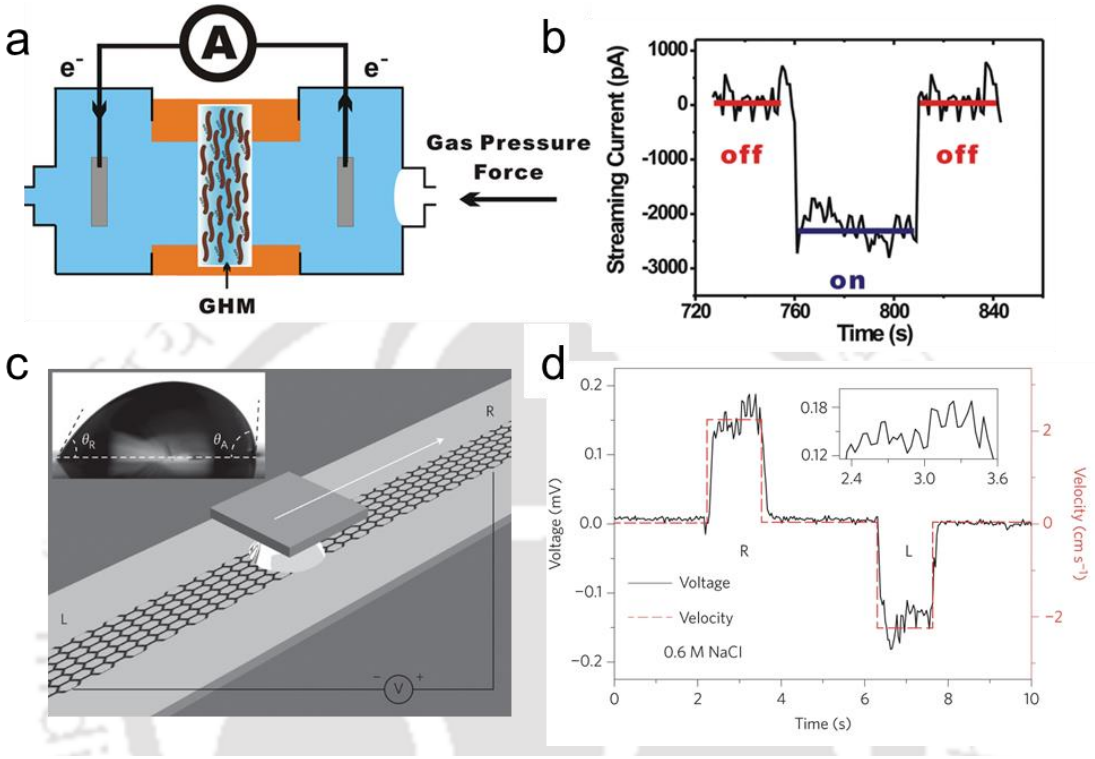

Figure 1.9: Electrokinetic streaming potential in two dimensional nanomaterials: (a) Schematic illustration of experimental set up for pressure-driven nanofluidic generator based on graphene hydrogel membrane. (b) Streaming current generated on flowing 0.1 M NaCl solution across the hydrogel membrane. (c) Experimental set-up demonstrating voltage generation upon moving a liquid droplet over monolayer graphene. (d) generation of voltage signals upon moving a droplet of 0.6 M NaCl solution left to right, inset shows voltage generation during droplet movement. (Images copied from (a)-(b) Adv. Mater. 2013, 25, 6064-6068. (c)-(d) Nat. Nanotechnol. 2014, 9, 378-383)

In 2017, Yin et al., reported the generation of electrical potential upon moving a droplet of ionic water over monolayer graphene flakes.[97] An output voltage of ~ 0.15 mV was reported to be obtained by moving a droplet containing 0.6 M NaCl at a constant speed of 2.25 cms^{-1}, whereas no notable potential was obtained when the movement was stopped. The adsorption of hydrated Na^+ ions and repulsion of Cl^- ions on graphene surface forms a thin layer of accumulated electrons along the interface of graphene-liquid. The movement of droplets accumulates Na^+ ions in the front end and it draws the electrons in the forward

TH-2654_156122042

direction generating a potential difference. The same group also demonstrated the generation of electricity by the motion of monolayer graphene on PET substrate in and out of ionic solutions by creating a water wave.[98] Open circuit potential and short circuit current up to 0.1 V and 11 µA was generated at a velocity of 1 m/s.

1.4.3.2: Reverse electrodialysis:

Reverse electrodialysis is yet another electrokinetic phenomenon exploited for the harvesting of electrical energy. In this process, devices with multiple chambers of electrolyte solutions were prepared, where semipermeable membranes separate the solutions with different electrolyte concentrations. The gradient of the chemical potential formed at the interface of the two liquids spontaneously drives ions of specific charges across the perm-selective membrane yielding a net flux of selective ions. Membranes with excellent nanofluidic ionic conductivity and ion-selectivity are the emerging candidates for the osmotic power generation.

Siria et al. fabricated nanofluidic devices of single boron nitride nanotubes (BNNT) to harvest osmotic power of several orders of magnitude higher than that of the commercial RED devices. A 1000 fold concentration gradient across a single BNNT generated a power density up to 4 kW/m^2. Feng et al. employed a cation-selective membrane of monolayer MoS_2 to develop an osmotic power generator. The selective flow of K^+ ions through negatively charged MoS_2 channels generated a power density as high as 106 Wm^{-2}. [99]

Recently, Ji et al. reported a 2D material-based osmotic power generator, containing lamellar nanochannels of oppositely charged graphene oxide membranes.[100] The polarity of the surface charges of the GO membrane was tuned by chemically modifying its functional groups. An output power density of 0.77 W m^{-2} was attained by arranging the positively and negatively charged membranes in alternative manners. Besides simple salt

TH-2654_156122042

solutions, the working of the devices was also demonstrated with various other sources such as fruit juice, acid rain, industrial waste, human urine thus extending its wide applicability from household to industries.

Guo et al. demonstrated the fabrication of exceptional nanofluidic systems, consisting of

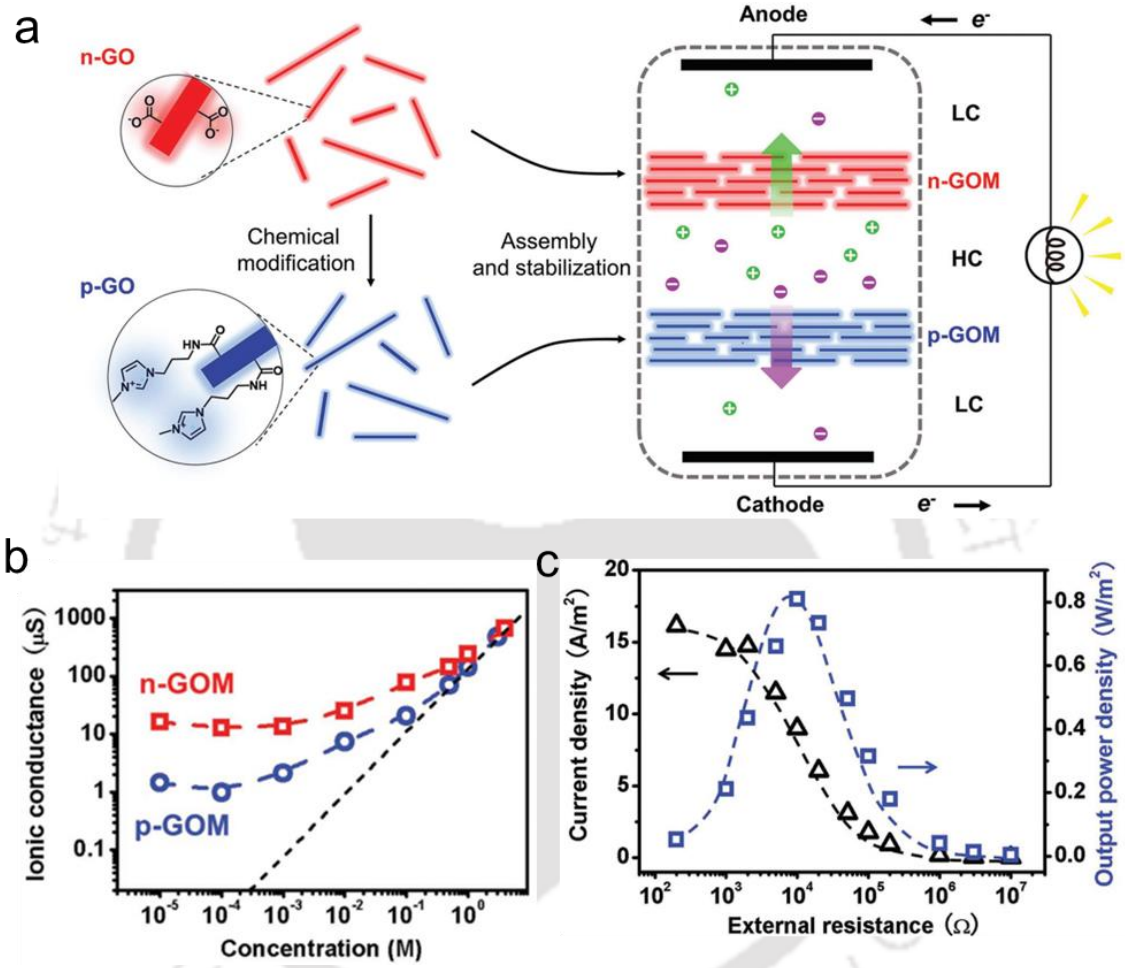

Figure 1.10: 2D material based osmotic power generator: (a) Schematic diagram to illustrate modification graphene oxide for fabrication of nanofluidic energy harvesting device. (b) Surface charge governed ionic conductance of positively charged and negatively charged graphene oxide nanofluidic devices. (c) Output power as a function of external load resistance. (Images copied from Adv. Func. Mater. 2017, 27, 1603623)

two distinct channels of variable heights and divergent surface properties, by using naturally occurring clay minerals. The interconnected network of 2D nanochannels of exfoliated kaolinite clay minerals was also exploited to harvest osmotic power up to 0.18 Wm^{-2} under a transmembrane concentration gradient of 100 fold.[101]

TH-2654_156122042

1.4.3.3: Evaporation

Xue et al. applied the natural evaporation process of water molecules from the surface of carbon black sheets to generate sustainable electricity.[102] Voltage up to 1 V was shown to generate for 8 continuous days, which was also accompanied by a short circuit current of

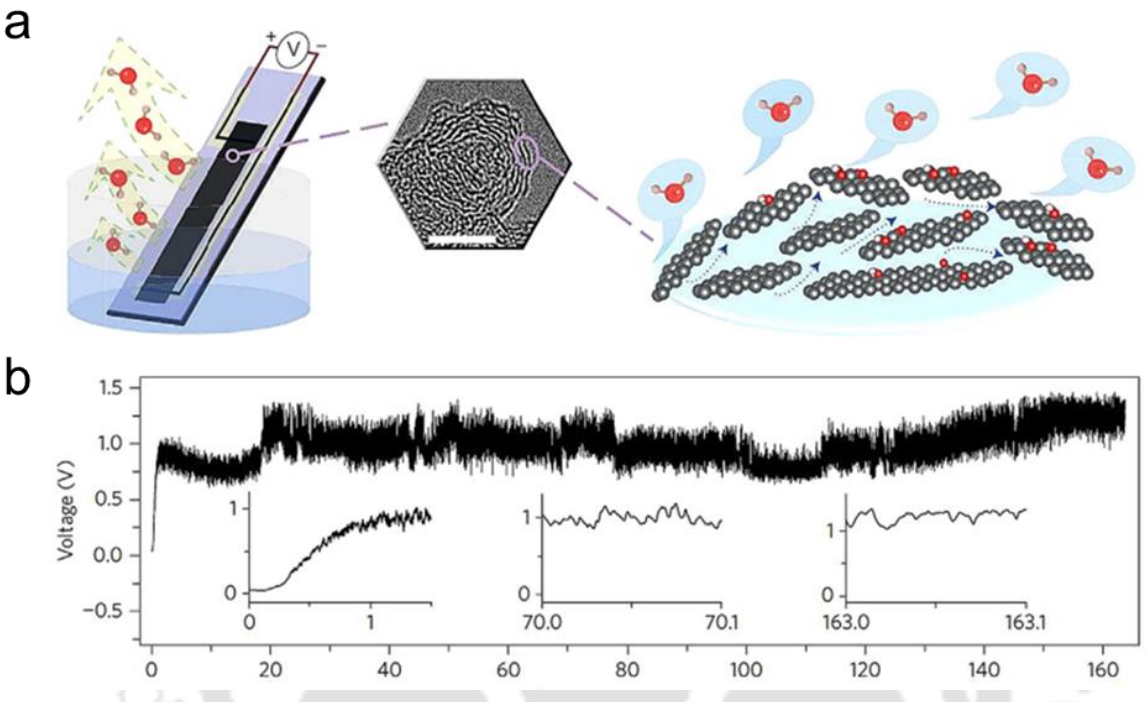

Figure 1.11: Evaporation induced energy generator: a) Schematic diagram of the experimental set-up to demonstrate evaporation induced voltage generation from the surface of carbon black sheets, inserted into deionized water. b) Open-circuit voltage generated up to 163 hours under fluctuating relative humidity between 53.5% and 66%, the insets show the measured curves of 0 to 1.5 h, 70.0 to 70.1 h and 163.0 to 163.1 hours. (Images copied from Nat. Nanotechnol. 2017, 12.

150 nA. The power generated as such was attributed to evaporation-driven streaming of the ionic solutions through nano capillaries of graphene. Recently Sun et al. employed Ni-Al layered hydroxide to fabricate flexible evaporation induced nanogenerators to yield voltage of ~ 0.7 V along with an output current of 1.3 µA.[103] It is noteworthy that the orientation of nanochannels between the LDH flakes can further tune the output performance of the electrical generator. Several reports demonstrating evaporation driven power generation by other layered materials like graphene oxide,[104] layered oxides like Al_2O_3 [105] are being published in recent years.

TH-2654_156122042

1.4.3.4: Moisture/ Hygroelectric Nanogenerators

Hygroelectricity was also generated from the interaction of surface-active nanomaterials with water molecules present in the atmosphere. The ubiquitous hydration/dehydration processes offer an outstanding platform to harvest sustainable energy. For example, Qu et al. exploited moisture responsiveness of heterogeneously distributed oxygen-containing groups in the matrix of GO to harvest moisture-induced electricity.[106] GO was chemically modified to create a gradient of oxygen-containing groups. While the hydrophilic fraction of GO film absorbs the water molecules, the gradient of oxygen-containing groups induces directed migration of the free H^+ ions across the 2D

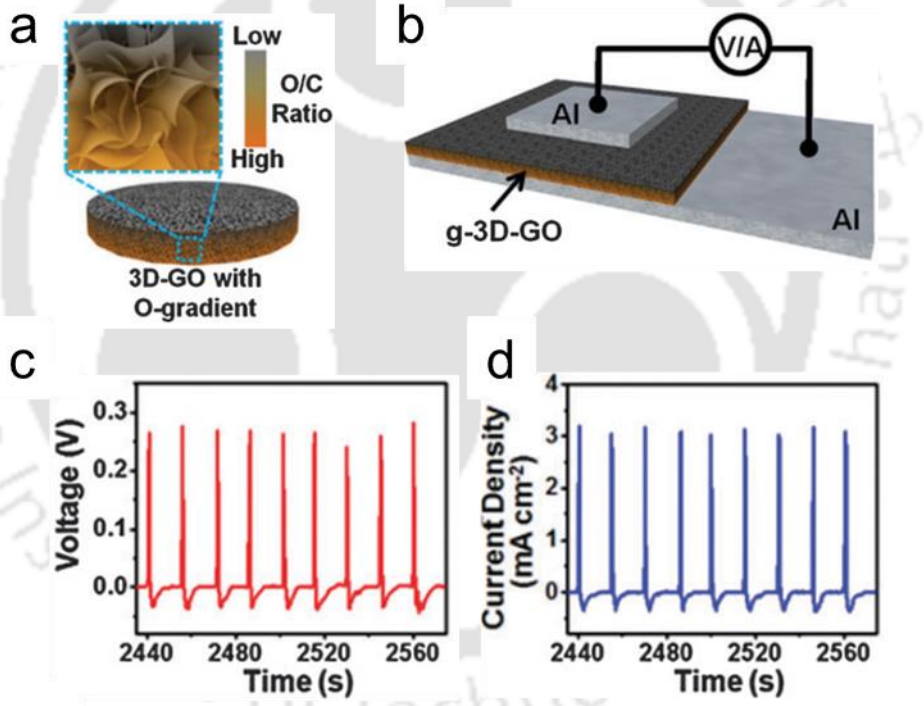

Figure 1.12: Moisture induced energy harvesting device: (a) Schematic representation of oxygen group gradient in a 3D-GO. (b) Schematic diagram of a moisture responsive energy device, g-3D-GO sandwiched between two Al electrodes. (c) Open-circuit voltage and (d) current density as a function of time in response to humidity, Δ RH = 75 %. (Images copied from Energy Environ. Sci., 2016, 9, 912—916)

nanochannels yielding a net potential difference. A similar moisture-induced nanogenerator was also prepared by using a superhydrophillic 3D assembly of GO. Within 2 seconds of exposure to humidity variation (75 %) 3D GO generated an output voltage of 0.26 V, which was accompanied by an output current of 3.2 mA/cm^2.

TH-2654_156122042

In recent years, metal-moisture batteries have emerged as promising candidates to harvest power from atmospheric water molecules. In metal-moisture batteries, metal atoms are consumed at the anode and water molecules of the atmosphere are utilized as the cathode reagent. Zhang et al. fabricated moisture batteries by using magnesium foil as the anode and HCl doped polyaniline foam as the cathode.[107] The highly porous structure of 3D protonated PANI foam traps atmospheric water molecules and provided the pathways necessary for ionic transmission (Mg^{2+} and OH^-). The discharge time of the battery was recorded to be as high as 249 hours at a discharge current of 0.05 mA. The open-circuit voltage was found to be increasing with the increasing humidity levels, and a stable voltage of ~ 1.8 V was obtained above 40 % RH. In a separate report, Qu et al. also demonstrated the designing of a GO-based Li battery that exhibits the ability to detect human respiration. At 20 % RH, the GO-based Li-battery generated an open-circuit voltage of ~ 0.9 V (output current ~ 2.5 μA/cm^2), which was increased to 2.1 V and 13 μA cm-2 at 90 % RH, respectively. Apart from its potential application as a respiration detector, the Li-GOF could also light up LEDs, revealing the potential of applications in submarine rescue operations.[108] Very recently, Yu et al. demonstrated the fabrication of a smart metal-water battery with dual responsiveness, towards humidity and pressure. This smart battery involves direct contact of a metal surface (such as Zn and Mg) with a moisture electrode composed of conductive polymer coated on macroporous Polyurethane (PU) foam. Here, the active metal played the role of the anode by spontaneously reducing H_2O and the semiconducting polymers (PPy and PANI) catalyzed the hydrogen evolution reaction. The open-circuit potential of this device was reported to be increasing with the increasing humidity levels, and maximum output potential of 1.8 V was recorded at 97 % RH. The

TH-2654_156122042

sensitivity of this smart battery towards humidity was exploited for application in the real-time detection of human respiration.[109]

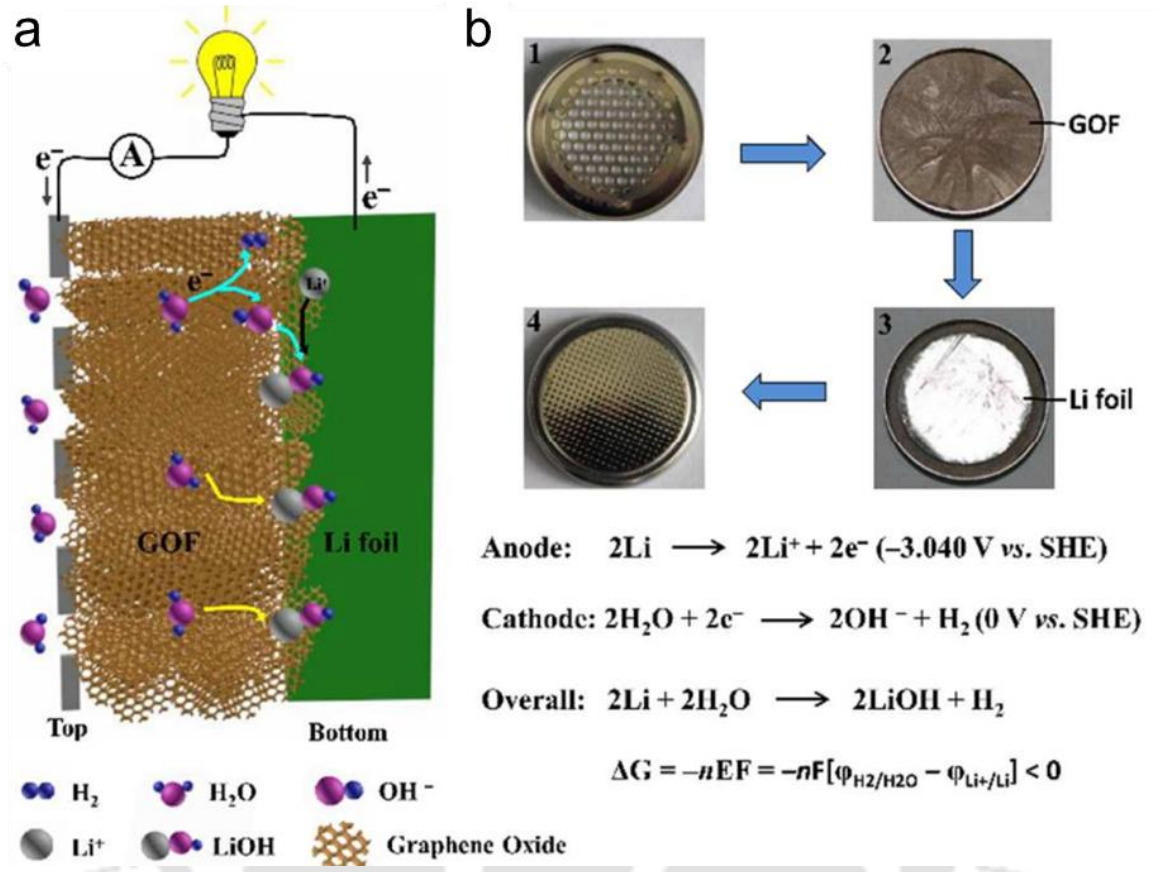

Figure 1.13: Metal-moisture batteries as efficient energy device: (a) Schematic demonstration of working mechanism of moisture responsive Li-GOF battery. (b) Digital photographs of a button cell assembled with GOF and Li foil, top cap of the cell is perforated to foe entrance of water molecules. (Images copied from J. Mater. Chem. A, 2016,4, 19154-19159)

Recently, He et al. developed a carbon:water system to generate electricity from quiescent water by using two differently polarized CNT yarns, namely pristine CNT(PCNT) and oxygen modulated CNT (OCNT), as the electrodes.[110] The flow of electric current was attributed to the difference in the charge transfer interaction of water molecules with the electrodes. In deionized water, a single device generated an open-circuit voltage of 0.28 V with output current recorded up to 6.7 µA. Notably, the device performance was not affected by the source of water. Water from different sources such as river water, tap water, or reclaimed water generated similar voltage (and current) values

TH-2654_156122042

thus revealing wide-scale application possibilities of the device under diverse circumstances.

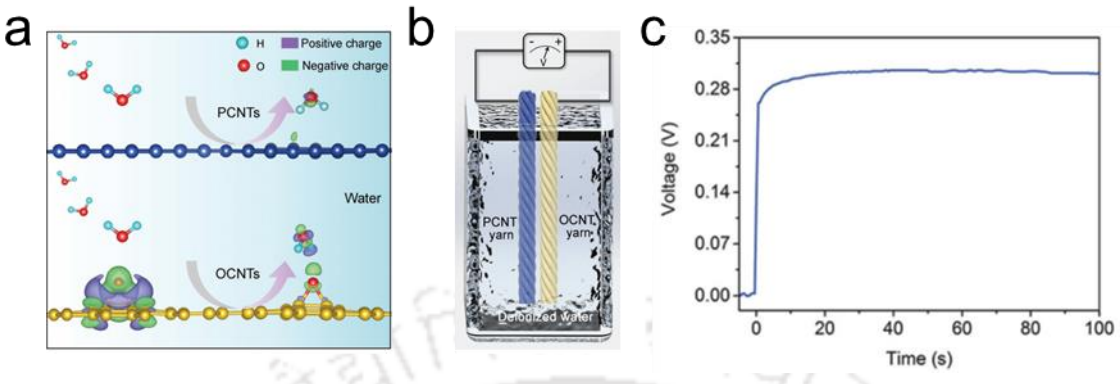

Figure 1.14: Energy generation from calm water: (a) An illustration of difference in charge density at the interface of water and PCNT and OCNT from DFT calculation. (b) Schematic diagram of experimental set up water-carbon device. (c) Output voltage as a function of time as soon as the device was immersed in deionised water. (Images copied from Adv. Mater. 2018, 30, 1707635)

1.5: CONCLUSION

In the last decade, atomically thin 2D materials have gained enormous recognition for their applicability in various renewable energy harvesting technologies from unconventional sources. Lamellar stacking of 2D nanosheets exhibit unique features such as selective molecular transport and surface-charge-governed ionic transport and possess enormous potential to accelerate the performance of energy harvesting devices. Additionally, reconstructed membranes of exfoliated nanomaterials yield robust and flexible devices with potential applications in wearable electronics. However, there are certain hurdles to overcome in this area such as expensive fabrication techniques, the relatively low output performance of the single device, and the long-term stability of devices which may add to the enormous heap of electronic wastes. Hence, extensive research is obligatory towards an ecological approach for the development of cost-effective and environmental friendly nanomaterial-based energy devices.

TH-2654_156122042

1.6: REFERENCES

1. Novoselov, K. S.; Geim, A. K.; Morozov, S. V.; Jiang, D.; Zhang, Y.; Dubonos, S. V.; Grigorieva, I. V.; Firsov, A. A., Electric Field Effect in Atomically Thin Carbon Films. *Science* **2004,** *306*, 666.

2. Hu, C.; Song, L.; Zhang, Z.; Chen, N.; Feng, Z.; Qu, L., Tailored graphene systems for unconventional applications in energy conversion and storage devices. *Energy Environ. Sci.* **2015,** *8*, 31-54.

3. Tarelho, J. P. G.; Soares dos Santos, M. P.; Ferreira, J. A. F.; Ramos, A.; Kopyl, S.; Kim, S. O.; Hong, S.; Kholkin, A., Graphene-based materials and structures for energy harvesting with fluids – A review. *Mater. Today* **2018,** *21*, 1019-1041.

4. Yang, P.-K.; Lee, C.-P., 2D-Layered Nanomaterials for Energy Harvesting and Sensing Applications. 2019.

5. Xue, Y.; Zhang, Q.; Wang, W.; Cao, H.; Yang, Q.; Fu, L., Opening Two-Dimensional Materials for Energy Conversion and Storage: A Concept. *Adv. Energy Mater.* **2017,** *7*, 1602684.

6. Khan, K.; Tareen, A. K.; Aslam, M.; Zhang, Y.; Wang, R.; Ouyang, Z.; Gou, Z.; Zhang, H., Recent advances in two-dimensional materials and their nanocomposites in sustainable energy conversion applications. *Nanoscale* **2019,** *11*, 21622-21678.

7. Zhang, P.; Wang, F.; Yu, M.; Zhuang, X.; Feng, X., Two-dimensional materials for miniaturized energy storage devices: from individual devices to smart integrated systems. *Chem. Soc. Rev.* **2018,** *47*, 7426-7451.

8. Lemme, M.; Li, L.; Palacios, T.; Schwierz, F., Two-dimensional materials for electronic applications. *MRS Bulletin* **2014,** *39*, 711-718.

TH-2654_156122042

9. Liu, G.; Jin, W.; Xu, N., Two-Dimensional-Material Membranes: A New Family of High-Performance Separation Membranes. *Angew. Chem. Inter. Edition* **2016,** *55*, 13384-13397.

10. Dervin, S.; Dionysiou, D. D.; Pillai, S. C., 2D nanostructures for water purification: graphene and beyond. *Nanoscale* **2016,** *8*, 15115-15131.

11. Liu, G.; Jin, W.; Xu, N., Graphene-based membranes. *Chem. Soc. Rev.* **2015,** *44*, 5016-5030.

12. Safaei, J.; Xiong, P.; Wang, G., Progress and prospects of two-dimensional materials for membrane-based water desalination. *Materials Today Advances* **2020,** *8*, 100108.

13. Deng, D.; Novoselov, K. S.; Fu, Q.; Zheng, N.; Tian, Z.; Bao, X., Catalysis with two-dimensional materials and their heterostructures. *Nat. Nanotechnol.* **2016,** *11*, 218-230.

14. Chia, X.; Pumera, M., Characteristics and performance of two-dimensional materials for electrocatalysis. *Nat. Catal.* **2018,** *1*, 909-921.

15. Tang, L.; Meng, X.; Deng, D.; Bao, X., Confinement Catalysis with 2D Materials for Energy Conversion. *Adv. Mater.* **2019,** *31*, 1901996.

16. Novoselov, K. S.; Jiang, D.; Schedin, F.; Booth, T. J.; Khotkevich, V. V.; Morozov, S. V.; Geim, A. K., Two-dimensional atomic crystals. *Proc. Natl. Acad. Sci. U. S. A.* **2005,** *102*, 10451-10453.

17. Shi, Y.; Hamsen, C.; Jia, X.; Kim, K. K.; Reina, A.; Hofmann, M.; Hsu, A. L.; Zhang, K.; Li, H.; Juang, Z.-Y.; Dresselhaus, M. S.; Li, L.-J.; Kong, J., Synthesis of Few-Layer Hexagonal Boron Nitride Thin Film by Chemical Vapor Deposition. *Nano Letters* **2010,** *10*, 4134-4139.

TH-2654_156122042

18. Izyumskaya, N.; Demchenko, D.; Das, S.; Özgür, Ü.; Avrutin, V.; Morkoç, H., Recent Development of Boron Nitride towards Electronic Applications. *Adv. Electron. Mater.* **2017,** *3*, 1600485.

19. Caldwell, J. D.; Aharonovich, I.; Cassabois, G.; Edgar, J. H.; Gil, B.; Basov, D. N., Photonics with hexagonal boron nitride. *Nat. Rev. Mater.* **2019,** *4*, 552-567.

20. Sajjad, M.; Morell, G.; Feng, P., Advance in Novel Boron Nitride Nanosheets to Nanoelectronic Device Applications. *ACS Appl. Mater. Interfaces* **2013,** *5*, 5051-5056.

21. Kuang, H.; Li, Y.; Huang, S.; Shi, L.; Zhou, Z.; Gao, C.; Zeng, X.; Pandey, R.; Wang, X.; Dong, S.; Chen, X.; Yang, J.; Yang, H.; Luo, J., Piezoelectric boron nitride nanosheets for high performance energy harvesting devices. *Nano Energy* **2021,** *80*, 105561.

22. Ryu, S.; Oh, H.; Kim, J., Facile Liquid-Exfoliation Process of Boron Nitride Nanosheets for Thermal Conductive Polyphthalamide Composite. *Polymers (Basel)* **2019,** *11*, 1628.

23. Watanabe, K.; Taniguchi, T.; Kanda, H., Direct-bandgap properties and evidence for ultraviolet lasing of hexagonal boron nitride single crystal. *Nat. Mater.* **2004,** *3*, 404-409.

24. Lei, W.; Mochalin, V. N.; Liu, D.; Qin, S.; Gogotsi, Y.; Chen, Y., Boron nitride colloidal solutions, ultralight aerogels and freestanding membranes through one-step exfoliation and functionalization. *Nat. Commun.* **2015,** *6*, 8849.

25. Wang, C.; Wang, Y.; Yao, Y.; Luo, W.; Wan, J.; Dai, J.; Hitz, E.; Fu, K.; Hu, L., A Solution-Processed High-Temperature, Flexible, Thin-Film Actuator. *Adv. Mater.* **2016,** *28* ,8618-8624.

TH-2654_156122042

26. Pendse, A.; Cetindag, S.; Rehak, P.; Behura, S.; Gao, H.; Nguyen, N. H. L.; Wang, T.; Berry, V.; Král, P.; Shan, J.; Kim, S., Highly Efficient Osmotic Energy Harvesting in Charged Boron-Nitride-Nanopore Membranes. *Adv. Funct. Mater.* **2021,** 2009586.

27. Wang, Q.; Bowen, C. R.; Lewis, R.; Chen, J.; Lei, W.; Zhang, H.; Li, M.-Y.; Jiang, S., Hexagonal boron nitride nanosheets doped pyroelectric ceramic composite for high-performance thermal energy harvesting. *Nano Energy* **2019,** *60*, 144-152.

28. Lee, G.-J.; Lee, M.-K.; Park, J.-J.; Hyeon, D. Y.; Jeong, C. K.; Park, K.-I., Piezoelectric Energy Harvesting from Two-Dimensional Boron Nitride Nanoflakes. *ACS Appl. Mater. Interfaces* **2019,** *11*, 37920-37926.

29. Swartzen-Allen, S. L.; Matijevic, E., Surface and colloid chemistry of clays. *Chem. Rev.* **1974,** *74*, 385-400.

30. Murray, H. H., Overview — clay mineral applications. *Appl. Clay Sci.* **1991,** *5*, 379-395.

31. Zhou, Y.; LaChance, A. M.; Smith, A. T.; Cheng, H.; Liu, Q.; Sun, L., Strategic Design of Clay-Based Multifunctional Materials: From Natural Minerals to Nanostructured Membranes. *Adv. Funct. Mater.* **2019,** *29*, 1807611.

32. Fujimura, T.; Shimada, T.; Hamatani, S.; Onodera, S.; Sasai, R.; Inoue, H.; Takagi, S., High Density Intercalation of Porphyrin into Transparent Clay Membrane without Aggregation. *Langmuir* **2013,** *29*, 5060-5065.

33. Borges, R. S.; Reddy, A. L. M.; Rodrigues, M.-T. F.; Gullapalli, H.; Balakrishnan, K.; Silva, G. G.; Ajayan, P. M., Supercapacitor Operating At 200 Degrees Celsius. *Sci. Rep.* **2013,** *3*, 2572.

34. Zhang, H.; Chhowalla, M.; Liu, Z., 2D nanomaterials: graphene and transition metal dichalcogenides. *Chem. Soc. Rev.* **2018,** *47*, 3015-3017.

TH-2654_156122042

35. Choi, W.; Choudhary, N.; Han, G. H.; Park, J.; Akinwande, D.; Lee, Y. H., Recent development of two-dimensional transition metal dichalcogenides and their applications. *Materials Today* **2017,** *20*, 116-130.

36. Naumis, G. G., 5 - Electronic properties of two-dimensional materials. In *Synthesis, Modeling, and Characterization of 2D Materials, and Their Heterostructures*, Yang, E.-H.; Datta, D.; Ding, J.; Hader, G., Eds. Elsevier: 2020; pp 77-109.

37. Kim, Y.; Park, T.; Na, J.; Yi, J. W.; Kim, J.; Kim, M.; Bando, Y.; Yamauchi, Y.; Lin, J., Layered transition metal dichalcogenide/carbon nanocomposites for electrochemical energy storage and conversion applications. *Nanoscale* **2020,** *12*, 8608-8625.

38. Yun, Q.; Li, L.; Hu, Z.; Lu, Q.; Chen, B.; Zhang, H., Layered Transition Metal Dichalcogenide-Based Nanomaterials for Electrochemical Energy Storage. *Adv. Mater.* **2020,** *32*, 1903826.

39. Mak, K. F.; Shan, J., Photonics and optoelectronics of 2D semiconductor transition metal dichalcogenides. *Nat. Photonics* **2016,** *10*, 216-226.

40. Ichimiya, H.; Takinoue, M.; Fukui, A.; Miura, K.; Yoshimura, T.; Ashida, A.; Fujimura, N.; Kiriya, D., Tuning Transition-Metal Dichalcogenide Field-Effect Transistors by Spontaneous Pattern Formation of an Ultrathin Molecular Dopant Film. *ACS Nano* **2018,** *12*, 10123-10129.

41. Chen, C.; Tao, L.; Du, S.; Chen, W.; Wang, Y.; Zou, Y.; Wang, S., Advanced Exfoliation Strategies for Layered Double Hydroxides and Applications in Energy Conversion and Storage. *Adv. Funct. Mater.* **2020,** *30*, 1909832.

42. Shao, M.; Zhang, R.; Li, Z.; Wei, M.; Evans, D. G.; Duan, X., Layered double hydroxides toward electrochemical energy storage and conversion: design, synthesis and applications. *Chem. Commun.* **2015,** *51*, 15880-15893.

TH-2654_156122042

43. Gong, Y.; Li, M.; Wang, Y., Carbon Nitride in Energy Conversion and Storage: Recent Advances and Future Prospects. *ChemSusChem* **2015,** *8*, 931-946.

44. Sun, Y.; Chen, D.; Liang, Z., Two-dimensional MXenes for energy storage and conversion applications. *Materials Today Energy* **2017,** *5*, 22-36.

45. Kannan, K.; Sadasivuni, K. K.; Abdullah, A. M.; Kumar, B., Current Trends in MXene-Based Nanomaterials for Energy Storage and Conversion System: A Mini Review. *Catalysts* **2020,** *10*.

46. Mei, J.; Liao, T.; Kou, L.; Sun, Z., Two-Dimensional Metal Oxide Nanomaterials for Next-Generation Rechargeable Batteries. *Adv. Mater.* **2017,** *29*, 1700176.

47. Hernandez, Y.; Nicolosi, V.; Lotya, M.; Blighe, F. M.; Sun, Z.; De, S.; McGovern, I. T.; Holland, B.; Byrne, M.; Gun'Ko, Y. K.; Boland, J. J.; Niraj, P.; Duesberg, G.; Krishnamurthy, S.; Goodhue, R.; Hutchison, J.; Scardaci, V.; Ferrari, A. C.; Coleman, J. N., High-yield production of graphene by liquid-phase exfoliation of graphite. *Nat. Nanotechnol.* **2008,** *3*, 563-568.

48. Khan, U.; O'Neill, A.; Lotya, M.; De, S.; Coleman, J. N., High-Concentration Solvent Exfoliation of Graphene. *Small* **2010,** *6*, 864-871.

49. Nicolosi, V.; Chhowalla, M.; Kanatzidis, M. G.; Strano, M. S.; Coleman, J. N., Liquid Exfoliation of Layered Materials. *Science* **2013,** *340*, 1226419.

50. Zhao, W.; Fang, M.; Wu, F.; Wu, H.; Wang, L.; Chen, G., Preparation of graphene by exfoliation of graphite using wet ball milling. *J. Mater. Chem.* **2010,** *20*, 5817-5819.

51. Li, L. H.; Chen, Y.; Behan, G.; Zhang, H.; Petravic, M.; Glushenkov, A. M., Large-scale mechanical peeling of boron nitride nanosheets by low-energy ball milling. *J. Mater. Chem.* **2011,** *21*, 11862-11866.

52. Lin, T.; Tang, Y.; Wang, Y.; Bi, H.; Liu, Z.; Huang, F.; Xie, X.; Jiang, M., Scotch-tape-like exfoliation of graphite assisted with elemental sulfur and graphene–sulfur

TH-2654_156122042

composites for high-performance lithium-sulfur batteries. *Energy Environ. Sci.* **2013,** *6*, 1283-1290.

53. Joensen, P.; Frindt, R. F.; Morrison, S. R., Single-layer MoS_2. *Mater. Res. Bull.* **1986,** *21*, 457-461.

54. Kim, G.; Kim, S.-S.; Jeon, J.; Yoon, S. I.; Hong, S.; Cho, Y. J.; Misra, A.; Ozdemir, S.; Yin, J.; Ghazaryan, D.; Holwill, M.; Mishchenko, A.; Andreeva, D. V.; Kim, Y.-J.; Jeong, H. Y.; Jang, A. R.; Chung, H.-J.; Geim, A. K.; Novoselov, K. S.; Sohn, B.-H.; Shin, H. S., Planar and van der Waals heterostructures for vertical tunnelling single electron transistors. *Nat. Commun.* **2019,** *10*, 230.

55. Zeng, Z.; Sun, T.; Zhu, J.; Huang, X.; Yin, Z.; Lu, G.; Fan, Z.; Yan, Q.; Hng, H. H.; Zhang, H., An Effective Method for the Fabrication of Few-Layer-Thick Inorganic Nanosheets. *Angew. Chem. Inter. Edition* **2012,** *51*, 9052-9056.

56. Nag, A.; Raidongia, K.; Hembram, K. P. S. S.; Datta, R.; Waghmare, U. V.; Rao, C. N. R., Graphene Analogues of BN: Novel Synthesis and Properties. *ACS Nano* **2010,** *4* , 1539-1544.

57. Gao, L.; Ren, W.; Zhao, J.; Ma, L.-P.; Chen, Z.; Cheng, H.-M., Efficient growth of high-quality graphene films on Cu foils by ambient pressure chemical vapor deposition. *Appl. Phys. Lett.* **2010,** *97*, 183109.

58. Liu, K.-K.; Zhang, W.; Lee, Y.-H.; Lin, Y.-C.; Chang, M.-T.; Su, C.-Y.; Chang, C.-S.; Li, H.; Shi, Y.; Zhang, H.; Lai, C.-S.; Li, L.-J., Growth of Large-Area and Highly Crystalline MoS_2 Thin Layers on Insulating Substrates. *Nano Letters* **2012,** *12* , 1538-1544.

59. Zhan, Y.; Liu, Z.; Najmaei, S.; Ajayan, P. M.; Lou, J., Large-Area Vapor-Phase Growth and Characterization of MoS_2 Atomic Layers on a SiO_2 Substrate. *Small* **2012,** *8* , 966-971.

TH-2654_156122042

60. Withanage, S. S.; Kalita, H.; Chung, H.-S.; Roy, T.; Jung, Y.; Khondaker, S. I., Uniform Vapor-Pressure-Based Chemical Vapor Deposition Growth of MoS_2 Using MoO3 Thin Film as a Precursor for Coevaporation. *ACS Omega* **2018,** *3*, 18943-18949.

61. Peng, Y.; Meng, Z.; Zhong, C.; Lu, J.; Yu, W.; Jia, Y.; Qian, Y., Hydrothermal Synthesis and Characterization of Single-Molecular-Layer MoS_2 and $MoSe_2$. *Chem. Lett.* **2001,** *30*, 772-773.

62. Sun, Z.; Liao, T.; Dou, Y.; Hwang, S. M.; Park, M.-S.; Jiang, L.; Kim, J. H.; Dou, S. X., Generalized self-assembly of scalable two-dimensional transition metal oxide nanosheets. *Nat. Commun.* **2014,** *5*, 3813.

63. Darr, J. A.; Zhang, J.; Makwana, N. M.; Weng, X., Continuous Hydrothermal Synthesis of Inorganic Nanoparticles: Applications and Future Directions. *Chem. Rev.* **2017,** *117*, 11125-11238.

64. Zhu, Y.; Murali, S.; Stoller, M. D.; Velamakanni, A.; Piner, R. D.; Ruoff, R. S., Microwave assisted exfoliation and reduction of graphite oxide for ultracapacitors. *Carbon* **2010,** *48*, 2118-2122.

65. Wu, W.; Xu, J.; Tang, X.; Xie, P.; Liu, X.; Xu, J.; Zhou, H.; Zhang, D.; Fan, T., Two-Dimensional Nanosheets by Rapid and Efficient Microwave Exfoliation of Layered Materials. *Chem. Mater.* **2018,** *30*, 5932-5940.

66. Matsumoto, M.; Saito, Y.; Park, C.; Fukushima, T.; Aida, T., Ultrahigh-throughput exfoliation of graphite into pristine 'single-layer' graphene using microwaves and molecularly engineered ionic liquids. *Nat. Chem.* **2015,** *7*, 730-736.

67. Zhao, Y.; Dyck, J. S.; Burda, C., Toward high-performance nanostructured thermoelectric materials: the progress of bottom-up solution chemistry approaches. *J. Mater. Chem.* **2011,** *21*, 17049-17058.

TH-2654_156122042

68. Prieto, A. L.; Sander, M. S.; Martín-González, M. S.; Gronsky, R.; Sands, T.; Stacy, A. M., Electrodeposition of Ordered Bi2Te3 Nanowire Arrays. *J. Am. Chem. Soc.* **2001,** *123*, 7160-7161.

69. Wang, Z. L.; Song, J., Piezoelectric Nanogenerators Based on Zinc Oxide Nanowire Arrays. *Science* **2006,** *312*, 242.

70. Duerloo, K.-A. N.; Ong, M. T.; Reed, E. J., Intrinsic Piezoelectricity in Two-Dimensional Materials. *J. Phys. Chem. Lett.* **2012,** *3*, 2871-2876.

71. Wu, W.; Wang, L.; Li, Y.; Zhang, F.; Lin, L.; Niu, S.; Chenet, D.; Zhang, X.; Hao, Y.; Heinz, T. F.; Hone, J.; Wang, Z. L., Piezoelectricity of single-atomic-layer MoS_2 for energy conversion and piezotronics. *Nature* **2014,** *514*, 470-474.

72. Fan, F.-R.; Tian, Z.-Q.; Lin Wang, Z., Flexible triboelectric generator. *Nano Energy* **2012,** *1*, 328-334.

73. Xing, F.; Jie, Y.; Cao, X.; Li, T.; Wang, N., Natural triboelectric nanogenerator based on soles for harvesting low-frequency walking energy. *Nano Energy* **2017,** *42*, 138-142.

74. Xia, K.; Chi, Y.; Fu, J.; Zhu, Z.; Zhang, H.; Du, C.; Xu, Z., A triboelectric nanogenerator based on cosmetic fixing powder for mechanical energy harvesting. *Microsyst. Nanoeng.* **2019,** *5*, 26.

75. Liang, X.; Jiang, T.; Liu, G.; Feng, Y.; Zhang, C.; Wang, Z. L., Spherical triboelectric nanogenerator integrated with power management module for harvesting multidirectional water wave energy. *Energy Environ. Sci.* **2020,** *13*, 277-285.

76. Yang, Y.; Zhu, G.; Zhang, H.; Chen, J.; Zhong, X.; Lin, Z.-H.; Su, Y.; Bai, P.; Wen, X.; Wang, Z. L., Triboelectric Nanogenerator for Harvesting Wind Energy and as Self-Powered Wind Vector Sensor System. *ACS Nano* **2013,** *7*, 9461-9468.

TH-2654_156122042

77. Kim, S.; Gupta, M. K.; Lee, K. Y.; Sohn, A.; Kim, T. Y.; Shin, K.-S.; Kim, D.; Kim, S. K.; Lee, K. H.; Shin, H.-J.; Kim, D.-W.; Kim, S.-W., Transparent Flexible Graphene Triboelectric Nanogenerators. *Adv. Mater.* **2014,** *26*, 3918-3925.

78. Shankaregowda, S. A.; Nanjegowda, C. B.; Cheng, X.; Shi, M.; Liu, Z.; Zhang, H., A Flexible and Transparent Graphene-Based Triboelectric Nanogenerator. *IEEE Trans. Nanotechnol.* **2016,** *15*, 435-441.

79. Chen, H.; Xu, Y.; Zhang, J.; Wu, W.; Song, G., Enhanced stretchable graphene-based triboelectric nanogenerator via control of surface nanostructure. *Nano Energy* **2019,** *58*, 304-311.

80. Chu, H.; Jang, H.; Lee, Y.; Chae, Y.; Ahn, J.-H., Conformal, graphene-based triboelectric nanogenerator for self-powered wearable electronics. *Nano Energy* **2016,** *27*, 298-305.

81. Qian, Y.; Sohn, M.; He, W.; Park, H.; Subramanian, K. R. V.; Kang, D. J., A high-output flexible triboelectric nanogenerator based on polydimethylsiloxane/three-dimensional bilayer graphene/carbon cloth composites. *J. Mater. Chem. A* **2020,** *8*, 17150-17155.

82. Li, W.; Zhang, Y.; Liu, L.; Li, D.; Liao, L.; Pan, C., A high energy output nanogenerator based on reduced graphene oxide. *Nanoscale* **2015,** *7*, 18147-18151.

83. Seol, M.; Kim, S.; Cho, Y.; Byun, K.-E.; Kim, H.; Kim, J.; Kim, S. K.; Kim, S.-W.; Shin, H.-J.; Park, S., Triboelectric Series of 2D Layered Materials. *Adv. Mater.* **2018,** *30*, 1801210.

84. Das, S.; Pandey, D.; Thomas, J.; Roy, T., The Role of Graphene and Other 2D Materials in Solar Photovoltaics. *Adv. Mater.* **2019,** *31*, 1802722.

TH-2654_156122042

85. Yang, L.; Yu, X.; Xu, M.; Chen, H.; Yang, D., Interface engineering for efficient and stable chemical-doping-free graphene-on-silicon solar cells by introducing a graphene oxide interlayer. *J. Mater. Chem. A* **2014,** *2*, 16877-16883.

86. Liu, Z.; Li, J.; Sun, Z.-H.; Tai, G.; Lau, S.-P.; Yan, F., The Application of Highly Doped Single-Layer Graphene as the Top Electrodes of Semitransparent Organic Solar Cells. *ACS Nano* **2012,** *6*, 810-818.

87. Lee, S. K.; Chu, D.; Yoo, J.; Kim, E. K., Formation of transition metal dichalcogenides thin films with liquid phase exfoliation technique and photovoltaic applications. *Sol. Energy Mater. Sol. Cells* **2018,** *184*, 9-14.

88. Memaran, S.; Pradhan, N. R.; Lu, Z.; Rhodes, D.; Ludwig, J.; Zhou, Q.; Ogunsolu, O.; Ajayan, P. M.; Smirnov, D.; Fernández-Domínguez, A. I.; García-Vidal, F. J.; Balicas, L., Pronounced Photovoltaic Response from Multilayered Transition-Metal Dichalcogenides PN-Junctions. *Nano Letters* **2015,** *15*, 7532-7538.

89. Tsai, M.-L.; Su, S.-H.; Chang, J.-K.; Tsai, D.-S.; Chen, C.-H.; Wu, C.-I.; Li, L.-J.; Chen, L.-J.; He, J.-H., Monolayer MoS_2 Heterojunction Solar Cells. *ACS Nano* **2014,** *8*, 8317-8322.

90. Pospischil, A.; Furchi, M. M.; Mueller, T., Solar-energy conversion and light emission in an atomic monolayer p–n diode. *Nat. Nanotechnol.* **2014,** *9*, 257-261.

91. Buriak, J. M.; Toro, C.; Choi, K.-S., Chemistry of Materials for Water Splitting Reactions. *Chem. Materi.* **2018,** *30*, 7325-7327.

92. Su, T.; Shao, Q.; Qin, Z.; Guo, Z.; Wu, Z., Role of Interfaces in Two-Dimensional Photocatalyst for Water Splitting. *ACS Catal.* **2018,** *8*, 2253-2276.

93. Faraji, M.; Yousefi, M.; Yousefzadeh, S.; Zirak, M.; Naseri, N.; Jeon, T. H.; Choi, W.; Moshfegh, A. Z., Two-dimensional materials in semiconductor photoelectrocatalytic systems for water splitting. *Energy Environ. Sci.* **2019,** *12*, 59-95.

TH-2654_156122042

94. Ghosh, S.; Sood, A. K.; Kumar, N., Carbon Nanotube Flow Sensors. *Science* **2003,** *299*, 1042.

95. Dhiman, P.; Yavari, F.; Mi, X.; Gullapalli, H.; Shi, Y.; Ajayan, P. M.; Koratkar, N., Harvesting Energy from Water Flow over Graphene. *Nano Letters* **2011,** *11*, 3123-3127.

96. Guo, W.; Cheng, C.; Wu, Y.; Jiang, Y.; Gao, J.; Li, D.; Jiang, L., Bio-Inspired Two-Dimensional Nanofluidic Generators Based on a Layered Graphene Hydrogel Membrane. *Adv. Mater.* **2013,** *25*, 6064-6068.

97. Yin, J.; Li, X.; Yu, J.; Zhang, Z.; Zhou, J.; Guo, W., Generating electricity by moving a droplet of ionic liquid along graphene. *Nat. Nanotechnol.* **2014,** *9*, 378-83.

98. Yin, J.; Zhang, Z.; Li, X.; Yu, J.; Zhou, J.; Chen, Y.; Guo, W., Waving potential in graphene. *Nat. Commun.* **2014,** *5*, 3582.

99. Siria, A.; Poncharal, P.; Biance, A.-L.; Fulcrand, R.; Blase, X.; Purcell, S. T.; Bocquet, L., Giant osmotic energy conversion measured in a single transmembrane boron nitride nanotube. *Nature* **2013,** *494*, 455-458.

100. Ji, J.; Kang, Q.; Zhou, Y.; Feng, Y.; Chen, X.; Yuan, J.; Guo, W.; Wei, Y.; Jiang, L., Osmotic Power Generation with Positively and Negatively Charged 2D Nanofluidic Membrane Pairs. *Adv. Funct. Mater.* **2017,** *27*, 1603623.

101. Cheng, H.; Zhou, Y.; Feng, Y.; Geng, W.; Liu, Q.; Guo, W.; Jiang, L., Electrokinetic Energy Conversion in Self-Assembled 2D Nanofluidic Channels with Janus Nanobuilding Blocks. *Adv. Mater.* **2017,** *29*, 1700177.

102. Xue, G.; Xu, Y.; Ding, T.; Li, J.; Yin, J.; Fei, W.; Cao, Y.; Yu, J.; Yuan, L.; Gong, L.; Chen, J.; Deng, S.; Zhou, J.; Guo, W., Water-evaporation-induced electricity with nanostructured carbon materials. *Nat. Nanotechnol.* **2017,** *12*, 317-321.

103. Sun, J.; Li, P.; Qu, J.; Lu, X.; Xie, Y.; Gao, F.; Li, Y.; Gang, M.; Feng, Q.; Liang, H.; Xia, X.; Li, C.; Xu, S.; Bian, J., Electricity generation from a Ni-Al layered double

TH-2654_156122042

hydroxide-based flexible generator driven by natural water evaporation. *Nano Energy* **2019,** *57*, 269-278.

104. Zhang, G.; Duan, Z.; Qi, X.; Xu, Y.; Li, L.; Ma, W.; Zhang, H.; Liu, C.; Yao, W., Harvesting environment energy from water-evaporation over free-standing graphene oxide sponges. *Carbon* **2019,** *148*, 1-8.

105. Shao, C.; Ji, B.; Xu, T.; Gao, J.; Gao, X.; Xiao, Y.; Zhao, Y.; Chen, N.; Jiang, L.; Qu, L., Large-Scale Production of Flexible, High-Voltage Hydroelectric Films Based on Solid Oxides. *ACS Appl. Mater. Interfaces* **2019,** *11*, 30927-30935.

106. Zhao, F.; Cheng, H.; Zhang, Z.; Jiang, L.; Qu, L., Direct Power Generation from a Graphene Oxide Film under Moisture. *Adv. Mater.* **2015,** *27*, 4351-4357.

107. Xiao, H.; Xie, P.; Qiu, S. J.; Rong, M. Z.; Zhang, M. Q., Ultrathin-graphite foam with high mechanical resilience and electroconductibility fabricated through morphology-controlled solid-state pyrolysis of polyaniline foam. *Carbon* **2018,** *139*, 648-655.

108. Ye, M.; Cheng, H.; Gao, J.; Li, C.; Qu, L., A respiration-detective graphene oxide/lithium battery. *J. Mater. Chem. A* **2016,** *4*, 19154-19159.

109. Fang, Z.; Feng, J.; Fu, X.; Li, J.; Hu, X.; Xie, X.; Yu, D., Humidity and Pressure Dual-Responsive Metal–Water Batteries Enabled by Three-In-One All-Polymer Cathodes for Smart Self-Powered Systems. *ACS Appl. Mater. Interfaces* **2020,** *12* , 23853-23859.

110. He, S.; Zhang, Y.; Qiu, L.; Zhang, L.; Xie, Y.; Pan, J.; Chen, P.; Wang, B.; Xu, X.; Hu, Y.; Dinh, C. T.; De Luna, P.; Banis, M. N.; Wang, Z.; Sham, T.-K.; Gong, X.; Zhang, B.; Peng, H.; Sargent, E. H., Chemical-to-Electricity Carbon: Water Device. *Adv. Mater.* **2018,** *30*, 1707635.

TH-2654_156122042

Chapter 2

Reconstruction of Soil Components into Multifunctional Freestanding Membranes

Summary*

In this chapter, multifunctional freestanding membranes are prepared by tuning the structure of ubiquitous soil components, viz. clay and humic acids. Crosslinking of exfoliated clay layers with purified humic acids not only conferred mechanical strength but also enhanced chemical robustness of the membranes. The percolated network of molecularly sized channels of the soil membranes exhibits characteristic nanofluidic phenomena. Electrical conductivity is induced to otherwise insulating soil membranes by heating in an inert atmosphere, without affecting their nanofluidic ionic conductivity. The soil membranes also provided a new platform to prepare and study mixed conducting materials. Strips of heated membranes shown to exhibit excellent sensitivity towards NH_3 gas under atmospheric conditions.

---

* Paper based on these studies has appeared in *ACS Omega*, 2019, **4**, 1292.

TH-2654_156122042

2.1: INTRODUCTION

Soil, also known as the skin of the earth, is a highly complicated but synergic mixture of living and non-living objects.[1,2] It plays pivotal roles in the environmental chemical cycles, and provides a basis for the survival of life on earth. Among various non-living objects in soil, clays and humic acids are the most active constituents. Clay minerals are layered aluminosilicates or phyllosilicates with a crystalline structure, which constitute a major part of the soil. The basic structure consists of a Si-O tetrahedral sheet, where Si atoms occupying the central position are tetrahedrally coordinated to four O atoms. The Al-O octahedral sheets contain Al atoms hexagonally bonded to six O atoms. The sheets of Si-O and Al-O are stacked on top of each other, and their ratio is the major differentiating factor among different types of layered silicates. For example, kaolinite is a 1:1 clay with repetitive layers of one tetrahedral and one octahedral sheet. Similarly, vermiculite is a 2:1 clay with one octahedral sheet sandwiched between two tetrahedral sheets. On the other hand, humic acids are organic substances formed by microbial decomposition of plant and animal residues. They are amorphous long-chain organic polymers with a wide range of molecular weights, and they are brown in color. The elementary structure is comprised of aromatic rings of the di- or trihydroxy-phenol type bridged by -O-, -CH2-, -NH-, -N=, -S-, and other groups and contains both free OH groups and the double linkage of quinones. [1]

In spite of their drastically different chemical and physical identities, clay and humic acids contribute similarly to the chemical functionalities of soil. For example, both clays and humic acids actively participate in detoxification of hazardous substances, preservation of vital minerals, maintenance of ideal pH, fertility and air/water ratios for plants growth.[1-6] Studies suggested that activities of clay and humic acids complement each other and an appropriate combination of the two is essential to obtain certain crucial functionalities of

TH-2654_156122042

soil.[1-7] Nonetheless, rational blends of these two naturally abandoned materials have not been optimally applied with a view to creating advanced materials for futuristic applications. Here, we attempt to utilize the ubiquitous chemistry of humic acids and clays to prepare multifunctional freestanding membranes with application possibilities in the areas like nanofluidic energy harvesting, water purification and sensing of toxic chemicals. In order to facilitate better interactions, layers of naturally occurring vermiculite clay were exfoliated into ultra-thin 2D sheets, and humic acids were purified through multiple steps of conjugative acid-base treatments.

2.2: SCOPE OF THE PRESENT INVESTIGATION

Clays are stacking layers of hydrous aluminum phyllosilicates consisting of corner-sharing SiO_4 tetrahedra and/or AlO_4 octahedra intercalated by aqueous solutions of charge-balancing cations. Owing to their well-defined structures having high chemical and thermal stability, clay minerals have received lots of attention from the scientific communities across the disciplines. As a result, they are being applied in a variety of advanced technologies such as nuclear waste managements, industrial oil absorbance, pharmaceuticals and anti-caking applications.[11] Clays are also highly tunable, can be easily modified to create free-standing proton-conducting membranes, ultra-sensitive smart materials and a range of polymeric nanocomposites.[12-15] On the other hand, humic acids are mixtures of acidic organic polymers that are believed to be a product of the natural break-down process of plant- and animal-based materials.[16-17] There have been significant contradictions regarding origin and structure of humic acids. However, its favorable contributions towards environmental chemical cycles have been proven beyond doubt. The phenolic and carboxylic functional groups of humic acids together with negative surface charges of clay layers are the major contributors of soil's cation exchange capacity, and

TH-2654_156122042

hence contents of the two are a primary characterization of soil nature. Unfortunately, application of humic acids in advanced technologies is limited by its complicated and undefined structures. They are being utilized as a cheap source of carbon, either to generate heat through combustion or to prepare porous materials by annealing at inert atmosphere.[18,19] Scant efforts have been made to utilize the large number of functional groups inherently present in humic acids for advanced technological applications. Notable applications of humic acids include adsorbents of inorganic and organic pollutants from water, and additives to fertilizer, paper and plastic materials.[20-22]

2.3: EXPERIMENTAL SECTION

Exfoliation of clay layers: Natural vermiculite clay was exfoliated into atomically thin flakes by employing a two-step ion exchange method. Typically, 50 mg of thermally expanded vermiculite crystals were refluxed with 100 ml saturated solution of NaCl for 24 hours followed by washing with deionised water (DI water) by centrifugation technique for 5-6 times. The removal of chloride was confirmed by silver nitrate test for chloride ion detection. The as obtained Na^+ ion exchanged clay was further refluxed with 2 M aqueous solution of LiCl (100 ml) for 24 hours. Li^+ ion exchanged vermiculite was vigorously washed with DI water (5-6 times) to remove the free ions. The as obtained slurry was re-dispersed in deionised water to obtain clay dispersions.

Extraction of humic acids: A two-step alkaline-acid treatment was employed to extract humic acid (HA) from samples of soil collected from the IITG campus. Typically, 100 g of the soil sample was stirred with 300 ml of 0.1 M aqueous NaOH solution at room temperature for 2 hours. The soil components were then allowed to settle for overnight and the supernatant liquid (200 ml) was collected, which was further centrifuged (5000 rpm) to

TH-2654_156122042

confirm removal of undesired components. The clear solution was then acidified with concentrated HCl to decrease the pH value to 1. At pH 1, a brown color material started precipitating which was collected by centrifugation and repeatedly washed for several times.

Preparation of soil membranes: 1 mg/ml aqueous dispersions of exfoliated vermiculite (VM) and humic acids were prepared in deionised water and mixed in appropriate proportions to prepare soil dispersions containing 20 %, 30 %, 50 % and 70 % of humic acids by weight. For example, to prepare 60 ml, 20 % HA membrane, 12 mL of HA dispersion (1 mg/ml) was mixed with 48 mL of VM dispersion (1 mg/ml) and sonicated for 5 minutes. Around 60 ml of soil dispersions were then vacuum filtered through cellulose nitrate membranes to prepare freestanding membranes, which were detached from the filtration membranes after air drying at room temperature.

Measurements of bending stiffness: Bending stiffness values of soil membranes were determined by employing Lorentzen & Wettre two-point method.[14,33] A known load (4.5 mg) was placed to one end of the rectangular strip (typically 25 mm × 4.5 mm × 0.045 mm) keeping the other end fixed to a glass slide. The following equation was used for the calculation:

$$S_b = \frac{60 \times F \times l^2}{\pi \times \theta \times b} \text{---------- (1)}$$

Where S_b is bending stiffness, F is defined as bending force (F = weight × gravitational constant), l is the distance between the clamp and the load, θ is the angle of deflection under the influence of load, b is the width of the strip.

TH-2654_156122042

The strips were then transferred to a chamber containing solvent vapours in order to study the change in bending angle of the strips on exposure to different solvent atmosphere.

Fabrication of Nanofluidic device: Soil membrane-based nanofluidic devices were fabricated by encapsulating rectangular soil strips (20 mm × 8 mm × 0.045 mm) into freshly prepared PDMS elastomer. In order to expose the nanochannel networks to different electrolyte solutions, two holes (~ 0.3 ml) were cut open through the fully cured PDMS stub at either end of rectangular strips. After soaking soil devices in water for 8 hours, aqueous solutions of KCl (~ 0.3 ml) were placed at both ends and allowed to reach equilibrium before measuring ionic conductance. A Keithley source meter instrument (Model 2450) connected to Ag/AgCl electrodes was employed to record the conductivity data.

Cation and dye filtration through soil membranes: 100 ppm and 50 ppm aqueous solutions (4 ml) of methylene blue dye and inorganic salts were passed through soil membranes by vacuum assisted filtration technique respectively. 4 ml of aqueous dye solutions (100 ppm) were passed through each soil membrane and time required to collect the filtrate was noted in order to test permeability of the membranes. The concentration of the dye before and after passing was determined by using a UV-Vis spectrophotometer instrument (Systronics, UV-VIS Spectrophotometer 117). Similarly, the concentrations of the cations were determined by employing a flame photometer instrument (Analab, µFlameCal10).

Permeability of the membranes were calculated by employing the equation:

$$Permeability = \frac{(membrane\ thickness)\times(amount\ of\ permeate)}{(membrane\ surface\ area)\times(time)\times(differential\ pressure\ )} \quad \text{---------- } (2)$$

TH-2654_156122042

Fabrication of sensing device: The sensing device was fabricated by connecting two Cu wires to silver paste painted on both ends of strips cut from heated 50 % HA membrane (dimension 1.5 cm x 4.5 mm x 0.049 mm). The as prepared device was mounted on an aluminium closed container placed on a hot plate (maintained at 100 °C). The container was connected to a nitrogen inlet and outlet to maintain inert atmosphere inside the system. The inside temperature of the container was recorded as 75°C during the measurements. The electrical resistance of the device was recorded by using a Keithley Source meter instrument (model 2450) as a function of time. Ammonia vapors with desired concentrations were introduced by injecting a calculated amount of ammonium hydroxide into the glass container. The response % was calculated by the equation:

$$Response\ \% = \frac{R_a - R_g}{R_a} \times 100$$

Where, R_a and R_g are the resistance in the absence and presence of ammonia vapors, respectively.

Characterization: Fourier transform infrared spectroscopy (FTIR) (PerkinElmer Spectrum Two) was employed to characterize the functional groups present in humic acids. The morphology of humic acids and the exfoliated vermiculite layers were characterized by field emission scanning electron microscopy (FESEM) (Zeiss, Model: Sigma), transmission electron microscope (TEM) (JEOL, JEM 2100) and atomic force microscope (AFM) (Agilent, Model 5500 series). X-ray diffraction characterisation was carried out by using Bruker D-205505 Cu-kα radiation (λ = 1.5406 Å). Tensile strength measurements of the soil membranes were carried out in a 5 kN Electromechanical Universal Testing (make: Zwick Roell: Z005TN).

TH-2654_156122042

2.4: RESULTS AND DISCUSSIONS

Humic acids were extracted and purified following the standard alkaline-acid treatment-based procedure.[23-25] A digital photograph of extracted humic acid dispersion is shown in Figure 2.1a. The purified humic acid samples displayed Infra-Red (IR), UV-Vis and fluorescence spectra similar to those reported in the contemporary literature.[25-28] The spectroscopic characterization of humic acids are shown in Figure 2.1a. IR bands at 3424 cm^{-1}, 2928 cm^{-1}, 1655 cm^{-1} and 1030 cm^{-1} suggest presence of –OH, –CH, –C=C, and C–O–C groups in the sample, respectively. Natural vermiculite $(Al,Mg,Fe^{3+})_4(Si,Al)_8O_{20}(OH)_4$, a smectite group 2:1 clay, is used here as the model clay system, XRD pattern of the same is shown in inset Figure 2.2b.[1] Two-steps ion exchange method was employed to obtain homogeneous aqueous dispersion of the clay sample as shown in Figure 2.2a. The microscopic analysis of the dispersion as shown in Figure 2.2, confirmed successful

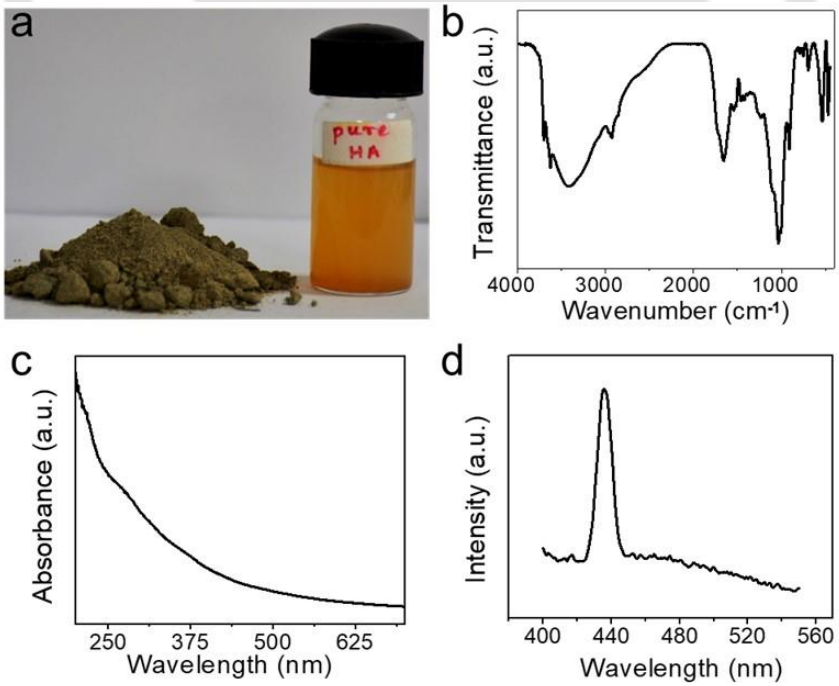

Figure 2.1: Characterization of humic acids: (a) Photograph showing aqueous dispersion of purified humic acid, extracted from soil sample shown in the inset. (b) Fluorescence (c) UV-Vis and (d) FTIR spectra of humic acids extracted from soil samples collected from Indian Institute of Technology Guwahati campus following standard procedure.

exfoliation of clay layers into thin flakes with lateral dimension extending up to 20 μm^2. Figure 2.2c shows the representative AFM (Atomic Force Microscope) image with height

TH-2654_156122042

profile having heights in the range of 4 to 8 nm. Representative FESEM (Field Emission Scanning Electron Microscope), TEM (Transition Electron Microscope) and HRTEM (High Resolution Transition Electron Microscope) images of the exfoliated vermiculite sheets are shown in Figure 2.2d, 2.2e and 2.2f respectively.

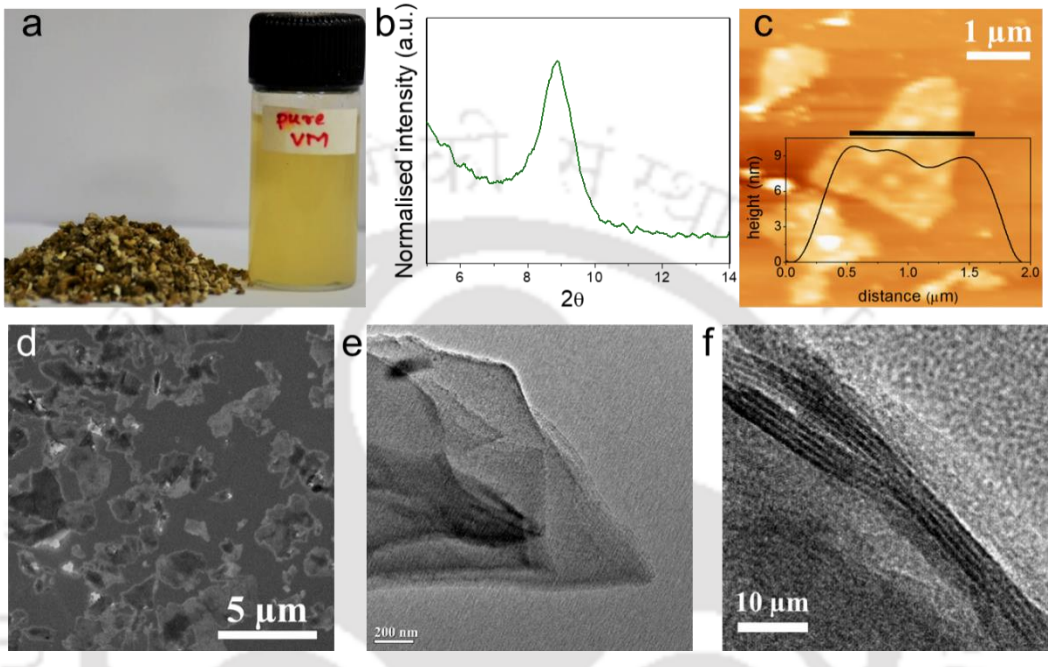

Figure 2.2: Characterization of vermiculite: (a) Photographs showing aqueous dispersion of vermiculite layers, exfoliated from vermiculite crystals as shown in the inset. (b) XRD pattern of vermiculite crystals. (c)AFM, (d) FESEM image along with height profile, (e) TEM and (f) HRTEM images of exfoliated vermiculite layers obtained by employing two-step ion-exchange method.

Aqueous dispersions of exfoliated clay layers and purified humic acids were mixed at different ratios and their colloidal stability was monitored over a period of three months. Pure humic acids and vermiculite dispersions started settling down after around 24 undisturbed hours; in contrast, humic acids-vermiculite dispersions remain stable up to three months indicating favorable interactions between the two, photos of the dispersions are compared in Figure 2.3a and 2.3b. Such augmentations of colloidal stability of bulk clay particles induced by humic acids are already documented in the relevant literature.[1,29-32] Humic acids bind to clay particles through following modes of interactions- (a) anion-exchange to clay edges, (b) cation- or water-bridges to clay surfaces (c) H-bonding to the surface Si–OH groups, and (d) van der Waals forces. While, unbound hydrophilic side

TH-2654_156122042

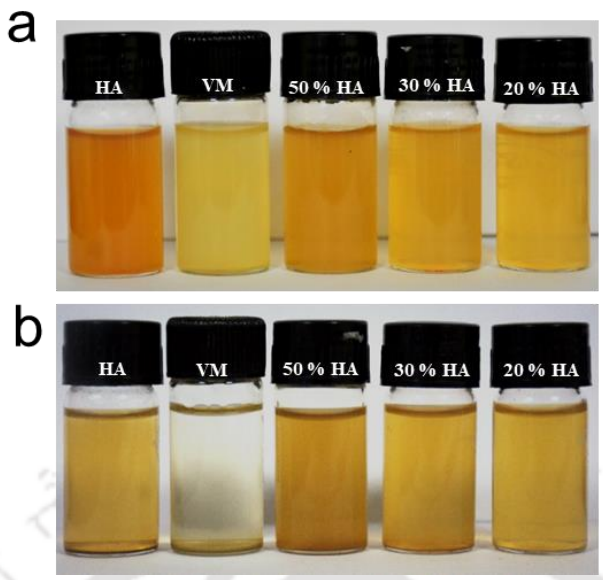

Figure 2.3: Photographs showing aqueous dispersions of HA, VM, 20 % HA, 30 % HA and 50 % HA at: (a) day 1 and (b) day 90.

Scheme 2.1: Schematic showing probable interactions of humic acid functional groups with silicate sheets of exfoliated vermiculite layers.

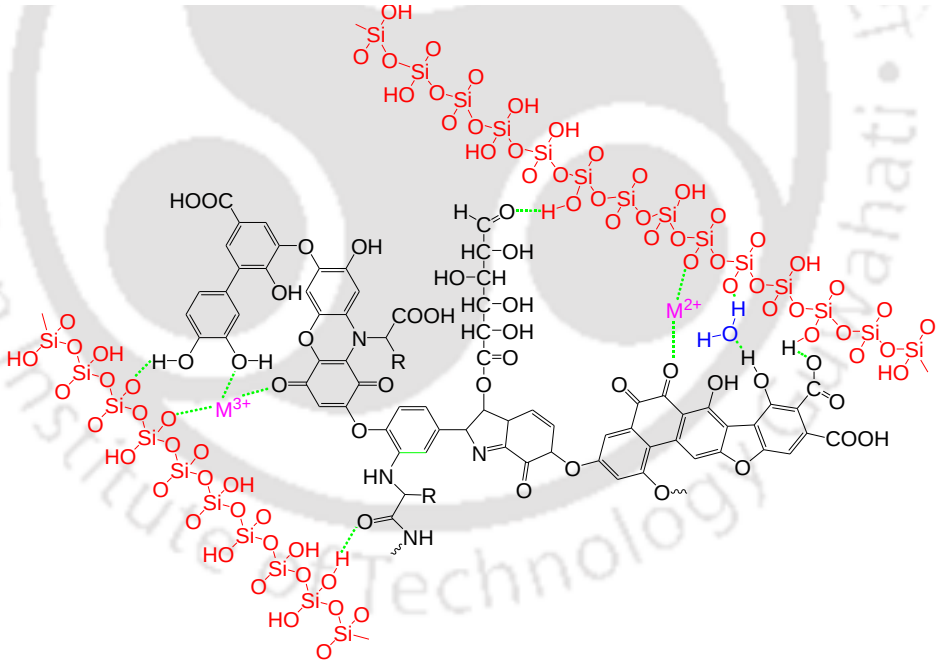

chains of humic acids assist dispersion of clay particles in water, the surface charges of clay layers prevent agglomeration of humic acids into polymeric particles. Exfoliation of bulk clay particles into nanoflakes increases not only surface to volume ratios, but also the number of defect sites necessary to interact with humic acids. Similarly, multiple steps of purification should free more functional groups in humic acid to interact with clay layers, and hence a pronounced crosslinking between the two are expected. A hypothetical model

TH-2654_156122042

depicting interactions between humic acid functional groups and silica sheets of exfoliated clay layers is shown in Scheme 2.1. The diverse crosslinking possibilities of humic acids and exfoliated clay layers should yield highly robust composite materials. Seeking a proof of this concept, dispersions of humic acids and exfoliated vermiculite layers were mixed in different weight ratios (20 %, 30 %, 50 % and 70 % humic acids) and vacuum filtrated through commercial filtration membranes to obtain freestanding membranes. A photo of the as prepared membrane containing 50 % humic acids (50 % HA) is shown in Figure 2.4a. Soil composites up to 50 % humic acids contents gave highly robust freestanding membranes, but composite with higher than 50 % humic acids yielded fragile membranes, which tends to break easily, hence not considered for future applications. The field emission scanning electron microscopy (FESEM) examination on the cross-section of the soil membrane revealed its lamellar structure, a representative image of the same is shown in Figure 2.4b. The lamellar structures of membranes are also supported by the presence of reflections in the range of 2θ = 6.5 to 5.8 degrees, in their respective powder X-ray diffraction (pXRD) patterns, as shown in Figure 2.4c. The interlayer spacing of the soil membranes calculated by applying Bragg's law were found to be in the range of 1.2 to 1.6 nm. Bending stiffness of the membranes were calculated

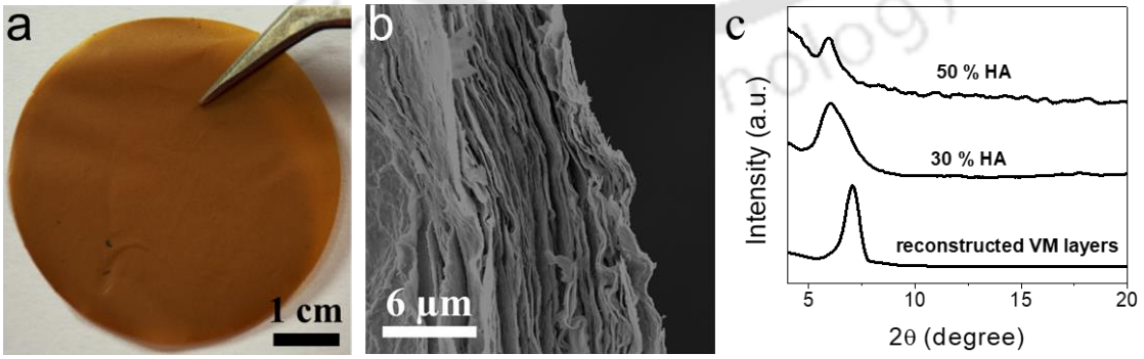

Figure 2.4. Freestanding soil membranes: (a) Digital photo, and (b) cross-sectional FESEM image of soil membrane containing 50 % humic acids (50 % HA). (c) XRD patterns of pure VM, 30 %, and 50 % HA composite membranes

by Lorentzen & Wettre two-point method[14,33] described in the Figure 2.5a. The bar

TH-2654_156122042

diagram in Figure 2.5b shows that the stiffness values of the soil membranes increase with increasing humic acids content in it. The crosslinking of exfoliated vermiculite with humic acid functional groups should prevent the sliding of vermiculite sheets

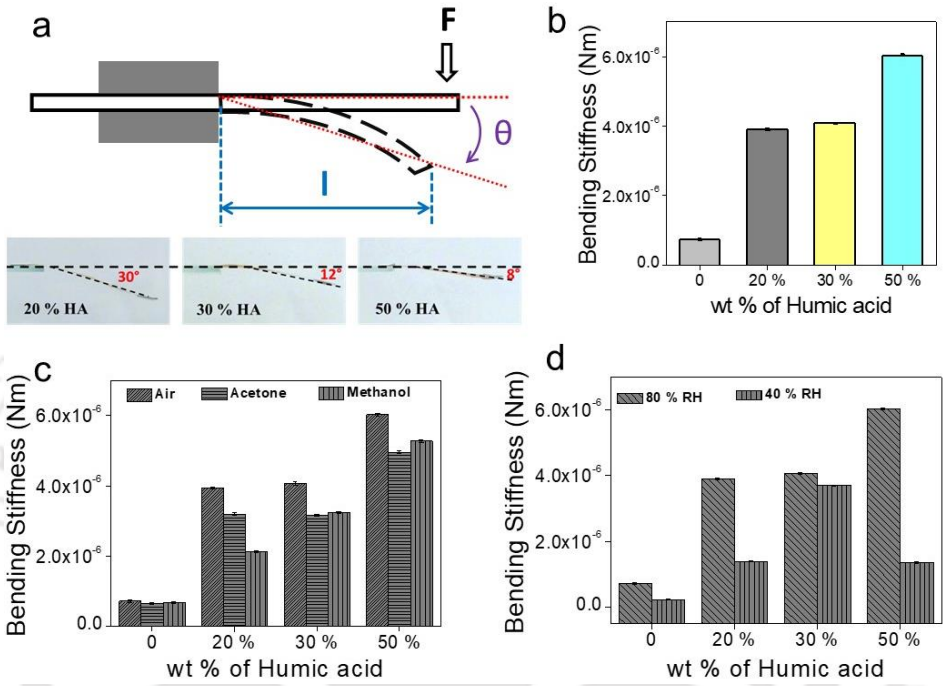

Figure 2.5. Bending stiffness measurement: (a) Schematic diagram describing parameters of the bending stiffness measurement along with photographs showing bending of 20 %, 30 % and 50 % HA strips. (b) Bending stiffness of soil membranes with different compositions. Bending stiffness of the soil membranes in (c) different solvent environment, and (d) different humidity.

from their specific position resulting in higher values of stiffness. The stiffness of the soil membranes was found to be also dependent on atmospheric humidity level or presence of solvent vapors. As described in the Figure 2.5c, in presence of acetone and ethanol stiffness of the membranes decreases, but it increases with increasing humidity level in the atmosphere (Figure 2.5d). The synergic effect of humic acids and exfoliated clay layers was also established by comparing tensile strength values of the soil membranes with that of pure vermiculite membrane (Figure 2.6a). While tensile strength values of 20 %, 30 %, and 50 % HA membranes were found to be 2.4, 3 and 4 times higher than that of pure vermiculite membrane, pure humic acids

TH-2654_156122042

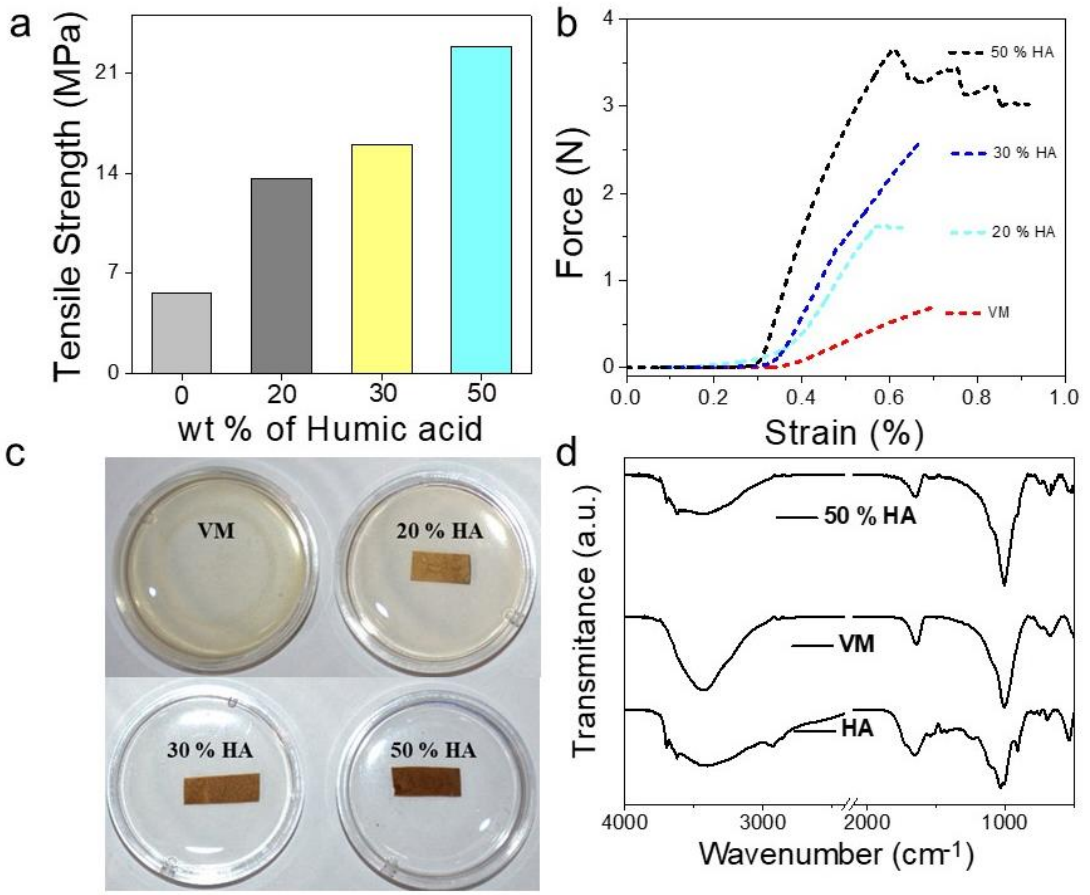

Figure 2.6. Mechanical strength of soil membranes: (a)Bar diagram showing tensile strength of soil membranes with different compositions. (b) Stress vs strain curves of soil membranes with different humic acid content. (c) Photographs showing solution stability of soil membranes dipped in water for 30 days after 2 hours of shaking. (d) FTIR spectra of 50 % HA membrane is compared with that of purified humic acids, exfoliated vermiculite layers: The diminishing intensity of IR band corresponding to O-H vibrations ($I_{3325\ cm\text{-}1}$) for soil membrane ($I_{3325\ cm\text{-}1}/I_{1030\ cm\text{-}1}$ = 0.25) as compared to that of pure humic acids ($I_{3325\ cm\text{-}1}/I_{1030\ cm\text{-}1}$ = 0.71) and vermiculite ($I_{3325\ cm\text{-}1}/I_{1030\ cm\text{-}1}$ = 0.88) support involvement of O-H groups in the crosslinking process.

did not yield any membrane upon vacuum filtration. The higher tensile strength values of soil membranes over pure vermiculite membranes can also be attributed to crosslinking effect (Scheme 1) of humic acids. The cross linker prevents sliding of the vermiculite sheets from their specific position to improve the mechanical properties. However, in the membranes with higher than 50 % humic acids, the cross-linker dominates over vermiculite fractions of the composites and hence the tensile strength values follow the opposite trends. For the same reason, soil samples with humic acids content significantly higher than that of two-dimensional

TH-2654_156122042

vermiculite flakes do not yield freestanding membranes. The stress-strain curve of the composite membranes is compared with that of pure vermiculite membrane in Figure 2.6b. The weight required to the break the strip was used as *maximum load* to calculate tensile strength by using following formula,

$$Tensile\ Strength\ (MPa) = \frac{Maximum\ load\ (N)}{Cross\ sectional\ area\ (mm^2)} \text{---------- (3)}$$

Crosslinking of clay layers by humic acids also fetched extraordinary underwater stability to the soil membranes. In order to verify underwater stability in realistic condition, small pieces (20 mm × 4 mm × 0.045 mm) of membranes were dipped into water and vigorously shaken for two hours. While pristine vermiculite membrane was disintegrated into an aqueous dispersion within 10 minutes of shaking, all the composite membranes remained unperturbed. Figure 2.6c shows photos of the soil membranes that survived for 30 days in water after 2 hours of vigorous shaking. Membranes with high solution-stability are vital for applications like water purifications, fuel cell, nanofluidics and solution based catalysis. Involvement of surface –OH groups on the crosslinking process is also supported by the diminishing intensity of IR band corresponding to –OH groups in the composite membranes as compared to that of purified humic acids and exfoliated vermiculite samples, shown in the Figure 2.6d. The diminishing intensity of IR band corresponding to O-H vibrations ($\mathbf{I_{3325\ cm^{-1}}}$) for soil membrane ($\mathbf{I_{3325cm^{-1}}/I_{1030cm^{-1}}}$ = 0.25) as compared to that of pure humic acids ($\mathbf{I_{3325cm^{-1}}/I_{1030cm^{-1}}}$= 0.71) and vermiculite ($\mathbf{I_{3325cm^{-1}}/I_{1030cm^{-1}}}$= 0.88) support involvement of -OH groups in the crosslinking process.

TH-2654_156122042

Distinct XRD reflections at low angle region of the soil membranes indicate periodic stacking of the layers with well-defined interlayer spacing. Such minuscule spaces in the 1-2 nm regime decorated with diverse organic and inorganic functional groups should exhibit unique molecular and/or ionic transport properties. Soil based nanofluidic devices as shown in Figure 2.7a were fabricated by encapsulating rectangular soil strips into freshly prepared polydimethylsiloxane (PDMS) elastomer. In Figure 2.7b, current versus voltage (*I*-*V*) curves recorded with the soil based nanofluidic device (50 % HA) with three different KCl concentrations are plotted. The linearity in the *I*-*V* curves confirmed the formation of a percolated network of nanofluidic channels across the soil membrane. Conductivity values of the nanofluidic devices were calculated from respective *I*-*V* curves at different salt concentrations, and were compared with bulk electrolyte solutions. As can be seen from Figure 2.7c, the conductivity of bulk solution varies linearly with concentration. In a clear contrast, conductivity of the soil membranes exhibits two distinct features. At high concentrations, it increases linearly with increasing salt concentrations, but for the salt concentrations below 0.1 M, conductivity remains unperturbed even after several orders of magnitude change in the concentration (from 0.1 to 10^{-6} M). This behavior of concentration dependent ionic conductivity, also known as surface-charge-governed ionic transport is a characteristic signature of nanofluidic channels.[12,34] Nanofluidic membranes exhibiting surface-charge-governed ionic transport up to 0.1 M salt concentration along with ease of fabrication and scaling up could be suitable for various technological applications. Soil-based nanofluidic membranes are also employed to harvest green energy from concentration differences. For that, devices comprising two compartments separated by soil membrane were fabricated by using PDMS elastomer, shown in the Figure

TH-2654_156122042

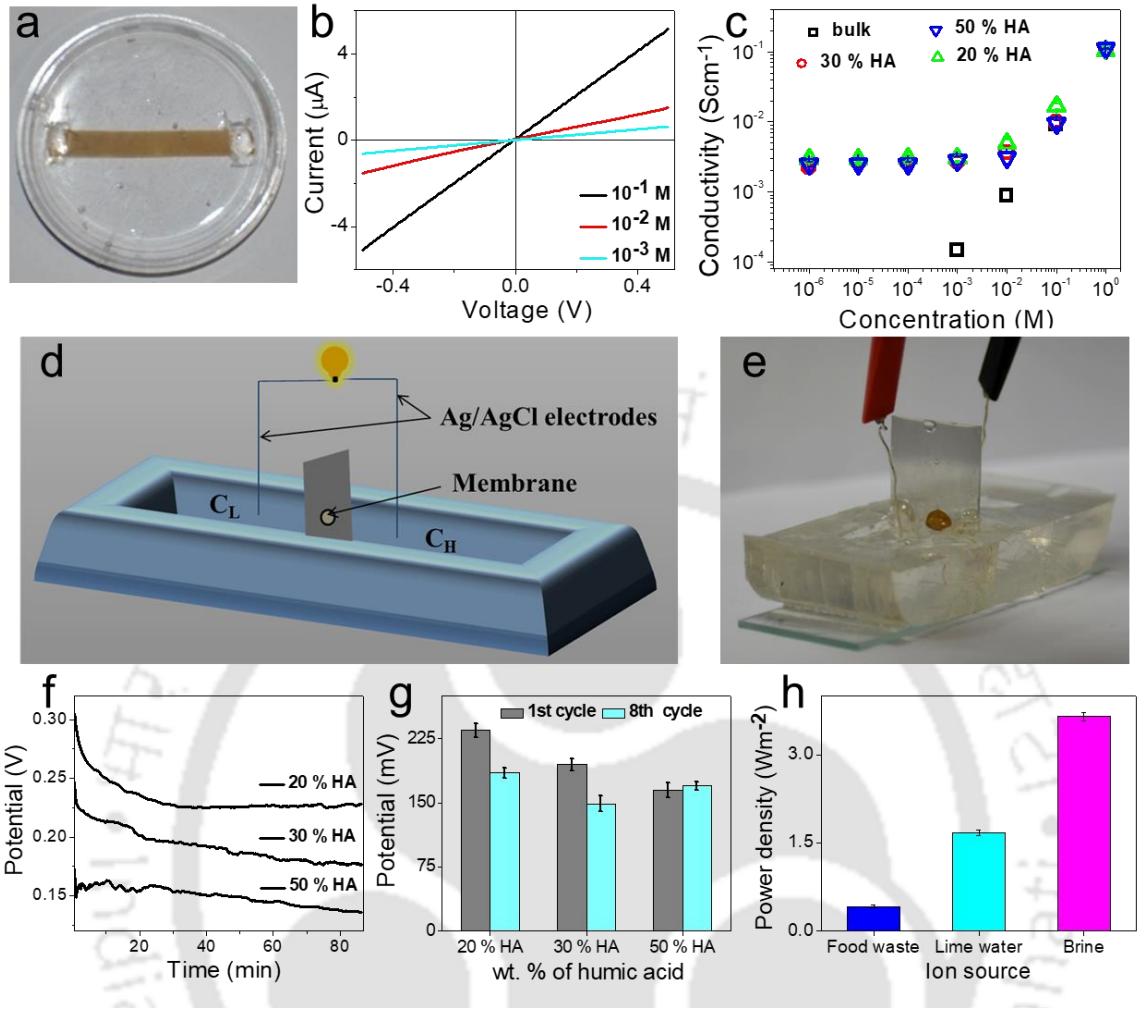

Figure 2.7. Nanofluidic characteristics of soil membranes: (a) Digital photograph of a vermiculite nanofluidic device encapsulated in PDMS polymer. (b) Representative I-V curves obtained with soil-based nanofluidic device at different KCl concentrations (c) Ionic conductivity as a function of KCl concentration for different soil-based nanofluidic devices and bulk solution. (d) Schematic representation, and (e) photograph of the nanofluidic device used for harvesting green energy from concentration difference. (f) Trans-membrane potential of soil membranes as a function of time, under three fold concentration gradient (C_H = 1M, C_L = 0.001 M) (g) Bar diagram comparing trans-membrane potential of soil membranes placed between electrolytes with three orders of concentration difference for 1st and 8th cycle. (h) Power harvested from naturally available ion sources by employing 50 % HA membrane-based nanofluidic device.

2.7d and 2.7e. Both compartments were filled with 2 mL aqueous KCl solutions of different concentrations, 1 M in high (C_H) and 10^{-3} M in the low (C_L) concentration chamber. Two Ag/AgCl electrodes were inserted into the electrolyte solutions to measure the transmembrane potentials and diffusion currents across the soil membranes. The transmembrane potentials recorded as a function of time for different soil membranes are shown in Figure 2.7f. Immediately after applying the

TH-2654_156122042

concentration gradient each of the devices displayed a maximum open circuit potential which declined with time to reach equilibrium at around 0.22, 0.19 and 0.15 V for 20 %, 30 % and 50 % HA membranes, respectively. Such potential differences obtained through nanofluidic membranes are attributed to concentration gradient driven selective cation transport across the membranes.[35] The equilibrium power output across the membranes were calculated by using equation (1) to be 2.85, 1.46 and 1.2 Wm^{-2} for 20 %, 30 % and 50 % HA respectively which is around 50 % higher than that was reported earlier for graphene oxide membranes.[36]

$$P_{max} = \frac{V_m \times I_\circ}{A} \text{---------} \quad (1)$$

Where V_m and I_o are the membrane potential and zero-volt current respectively, and A is the diffusive membrane area. The stability in power output by soil membranes was ascertained by repeating the experiment for several times and the transmembrane potentials obtained on 1st and 8th cycle are shown as a function of humic acid content in the Figure 2.7g. Soil membranes displayed remarkably high cation transference numbers 1.00, 0.94 and 0.97 for 20 %, 30 % and 50 % HA membrane, respectively, calculated by using the equation (2).

$$E_{diff} = (2t_+ - 1)\frac{RT}{zF}\ln\frac{C_H}{C_L} \text{----------} \quad (2)$$

Where, E_{diff} is the stable membrane potential of the device at 8th run, R is the universal gas constant, T is the room temperature, z is the no. of moles of electrons, F is the Faraday constant, C_H and C_L are the concentration of the salt solution at high and low concentration chamber, respectively. As the stability of the soil membranes plays vital role in these kinds of applications, stability of soil membranes in energy harvesting devices was evaluated by exposing the same to electrolyte solutions for

TH-2654_156122042

several days. Soil membranes were also tested for harvesting green energy from natural ion sources such as food waste, lime-juice and simulated seawater. Figure 2.7h shows power obtained by adding natural ion sources to high concentration chamber while filling the low concentration chamber with DI water. In order to check the stability of RED devices in water, the fabricated devices comprising of 50 % HA, 30 % HA, 20 % HA and VM membranes were filled with electrolyte solutions in both the chamber and the stability of the devices were observed by taking

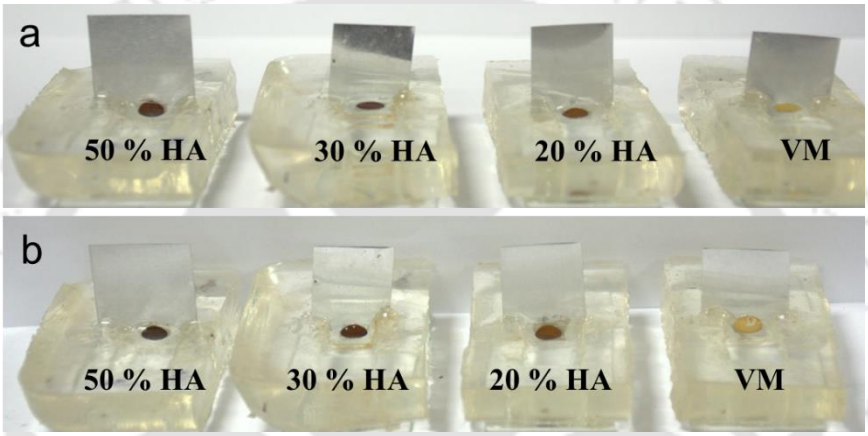

Figure 2.8. Photographs of the RED devices after (a) 12 hours and (b) 7 days of immersing in electrolyte solutions.

photographs in an interval of several hours. The device with VM membrane broke after 12 hours while the other devices made of composite membranes remained stable till 7 days. The device of pure vermiculite membrane collapsed within 12 hours while the devices composed of composite membranes remained stable up to 10 days as demonstrated in Figure 2.8.

The molecularly thin nanofluidic channels of soil membranes enriched with surface charges also enable the selective-cation-transport behavior. 50 ppm aqueous solutions of NaCl, KCl and LiCl were vacuum filtered through composite membranes (thickness 44 microns), and concentration of the cations in the filtrate was determined by using a Flame-photometer instrument. The bar diagrams in

TH-2654_156122042

Figure 2.9a, showing concentrations of the cations permeated through the composite membranes clearly illustrate ion-selective nature of the membrane. For example, through 70 % HA membrane K^+ ion with a hydration radius of 3.3 Å was transported 2 and 3 times higher than that of Na^+ and Li^+ ions with hydration radius 3.6 and 3.8

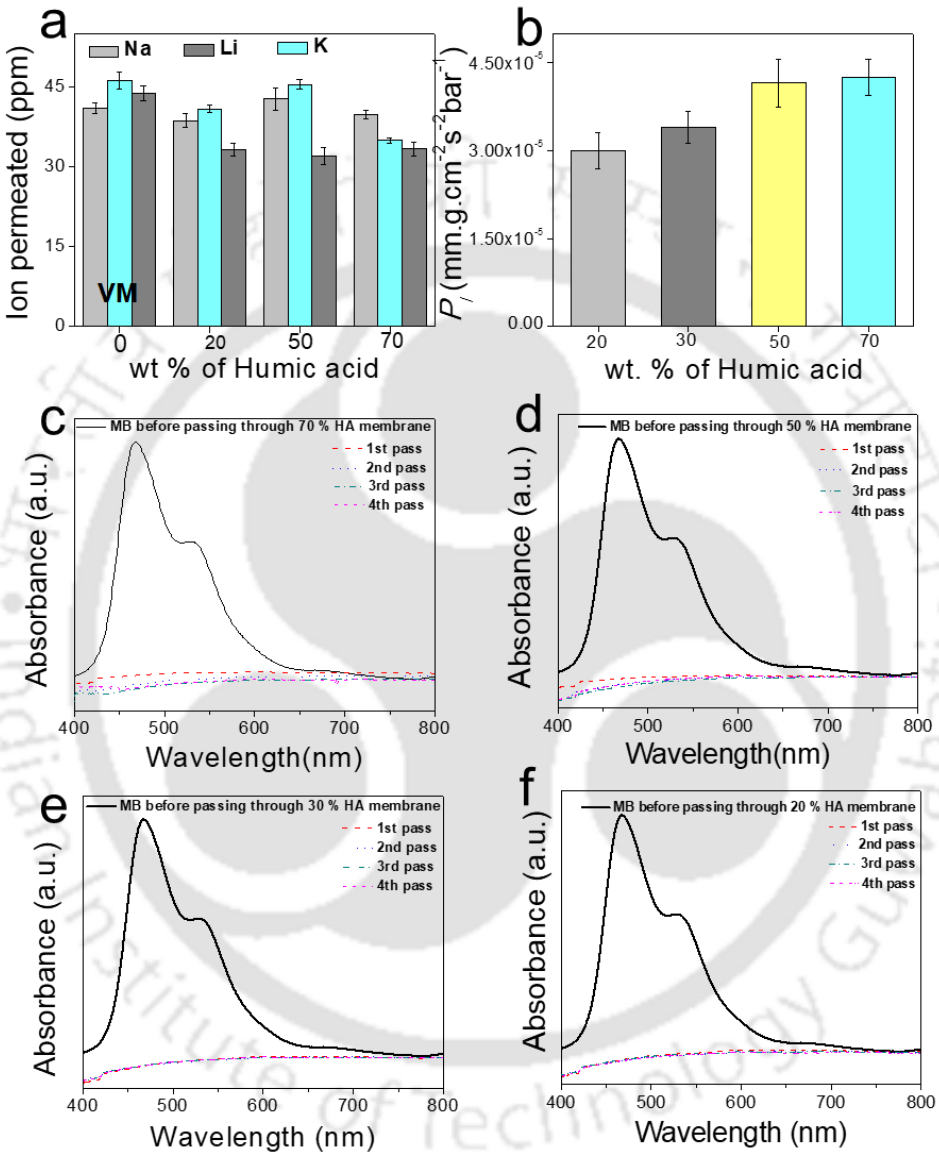

Figure 2.9. Soil membranes for molecular separation: (a) ion permeation efficiency of soil membranes. (b) Permeability of liquids through different soil membranes. UV-Visible spectra comparing the absorbance of methylene blue before and after passing through (c) 70 % HA membrane, (d) 50 % HA membrane, (e) 30 % HA membrane and (f) 20 % HA membrane respectively for four consecutive times.

Å, respectively. The same trend of ion permeation was also followed by 20 %, and 50 % HA membranes. In spite of smaller interlayer spacing (d = 1.37 nm), pure vermiculite membrane did not show notable selectivity towards any particular

TH-2654_156122042

cations. The rich chemical functionalities of humic acids in the soil membranes are also utilized to separate cationic dyes from aqueous solutions. In order to investigate the efficiency of dye separation, 60 ml solutions of 100 ppm methylene blue dye were passed through soil membranes (30 µm), and the concentrations of the dye molecules were measured before and after passing through each membranes by employing UV-Visible spectroscopy. The soil membranes could easily remove up to 60 mg of the dye molecule as illustrated in Figure 2.9c to 2.9f. Remarkably, soil membranes exhibit much higher removal efficiency under vacuum assisted filtration than its absorption capacity, by dipping the membranes in dye solution. A 50 % HA membrane (weight 10 mg) could remove up to 61.2 mg MB dye under vacuum filtration method, while it could absorb only 12.24 mg when soaked in aqueous dye solution of similar concentrations for two hours, suggesting the same to be a filtration process not absorption. From the time required to vacuum filter the dye solution, the liquid permeability of the soil membranes of different composition were calculated. As shown in the bar diagram of Figure 2.9b, the permeability of the 70 % HA membrane (4.25×10^{-5} mm g cm^{-2} s^{-1} bar^{1}) was found to be slightly higher than that of other membranes.

As both humic acids and clay are electrically non-conducting, pristine soil membranes are insulating in nature. However, electronic conductivity has been induced to the soil membranes by heating them under N_2 atmosphere. Figure 2.10b shows *I-V* curve of the heated strips measured by painting conductive silver paste on either ends. Moreover, conductivities of the heated soil membranes were found to be linearly dependent on the humic acids contents in the starting mixture, see Figure 2.10c. The electrical conductivity obtained as such are attributed to the removal of

TH-2654_156122042

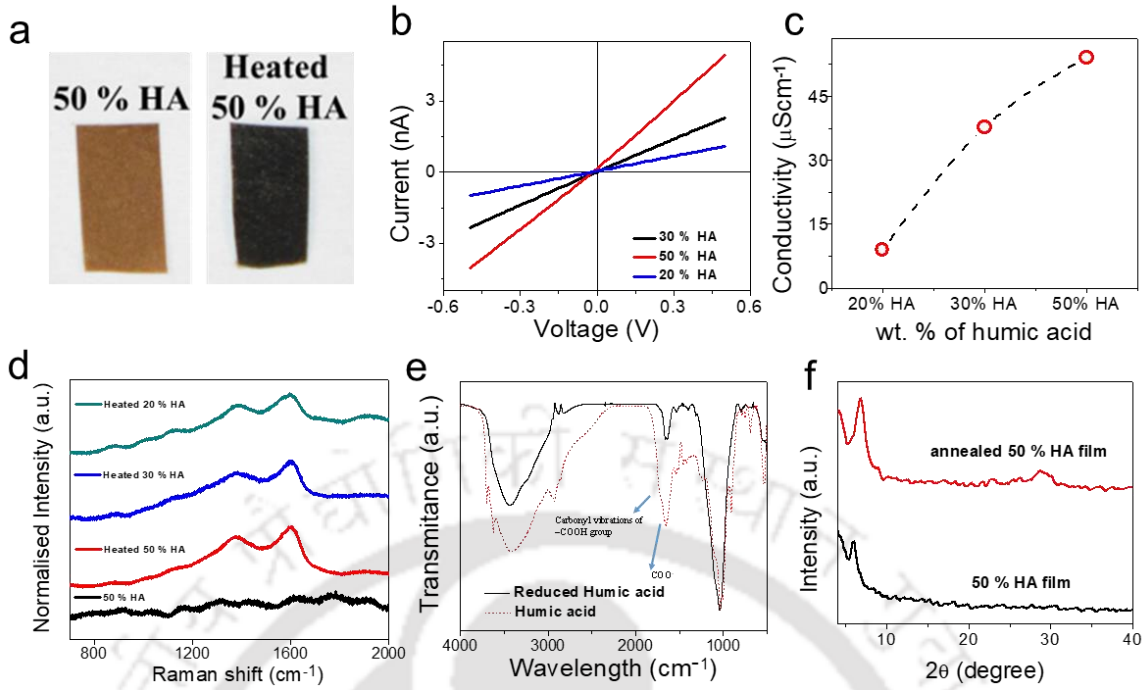

Figure 2.10. Heated soil membranes: (a) Digital photograph showing color change of 50 % HA-VM membrane upon annealing at 550 °C. (b) Characteristic I-V curves of soil membranes heated up to 550 ° C under N2 atmosphere. (c) Electrical conductivity of the membranes as a function of humic acids contents in the initial mixture. (d) Raman spectra of 20 %, 30 % and 50 % HA membranes heated at 550 °C. (e) FT-IR spectra of Humic acid and reduced humic annealed at 500 ^{o}C in nitrogen atmosphere. The conversion of carboxyl functionality is demonstrated by the disappearance of carbonyl peak at 1653 cm$^{-1.}$ (f) XRD pattern of 50 % HA film before and after heating at 550° C in nitrogen atmosphere.

the organic functional groups from humic acids during the heat treatment process, which is also apparent from the color transformation of soil strips from brown to black, digital photos of a 50 % HA strip before and after annealing at 550 °C is shown at the inset of Figure 2.10a. Also the appearance of G band in the Raman spectra of heat-treated soil strips, shown in Figure 2.10d, suggest enhancement of graphitic/amorphous carbon ratios in the samples, which can lead to a continuous network of graphitic carbons in the sample. The removal of organic functional groups from humic acid on heat treatment is further supported by comparing the IR spectra of the heated humic acid with pre heated humic acid as shown in Figure 2.10e. The conversion of carboxyl functionality is demonstrated by disappearance of sharp carbonyl peak at 1653 cm^{-1}. The heat treatment also reduced interlayer

TH-2654_156122042

spacing of soil membranes from 1.6 nm to 1.29 nm, shown in Figure 2.10f. A characteristic I-V curve of the heated pure humic acid shown in supporting Figure 2.11a confirms the induction of electrical conductivity in heated humic acids. At present, electrical conductivity of the heated soil samples is very low. However, for applications like chemical sensing or bio-sensing more than higher values of

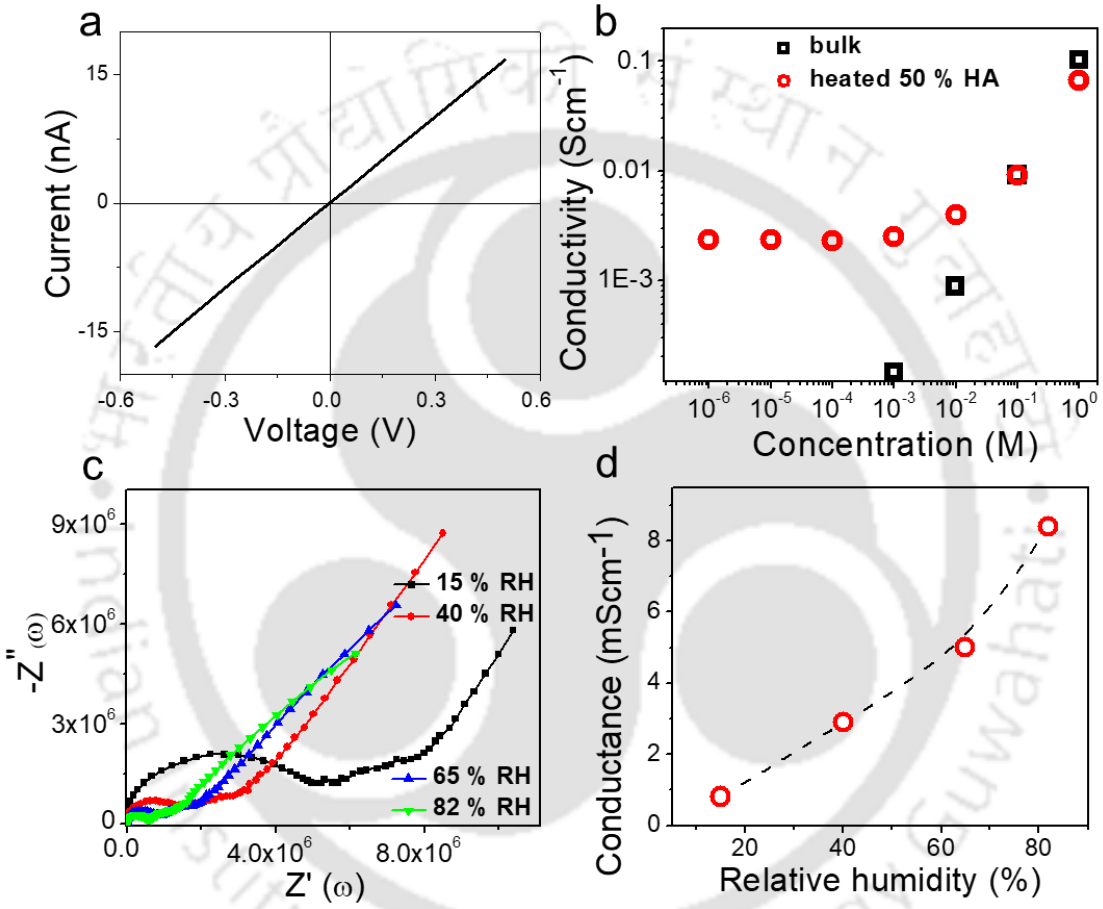

Figure 2.11. Mixed conductivity of soil membranes: (a) Characteristic I-V curve of pure humic acids heated at 550° C in nitrogen atmosphere (b) Surface-charge-governed ionic conductivity of the heated soil membrane (50 % HA). (c) Representative cole-cole plots for the heated membrane at different relative humidity. (d) Total conductivity as a function of relative humidity.

conductivity higher change in conductivity (with respect to change in external atmosphere) is important. Moreover, tuning the composition and annealing temperature can further improve conductivity of the soil membranes. It is noteworthy that high temperature annealing process that fetched electrical conductivity to the soil strips did not affect its nanofluidic ionic conductivity. The

TH-2654_156122042

residual functional groups of soil components are found to sufficient to exhibit surface-charge-governed ionic transport as shown in Figure 2.11b. Systems with such interpenetrating ionic and electronic conductivity have large potential for technological applications. The mixed conducting properties of heated soil strips were studied by measuring conductivity at different relative humidity (RH) by employing an impedance analyzer (Multi Autolab/M204 potentiostat/galvanostat equipped with FRA32M module) in the frequency range from 500 KHz to 1Hz, with a perturbation voltage amplitude of 100 mV. Representative cole–cole plots obtained for device made from heated soil strip at different relative humidity are shown in Figure 2.11c. Total conductivities (σ) of the membrane were calculated by using the formula $\sigma = L/(R \times A)$, where L is the distance between the two electrodes, A is the cross-sectional area of the strip. The AC impedances (R) were obtained by fitting the data of cole–cole plot to an equivalent circuit, employed earlier to study mixed conducting properties of graphene oxide-reduced graphene oxide based membranes.[37] As shown in Figure 2.11d, total conductivity decreases with decreasing relative humidity of the atmosphere, suggesting ionic (proton) conductivity as a major contributor to the overall conductivity of the heated soil strips.

Freestanding-mixed-conducting-membranes prepared from low-cost starting materials with tuneable electrical conductivity could be ideal for gas sensing applications. A soil-based gas-sensing device was fabricated by connecting two Cu wires to silver paste painted on both ends of a rectangular soil strip (50 % HA) of dimensions 20 mm × 6 mm × 0.045 mm. The soil device thus prepared was placed in a closed aluminium container as illustrated in the schematic of Figure 2.12a. The

TH-2654_156122042

electrical resistance of the same was recorded as a function of time using a source meter instrument. Calculated amounts of ammonia vapor were introduced into the

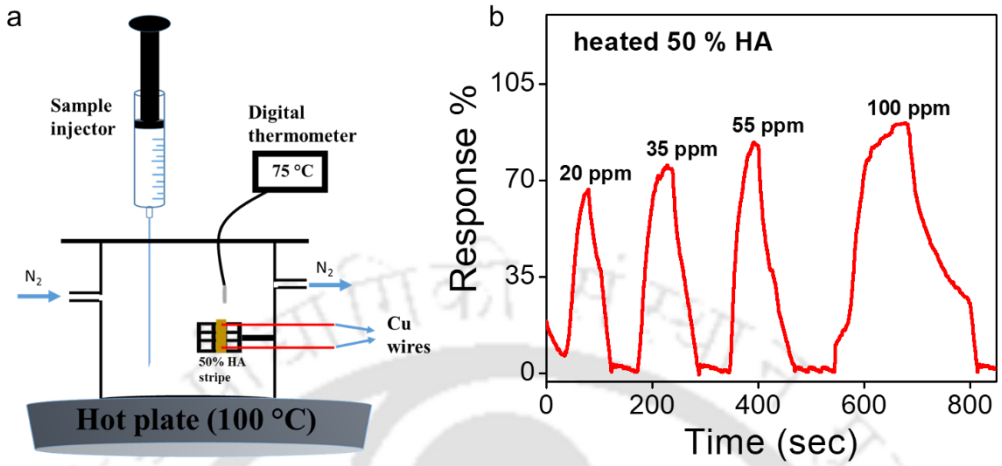

Figure 2.12: Soil membranes for gas sensing application: (a) Schematic representation of experimental set up used for NH_3 vapor sensing (b) Response curve for heated 50 % HA strip towards different concentrations of ammonia vapor is compared with that of acetone and ethanol vapors.

chamber through a liquid injection syringe. The real-time response curve recorded for heated soil membrane at four different concentrations of NH_3 vapor is shown in Figure 2.12b.

The heated soil membrane showed 70 % responsiveness towards 20 ppm of ammonia vapours. The high sensitivity of heated soil membrane towards ammonia vapours can be attributed to smaller flake sizes, higher defect density and larger interlayer spacing. However, under similar conditions heated soil membrane did not show any sensitivity towards ethanol and acetone vapors.

2.5: CONCLUSION

The work here demonstrated that naturally abundant soil components can be engineered to prepare advanced materials for futuristic applications. Clay layers exfoliated by ion exchange methods were cross-linked by purified humic acid

TH-2654_156122042

molecules to yield mechanically robust soil membranes possessing great potential toward solution based applications. The percolated network of ultra-thin nanochannel exhibiting fascinating transport properties could find applications in the areas of selective molecular/ionic transport, catalysis, energy harvesting, and storage. The interpenetrating ionic and electronic conductivities of heated soil membranes prepared from dirt cheap raw materials by employing a straightforward and scalable method could provide new platform to study mixed conducting materials. Such materials could be ideal in the areas like the solid state fuel cell, battery, and supercapacitor, gas sensing and separation. Exhaustive investigations into various ways of tuning soil chemistry may also provide means to alter quality of the soil in the natural environments.

TH-2654_156122042

2.6: REFERENCES

1. Evangelou, V. P. Environmental Soil and Water Chemistry: Principles and Applications; John Wiley & Sons: New York, 1998; pp 476-498
2. Manahan, S. E. Fundamentals of Environmental Chemistry. 2nd ed.; *CRC Press LLC*: 2001.
3. Wang, Y. B.; Wu, C. Y.; Wang, X. J.; Zhou, S. G. The role of humic substances in the anaerobic reductive dechlorination of 2,4-dichlorophenoxyacetic acid by Comamonas koreensis starin CY01. *J. Hazard. Mater.* **2009**, *164*, 941-947.
4. Zhou, S.; Chen, S.; Yuan, Y.; Lu, Q. Influence of humic acid complexation with metal ions on extracellular electron transfer activity. *Sci. Rep.-UK* **2015**, *5*.
5. Zhou, J. L.; Rowland, S. J.; Braven, J.; Mantoura, R. F. C.; Harland, B. J. Tefluthrin sorption to mineral particles: Role of particle organic coatings. *Int. J. Environ. An. Ch.* **1995**, *58*, 275-285.
6. Boyd, S. A.; Sheng, G. Y.; Teppen, B. J.; Johnston, C. J. Mechanisms for the adsorption of substituted nitrobenzenes by smectite clay. *Environ. Sci. Technol.* **2001**, *35*, 4227-4234.
7. Wang, K. J.; Xing, B. S. Structural and sorption characteristics of adsorbed humic acid on clay minerals. *J Environ Qual* **2005**, *34* , 342-34
8. Bortnikov, N. S.; Novikov, V. M.; Soboleva, S. V.; Savko, A. D.; Boeva, N. M.; Zhegallo, E. A.; Bushueva, E. B. The role of organic matter in the formation of fireproof clay of the Latnenskoe deposit. *Dokl Earth Sci* **2012**, *444* , 634-638.
9. Refaey, Y.; Jansen, B.; El-Shater, A. H.; El-Haddad, A. A.; Kalbitz, K. The Role of Dissolved Organic Matter in Adsorbing Heavy Metals in Clay-Rich Soils. *Vadose Zone J* **2014**, *13*.
10. Laura, E.; McAllister, K. T. S. Role of Clay and Organic Matter in the Biodegradation of Organics in Soil. *Springer: Dordrecht*, **2010**.

TH-2654_156122042

11. Murray, H. H. Overview — clay mineral applications. *Applied Clay Science* **1991**, *5* , 379-395.

12. Shao, J. J.; Raidongia, K.; Koltonow, A. R.; Huang, J. Self-Assembled two-dimensional nanofluidic proton channels with high thermal stability. *Nat. Commun.* **2015**, *6*, 7602.

13. Gogoi, R. K.; Saha, K.; Deka, J.; Brahma, D.; Raidongia, K. Solvent-driven responsive bilayer membranes of clay and graphene oxide. *J. Mater. Chem. A* **2017**, *5*, 3523-3533.

14. Gogoi, R. K.; Raidongia, K. Strategic shuffing of clay layers to imbue them with responsiveness. *Adv. Mater.* **2017**, *29*, 1701164.

15. Bitinis, N.; Hernandez, M.; Verdejo, R.; Kenny, J. M.; Lopez-Manchado, M. A. Recent advances in clay/polymer nanocomposites. *Adv. Mater.* **2011**, *23*, 5229-5236.

16. Stevenson, F. J. Humus Chemistry: Genesis, Composition, Reaction. *Wiley Interscience: New York*, **1982**.

17. Sutton, R.; Sposito, G. Molecular structure in soil humic substances: The new view.*Environ Sci Technol* **2005**, *39*, 9009-9015.

18. Zhu, W.; Zhao, F.; Yao, J. F.; Zhang, X. Y.; Wang, H. T.; Xia, C. R.; Li, C. Z. Humic acids as a complexible fuel for combustion synthesis of ceramic nanoparticles. *J Am Ceram Soc* **2007**, *90*, 4012-4014.

19. Baskakov, S. A.; Lobach, A. S.; Vasil'ev, S. G.; Dremova, N. N.; Martynenko, V. M.; Arbuzov, A. A.; Baskakova, Y. V.; Volodin, A. A.; Volkov, V. I.; Kazakov, V. A.; Shul'ga, Y. M. High-Temperature Carbonization of Humic Acids and a Composite of Humic Acids with Graphene Oxide. *High Energ Chem+* **2016**, *50*, 43-50.

20. Mendez, E. M. P.; Havel, J.; Patocka, J. Humic substances- compounds of still unknown structure: applications in agriculture, industry, environment and biomedicine. *J. Appl. Biomed.* **2005**, *3*, 13-24.

TH-2654_156122042

21. Luo, W. J.; Gao, Q.; Wu, X. L.; Zhou, C. G. Removal of cationic dye(methylene blue) from aquoeus solution by humic acid modified expanded perlite. *Sep. Sci. Technol.* **2014**, *49*, 2400-2411.

22. Shenvi, S. S.; Isloor, A. M.; Ismail, A. F.; Shilton, S. J.; Al Ahmed, A. Humic acid based biopolymeric membrane for effective removal of methylene blue and rhodamine B. *Ind. Eng. Chem. Res.* **2015**, *54*, 4965-4975.

23. Deserra, M. O.; Schnitze,M. Extraction of Humic Acid by Alkali and Chelating Resin. *Can J Soil Sci* **1972**, *52*, 365-&.

24. Paul, S.; Sharma, T.; Saikia, D.; Saikia, P. P.; Borah, D.; Baruah, M. K. Evaluation of pKa Values of Soil Humic Acids and their Complexation Properties. *International Journal of Plant & Soil Science* **2015**, *6*, 218-228.

25. Schepetkin, I. A.; Khlebnikov, A. I.; Ah, S. Y.; Woo, S. B.; Jeong, C. S.; Klubachuk, O. N.; Kwon, B. S. Characterization and biological activities of humic substances from mumie. *J Agr Food Chem* **2003**, *51*, 5245-5254.

26. Rodrigues, A.; Brito, A.; Janknecht, P.; Proenca, M. F.; Nogueira, R. Quantification of humic acids in surface water: effects of divalent cations, pH, and filtration. *J Environ Monitor* **2009**, *11*, 377-382.

27. Bayer, C.; Martin-Neto, L.; Mielniczuk, J.; Saab, S. D.; Milori, D. M. P.; Bagnato, V. S. Tillage and cropping system effects on soil humic acid characteristics as determined by electron spin resonance and fluorescence spectroscopies. *Geoderma* **2002**, *105*, 81-92.

28. Monsallier, J. M.; Scherbaum, F. J.; Buckau, G.; Kim, J. I.; Kumke, M. U.; Specht, C. H.; Frimmel, F. H. Influence of photochemical reactions on the complexation of humic acid with europium(III). *J Photoch Photobio A* **2001**, *138*, 55-63.

29. Balcke, G. U.; Kulikova, N. A.; Hesse, S.; Kopinke, F. D.; Perminova, I. V.; Frimmel, F. H. Adsorption of humic substances onto kaolin clay related to their structural features. *Soil Sci Soc Am J* **2002**, *66*, 1805-1812.

TH-2654_156122042

30. Tombacz, E.; Libor, Z.; Illes, E.; Majzik, A.; Klumpp, E. The role of reactive surface sites and complexation by humic acids in the interaction of clay mineral and iron oxide particles. *Org Geochem* **2004**, *35*, 257-267.

31. Nascimento, F. H.; Masini, J. C. Influence of humic acid on adsorption of Hg(II) by vermiculite. *J Environ Manage* **2014**, *143*, 1-7.

32. Zhang, L. C.; Luo, L.; Zhang, S. Z. Integrated investigations on the adsorption mechanisms of fulvic and humic acids on three clay minerals. *Colloid Surface A* **2012**, *406*, 84-90.

33. Mark, R. E.; Habeger, C. C.; Borch, J.; Lyen, M. B. *Handbook of Physical Testing of Paper*. CRC Press: **2001**.

34. Raidongia, K.; Huang, J. Nanofluidic ion transport through reconstructed layered materials. *J. Am. Chem. Soc.* **2012**, *134*, 16528.

35. Lee, S. W.; Kim, H. J.; Kim, D. K. Power Generation from Concentration Gradient by Reverse Electrodialysis in Dense Silica Membranes for Microfluidic and Nanofluidic Systems. *Energies* **2016**, *9*, 49-60.

36. Ji, J.; Kang, Q.; Zhou, Y.; Feng, Y.; Chen, X.; Yuan, J.; Guo, W.; Wei, Y.; Jiang, L. Osmotic power generation by positively and negatively charged 2D nanofluidic membrane pairs. *Adv. Func. Mater*. **2016**, *27*, 1603623.

37. Bayer, T.; Bishop, S. R.; Perry, N. H.; Sasaki, K.; Lyth, S. M. Tunable mixed ionic/electronic conductivity and permittivity of graphene oxide paper for electrochemical energy conversion. *ACS Appl. Mater. Interfaces* **2016**, *8*, 11466−11475.

TH-2654_156122042

Chapter 3

Electrical power Generation from the Contrasting Interfacial Activities of Boron- and Nitrogen- Doped Reduced Oxide Membranes

Summary*

In the present chapter, the complementary charge transfer activities of boron (B-r-GO) and nitrogen (N-r-GO) doped reduced graphene oxide (r-GO) flakes are exploited to extract energy from serene water resources. B-r-GO and N-r-GO samples prepared by annealing graphene oxide sheets with boric acid and urea were individually coated on cellulose membranes to fabricate B-r-GO/N-r-GO devices, which produces open-circuit voltages up to 570 mV when dipped in water. The power-output were found to be tunable by varying parameters like coating area, dopant amounts, annealing temperature, and ionic conductivity. The potential-drops due to the prolong soaking of B-r-GO/N-r-GO devices (for a few days) can be completely recovered through vacuum drying. In order to open-up the possibility of fabricating wearable energy devices the B-r-GO/N-r-GO samples are also coated on arbitrary substances like jeans cloths. The DFT calculations indicate that compared to N-r-GO, the B-r-GO structure is more stable and has considerably higher charge transfer activity with water molecules.

---

* Paper based on these studies has appeared in *ACS Appl. Nano Mater.*, 2019, **2**, 7997.

TH-2654_156122042

3.1: INTRODUCTION

The growing levels of greenhouse-gases and the depleting levels of fossil fuels are posing serious threats to our civilization. There is an urgent need for eco-friendly energy resources. Numerous techniques have been developed to extract energy from sustainable resources like environmental heat, wind, light, and waves. Unfortunately, the society is yet to be independent from the fossil fuels based energy resources.[1-5] Water has always been at the centre of attention in the environmentally benign energy harvesting processes. The vast mechanical energy stored in the flowing water has been harnessed into electricity for more than hundred years. But, the requirement of large infrastructures like huge dams, generators and waterwheels renders it incompatible with small-scale energy production projects. Several efforts are being devoted to overcome the obstacles in harvesting energy from naturally abundant water resources. For example, nanofluidic phenomena such as electrokinetic streaming potential, ionic current rectification and selective transport of cations (or anions) were exploited to extract electricity from flowing water.[6-12] Moisture driven ion-transfer processes on the surface of graphene oxide, porous carbon, and TiO_2 were also employed to generate electric potential.[13-17] Similarly, the interaction between streaming water (or water-based solutions) and surface-active nanomaterials such as carbon nanotubes, graphene and InAs nanowires have shown to produce electrical energy.[18-21] Electrical power has also been generated by sliding of water droplets along the surfaces of conducting nanomaterials like graphene.[22] Xue *et al.* recently demonstrated that even evaporation of water from the surface of nanostructured materials produces electricity.[23] However, all those processes require either a rapid flow or a fast evaporation of water molecules, these conditions restrict their widespread application in practical scenarios of day to day life. In a recent study, He *et al.* have shown that electrical energy up to hundreds of millivolts can be generated from quiescent water just by dipping two

TH-2654_156122042

yarns of carbon nanotube containing different amount of oxygen functionality.[24] As the atmospheric oxygen and water molecules tend to oxidize the surface of carbon-based nanomaterials, these devices have the drawbacks of short lifetime and limited options for compositional tuning to improve their performance.

3.2: SCOPE OF THE PRESENT INVESTIGATION

Heteroatom doping into the carbon lattice of graphene have been efficaciously applied for controllable tuning of various chemical and electronic properties by disorienting the homogenously conjugated electron network. Chemical doping modulates the band structure in graphene by inducing a bandgap between valance and conduction bands, which in turn imbues unique electrical properties. The exclusive properties of doped graphene sheets as compared to that of pristine graphene flakes set-up the platform for a wide range of potential applications.[25] Although the incorporation of various elements (such as nitrogen, phosphorus, sulfur, oxygen, and boron) into graphene lattice has been carried out successfully, doping of nitrogen and boron atoms has drawn substantial attention among the researchers. Both these atoms exhibit similar atomic radii to that of carbon atoms. Nitrogen is more electronegative than carbon induces n-type doping characteristics to graphene flakes. Nitrogen incorporation into the carbon lattice induces three major types of bonding configuration with carbon such as (1) sp^2 quaternary or graphitic nitrogen where the carbon atoms in the hexagonal ring are substituted by nitrogen atoms. (2) sp^2 pyridinic nitrogen where nitrogen atoms substitute carbon atoms at the inner defect edge of graphene while donating two p electrons to the π system, and (3) sp^3 pyrrolic nitrogen bonding to two other carbon atoms in the five-membered ring while donating two p electrons to the π system. It is noteworthy that each type of doping induces different properties to the doped-graphene samples. N-doping modulates and activates the graphene surface thereby increases the surface activity of the flakes. Furthermore, the electronegativity difference

TH-2654_156122042

between N and C atoms enhances the performance of N-doped graphene as compared to that of graphene by virtue of several properties such as reduced work function, tuneable polarization of graphene surface, and higher surface energy.[26-27]

Boron, on the other hand, being electropositive than carbon induces p-type doping characteristics to pristine graphene samples. Although the research on B-doped graphene is not as extensive as N-doped graphene, it has been demonstrated theoretically that the substitution of boron into graphene lattice is energetically more favourable.[28] Several reports demonstrating high concentration doping of boron atoms (up to 20 %) into graphene lattice have been published in recent years.[29-30] However, unlike N-doped graphene, the structure of B-doped graphene is not fixed and well understood. The distribution of substituted boron in carbon lattice is strongly influenced by the synthesis techniques and conditions.

In this chapter, we demonstrate the fabrication of an energy harvesting device by employing boron and nitrogen doped reduced graphene oxide (r-GO) films to harvest electricity from calm water. As boron and nitrogen atoms manipulate the electron density of r-GO flakes in the opposite directions producing p-type and n-type semiconductors,[31] they attract the opposite poles of the water molecules leading to a charge separation process and hence breaks the electrical neutrality.

3.3: EXPERIMENTAL SECTION

Materials and chemicals: Graphite powder was purchased from Sigma Aldrich. Boric acid, Urea, Potassium permanganate, Sulphuric acid, Hydrochloric acid, Hydrazine hydrate and N-methyl-2-pyrrolidone were purchased from Merck. Polydimethylsiloxane was purchased from Ellsworth Adhesives India Private Limited.

Synthesis of graphene oxide: GO was synthesized by employing modified Hummers' method. Typically, 1 g of graphite powder was added to 50 mL concentrated sulphuric acid

TH-2654_156122042

pre-cooled to temperature below 5 °C. 6 gm $KMnO_4$ was slowly added to this ice cold mixture under continuous stirring. The mixture was then transferred to a water bath at 35 °C and stirred for 2 hours, which was followed by transferring the mixture back to ice bath and slow addition of 100 mL DI water. The yellow coloured slurry obtained upon addition of 8 mL of hydrogen peroxide to this mixture was separated and washed with 20% HCl for multiple time followed by washing with acetone.

Synthesis of B-r-GO and N-r-GO: In order to prepare B-r-GO samples GO and boric acid (in the ratio of 1:0.25, 1:0.5, 1:2) were dispersed in 100 ml DI water and stirred for 12 hours. The liquid water molecules were then evaporated at 60 °C to obtain a solid mixture which was heated at 550 °C, 650 °C, 750 °C and 900 °C for 2 hours under continuous flow of argon. Similar to B-r-GO samples, N-r-GO samples were prepared by mixing GO and Urea (in the ratio of 1:6, 1:12, and1:24) in water followed by evaporation of the liquid at 60°C. The solid mixture as obtained was heated at 550 °C, 650 °C, 750 °C and 900 °C for 2 hours under flowing Ar gas.

Fabrication of B-r-GO/N-r-GO device: 4 mg/mL dispersion of both B-r-GO and N-r-GO were prepared independently, by dispersing the samples in N-methyl-2-pyrrolidone (NMP) under ultra-sonication for 2 hours. 0.5 mL of each B-r-GO and N-r-GO dispersion was coated onto two separate cellulose nitrate filtration membrane (surface area, 283 mm^2) through vacuum assisted filtration process. B-r-GO and N-r-GO coated membranes were connected to Cu wires with the help of conducting silver paste and separated by a glass slide of thickness 1 mm.

Preparation of B-r-GO-PDDA and N-r-GO-melamine: 4 mg/mL (0.5 mL) dispersion of B-r-GO in NMP was coated on a cellulose membrane by vacuum filtration followed by a coating of 20 µL poly (diallyldimethylammonium chloride) solution (20 wt. % in water). The membrane was air dried to obtain B-r-GO-PDDA film. 4 mg/mL (0.5 mL) dispersion

TH-2654_156122042

of N-r-GO in NMP was mixed with 2mg/mL (0.5 mL) melamine was mixed and coated on a cellulose membrane via vacuum filtration followed by air drying to obtain N-r-GO-melamine film.

B-r-GO/N-r-GO device on jeans: 0.5 mL, 4mg/mL dispersion of both B-r-GO and N-r-GO samples were independently coated on a jeans fabric by vacuum assisted filtration process. Copper wires were connected to the coated samples by using conductive silver paste followed by spreading a thin layer of freshly prepared PDMS elastomers, which was cured at 50 °C.

Computational Details: All the calculations were performed by Dr. Suresh kumar and Dr. Hemant Kumar Srivastava, using Gaussian-09 (revision D.01) program package.[37] 3×3 graphene supercell (having 3 complete rings in X and Y direction) containing 70 carbon atoms were constructed. N-doped and B-doped graphene structures were created by replacing 4 carbon atoms from the graphene supercell with nitrogen or boron atoms as depicted in Figure 5a and 5b. One water molecule was placed near the doped atom/s and geometry optimization was carried out. Geometries of all the considered supercell structures were fully optimized using generalized gradient corrected exchange and correlation functional PBEPBE.[37] The double-ζ quality 6-31G basis set with one polarization function and one diffuse function was used. Thus PBEPBE/6-31+G(d) level of DFT was used in all the calculations. Frequency calculations, at the same method and basis set, were performed to confirm that the obtained stationary points are minima on the potential energy surface. Natural Bond Orbital (NBO) calculations were also carried out to estimate the stabilization gained due to charge transfer between water molecules and graphene and vice-versa.[38] Supramolecular approach was used to calculate the interaction energy values between water molecule and doped graphene sheet.[39-40]

TH-2654_156122042

Characterization: All electrochemical measurements and electrical conductivity were done using source meter instrument (Keithley 2450). The morphology of the samples was characterized by field emission scanning electron microscope (FESEM) (Zeiss, Model: Sigma), and field emission transmission electron microscope (FETEM) (JEOL, JEM 2100F). Percentage composition of the Boron and Nitrogen were analysed by X-ray photoelectron spectroscopy (model: PHI 5000 Versa Probe II). Graphitic nature of the B-r-GO and N-r-GO samples was confirmed by Raman Spectroscopy (make: Horiba Jobin Vyon, model: LabRam HR).

3.4: RESULTS AND DISCUSSION

Graphene oxide (GO) samples employed here was prepared by following modified Hummers' method and purified by two steps HCl-acetone washing process.[32] The as obtained GO sample was independently mixed with urea and boric acid, and heated under argon atmosphere at different temperature (550, 650, 750 and 900 °C) to prepare N-doped (N-r-GO) and B-doped (B-r-GO) r-GO samples respectively. A detailed illustration of the

TH-2654_156122042

synthesis procedure is shown in Scheme 3.1. The morphological studies under electron and atomic force microscopes (AFM) revealed that the two-dimensional (2D) morphology of GO sheets was retained even after high temperature doping process of the B and N atoms. The representative AFM images of B-r-GO and N-r-GO samples prepared by annealing the reaction mixture at 750 °C are shown in Figure 3.1a and 3.1b respectively. While the lateral dimensions of the flakes vary in the range of 3 to 5 μm, the thicknesses of the flakes were found to be in the range of 2 to 5 nm. Representative AFM height profiles are shown at the

Scheme 1: Schematic illustration of synthesis of B-r-GO flakes and N-r-Go flakes from graphene oxide

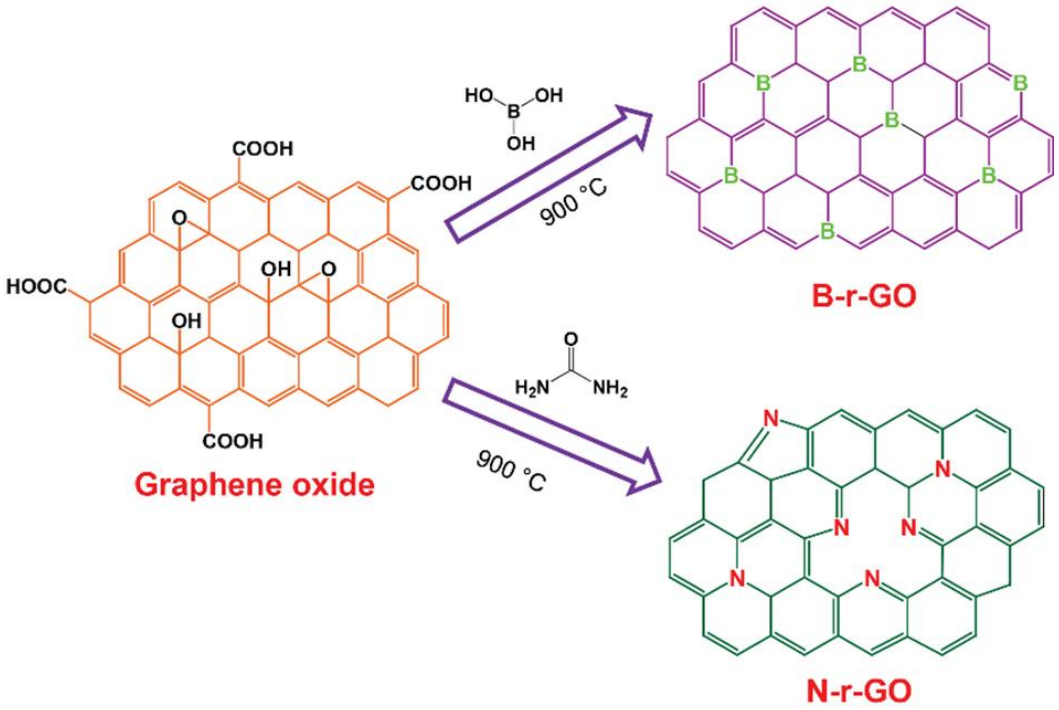

inset of Figure 3.1a and 3.1b. The Transmission Electron Microscopic (TEM) examination further supported the morphological information obtained from the AFM analysis (typical

TH-2654_156122042

images are shown in Figure 3.1c and 3.1d respectively). The graphitic nature of the N-r-GO and B-r-GO samples were confirmed by the appearance of the G-band (at around 1560

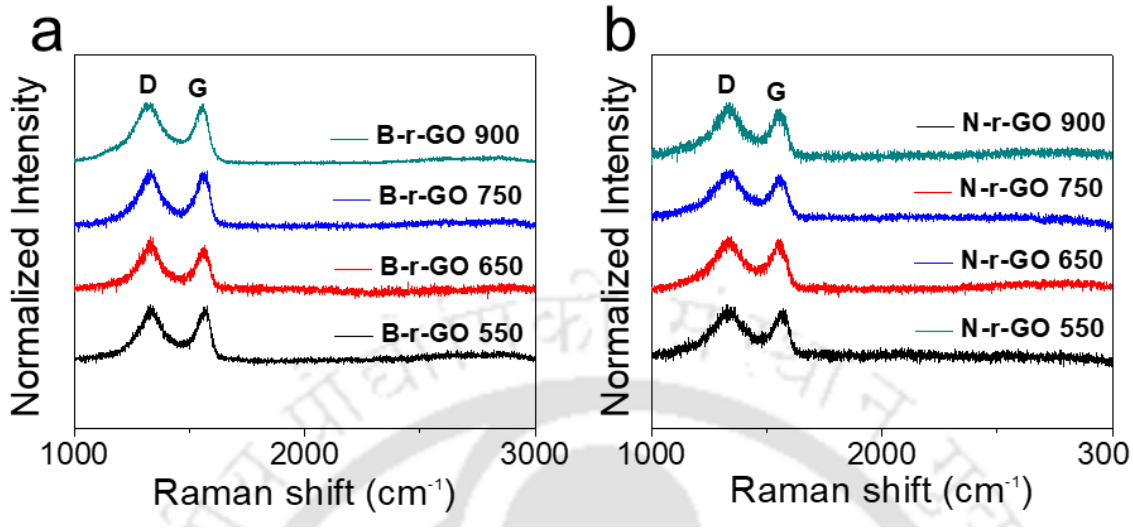

Figure 3.2: Raman spectra of (a) B-r-GO samples and (b) N-r-GO samples annealed at different temperatures.

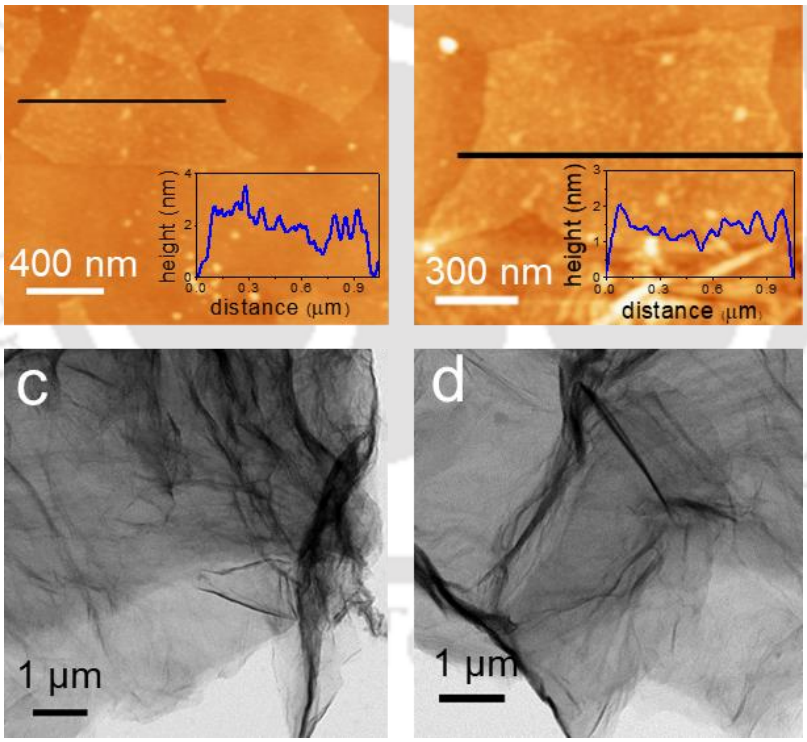

Figure 3.1: Characterization of B-r-GO and N-r-GO flakes: (a) AFM image along with the height profile of B-r-GO, and (b) AFM images along with height profile of N-r-GO. (c) TEM image of B-r-GO flakes prepared by heating graphene oxide samples with boric acid at 750 °C, and (d) TEM image of N-r-GO flakes prepared by heating graphene oxide samples with urea at 750 °C.

cm^{-1}) in their respective Raman spectrum as shown in Figure 3.2. All the doped samples exhibit a strong G band representing in-plane stretching of sp^2 hybridised carbon atoms.

TH-2654_156122042

The strong D band appeared at around 1330 cm^{-1} for all the samples are attributed to the structural defects and hetero atom doping.

The extent of doping in the r-GO samples were determined by the X-ray photoelectron spectroscopic (XPS) analysis shown in Figure 3.3 and Figure 3.4. Figure 3.3 shows the XPS spectra of B-r-GO and N-r-GO samples heated at 550 °C whereas Figure 3.4 shows the XPS spectra of B-r-GO and N-r-GO samples heated at 650 °C, 750 °C and 900 °C . The appearance of peaks at 400 eV in the N-r-GO samples, and 192 eV in the B-r-GO samples confirmed successful doping of N and B atoms into the graphene sheets. The percentages of doping in both N-r-GO and B-r-GO samples were found to be increasing with the increasing annealing temperature. For example, the percentage of N-atom calculated in N-r-GO sample prepared at 550 °C was calculated to be 10.4 %, which was increased to 20 % when annealing temperature was increased to 900 °C. Similarly, the percentage of B-atom in B-r-GO samples increased from 0.5 to 1.8 % when annealing temperature was elevated from 550 to 900 °C. A table of compositional data obtained from

TH-2654_156122042

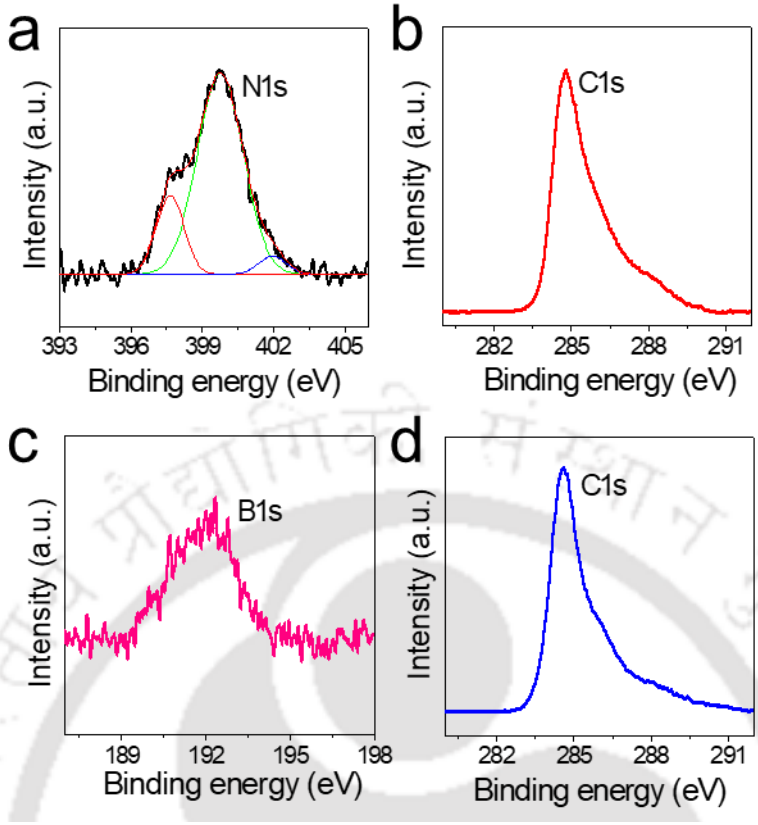

Figure 3.3: Composition of B-r-GO and N-r-GO flakes: (a) N1s spectra, and (b) C1s XPS spectra of N-r-GO doped samples prepared at 550 °C. Deconvolution of N1s spectra revealed the presence of three kind of N atoms (pyridinic N, pyrrolinic N and graphitic N) in the N-r-GO flakes. (d) B1s spectra, and (e) C1s XPS spectra of B-r-GO doped samples prepared at 550 °C.

Table 3.1: Composition of N-r-GO and B-r-GO from XPS analysis

a

Sample	% of N doping	N/C ratio
N-r-GO_{550}	10.4	0.115
N-r-GO_{650}	15.8	0.185
N-r-GO_{750}	21.5	0.27
N-r-GO_{900}	20.5	0.25

b

Sample	% of N doping	N/C ratio
B-r-GO_{550}	0.5	0.005
B-r-GO_{650}	0.7	0.007
B-r-GO_{750}	1.3	0.013
B-r-GO_{900}	1.8	0.018

c

Samples	Pyridinic N	Pyrrolic N	Graphitic N	Ratio (N_{py}:N_{pyr}:N_{grap})
N-r-GO-550	397.5 eV (peak area = 77)	399.7 eV (peak area = 463.67)	402 eV (peak area = 34)	2:13:1
N-r-GO-650	397.6 eV (peak area = 85)	399.47 eV (peak area = 331)	402 eV (peak area = 16)	5:20:1
N-r-GO-750	397.59 eV (peak area = 105)	399.9 eV (peak area = 446)	403 eV (peak area = 24.4)	4:18:1
N-r-GO-900	398 eV (peak area = 172)	400 eV (peak area = 845)	402.3 eV (peak area = 66)	3:12:1

XPS study is shown in Table 3.1a and Table 3.1b. The N 1s spectra of N-r-GO samples

TH-2654_156122042

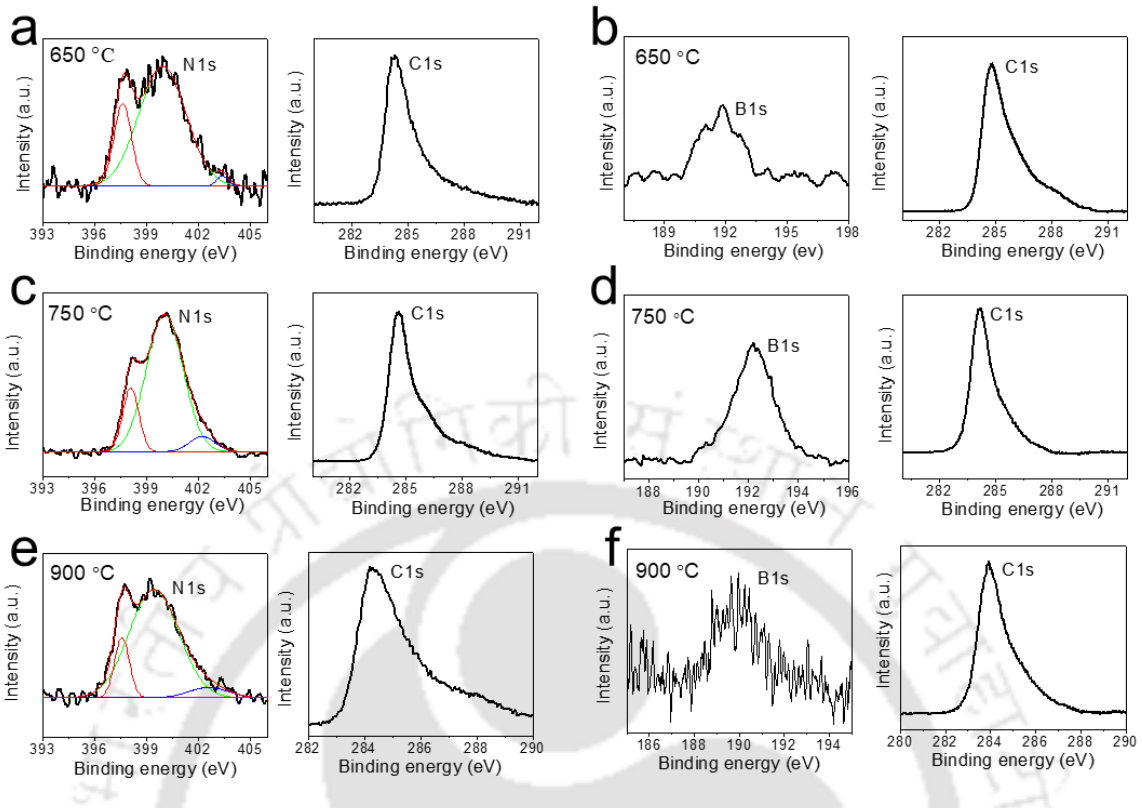

Figure 3.4: Composition of B-r-GO and N-r-GO flakes: XPS analysis of N-r-GO samples heated at (a) 650 °C, (c) 750 °C and (e) 900 °C. XPS analysis of B-r-GO samples heated at (b) 650 °C, (d) 750 °C and (f) 900 °C.

were deconvoluted into three peaks representing three kinds of N-atoms (pyridinic, pyrrolic and graphitic) possible in a graphitic matrix. From the areas of the deconvoluted peaks, the ratio of different N-atoms were determined to be in the range of 2:13:1 to 5:20:1. A table containing $N_{pyridinic}$/ $N_{pyrrolic}$/ $N_{graphitic}$ ratios of the samples prepared at different temperature is presented in the Table 3.1c. The uniform doping of boron and nitrogen atoms throughout the r-GO flakes were confirmed by the SEM-EDX mapping of the atoms in B-r-GO and N-r-GO samples as illustrated in Figure 3.5.

In order to harvest energy from calm water, both B-r-GO and N-r-GO samples were independently dispersed in N-methyl-2-pyrrolidone with the help of an ultra-sonic bath and coated on ashless cellulose filtration membranes through vacuum filtration. The electrical conductivities of the samples were calculated from the *I-V* curves (Figure 3.6a) recorded with stripes of dimension ~ 15 × 4 × 0.0080 mm^3. Cu wires pasted at either ends of the

TH-2654_156122042

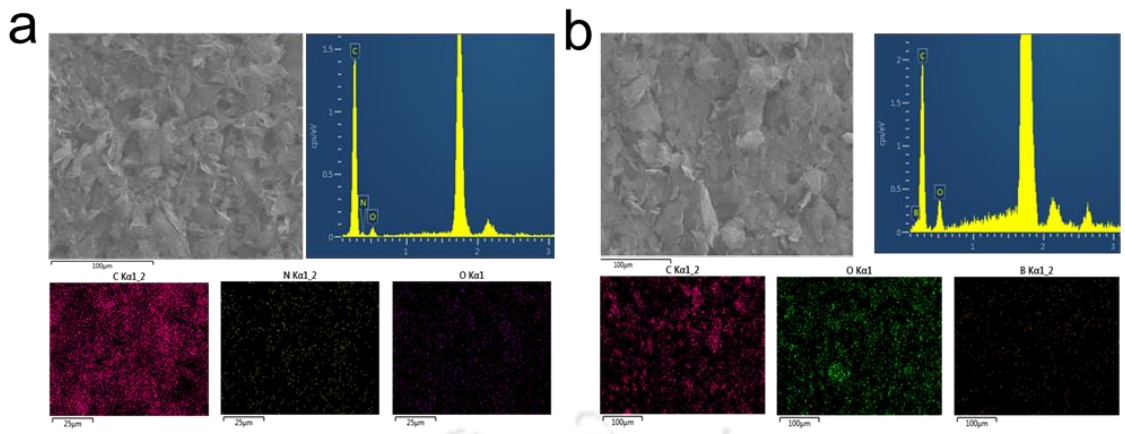

Figure 3.5: SEM-EDX analysis of (a) N-r-GO flakes and (b) B-r-GO flakes.

strips with the help of conductive silver paste to facilitate conductivity measurements. As shown in Figure 3.6b, the electrical conductivities of both N-r-GO and B-r-GO stripes were found to be increasing with the increasing annealing temperature. For any given annealing

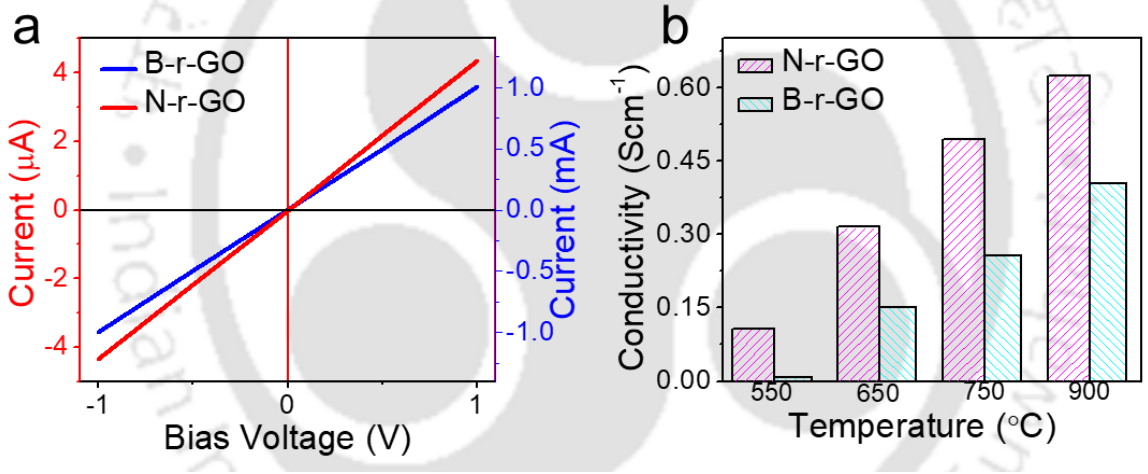

Figure 3.6: Conductivity of B-r-GO/N-r-GO samples: (a) Characteristic I-V curves of N-r-GO and B-r-GO samples prepared at 550 °C. (b) Bar diagram showing electrical conductivity of N-r-GO and B-r-GO samples prepared by heating at different temperatures.

temperature, the conductivity of N-r-GO samples were calculated to be higher than that of B-r-GO samples (Figure 3.6b).

A schematic representation of the experimental set-up employed for the water induced electricity generation is shown in Figure 3.7a. Typically, the B-r-GO and N-r-GO coated filter papers (digital photographs shown in Figure 3.7b and Figure 3.7c) connected to Cu wires were mounted on the opposite sides of a glass slide maintaining a separation of ~ 1 mm. The Cu wires were then connected to a source meter instrument (Keithley 2450) to

TH-2654_156122042

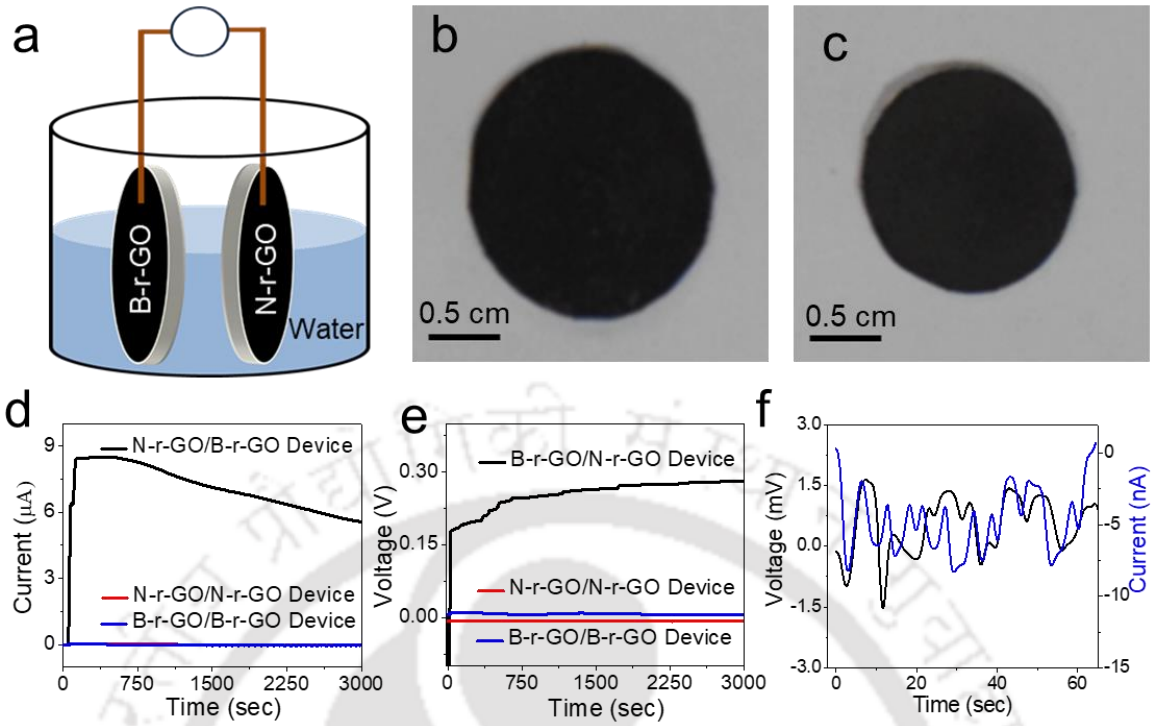

Figure 3.7: Water induced electricity generation by B-r-GO/N-r-GO device: (a) Schematic of the experimental set-up employed for harvesting energy from calm water. Digital photographs of (b) B-r-GO and (c) N-r-GO coated on ashless cellulose filtration paper of surface area 283 mm^2. (d) Open-circuit voltage, and (e) generated current upon dipping B-r-GO/N-r-GO device (black curve), N-r-GO/N-r-GO device (red curve) and B-r-GO/B-r-GO device (blue curve) in calm water. (f) Control experiment showing open-circuit potential (black curve) and current (blue curve) generated on dipping cellulose filter papers connected to Cu wires without being coated with B-r-GO and N-r-GO flakes.

measure the open-circuit potential. An open-circuit potential difference of around 250 mV was generated as soon as the B-r-GO/N-r-GO device was dipped into water, which was improved to 280 mV within 20 sec of soaking before reaching the steady state. In order to avoid the probable electrochemical reaction between water and Cu wires only 75 % area of the B-r-GO/N-r-GO device was submersed into water, the regions of the B-r-GO and N-r-GO films in contact with Cu wires were kept away from the direct contact with water. Figure 3.7d shows the open-circuit potential (black curve) generated with a B-r-GO/N-r-GO device containing two ashless cellulose membranes of ~ 280 mm^2 area, independently coated with B-r-GO and N-r-GO samples (2 mg each). However, no such voltage was developed when similar devices were made with two membranes coated with B-r-GO (B-r-GO/B-r-GO device) or N-r-GO (N-r-GO/N-r-GO device) samples, the blue and red

TH-2654_156122042

curves in Figure 3.7d respectively. Control experiments were also carried out by dipping Cu wires and cellulose membrane independently under similar device configuration, and shown in Figure 3.7f. Simultaneous to the voltage generation, the B-r-GO/N-r-GO device also produced a current of around 9 µA (Figure 3.7e). Remarkably, the voltage output was found to be constant for the experimental timescale (3000 sec), but the current values started decreasing gradually after around 700 seconds. This gradual decrease in the current values of B-r-GO/N-r-GO device is attributed to water induced enhancements of the resistance of Cu-(B-r-GO/N-r-GO) contact areas due to the mismatched wettability of B-r-GO, N-r-GO membrane and Cu wires. The B-r-GO/N-r-GO device was also tested for

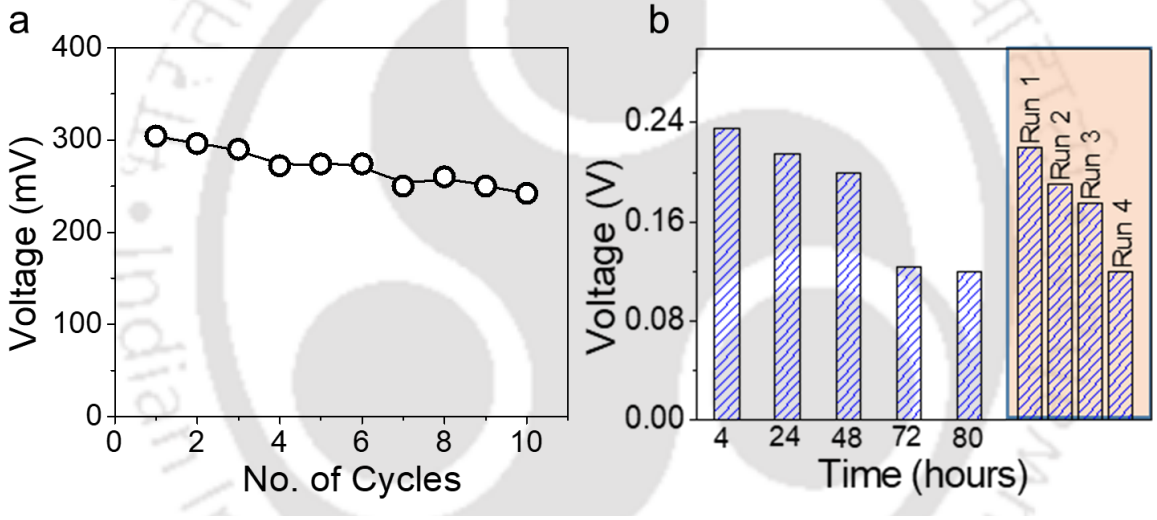

Figure 3.9: Under water stability of B-r-GO/N-r-GO device: (a)Open-circuit potential generated upon dipping the B-r-GO/N-r-GO device in calm water for ten repetitive cycles. (b)Open-circuit potential generated by a B-r-GO/N-r-GO device as function of time when it was soaked in water. After being studied for 80 hours, the device was dried and re-soaked in water prior to open-circuit potential measurement and the same was repeated for 4 cycles.

repetitive cycles of water soaking. It displayed a potential output of 242 mV even after 10 cycles of soaking in water followed by drying in air as shown in the Figure 3.8a. Similarly, the power generated by the B-r-GO/N-r-GO device was also studied for a few days of soaking in water. Figure 3.8b shows that after soaking the device in water for 60 hours it generated an open-circuit voltage of 200 mV, after which voltage values decreased gradually and reached 120 mV after 80 hours of soaking in water. Air-drying of the B-r-

TH-2654_156122042

GO/N-r-GO device for 24 hours recovered almost 78 % of potential difference (220 mV) produced by the pristine device in contact with the calm water. The decrease in the open-circuit potential indicates chemical modification of the active sites of the flakes.

In order to understand whether B-r-GO, N-r-GO, or both kinds of flakes are undergoing chemical modification, devices were fabricated with "pre-soaked" B-r-GO coated membrane with "freshly prepared" N-r-GO coated membrane and vice versa. Figure 3.9a

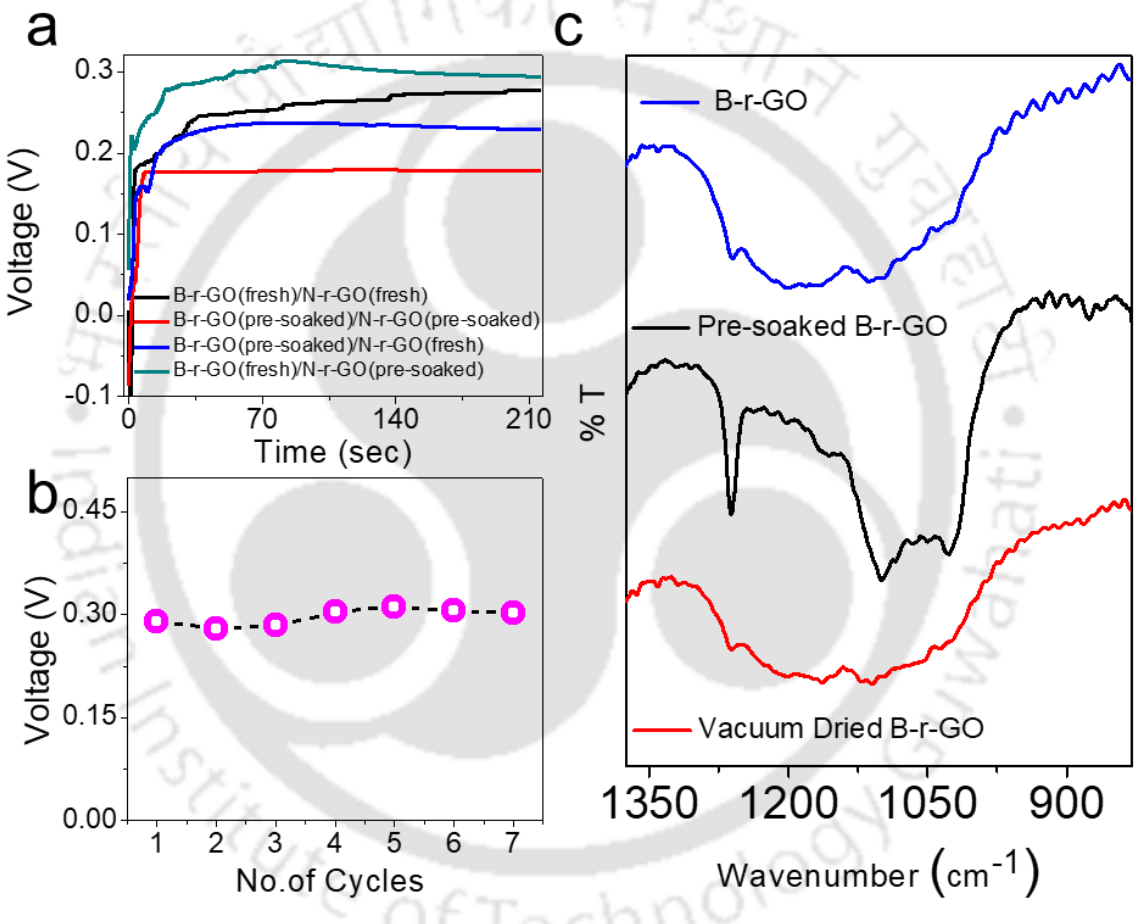

Figure 3.9: (a) Open-circuit potential generated by different combinations of "pre-soaked" and "fresh" B-r-GO and N-r-GO devices. (b) Open-circuit voltage generated by the B-r-GO/N-r-GO device in water after vacuum drying of B-r-GO at 120 °C for seven cycles. (c) Infrared Spectra of B-r-GO flakes before and after soaking in water. Blue curve represents the FTIR spectrum of freshly prepared B-r-GO flakes, black curve showing the IR spectra of pre-soaked B-r-GO flakes and red curve showing the IR spectra of vacuum dried B-r-GO flakes at 120 °C.

shows the potential generated by devices made from different combinations of "pre-soaked" and "freshly prepared" B-r-GO, and N-r-GO coated membranes. As can be seen from Figure 3.9a, replacement of "pre-soaked" N-r-GO part of the device with a "freshly

TH-2654_156122042

prepared" N-r-GO coated membrane (by keeping the "pre-soaked" B-r-GO membrane intact) did not recover the output voltage values. On the other hand, when "pre-soaked" B-r-GO membrane of the device was replaced with a "freshly prepared" B-r-GO membrane (keeping the "pre-soaked" N-r-GO membrane intact), complete recovery of the voltage output was observed. This observation suggests that the chemical modification took place at the active sites of the B-r-GO flakes.

In order to get further insights, FTIR spectra of the B-r-GO flakes before and after soaking in water were recorded. As can be seen from Figure 3.9c, upon prolonged soaking in water, new peaks corresponding to B-O-H bending (1102 cm^{-1}),[33] C-OH stretching (1025 cm^{-1}) and B-O stretching (1258 cm^{-1}) modes appeared in the FTIR spectrum of B-r-GO flakes. The appearance of these new peaks at the IR spectrum supported the hypothesis about water induced chemical modification of the B-r-GO flakes. The B-r-GO coated membrane was then heated at 120 ^{o}C for 2 hours in a vacuum oven. Remarkably, after vacuum-drying all the peaks corresponding to oxygenated surface functional groups disappeared from the FTIR spectrum of B-r-GO flakes. The vacuum-dried B-r-GO flakes were then reused for fabricating B-r-GO/N-r-GO devices, and complete recovery of the voltage was observed. The soaking of B-r-GO/N-r-GO devices followed by vacuum-drying was repeated for multiple times, and each time a complete recovery of the voltage was observed (Figure 3.9b).

The voltage and current outputs of B-r-GO/N-r-GO devices were investigated by adding different electrolytes like NaCl, KCl or HCl to water in the concentration range from 10^{-6} M to 1 M. While current values generated by the B-r-GO/N-r-GO devices were found to be increasing with increasing electrolyte concentrations, the voltage outputs were found to be constant for the concentration range from 10^{-6} M to 10^{-3} M, as shown in Figure 3.10. However, with further increase in the electrolyte concentrations (beyond 10^{-3} M) the

TH-2654_156122042

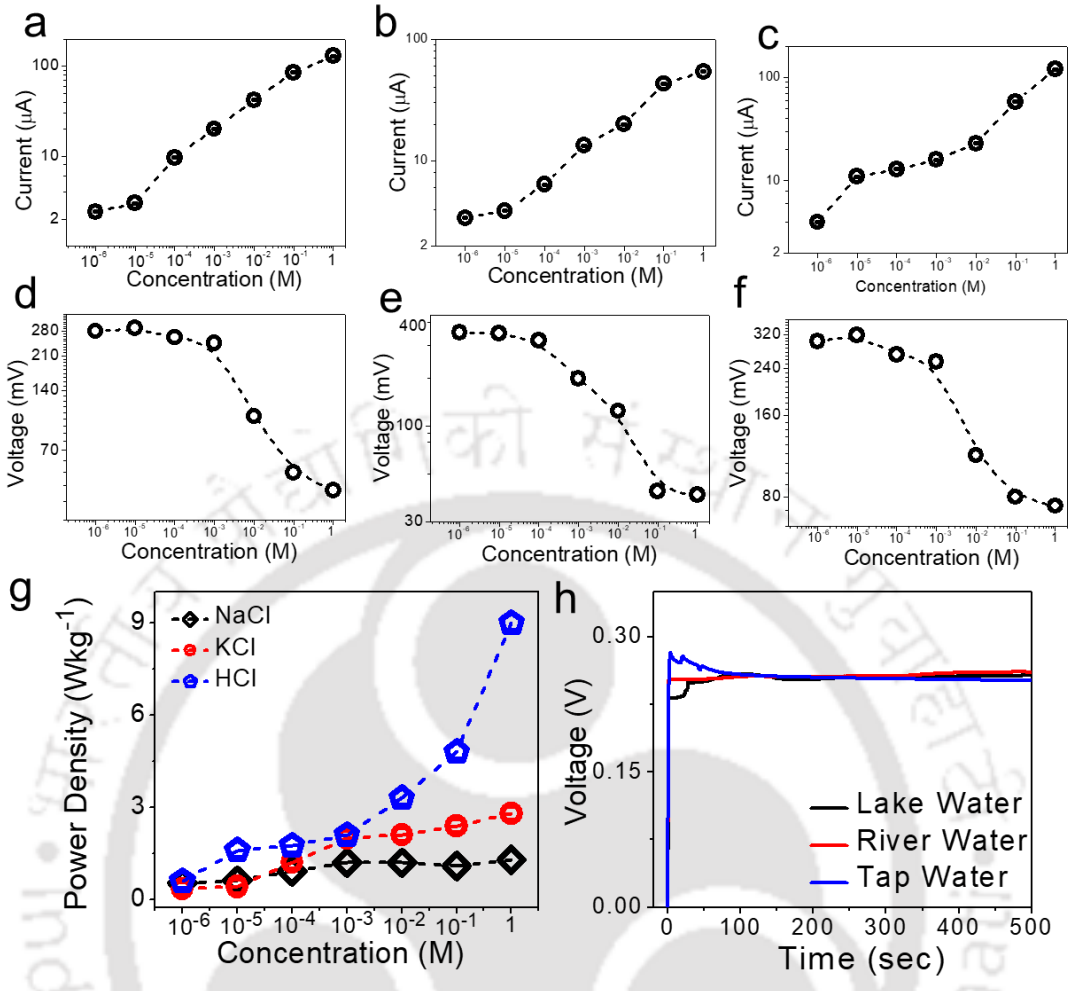

Figure 3.10: Performance of B-r-GO/N-r-GO device at different electrolyte concentration: Current generated by the B-r-GO/N-r-GO device as a function of electrolyte concentration for (a) KCl, (b)NaCl and (c) HCl. Open circuit-voltage generated by the B-r-GO/N-r-GO device as a function of different electrolyte concentration for (d) KCl, (e) NaCl and (f) HCl. (g) Power output of B-r-GO/N-r-GO device in different electrolye solutions of varied concentration (10^{-6} M to 1 M), The B-r-GO and N-r-GO samples were prepared at 750°C. (h) Open-circuit voltage generated by B-r-GO/N-r-GO devices in contact with different water sources.

voltage outputs started decreasing sharply, which is attributed to the blockage of the active sites of the B-r-GO and N-r-GO flakes by the excessive ions present in the solution. The increase in the current values is attributed to the enhanced ionic current of the solution. The combined effect of simultaneous change in the current and voltage values led to slight enhancement in the power output values of B-r-GO/N-r-GO device with increasing electrolyte concentrations, as shown in Figure 3.10g. The efficiency of power generation from the B-r-GO/N-r-GO device was also tested for arbitrary water sources like tap water, lake water, and river water. As shown in Figure 3.10h, the potential output was not affected

TH-2654_156122042

by the source of water opening up the possibilities of sustainable power harvesting from a wide range of water sources readily available to us. In Table 3.2, ionic conductance of different water samples (tap water, lake water, and river water), were listed. The

Table 3.2: Tabular representation comparing ionic conductance of different water samples with that of the salt solutions of concentration 0.1 mM and the power output generated by the B-r-GO/N-r-GO device in different water samples and salt solutions of comparable conductance.

Sources	Conductance(S)	Voltage (mV)	Current (A)	Power Density (Wkg^{-1})
DI water	3.48×10^{-6}	280	9	1.26
Tap water	4.7×10^{-5}	270	16.3	2.2
River water	2.3×10^{-5}	259	12.6	1.6
Lake water	2.2×10^{-5}	256	12	1.53
KCl (0.1 mM)	1.2×10^{-5}	260	10.4	1.35
NaCl (0.1 mM)	1.6×10^{-5}	290	11.3	1.63
HCl (0.1 mM)	1.8×10^{-5}	270	9.6	1.3

performance B-r-GO/N-r-GO device with arbitrary water samples was found to be similar to that of NaCl, KCl or HCl solutions of similar ionic conductivity values. It is noteworthy that the power generation of the B-r-GO/N-r-GO devices can also be easily tuned by changing the coating area. As shown in Figure 3.11a, the output current increases with increasing coating area of the B-r-GO and N-r-GO flakes. The power generation of B-r-GO/N-r-GO devices was also found to be dependent upon the temperature employed during the preparation of B-r-GO and N-r-GO samples. The open-circuit voltage output was in the same range (~ 250- 300 mV) for all the devices prepared at different annealing temperature, however, the output current was improved up to 10 fold upon increasing the reduction temperature from 550 ˚C to 900 ˚C. As a result, the power output was calculated to be enhancing upon increasing reduction temperature, and a maximum power output of 3.3 Wkg^{-1} was calculated for the device fabricated from B-r-GO and N-r-GO samples reduced

TH-2654_156122042

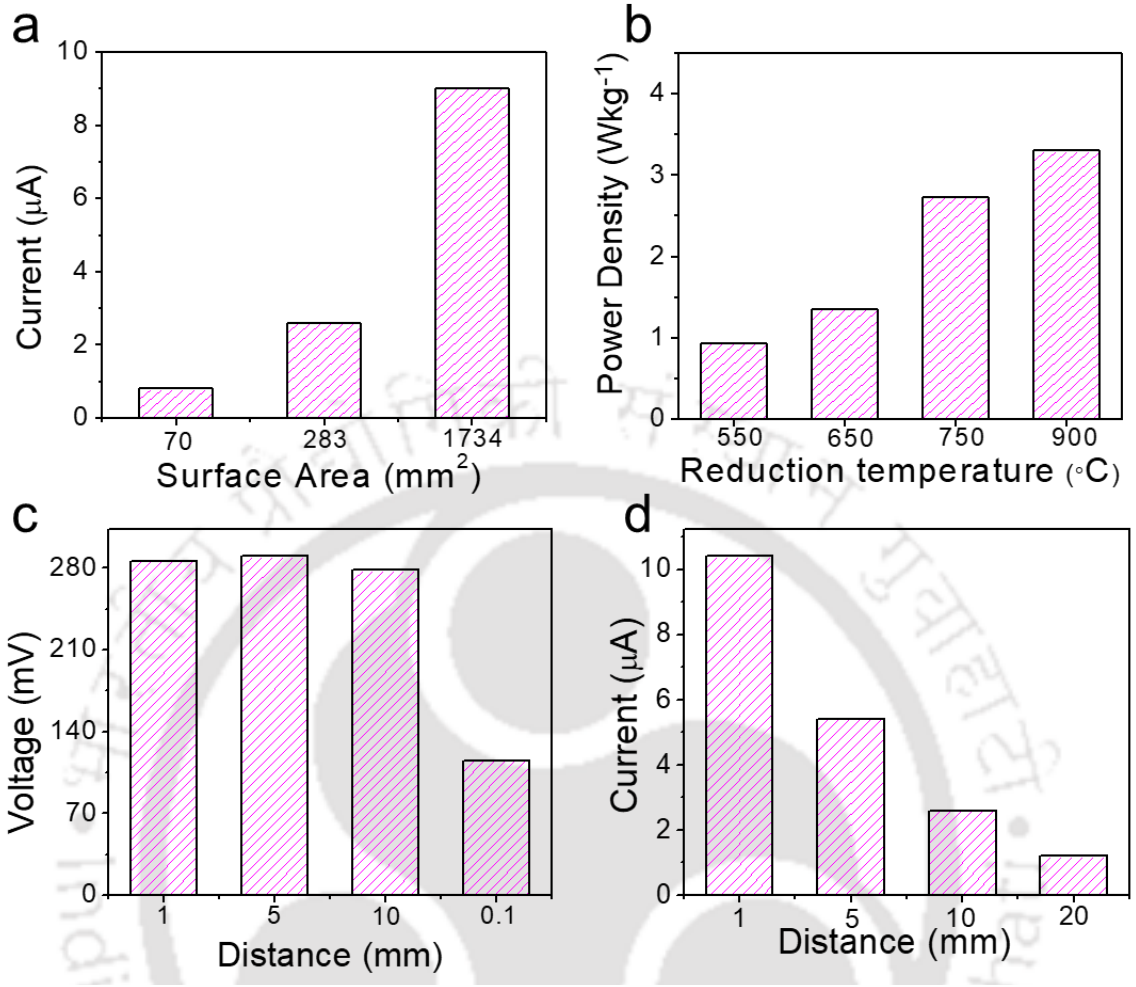

Figure 3.11: Factors affecting the power output of B-r-GO/N-r-GO devices: (a) Bar diagram showing short-circuit current generated by B-r-GO/N-r-GO devices with different coating areas. The B-r-GO and N-r-GO samples were prepared at 550 °C. (b) Bar diagram showing power output of B-r-GO/N-r-GO devices fabricated with samples prepared at different temperature. (c) open-circuit voltage generated by the B-r-GO/N-r-GO device in water as a function of distance between the B-r-GO and N-r-GO coated films. 0.1 mm corresponds to thickness of the cellulose membranes when B-r-GO and N-r-GO films were bought in contact with each other. (d) Current generated by the B-r-GO/N-r-GO device in water as a function of distance between the B-r-GO and N-r-GO coated films.

at 900 ˚C, shown in Figure 3.11b. The enhanced energy efficiency of the sample prepared at higher temperature is attributed to the higher electrical conductivity of the flakes.

Similarly, the potential and current output of B-r-GO/N-r-GO devices were also studied by varying the distance between B-r-GO and N-r-GO coated membranes. As can be seen from Figure 3.11c and Figure 3.11d, the varying distance between the membranes did not alter the potential values, unless they were brought into direct contact with each other (0.1 mm). However, the output current values were found to be decreasing with increasing distance

TH-2654_156122042

between B-r-GO and N-r-GO coated membranes, this effect is similar to that of decreasing ionic conductivity of the medium.

Similar to He *et al.* here again the power generation from serene water body is attributed to the complementary charge transfer activities of p-type and n-type semiconductor materials.[24] Doping of boron atoms in r-GO flakes creates electron deficient centres in the 2D network of sp^2 carbon atoms. Similarly, doping of nitrogen atoms generates electron rich cites. Therefore, while B-r-GO flakes interact with the negative poles of the water, N-r-GO flakes interact with the positive poles, which create a situation similar to two conductive electrodes submersed in solutions of different (or opposite) chemical potentials and it leads to development of potential gradient across the electrodes. In order to further support our hypothesis the B-r-GO coated membrane was doped with a cationic polymer, Poly(diallyldimethylammonium chloride) (PDDA), keeping the N-r-GO coated membrane unaltered. As the presence of cationic polymer induced stronger attraction of B-r-GO coated membrane towards partial negative charge of water molecules, the cationic polymer modified PDDA-B-r-GO/N-r-GO device showed 33 % enhancement in the open-circuit potential as compared to B-r-GO/N-r-GO device shown in Figure 3.12a. On the other hand, when cationic polymer was doped with N-r-GO coated membrane keeping the B-r-GO coated membrane unaltered, the B-r-GO/N-r-GO-PDDA device shown 53 % reduction in open-circuit potential, which is attributed to the reduction in the attraction of N-r-GO towards the positive pole of the water molecules. Similarly, when N-r-GO coated membrane was doped with a nitrogen rich compound (melamine) keeping the B-r-GO coated membrane unaltered, 43 % enhancement in open-circuit potential was observed. Remarkably, device prepared with melamine doped N-r-GO coated membrane and cationic

TH-2654_156122042

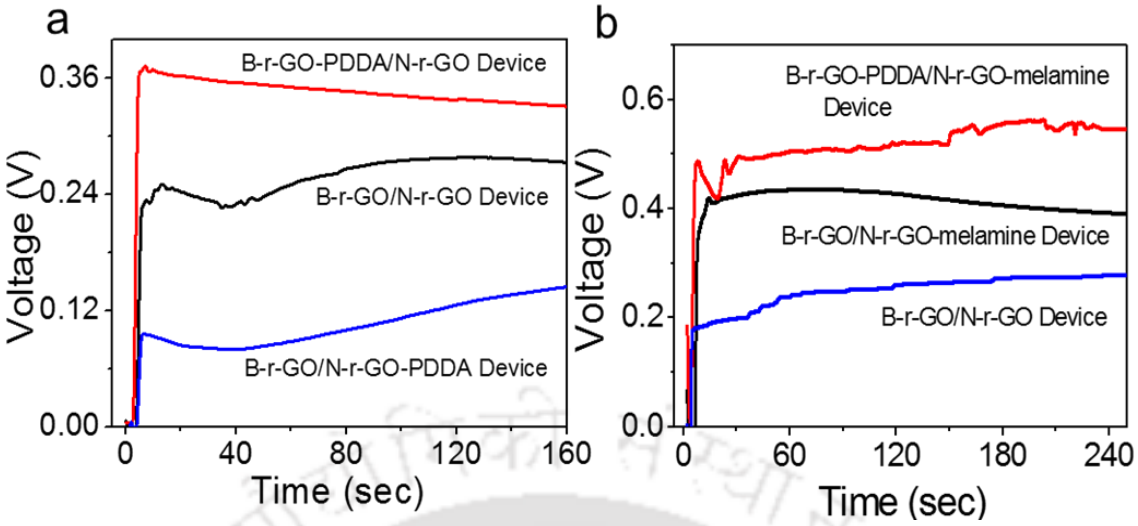

Figure 3.12: (a) Water induced Open-circuit potential generated by B-r-GO-PDDA/N-r-GO device (red curve) and B-r-GO/N-r-GO-PDDA (blue curve) device as a function of time compared to that of B-r-GO/N-r-GO (black curve) device. (b) Water induced Open-circuit potential generated by B-r-GO/N-r-GO-melamine (black curve) device and B-r-GO-PDDA/N-r-GO-melamine (red curve) device as a function of time compared to that of B-r-GO/N-r-GO (blue curve) device.

polymer doped B-r-GO coated membrane shown 90 % enhancement in the open-circuit potential values, as shown in Figure 3.12b.

In order to obtain further insight in to the interface of B-r-GO and N-r-GO flakes with water, Dr. Suresh Kumar and Dr. Hemant Kumar Srivastava carried out the DFT calculations. A 3×3 graphene supercell (having 3 complete rings in X and Y direction) containing 70 carbon atoms were constructed. N-r-GO and B-r-GO graphene structures

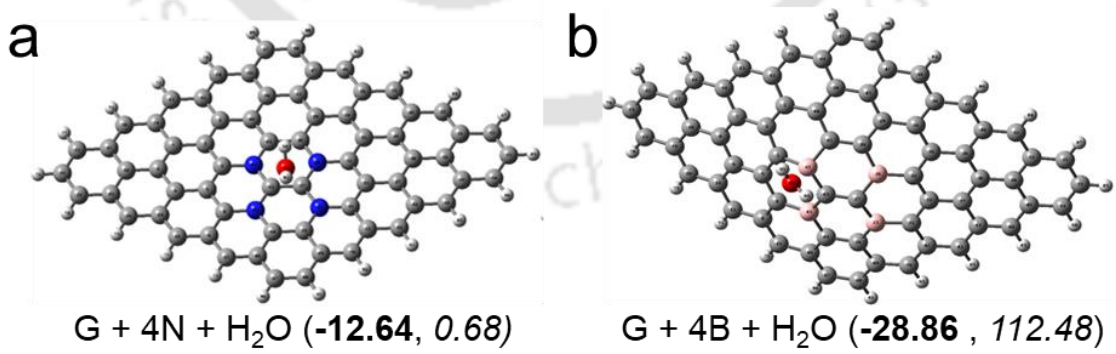

Figure 3.13: (a) N-doped and (b) B-doped graphene 3X3 supercells optimized at PBEPBE/6-31+G(d) level of DFT. 'G' indicates the graphene 3X3 supercell. '4N' indicates that four carbon atoms from G were replaced by four nitrogen atoms. '4B' indicates that four carbon atoms from G were replaced by four boron atoms. Nitrogen, oxygen, and boron atoms are depicted in blue, red and pink color respectively. The **bold** and italics numbers in the parenthesis represents interaction energy values in kcal/mol, and stabilization energy gained as a result of charge transfer between water molecule and doped graphene structures in kcal/mol

TH-2654_156122042

were created by replacing 4 carbon atoms from the graphene supercell with nitrogen or boron atoms as depicted in Figure 3.13a and 3.13b respectively. One water molecule was placed near the doped atom/s and full geometry optimization was carried out. It was observed that water molecule is situated at similar distance from all four nitrogen atoms in 4N-r-GO flake. On the other hand, water molecule is closer to one of the boron atom in case of 4B-r-GO flake. This arrangement facilitates the stronger interaction and faster charge transfer in 4B-r-GO. All the boron-carbon bond distances are between 1.53-1.60 Å while all the nitrogen-carbon bond distances are between 1.39-1.42 Å. Interestingly N-C-N, C-N-C, C-C-N and C-C-C bond angles varies from 117°-120° in 4N-r-GO. However, B-C-B, C-B-C, C-C-B and C-C-C bond angles varies from 112°-121° in 4B-r-GO. This higher variation in the bond angles facilitates some distortion in 4B-r-GO. This distortion is clearly visible if we compare the dihedral angles which is close to 179° in 4N-r-GO and much lower in 4B-r-GO.

Supramolecular approach was used to calculate the interaction energy (IE) values between water molecule and doped graphene sheets and presented in Figure 3.13. Although both doped graphene structures show stable complex formation, 4B-r-GO have much higher IE values (28.86 kcal/mol) compared to 4N-r-GO (12.64 kcal/mol). This indicates the higher stability of 4B-r-GO structure. In order to understand the differences in IE values, bond distances and other geometrical parameters in detail, NBO calculations were performed. The stabilization energy (E2) gained as a result of charge transfer between water molecules and doped graphene structures was calculated by the second-order perturbative estimates of donor–acceptor interactions in the NBO basis. There was no notable charge transfer in the 4N-r-GO case and total E2 was calculated to be 0.6 kcal/mol. On the other hand, 4B-r-GO shown strong stabilization and charge transfer effect. The total E2 in 4B-r-GO was calculated to be 112.48 kcal/mol which is considerably higher than that of 4N-r-GO sample.

TH-2654_156122042

Interestingly most of the charge transfers were observed from water molecule to graphene sheets and charge transfers from graphene to water molecule were negligible. These observations clearly indicate that the 4B-r-GO have the higher stability along with stronger charge transfer and interaction capability.

In order to further support the hypothesis of different effects of water-contact on the surface of B-r-GO and N-r-GO samples both the samples were independently exposed to water vapor and its effect on the electrical conductivities were studied. For this experiment, devices were fabricated by connecting Cu wires through conductive silver paste to B-r-GO and N-r-GO coated films of dimension ~ 280 mm^2. The as prepared devices were mounted onto a sealed glass container maintained at relative humidity (RH) levels of 10 % and conductance was monitored as a function of time using a source meter instrument (Keithley 2450). Entire system was exposed to an IR lamp to prevent condensation of water vapors. When the RH level of the sample chamber was suddenly increased to 65 % the electrical conductance of N-r-GO sample decreased sharply (Figure 3.14a), which is attributed to the

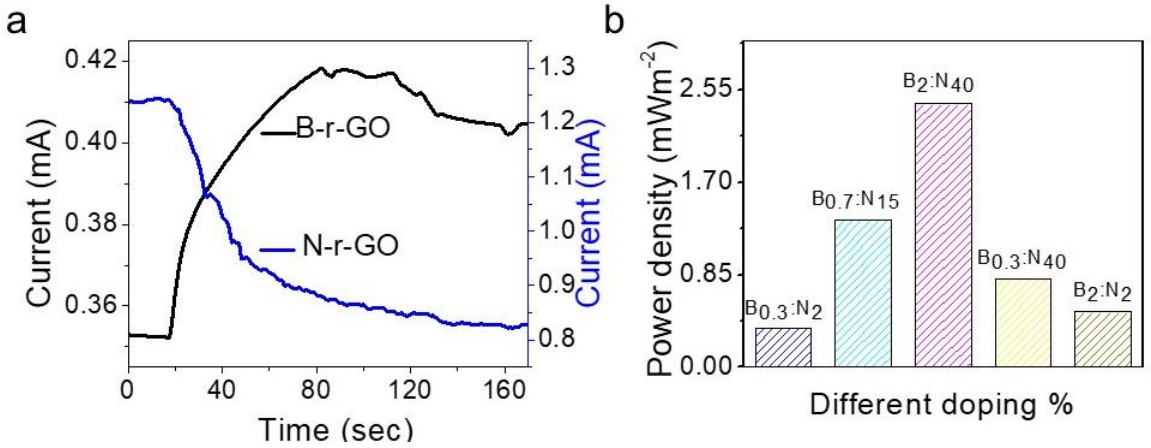

Figure 3.14: (c) Electrical conductivity of individual B-r-GO (black) and N-r-GO (blue) devices as a function of time. At around 20 second, the relative humidity of the surrounding environment was drastically varied from 10 % to 65 %. (d) Power output of the B-r-GO/N-r-GO devices with different amounts of boron and nitrogen atoms doped in the r-GO flakes.

electron rich environment of N-r-GO flakes. At room temperature, water molecules constantly dissociates into H^+ and OH^- ions, and the hydronium ions created by the

TH-2654_156122042

dissociation of water molecules act as an electron trap for charge carriers in n-type semiconductors, and hence the electrical conductivity decreases with increasing RH level of the chamber.[34] On the other hand, the electrical conductivity of the B-r-GO sample (p-type semiconductor) increases upon exposer to sudden rise in RH level (Figure 3.14a), which is again attributed to the electron deficient nature of the B-r-GO sample. The OH^- ions produced from water dissociation now interact with electron deficient B centres to trigger a charge transfer process from OH^- ions to B-r-GO flakes leading to an enhancement of the electrical conductivity.[34,35]

The effect of boron and nitrogen doping in the electricity generation was further established by fabricating devices with varied percentage of dopants. As shown in Figure 3.14b, decreasing the amount of B and N dopants to 0.35 and 2 % respectively, leads to nearly 4-fold decrease in the power output (0.36 watt/kg). Whereas the 2-fold enhancement in power output (2.42 watt/kg) was observed when the dopants amount was enhanced to 2 and 40 % for B-r-GO and N-r-GO respectively. Similarly, device consisting of B-r-GO with least amount of boron (0.35 %) and N-r-GO with highest amount of nitrogen (40 %) displayed 0.51 watt/kg power output. On the contrary, device consisting of B-r-GO with highest amount of boron (2 %) and N-r-GO with lowest amount of nitrogen (2 %) displayed only 0.81 watt/kg power output, contact with still water.

Interestingly, B-r-GO and N-r-GO samples can also be coated on various other materials to harvest energy from water of arbitrary sources. For example, B-r-GO and N-r-GO pastes were coated in two circular areas of ~ 280 mm^2 in a piece of jeans (cloth) maintaining a separation of around 0.5 mm, followed by coating of a thin layer of PDMS (polydimethylsiloxane) on it, (inset of Figure 3.15b). When immersed into tranquil water the jeans devices produced an open-circuit voltage of 275 mV (Figure 3.15a), which was remained stable up to 32 hours. Robustness of PDMS coated fabric device is illustrated in

TH-2654_156122042

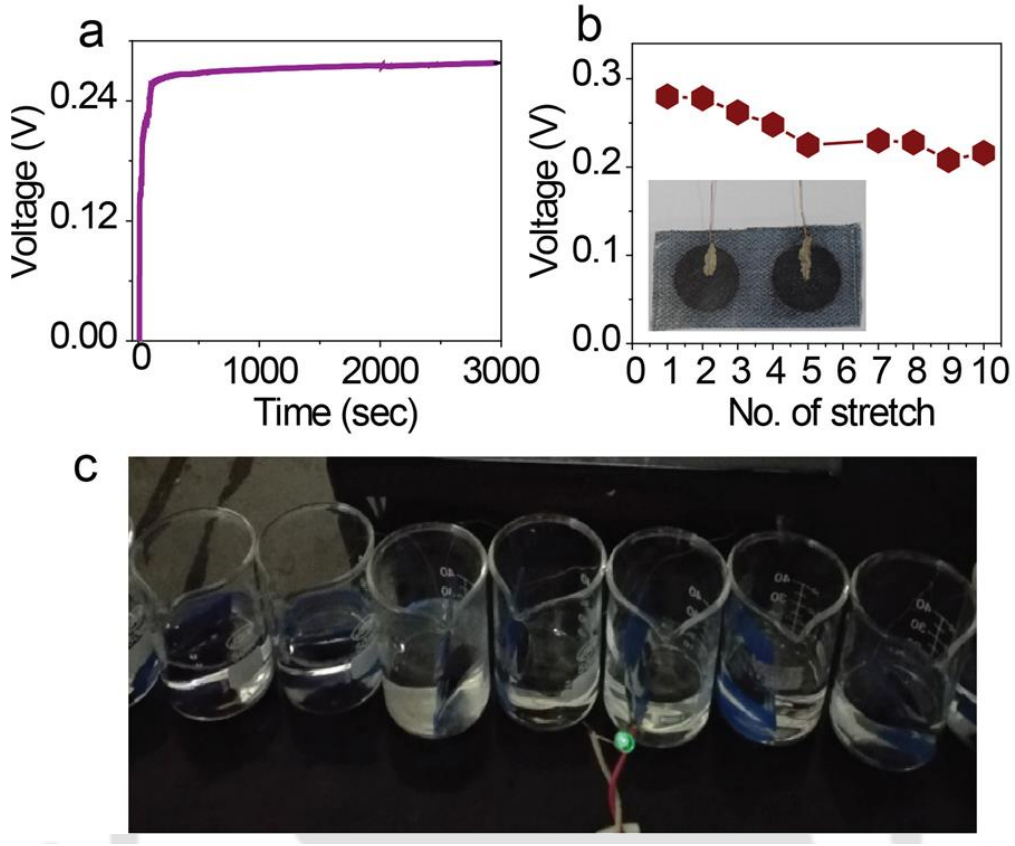

Figure 3.15: Power generation by B-r-GO/N-r-GO devices coated on jeans. (a) Open-circuit voltage generated by the B-r-Go/N-r-GO device coated jeans cloth upon dipping in water. (b) Open-circuit voltage generated by the jeans-coated device up to 10 cycles of stretching. (c) Photograph showing lighting a LED of 3 V by dipping ten (10) B-r-GO/N-r-GO devices connected in series in calm water. The B-r-GO and N-r-GO samples were prepared at 650 °C and coating area was 283 mm^2 on cellulose filter paper.

Figure 3.15b where a stable voltage of 220 mV is generated after stretching it for 10 times. Further, to demonstrate the applicability of energy derived from calm water nine B-r-GO/N-r-GO devices were connected in series to light up a Light emitting device (LED) of 3 V as shown in Figure 3.15c.

3.5: CONCLUSION

In conclusion, we have demonstrated that the complementary charge transfer activities of boron and nitrogen doped r-GO flakes with water molecules can be exploited to extract energy from serene water resources. The power generated from the contrasting interfacial interactions was further improved by varying parameters like coating area, extend of doping, annealing temperature, and ionic conductivity of the medium. The B-r-GO/N-r-GO

TH-2654_156122042

devices in contact with water maintain a significant potential difference for a prolonged period of time (up to 80 hours) and the lost efficiency can be recovered through vacuum drying. The B-r-GO/N-r-GO devices can also be fabricated in arbitrary substances like piece of jeans-cloths, and hence it opens-up possibilities of fabricating wearable energy harvesting devices for applications in remote areas. Stronger charge transfer and favourable geometrical parameters in B-r-GO structure facilitate higher stability and higher interaction energy of this structure compared to N-r-GO, as indicated by DFT calculations.

TH-2654_156122042

3.6: REFERENCES

1. Chen, X.; Li, C.; Grätzel, M.; Kostecki, R.; Mao, S. S. Nanomaterials for Renewable Energy Production and Storage. *Chem. Soc. Rev.* **2012,** *41*, 7909-7937.
2. Guo, K. W. Green Nanotechnology of Trends in Future Energy: A Review. *Int. J. Energy Res.* **2012,** *36*, 1-17.
3. Hussein, A. K. Applications of Nanotechnology in Renewable Energies—A Comprehensive Overview and Understanding. *Renewable Sustainable Energy Rev.* **2015,** *42*, 460-476.
4. Mao, S. S.; Chen, X. Selected Nanotechnologies for Renewable Energy Applications. *Int. J. Energy Res.* **2007,** *31*, 619-636.
5. Wang, Z. L.; Wu, W. Nanotechnology-Enabled Energy Harvesting for Self-Powered Micro-/Nanosystems. *Angew. Chem.* **2012,** *51*, 11700-11721.
6. Guo, W.; Cheng, C.; Wu, Y.; Jiang, Y.; Gao, J.; Li, D.; Jiang, L. Bio-Inspired Two-Dimensional Nanofluidic Generators Based on a Layered Graphene Hydrogel Membrane. *Adv. Mater.* **2013,** *25,* 6064-6068.
7. Xu, Y.; Chen, P.; Zhang, J.; Xie, S.; Wan, F.; Deng, J.; Cheng, X.; Hu, Y.; Liao, M.; Wang, B.; Sun, X.; Peng, H. A One-Dimensional Fluidic Nanogenerator with a High Power Conversion Efficiency. *Angew. Chem.* **2017,** *56,* 12940-12945.
8. Wang, C.; Choi, E.; Jang, G. T.; Park, J. In Effect of Ion Current Rectification on Energy Harvesting by Reverse Electrodialysis, 2016 IEEE 29th International

TH-2654_156122042

Conference on Micro Electro Mechanical Systems (MEMS), 24-28 Jan. 2016; 2016; pp 1240-1243.

9. Ji, J.; Kang, Q.; Zhou, Y.; Feng, Y.; Chen, X.; Yuan, J.; Guo, W.; Wei, Y.; Jiang, L. Osmotic Power Generation with Positively and Negatively Charged 2D Nanofluidic Membrane Pairs. *Adv. Funct. Mater.* **2017,** *27*, 1603623.
10. Lee, S.; Kim, H.; Kim, D.-K. Power Generation from Concentration Gradient by Reverse Electrodialysis in Dense Silica Membranes for Microfluidic and Nanofluidic Systems. *Energies* **2016,** *9*, 49.
11. Hong, J. G.; Zhang, B.; Glabman, S.; Uzal, N.; Dou, X.; Zhang, H.; Wei, X.; Chen, Y. Potential Ion Exchange Membranes and System Performance in Reverse Electrodialysis for Power Generation: A Review. *J. Membr. Sci.* **2015,** *486*, 71-88.
12. Lin, L.; Zhang, L.; Wang, L.; Li, J. Energy Harvesting from Enzymatic Biowaste Reaction through Polyelectrolyte Functionalized 2D Nanofluidic Channels. *Chem. Sci.* **2016,** *7*, 3645-3648.
13. Zhao, F.; Cheng, H.; Zhang, Z.; Jiang, L.; Qu, L. Direct Power Generation from a Graphene Oxide Film under Moisture. *Adv. Mater.* **2015,** *27*, 4351-4357.
14. Huang, Y.; Cheng, H.; Shi, G.; Qu, L. Highly Efficient Moisture-Triggered Nanogenerator Based on Graphene Quantum Dots. *ACS Appl. Mater. Interfaces* **2017,** *9*, 38170-38175.
15. Huang, Y.; Cheng, H.; Yang, C.; Zhang, P.; Liao, Q.; Yao, H.; Shi, G.; Qu, L. Interface-Mediated Hygroelectric Generator with an Output Voltage Approaching 1.5 Volts. *Nat. Commun.* **2018,** *9*, 4166.

TH-2654_156122042

16. Zhao, F.; Liang, Y.; Cheng, H.; Jiang, L.; Qu, L. Highly Efficient Moisture-Enabled Electricity Generation from Graphene Oxide Frameworks. *Energy Environ. Sci.* **2016,** *9*, 912-916.
17. Shen, D.; Xiao, M.; Zou, G.; Liu, L.; Duley, W. W.; Zhou, Y. N. Self-Powered Wearable Electronics Based on Moisture Enabled Electricity Generation. *Adv.Mater.* **2018,** *30*, 1705925.
18. Ghosh, S.; Sood, A. K.; Kumar, N. Carbon Nanotube Flow Sensors. *Science* **2003**, *299*, 1042-1044.
19. Newaz, A. K. M.; Markov, D. A.; Prasai, D.; Bolotin, K. I. Graphene Transistor as a Probe for Streaming Potential. *Nano Lett.* **2012,** *12*, 2931-2935.
20. Xu, Y.; Chen, P.; Peng, H. Generating Electricity from Water through Carbon Nanomaterials. *Chem. Eur. J.* **2018,** *24*, 6287-6294.
21. Chen, Y.; Liang, D.; Gao, X. P. A.; Alexander, J. I. D. Sensing and Energy Harvesting of Fluidic Flow by InAs Nanowires. *Nano Lett.* **2013,** *13*, 3953-3957.
22. Yin, J.; Li, X.; Yu, J.; Zhang, Z.; Zhou, J.; Guo, W. Generating Electricity by Moving a Droplet of Ionic Liquid Along Graphene. *Nat. Nanotechnol.* **2014,** *9*, 378.
23. Xue, G.; Xu, Y.; Ding, T.; Li, J.; Yin, J.; Fei, W.; Cao, Y.; Yu, J.; Yuan, L.; Gong, L.; Chen, J.; Deng, S.; Zhou, J.; Guo, W. Water-Evaporation-Induced Electricity with Nanostructured Carbon Materials. *Nat. Nanotechnol.* **2017,** *12*, 317.
24. He, S.; Zhang, Y.; Qiu, L.; Zhang, L.; Xie, Y.; Pan, J.; Chen, P.; Wang, B.; Xu, X.; Hu, Y.; Dinh, C. T.; De Luna, P.; Banis, M. N.; Wang, Z.; Sham, T.-K.; Gong, X.; Zhang, B.; Peng, H.; Sargent, E. H. Chemical-to-Electricity Carbon: Water Device. *Adv. Mater.* **2018,** *30*, 1707635.
25. Chen, N.; Huanga, X.; Qu, L. Heteroatom substituted and decorated graphene: preparation and applications. *Phys. Chem. Chem. Phys.* **2015**, *17*, 32077-32098.

TH-2654_156122042

26. Kaur, M; Kaur, M.; Sharma, V. K. Nitrogen-doped graphene and graphene quantum dots: A review on synthesis and applications in energy, sensors and environment. *Adv. Colloid Interface Sci*. **2018**, *259*, 44–64.

27. Wang, H.; Maiyalagan, T.; Wang, X. Review on Recent Progress in Nitrogen-Doped Graphene: Synthesis, Characterization, and Its Potential Applications. *ACS Catal*. **2012**, *2*, 781−794.

28. Dieb, T. M.; Hou, Z.; Tsuda, K. Structure prediction of boron-doped graphene by machine learning. *J. Chem. Phys*. **2018**, *148*, 241716-241723.

29. Agnoli, S.; Favarob, M. Doping graphene with boron: a review of synthesis methods, physicochemical characterization, and emerging applications. *J. Mater. Chem. A* **2016**, *4*, 5002–5025.

30. Panchakarla, L. S.; Subrahmanyam, K. S.; Saha, S. K.; Govindaraj, A.; Krishnamurthy, H. R. ; Waghmare, U. V.; Rao, C. N. R. Synthesis, Structure, and Properties of Boron- and Nitrogen-Doped Graphene. *Adv. Mater*. **2009**, *21*, 4726–4730.

31. Zhang, Y.-H.; Chen, Y.-B.; Zhou, K.-G.; Liu, C.-H.; Zeng, J.; Zhang, H.-L.; Peng, Y. Improving Gas Sensing Properties of Graphene by Introducing Dopants and Defects: A First-Principles Study. *Nanotechnology* **2009,** *20*, 185504.

32. Hummers, W. S.; Offeman, R. E. Preparation of Graphitic Oxide. *J. Am. Chem. Soc.* **1958**, *80*, 1339-1339.

33. Sudeep, P.M.; Vinod, S.; Ozden, S.; Sruthi, R.; Kukovecz, A.; Konya, Z.; Vajtai, R.; Anantharaman, M. R.; Ajayan, P. M.; Narayan, T. N. Functionalized Boron Nitride Porous Solids. *RSC. Adv*. **2015**, *5*, 93964-93968.

TH-2654_156122042

34. Choi, S.-J.; Yu, H.; Jang, J.-S.; Kim, M.-H.; Kim, S.-J.; Jeong, H. S.; Kim, I.-D. Nitrogen-Doped Single Graphene Fiber with Platinum Water Dissociation Catalyst for Wearable Humidity Sensor. *Small* **2018,** *14*, 1703934.

35. Rathi, K.; Pal, K. Impact of Doping on GO: Fast Response–Recovery Humidity Sensor. *ACS Omega* **2017,** *2*, 842-851.

36. Gaussian 09, Revision D.01, Frisch, M. J.; Trucks, G. W.; Schlegel, H. B.; Scuseria, G. E.; Robb, M. A.; Cheeseman, J. R.; Scalmani, G.; Barone, V.; Mennucci, B.; Petersson, G. A.; Nakatsuji, H.; Caricato, M.; Li, X.; Hratchian, H. P.; Izmaylov, A. F.; Bloino, J.; Zheng, G.; Sonnenberg, J. L.; Hada, M.; Ehara, M.; Toyota, K.; Fukuda, R.; Hasegawa, J.; Ishida, M.; Nakajima, T.; Honda, Y.; Kitao, O.; Nakai, H.; Vreven, T.; Montgomery, J. A.; Peralta, Jr.; J. E.; Ogliaro, F.; Bearpark, M.; Heyd, J. J.; Brothers, E.; Kudin, K. N.; Staroverov, V. N.; Keith, T.; Kobayashi, R.; Normand, J.; Raghavachari, K.; Rendell, A.; Burant, J. C.; Iyengar, S. S.; Tomasi, J.; Cossi, M.; Rega, N.; Millam, J. M.; Klene, M.; Knox, J.E.; Cross, J. B.; Bakken, V.; Adamao, C.; Jaramillo, J.; Gomperts, R.; Stratmann, R. E.; Yazyev, O.; Austin, A. J.; Cammi, R.; Pomelli, C.; Ochterski, J. W.; Martin, R. L.; Morokuma, K.; Zakrzewski, V. G.; Voth, G. A.; Salvador, P.; Dannenberg, J. J.; Dapprich, S.; Daniels, A. D.; Farkas, O.; For-esman, J. B.; Ortiz, J. V.; Cioslowski, J.; J. Fox, D. Gaussian, Inc., Wallingford CT, **2013**.

37. Perdew, J. P.; Burke, K.; Ernzerhof, M. Generalized Gradient Approximation Made Simple. *Phys. Rev. Lett.* **1996**, *77*, 3865-3868.

38. Foster, J. P.; Weinhold, F. Natural Hybrid Orbitals. *J. Am. Chem. Soc.* **1980**, *102*, 7211-7218.

TH-2654_156122042

39. Rezac, J.; Hobza, P. Benchmark Calculations of Interaction Energies in Noncovalent Complexes and Their Applications. *Chem. Rev.* **2016**, *116*, 5038-5071.

40. Srivastava, H. K.; Sastry, G. N. Viability of Clathrate Hydrates as CO_2 Capturing Agents: A Theoretical Study. *J. Phys. Chem. A* **2011**, *115*, 7633-7637.

TH-2654_156122042

Chapter 4

Clay-Based Nanofluidic Membrane Derived from Vermiculite Nanoflakes for Pressure-Responsive Power Generation

Summary*

The intrinsic thermal and chemical stability of vermiculite clay is exploited here to fabricate a robust and responsive energy device that consumes atmospheric water molecules as the cathode reagent. Nanofluidic membrane of clay was prepared by reconstructing exfoliated nanolayers of natural vermiculite clay, and doped with polydiallyldimethylammonium chloride (PDDA). X-ray diffraction studies determined the height of the two-dimensional (2D) nanofluidic channels to be ~ 0.41 nm. Application of a modest pressure of 56 kPa, on the aluminum foil placed on top of a PDDA doped nanofluidic vermiculite membrane (PDDA-VM), yields a stable potential of ~ 0.8 V. The output current value of the clay-based devices can be tuned by varying parameters like intercalating cations, device geometry, the thickness of the polymeric coating, and applied pressure. The natural clay-based energy device is found to be highly robust, exposure to liquid nitrogen (-195 °C), heat pulse (450 °C), water streams, and mechanical stress (100 N) did not deteriorate its performance. Interestingly, the PDDA doped vermiculite membranes exhibit extraordinary fire-retardant properties with ~ 70 % recovery in power output after being exposed to an open flame.

---

* Paper based on these studies has appeared in *ACS Appl. Nano Mater*. 2021, *4*, 4872

TH-2654_156122042

4.1: INTRODUCTION

Generation and storage of energy hold an imperative position in the massive advancement of emerging areas such as smart electronics, sensor technologies, and electric vehicles. In recent years, immense progress has been achieved towards designing novel electrochemical energy storage systems with new generation technologies like stretchable batteries and supercapacitors,[1-2] wearable electronics,[3] miniatured implantable batteries[4] and stimuli responsive batteries.[5] However, for widespread acceptance and commercialization of such systems, certain hurdles need to be resolved which includes complex fabrication techniques, low energy and power densities, and handling risks such as electrolyte leakage and flammability. Over the years, a class of non-aqueous metal-air batteries has gained enormous attention owing to its high energy density as compared to Li-ion batteries and high level of safety. Metal-air batteries use a mettalic anode and oxygen gas from the atmosphere as the cathode material. Recently, metal-water batteries based on similar principle have been developed that involves metal oxidation at anode and water reduction at cathode.

The vast amount of gaseous water molecules omnipresent in our atmosphere is recognized to be a never ending source of electric charge, and hence it can serve as an endless source of electrical energy.[6-9] By the virtue of its inherent advantages like environmental friendliness, operational simplicity, and self-regenerating nature, in the recent years, these atmospheric water molecules have drawn significant interest as a potential source of energy. The energy of atmospheric water is considered to be an ideal choice to power self-sufficient electronic equipment like Internet of things (IoT) devices, where minimum external inputs and human interventions are desired.[10] The most recent efforts to extract energy from moist air involve creation of an artificial hydrological cycle

TH-2654_156122042

in a miniature form, where atmospheric water molecules are condensed by a hygroscopic material and subsequently allowed to diffusion through nanofluidic channels having gradient of surface charges.[11-17] In an alternative approach, the chemical reactivity of the atmospheric water has been exploited to prepare metal-moisture battery based energy generating devices. Where, metal atoms are consumed at the anode, and atmospheric water molecules are utilized as the cathode reagent. For example, moisture batteries were formed by the direct contact of magnesium with foamed polyaniline[18] and Li foil with graphene oxide film.[19] Similarly, a dual responsive smart metal−water battery was prepared through direct contact of Mg or Zn anode with an all-polymer moisture electrode.[20] Here, the hygroscopic nature of PDDA doped vermiculite membrane was exploited to fabricate highly robust, pressure-responsive energy devices. The energy device prepared on the basis of metal-moisture battery can sustain its functioning even after exposing to direct fire for more than 2 minutes.

4.2: SCOPE OF THE PRESENT INVESTIGATION

Vermiculite is a natural clay mineral famous for its outstanding thermal stability, and water holding capacity. Its 2:1 layers are composed of one octahedral sheet sandwiched between two silicate-based tetrahedral sheets, and the space between the layers is occupied by charge balancing interlayer cations. Layers of vermiculite can be readily exfoliated and reassembled to prepare flexible freestanding membranes. The reconstructed vermiculite membrane displays many fascinating properties such as extraordinary proton conductivity,[21-22] self-repairing ability,[23] switchable wettability,[24] environmental responsiveness,[25] nanoconfined catalytic activity,[26] and extraordinary thermal and chemical stability.[27-28] The electrically insulating vermiculite membrane also possesses very high intrinsic conductivity and eliminates the needs of external electrolytes.[23] Nanofluidic membrane with such remarkable properties could play crucial rules in fabricating energy

TH-2654_156122042

harvesting and storage devices aimed for high temperature applications. Clay minerals are known for their thermal insulation and stability. Layer by layer assembly of exfoliated clay has been utilized to control flammability by forming a shield over the surface of inflammable materials. Over the years, exfoliated layers of clay minerals have been exploited for various applications owing to their thermal insulation and flame retardancy. However, flame retardant energy devices are so far not reported to the best our knowledge. Moreover, clay based polymeric membranes are also known for protecting flammable materials from the exposure to open fire.[29-32] Here, we have developed an energy delivering systems based on the principle of metal-moisture batteries, where PPDA doped vermiculite membrane (VM-PDDA) played three vital rules, as solid-state electrolyte, atmospheric humidity collector, and separator. Application of a humble pressure of 56 kPa to the inflammable energy device of effective device dimension ~ 1.5 cm × 1.5 cm produced a potential difference of 0.8 V, with an output-current of 1.8 mA. The vermiculite-based energy devices exhibit several advantages like pressure perceptibility, thermal robustness, simplicity in fabrication, ease of operation, and environmental sustainability.

4.3: EXPERIMENTAL SECTION

Materials and Chemicals: Raw vermiculite crystals, Polydiallyldimethylaluminium chloride (PDDA), Potassium chloride, Sodium chloride, Lithium chloride, and Hydrochloric acid were purchased from Sigma Aldrich. Aluminium sheets were purchased from local vendor.

Exfoliation of vermiculite clay

In order to prepare vermiculite nanoflakes, 50 mg of thermally expanded vermiculite particle was refluxed in a saturated solution of NaCl for 24 hours followed by washing with (deionized) DI water until the removal of chloride ions. The as-obtained Na^+

TH-2654_156122042

exchanged vermiculite sample was further refluxed with a solution of 2 M LiCl for 24 hours followed by cleaning with DI water until the removal of chloride ions. Thus obtained Li^+ vermiculite slurry was dried and re-dispersed in DI water. 30 mL of the vermiculite dispersion (2 mg/mL) was vacuum filtered through a cellulose nitrate membrane to prepare freestanding VM.

Fabrication of VM/Al device

Typically, vermiculite strip of dimension ~ 1.5 cm ×1.5 cm × 0.006 cm was cut-out from air-dried VM membrane and connected to a Cu wire by employing conductive silver paste. The surface of VM strip connected to the Cu wire was pasted to a cardboard with the help of a doubled sided sticky tape. An Al film of similar dimension was pasted to the other end of the cardboard with the help of doubled sided tape. The card board was flapped such a way that the open surface of Al film can make a homogeneous contact with that of the VM strip. In order to apply pressure on VM/Al devices, pre-calibrated weights were placed on the Al side of the cardboard.

Fabrication of PDDA-VM/Al device

Aqueous solutions (20 µL, 20 %) of PDDA (polydiallyldimethylaluminium chloride) of definite volumes were drop casted to one side of the VM strips (typical dimensions ~ 1.5 cm × 1.5 cm × 0.006 cm) and allowed to dry at room temperature. A Cu wire was then pasted to the PDDA coated side of VM stripe with the help of conductive silver paste. The silver paste coated surface of PDDA-VM strip was then pasted to a cardboard with the help of a doubled sided sticky tape. Similarly, an Al film of similar dimension was pasted to the other end of the card-board. The card board was flapped in middle to press the open surface of Al film on the VM side of the PDDA-VM strip. Similar to VM/Al devices, pressure was applied by placing pre-calibrated weights on Al side of the cardboard.

TH-2654_156122042

Characterization

The morphology of the vermiculite samples was characterized by atomic force microscope (AFM) (Oxford, Model: Cypher), field emission scanning electron microscope (FESEM) (Zeiss, Model: Sigma), and field emission transmission electron microscope (FETEM) (JEOL, JEM 2100F). Interlayer spacing between the vermiculite nanochannels was determined by X-ray diffractometer (XRD) (Rigaku, Model: Micromax- 007HF). All electrochemical measurements were carried out by using a source meter instrument (Keithley 2450). Percentage composition of Al and O in fresh and corroded Al foils were analysed by X-ray photoelectron spectroscopy (Thermo Fisher Scientific Pvt. Ltd., Model: ESCALAB Xi+). Surface morphology of fresh and corroded Al foils were characterized by optical microscope (Olympus BX51).

4.4: RESULTS AND DISCUSSION

The exfoliated layers of vermiculite employed in this project was prepared through a two-step ion exchange method.[21] Details of the exfoliation process is discussed in the experimental section. A schematic illustration of structure and chemical composition along with the synthesis and fabrication method is shown in Schematic 4.1. Morphological characterizations of the exfoliated 2D sheets are done by Atomic force microscopy (AFM) and Field emission transmission electron microscopy (FETEM) and are presented in Figure 4.1b and Figure 4.1c. In brief, lateral dimension of the sheets varies between 2 - 5 μm^2, and thicknesses are found to be in the range of 3-4 nm. Aqueous dispersions of the exfoliated clay layers (2 mg/ml) (Figure 4.1a) were vacuum filtered through cellulose nitrate

TH-2654_156122042

Scheme 4. 1. Schematic illustration of crystal structure of vermiculite clay and fabrication of PDDA doped VM membrane (PDDA-VM)

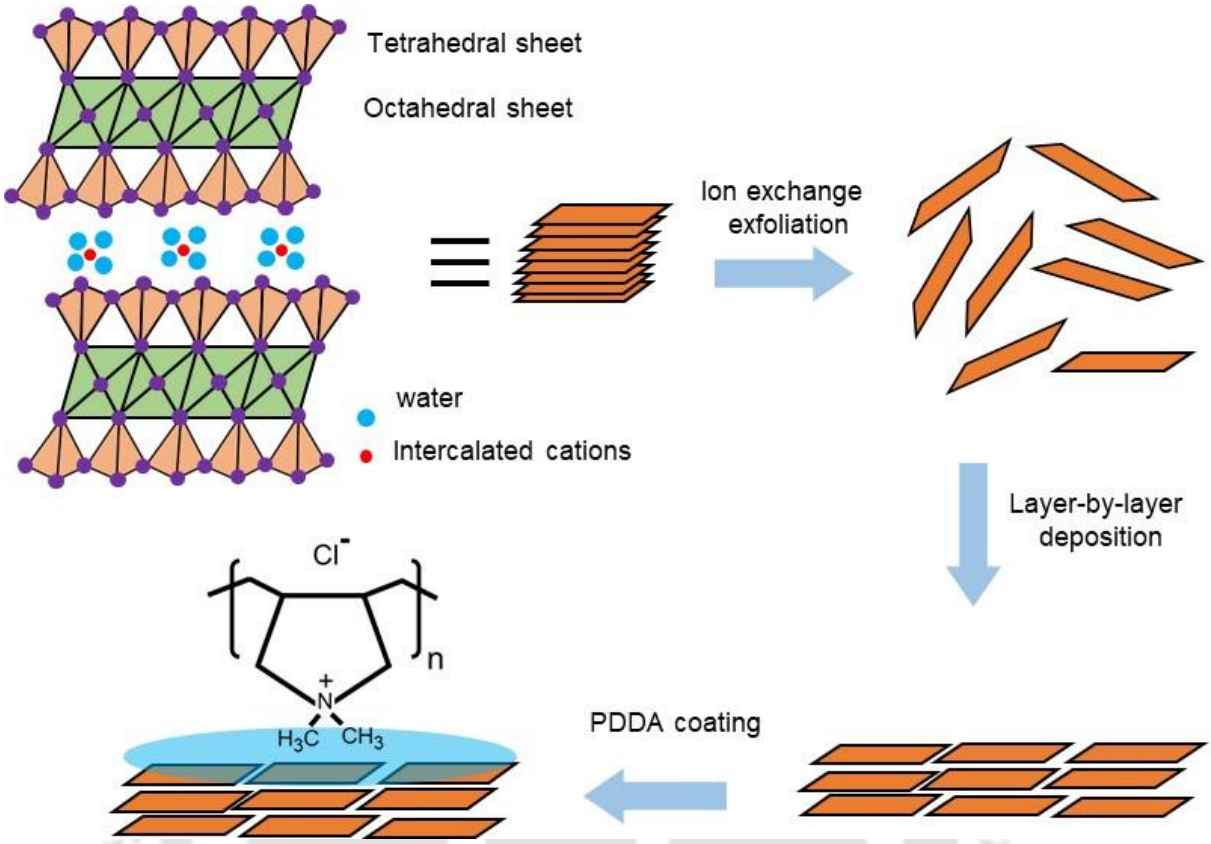

membranes to prepare freestanding vermiculite membranes. Digital photo of a flexible VM is shown in Figure 4.1d. The lamellar cross-section of the thus prepared membrane is revealed by the Field Emission Scanning Electron Microscopic (FESEM) examination as shown in Figure 4.1e. The layered nature of VM is also evident from the well-defined (002) reflection in the corresponding powder X-ray diffraction (pXRD) pattern, shown in Figure 4.1f. PDDA was doped on to the freestanding VM membrane just by adding a droplet of

TH-2654_156122042

the aqueous dispersion of the cationic polymer. Typically, a 50 µL droplet of PDDA (20 %) was spread onto a VM membrane of dimension ~ 4 cm × 4 cm × 45 µm, and allowed to dry at room temperature. The lamellar nature of the PDDA-VM is evident from the

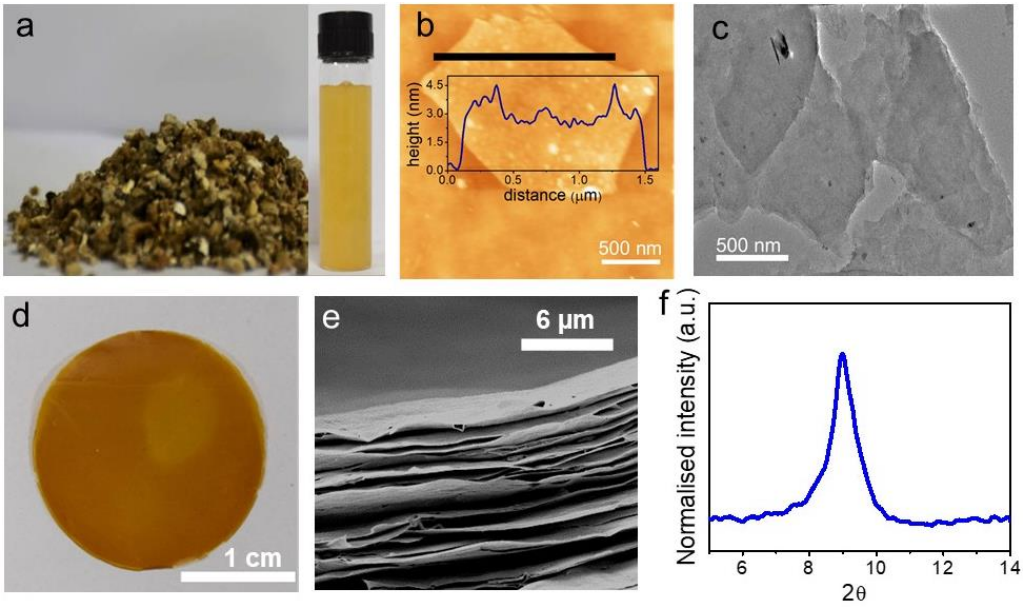

Figure 4.1: Characterisation of Vermiculite nanoflakes: (a) Digital photograph of raw vermiculite crystals, inset showing the aqueous dispersion of exfoliated VM nanoflakes. (b) AFM image of VM nanoflakes, inset showing the corresponding height profile. (c) FETEM image of VM nanoflakes. (d) Digital photograph, and (e) Cross-sectional FESEM image of a vermiculite membrane. (f) XRD pattern of VM membrane with characteristic peak proves the lamellar stacking of VM nanosheets.

corresponding pXRD pattern. In Figure 4.2a, XRD pattern of PDDA-VM is compared with that of a pristine VM membrane. The slight shift in the position of (002) reflection from d = 1.39 nm of VM to d = 1.45 of PDDA-VM is attributed to enhanced tendency of PDDA-VM to trap water molecules inside the corresponding nanofluidic channels. As reported earlier, in the wet-stage, the interlayer space of VM exhibit excellent nanofluidic ionic conductivity.[21] Representative I-V curves and surface-charge-governed ionic conductivity of a vermiculite nanofluidic device is shown in Figure 4.2b and Figure 4.2c. In this experiment, ionic conductivity of VM was measured by placing aqueous KCl solutions of different concentrations to both the reservoirs of nanofluidic device. PDDA doping did not alter the surface-charge-governed ionic conductivity of the VM membrane measured with

TH-2654_156122042

aqueous salt solutions (Figure 4.2c). However, it drastically improved the ionic conductivity measured in the dry state, in the absence of liquid electrolytes. A digital photo of the device used for measuring ionic current in the dry state is shown in Figure 4.2d. Due to its extraordinary water holding capacity, VM display a humidity dependent ionic conductivity in the dry condition. As shown in the bar diagram of Figure 4.2e, in dry state, the conductivity of VM increased from 0.4 $mScm^{-1}$ at RH = 35% to 1.9 $mScm^{-1}$ at RH = 80 %. Doping of PDDA improved the conductivity of VM film by a factor of 8 and 2.6, at RH value 35 % and 80 %, respectively (Figure 4.2e). The humidity dependent conductivity measurements suggest PDDA to be an active component that helps to trap the atmospheric moisture on VM membrane. Doping of PDDA also improved the tensile strength of VM membrane from 14.8 to 16.4 MPa. The *stress vs stain* curve of the VM membrane recorded before and after PDDA doping is shown in Figure 4.2f.

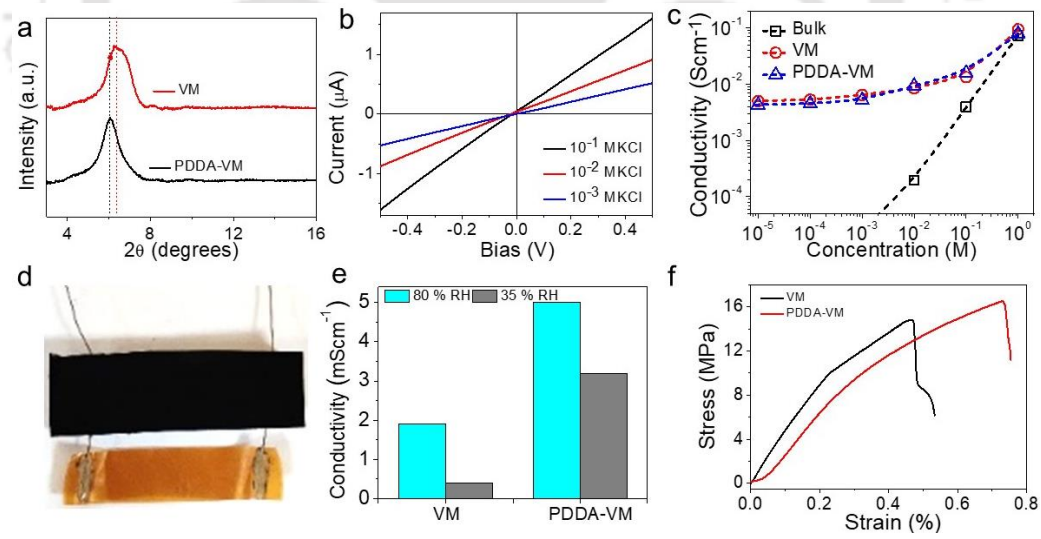

Figure 4.2: (a) XRD pattern of VM membrane compared to that of PDDA-coated VM membrane. (b) Representative I-V curves recorded with solutions of different KCl concentrations through vermiculite nanochannels. (c) Ionic conductivity versus concentration plot of vermiculite nanochannels (red curve), PDDA-coated vermiculite nanochannels (blue curve) are compared with that of the bulk (black curve) water. (d) Photo of free standing VM device to measure i-v curves. (e) Bar diagram comparing conductivity of VM strip and PDDA-VM strip at two different humidity of 80 % and 35 %. (f) Stress vs Strain curve of a pristine VM film as compared to that of PDDA-VM film.

TH-2654_156122042

Vermiculite clay is known for its exceptional water holding capacity.[33] Due its high affinity towards water molecules, under humid condition, the interlayer space of reconstructed vermiculite clay is sufficiently hydrated to form interconnected water channels. As a result, the nanochannels of freestanding membrane exhibits nanofluidic ionic conductivity even without any direct contact with the water reservoirs.[23] Figure 4.3a shows *I-V* curves

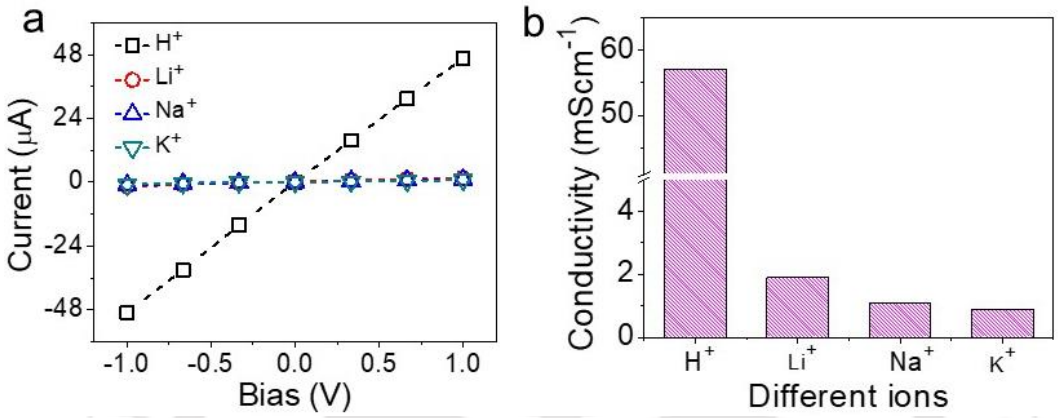

Figure 4.3: Hydrated nanofluidic channels of freestanding vermiculite membrane: (a) Representative I-V curves of vermiculite strips (with different intercalating cations) recorded in dry condition (at 80 % RH). (b) Bar diagram showing conductivity of vermiculite strips with different interlayer cations at 80 % RH.

recorded with freestanding vermiculite membrane with different intercalating cations (K^+, Na^+, Li^+ and H^+) without any contact with the liquid water sources. At the time of measurement, the relative humidity of the atmosphere was recorded to be 80 %. Digital photo of a freestanding vermiculite device is shown in the inset of Figure 4.2d. Remarkably, the slope of the *I-V* curve, which represents the magnitude of the ionic conductance, was found to be dependent on the size of the interlayer cations. For example, while the membrane prepared with K^+ ion exchanged vermiculite flake exhibits lowest ionic conductivity, and the membrane with smallest (H^+) ions exhibits the highest conductivity. A bar diagram of the ionic conductivities as a function of the radius of interlayer cations is shown in Figure 4.3b. This dependence of ionic conductivity on the radius of the intercalating cations further supports the presence of interconnected water channels in the freestanding vermiculite membrane.

TH-2654_156122042

The fabrication steps of the pressure responsive energy device (PDDA-VM/Al) are illustrated in Figure 4.4a. Typically, an aqueous solution of PDDA (20 %, 15 µL) was

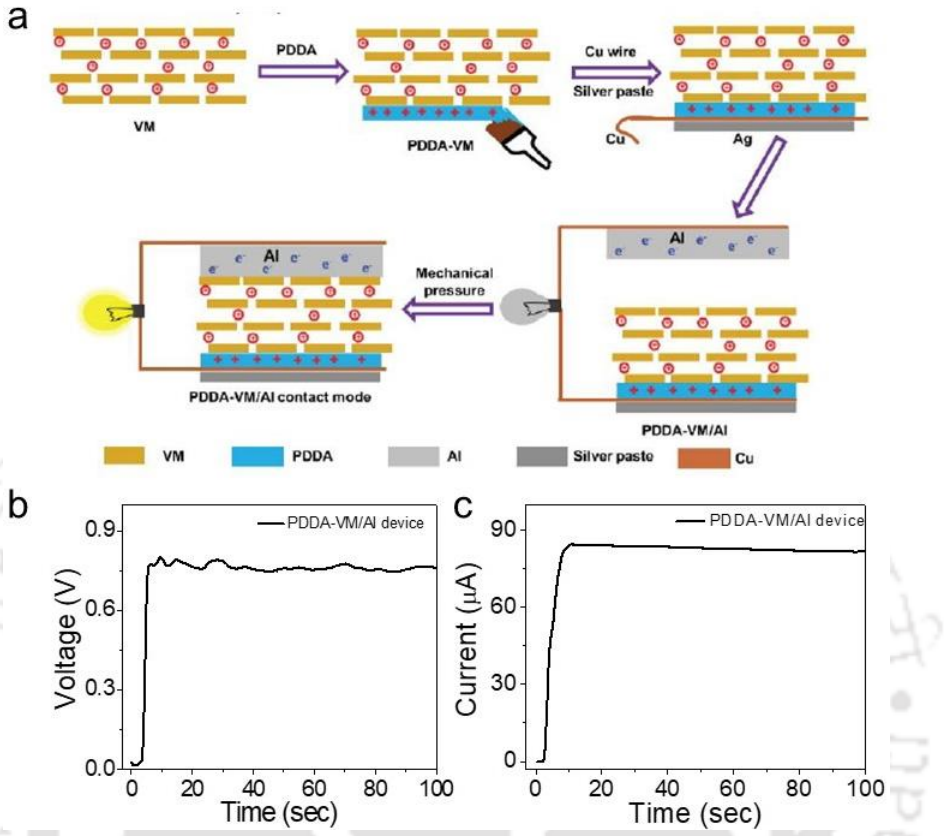

Figure 4.4: Pressure responsive power generation in PDDA-VM/Al devices: (a) Schematic illustration of the fabrication process of energy harvesting devices. (b) Open-circuit voltage, and (c) output current a PDDA-VM/Al device (1.5 cm × 1.5 cm, 15 µL PDDA, Li^+ ion) upon application of 56 kPa pressure.

dropped to a VM stripe of dimension ~1.5 cm × 1.5 cm × 60 µm and allowed to dry at room temperature. The PDDA coated side of the VM strip was then connected to a Cu wire with the help of conductive silver paste. The other end of the vermiculite stripe was pressed against an aluminum sheet of similar dimension. As soon as the PDDA coated vermiculite membrane (1.5 cm × 1.5 cm) was brought into the contact with aluminum foil, the PDDA-VM/Al device generated electrical currents of magnitude around 90 µA, accompanied by an open-circuit potential of 0.8 V (Figure 4.4b and 4.4c). The power generated simply by applying a pressure of 56 kPa between the two layers of PDDA-VM/Al device was calculated to be 0.35 Wm^{-2}. The output power density was also calculated under different

TH-2654_156122042

load conditions with an optimum power output at a resistance of 200 kΩ and shown in Figure 4.5.

The significance of hygroscopic PDDA in the electrochemical performance of the PDDA-VM/Al device was evaluated by performing the experiment in absence of PDDA. A

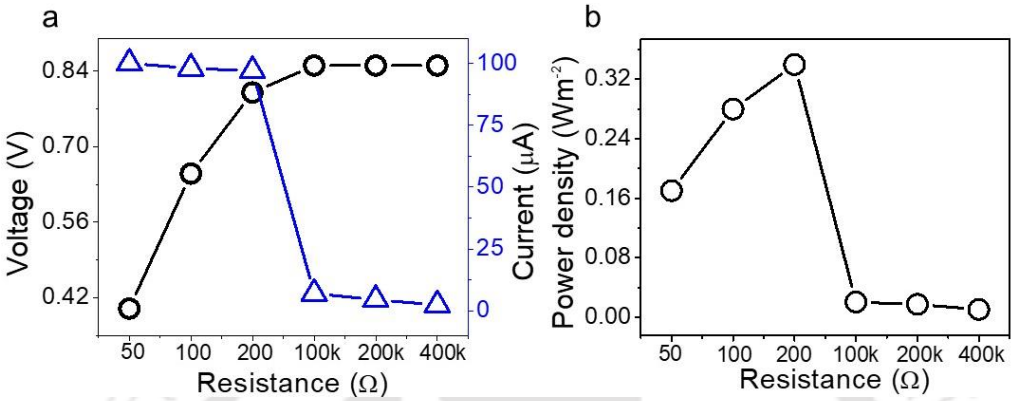

Figure 4.5: (a) Open-circuit voltage and output current of PDDA-VM/Al device in contact mode with different load resistance. (b) Calculated power density of the PDDA-VM/Al device with different load resistance.

freestanding VM film (1.5 cm × 1.5 cm) was brought into the contact Al film of similar dimension, it produced an output current of just ~ 0.1 μA, whereas an open-circuit potential of magnitude ~ 1 V was obtained (as shown in Figure 4.6). A schematic diagram of the device is shown in Figure 4.6a. The PDDA-VM/Al devices were also prepared with varying amount of PDDA coating. Under identical pressure of 56 kPa, the output current values

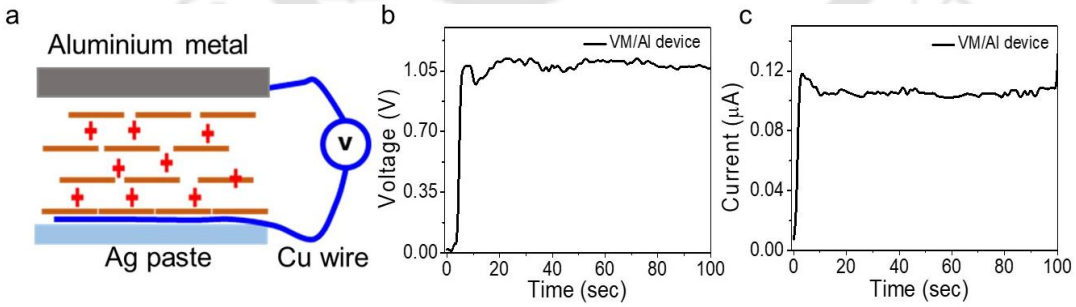

Figure 4.6: (a) Schematic representation of a VM/Al device, (b) Open-circuit voltage, and (c) current generated by a VM/Al device (1.5 cm × 1.5 cm, Li^+ ion) upon application of a pressure (56 kPa).

TH-2654_156122042

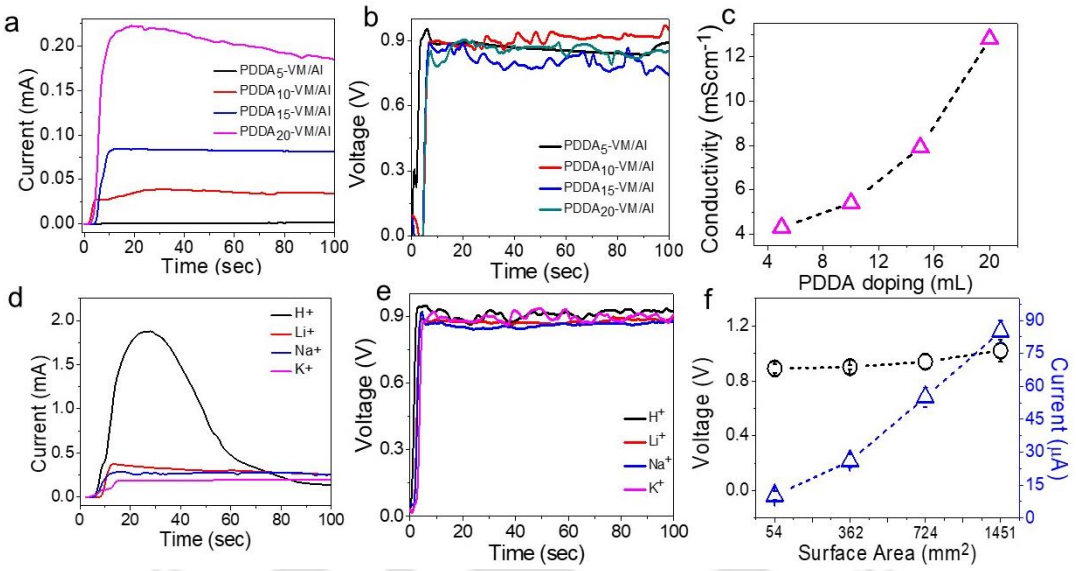

Figure 4.7: Pressure driven current output from PDDA-VM/Al devices: (a) Output current and (b) open-circuit voltage of PDDA-VM/Al devices (1.5 cm × 1.5 cm, 56 kPa, and Li^+ ion) coated with varied amount of PDDA. (c) Conductivity of PDDA-VM strip as a function of PDDA content at 65 % RH (d) Current values and (e) open-circuit voltage generated by PDDA-VM/Al devices (2 cm × 2 cm) prepared with vermiculite membranes intercalated with different intercalating cations (20 µL PDDA coating, and 56 kPa applied pressure). (f) Open-circuit voltage and current generated by the PDDA-VM/Al device as a function of contact area (Li^+ ion, 15 µL PDDA, and 56 kPa).

were found to be increasing with increasing PDDA coating (Figure 4.7a), but no such deviation was observed in the output potential values (~ 0.8 V) as shown in Figure 4.7b. The enhancement in the output current with increasing PDDA content is attributed to increasing conductivity of VM film with increasing PDDA content as shown in Figure 4.7c. In order to further confirm the role of the nanofluidic ion transport on the output performance of device, PDDA-VM/Al devices (device dimension = 2 cm × 2 cm, PPDA coating = 20 µL) were fabricated with VM membranes containing different interlayer cations. As can be seen in Figure 4.7d, under identical pressure (56 kPa), devices prepared with similar interlayer cations (K^+, Na^+, and Li^+) did not show a significant difference in the output current values. But, the PDDA-VM/Al device prepared with H^+ ion exchanged VM exhibited a sharp rise in the current values (up to 1.8 mA), which started declining after a short pulse of around 30 seconds, and finally got saturated to a lowest current value of around 0.15 mA after ~ 80 seconds. Miniscule radius and high mobility of H^+ ion in VM

TH-2654_156122042

nanochannels originating from Grotthuss like hoping mechanism[21] is attributed for the sharp rise and quick dissipation of the current values in H^+ ion-exchanged PDDA-VM/Al device. It is worth noting that no significant deviation in the voltage values was observed among the PDDA-VM/Al devices of varying interlayer cations (Figure 4.7e). Similarly, the increasing exposed surface area of the VM and Al layers also improved the output current values of PDDA-VM/Al device without a significant effect on the open-circuit potential values (Figure 4.7f).

The output current values of PDDA-VM-Al devices can also be tuned by increasing the magnitude of pressure applied upon it (Figure 4.8a). The increasing pressure facilitates a better interfacial contact between VM and Al surfaces leading to the improvements in the movement of ions. In order to get a further insight into the hypothesis, the characteristic *I-V* curves were recorded for a PDDA-VM/Al device at different applied pressure as shown in Figure 4.8b. Conductivity of the device, as calculated from the slope of the *I-V* curves, was found to be increasing with the increasing applied pressure (Figure 4.8c).

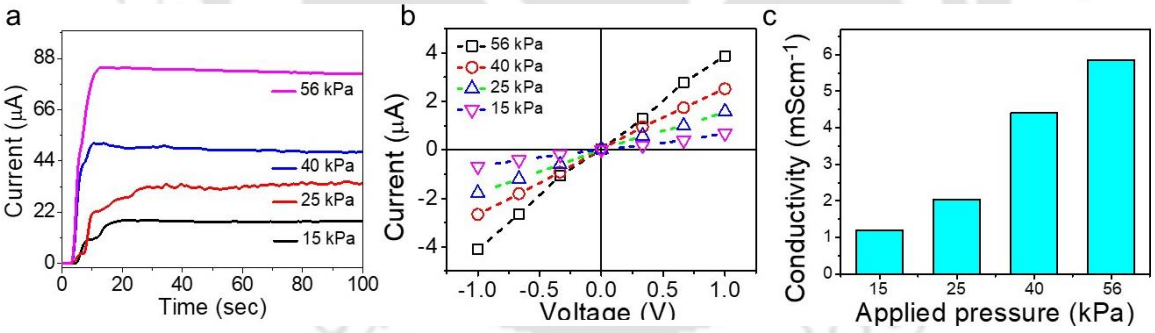

Figure 4.8: Pressure-induced conductivity: (a) Current obtained from PDDA-VM/Al devices under different applied pressure (1.5 cm × 1.5 cm; 15 µL PDDA, and Li^+ ion). (b) Representative i-v curves of PDDA-VM/Al device recorded at different applied pressure, and (c) bar diagram showing conductivity of PDDA-VM/Al device as a function of applied pressure.

In order to further confirm the stability of the power output from PDDA-VM/Al devices, the two layers (dimension = 1.5 cm ×1.5 cm) were subjected to a pressure of 56 kPa and recorded the voltage and current values at a regular interval of time for two days. As shown in Figure 4.9a, under humid condition (RH ≈ 80%) the voltage output of PDDA-VM/Al

TH-2654_156122042

device was found to be stable up to 48 hours. In contrast to the open-circuit potential, the output current values shown a declining trend with time. However, even after 48 hours of

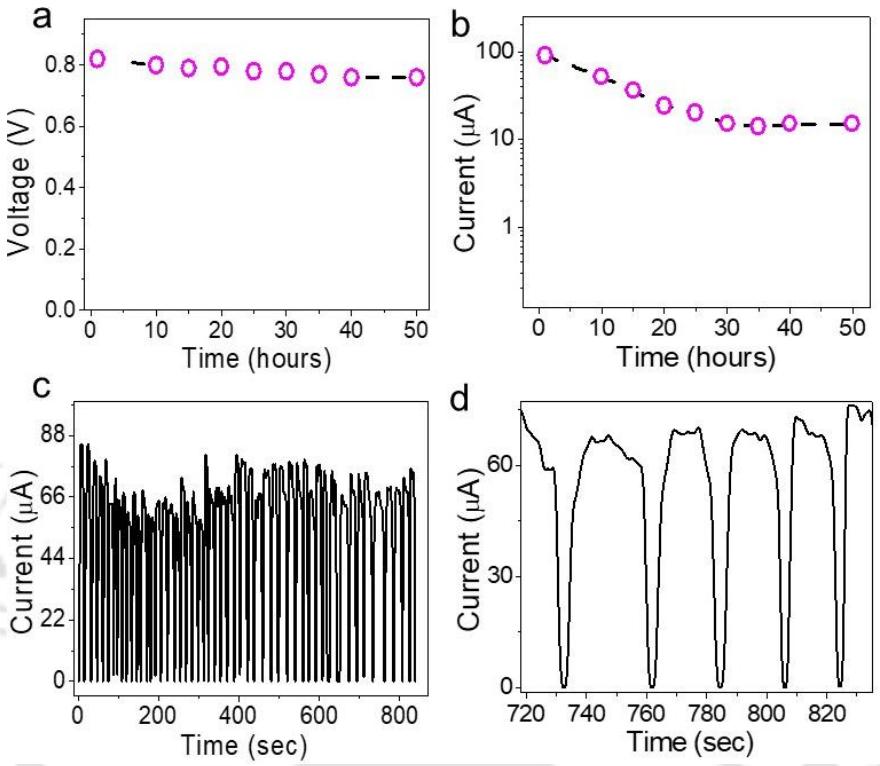

Figure 4.9: Robustness of vermiculite based pressure responsive devices: (a) Open-circuit voltage, and (b) current generated by a PDDA-VM/Al device (1.5 cm × 1.5 cm; 15 µL PDDA, and Li^+ ion) upon application of pressure (56 kPa) for a prolonged period of 48 hours. (c) Short circuit current generated by the PDDA-VM/Al device recorded for 50 cycles. (d) Representative cycles of output current recorded after application of fluctuating pressure (~0.05 Hz) on a PDDA-VM/Al device (1.5 cm × 1.5 cm; 15 µL PDDA, and Li^+ ion).

pressing the PDDA-VM/Al device yielded a current value of ~15 µA (Figure 4.9b). Additionally, the performance of the pressure responsive device was also studied under high frequency mechanical movements. The pressure on the aluminium side of the PDDA-VM/Al device (device dimension = 1.5 cm ×1.5 cm, PPDA coating = 15 µL) was manually fluctuated at a frequency of ~0.05 Hz. As shown in Figure 4.9c, with the fluctuating mechanical movements the output current of the PDDA-VM/Al device also fluctuated without any significant decay in the performance. The study was continued up to 850 seconds, and four representative cycles of the current response by the PDDA-VM/Al device are shown in Figure 4.9d.

TH-2654_156122042

In order to gain insights on to the origin of the prolong power generation process, the performance of PDDA-VM/Al device was monitored at different humidity conditions. The output current value was found to be declined (from 80 µA to - 20 µA, within 5-6 hours) when PDDA-VM/Al device was placed inside a desiccator (RH ≈ 12%). The detailed experimental set-up used for maintaining the desired humidity condition is demonstrated in Figure 4.10a. In the initial hours, the current values dropped very rapidly, but gradually

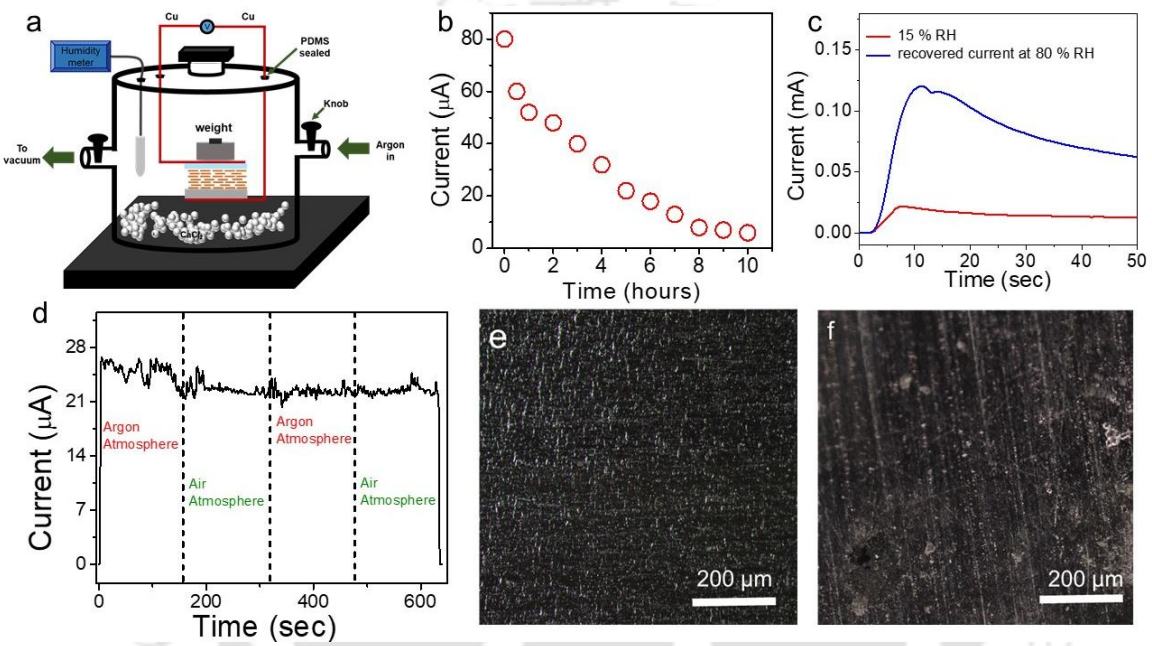

Figure 4.10: Effect of atmospheric humidity on output current: (a) Schematic representation of humidity control chamber, (b) Output current of a PDDA-VM/Al device as a function of time at a low humid condition (RH 12 %), and (c) Recovery of output-current for PDDA-VM/Al device when exposed to a higher humidity of 80 %. (d) Output-current of a PDDA-VM/Al device in alternating argon and air atmosphere at 20 % relative humidity. Optical microscope images of (e) fresh Al foil and (f) corroded Al foil.

become stable after 8 hours (Figure 4.10b). Remarkably, the output current was quickly recovered when device was brought back into a humid area (RH = 80 %, for five minute) (Figure 4.10c). The variation in the output current values with the atmospheric humidity levels confirms the consumption of atmospheric water molecules as the cathode reagent. In order to rule out the possibility of the involvement of atmospheric oxygen molecules in the cathodic reaction (like metal-O_2 batteries), the output current was measured by consecutively exposing the device to argon and air atmosphere. The PDDA-VM/Al device

TH-2654_156122042

did not show any drop in the current values under argon atmosphere (as evident from Figure 4.10d). Similarly, after 5 days, of continuous power output Al-electrode of a PDDA-VM/Al device was observed under optical microscope. The microscopic images in Figure 410e and 410f clearly suggest corrosion of the Al-surface during the operation. The surface of the aluminium electrode was also examined by using X-ray photoelectron spectroscopy (XPS) both before and after the discharge process. In Figure 411a and 411b, the XPS survey scan of pristine Al foil is compared with the one after applying pressure for power generation for 5 days. The analysis of the XPS data suggest that during the operation, the Al/O ratio

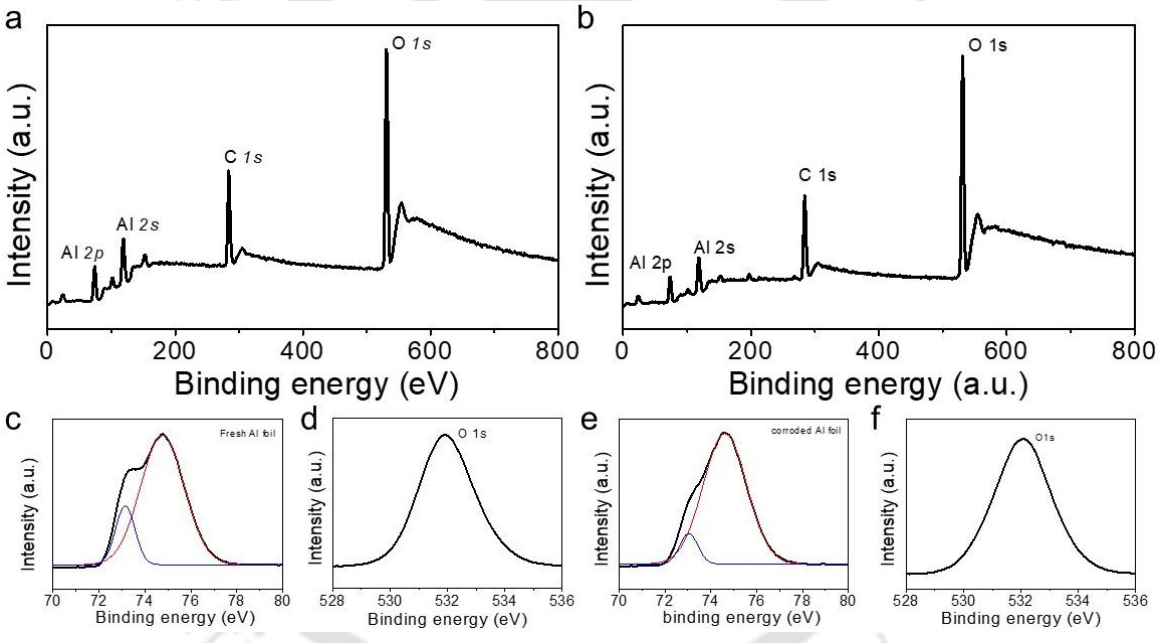

Figure 4.11: XPS survey scan of Al electrode recorded (a) before and (b) after 5 days of continuous power generation, the presence of peaks corresponding to C along with Al and O is attributed to the absorption of carbon dioxide on the surface. Moreover, the sample was attached to the XPS stub with the help of a conductive carbon tape. XPS Al 2p peaks of (c) fresh Al foil and (e) corroded Al foil, XPS peaks of O1s of (d) fresh Al foil and (f) corroded Al foil.

of the pristine foil was decreased from 0.48 to 0.36, indicating consumption of Al atom in the energy generation process. Similarly, the Al 2p spectrum of pristine Al foil, shown in Figure 4.11c, exhibits two maximus, which were deconvoluted into two peaks corresponding to Al_2O_3 and $Al(OH)_3$ species centered at 74.7 eV and 73.1 eV, respectively.

TH-2654_156122042

On the contrary, Al 2p spectrum of corroded Al foil (Figure 4.11e) displayed a distinct peak centered at 72.6 eV, representing the $Al(OH)_3$ species.

Based on the experimental findings the working mechanism of PDDA-VM/Al-based devices can be summarized in Schematic 4.1. Vermiculite is known for its extraordinary attractions towards water molecules, under the experimental conditions (80% RH) the PDDA-VM absorbs water molecules from atmospheric humidity levels. When a hydrated PDDA-VM is pressed against an aluminum foil it generates an interfacial electrochemical potential driven by their intrinsic differences in the redox potential. Under the influence of interfacial potential, some of the water molecules absorbed from the atmospheric humidity get dissociated into H^+ and OH^- ions. While the H^+ ion travels towards the negative surface charges of vermiculite, the OH^- ions are attracted by the Aluminum. In order to complete

Scheme 4.1. Schematic illustration of the working mechanism of PDDA-VM/AL device

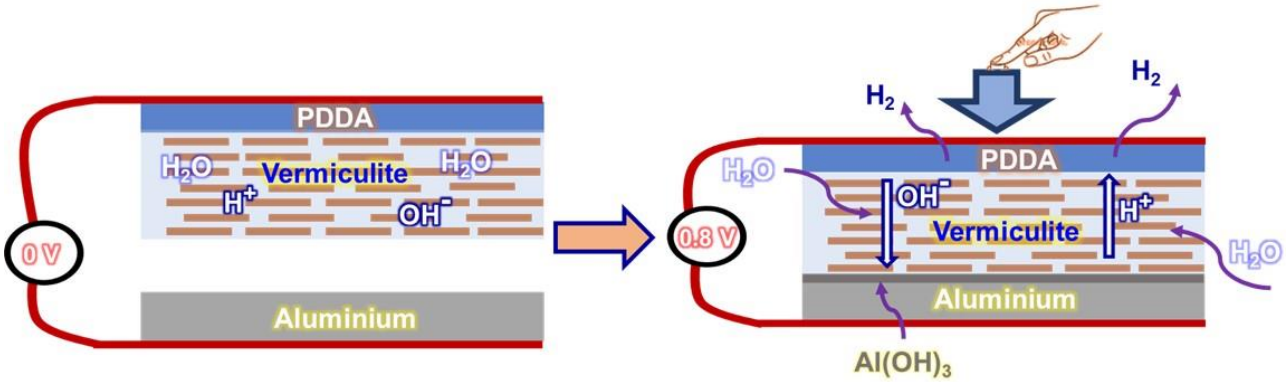

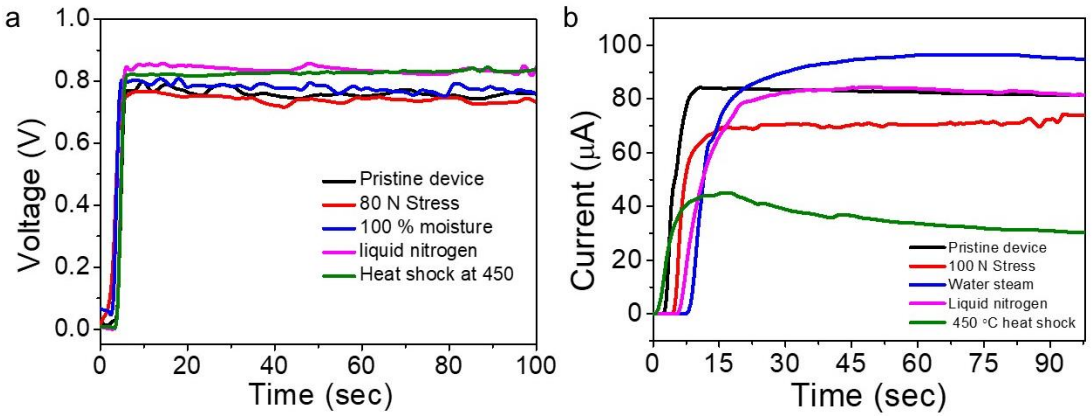

Figure 4.12: (a) Open-circuit voltage and (b) short circuit current generated by PDDA-VM/Al devices after being exposed to various chemical and thermal shocks is compared with that of a pristine device (1.5 cm × 1.5 cm; 15 µL PDDA, and Li^+ ion).

TH-2654_156122042

the cycle, the pressure-induced interfacial potential (~ 0.8 volts) reduced some of the H^+ ions to H_2 gas at the Cu electrode. Similarly, the OH^- ions react with Al foil and formed $Al(OH)_3$ after release 3 electrons.

Cathode: $2H_3O^+ + 2e^- \rightarrow 2H_2O + H_2$

Anode: $Al + 3OH^- \rightarrow Al(OH)_3 + 3e^-$

By the virtue of extraordinary thermal and chemical stability of the natural clay minerals the vermiculite based energy devices are very robust. Various chemical and thermal shocks like exposure to hot water steam, liquid nitrogen (-195 °C), heat shocks (450 °C), and mechanical stress did not deteriorate its performance. Figure 4.12a compares the open-circuit voltage of a PDDA-VM/Al device (dimension = 1.5 cm ×1.5 cm, PPDA coating = 15 µL) before and after exposure to water steam, heat shocks, liquid nitrogen and mechanical stress (100 N). While, the open-circuit potential remained unchanged, the current value was found to be increased by about 15 µA upon exposure to the water steam, and it was decreased to 40 µA upon exposure to the heat pulses (Figure 4.12b), and these changes are attributed to an increase (or decrease) in the moisture contents of VM.

One of the most interesting aspect of the clay based pressure responsive device is that it exhibits remarkable fire retardant properties. As shown in Figure 4.13a and 4.13b, PDDA-VM membrane did not catch fire even after being exposed to a direct flame for 120 seconds. The shape of the membrane remains indistinguishable after being continuously exposed to the flame for more than 2 minutes. However, the color of the membrane turned black due to the deposition of carbon particles from the fire. A digital photograph of the PDDA-VM membrane after being exposed to flame is shown in Figure 14.13c. Mechanical stability of the flame treated membrane is also evident from the stress-strain curves shown in Figure 14.13d. The energy device fabricated by using flame exposed PDDA-VM membranes (for 2 minutes) displayed an open-circuit potential of around 0.7 V, and the output current was

TH-2654_156122042

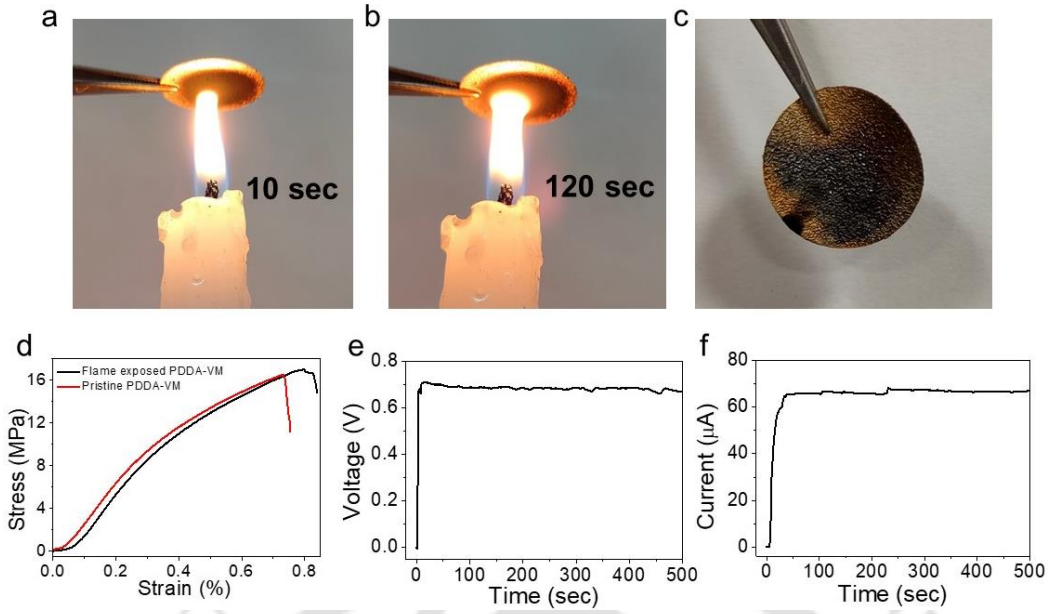

Figure 4.13: Flame retardant energy harvesting system: Digital photographs of PDDA-VM membrane exposed to an open flame for (a) 10 sec and (b) 120 sec. (c) Photograph of PDDA-VM membrane after flamer treatment. (d) A comparison of stress-strain curve of a PDDA-VM strip before and after exposure to flame. (e) Open-circuit potential, and (f) output current of a PDDA-VM/Al device fabricated by a membrane exposed to flame for 2 minutes.

measured as 68 μA, shown in Figure 14.13e and 14.13f. Recovery of more than 70 % of the power output after being directly exposed to open fire is a remarkable characteristic of PDDA-VM/Al device, which could provide a new avenue to prepare high-temperature energy devices.

It is worth noting that the output current (or voltage) values generated by pressure responsive devices can be add up by assembling multiple devices in parallel (or series) connection. Figure 14.14a shows that a total current value of up to 3.3 mA can be obtained by adding eleven Li^+ ion containing PDDA-VM/Al devices (device dimension = 2 cm × 2 cm, PPDA coating = 20 μL) in parallel connection. Similarly, when these devices were connected in series it yielded a potential value of 10.8 V (Figure 14.14b). The current and voltage values of these individual devices were recorded to be 0.3 mA and 0.8 V, respectively. As Figure 14.14c, four of Li^+ containing PDDA-VM/Al devices (2 cm × 2 cm, PPDA coating = 20 μL) were connected in series and pressed with a binder clamp to light a LED of 3 V for more than 48 hours. A similar configuration was also exploited to

TH-2654_156122042

power small electronic devices like calculator and humidity sensor. In order to power these electronic devices, a weight of 950 gm was placed on the top of an array of four PDDA-

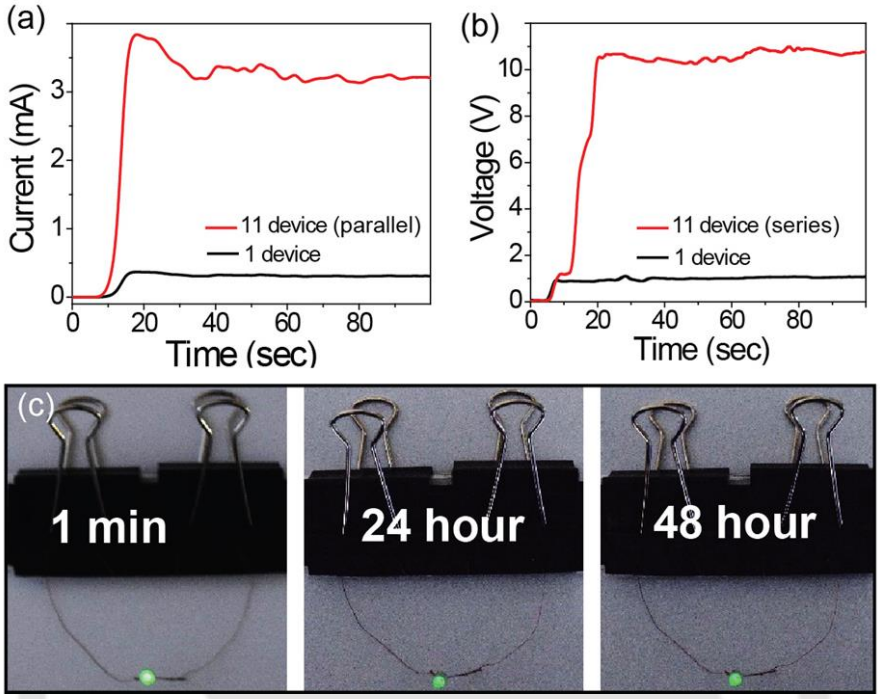

Figure 14.14: Application of clay-based energy devices: (a) Voltage, and (b) current generated by assembling 11 PDDA-VM/Al devices (2 cm × 2 cm; 20 µL PDDA, and Li^+ ion) in parallel and series connections is compared with that of individual devices. (c) Digital photographs show powering of a LED by an assembly (series connections) of four PDDA-VM/Al devices (2 cm × 2 cm; 20 µL PDDA, and Li^+ ion) pressed by binder clips for 48 hours.

VM/Al devices connected in series.

4.5: CONCLUSION

In conclusion, we have demonstrated fabrication of a pressure-responsive energy device to generate electrical energy from atmospheric moisture by exploiting the principles of metal-water batteries. Application of a humble weight (~ 1 kg) on PDDA-VM/Al devices can yield open-circuit potential up to hundreds of millivolts for a prolonged period (up to 48 hours). Depending upon the requirements of the electronic devices, the output current value of clay-based devices can be tuned by varying parameters like device geometry (or device size), intercalating cations, polymeric coating, and applied pressure. By the virtue of the natural stability of clay minerals, the PDDA-VM/Al devices exhibit extraordinary

TH-2654_156122042

robustness with outstanding fire retardant properties. The PDDA-VM/Al devices recovered ~ 70 % of power output after being exposed to a direct flame opening up opportunities for the development of futuristic fire-retardant energy devices. Additionally, these devices can extract energy even after subjected to various challenging environments like exposure to liquid nitrogen (-195 °C), high-temperature heat pulses (450 °C), water steam, and mechanical stress (100 N). Looking at the variety of reconstructed layered materials based nanofluidic membranes reported in the recent literature, pressure responsive moisture batteries should offer many exciting new opportunities for studying and manufacturing of electrochemical energy harvesting devices.

TH-2654_156122042

4.6: REFERENCES

1. Zhai, Q.; Xiang, F.; Cheng, F.; Sun, Y.; Yang, X.; Lu, W.; Dai, L. Recent advances in flexible/stretchable batteries and integrated devices. *Energy Storage Mater*. **2020**, *33*, 116-138.
2. Song, W.-J.; Lee, S.; Song, G.; Park, S. Stretchable Aqueous Batteries: Progress and Prospects. *ACS Energy Lett*. **2019**, *4*, 177–186.
3. Song, W.-J.; Yoo, S.; Song, G.; Lee, S.; Kong, M.; Rim, J.; Jeong, U.; Park, S. Recent Progress in Stretchable Batteries for Wearable Electronics. *Chem electro Chem.* **2019**, *2*, 181-199.
4. Nathan, M. Microbattery technologies for miniaturized implantable medical devices. *Curr Pharm Biotechnol.* **2010**, *4*, 404-410.
5. Wang, F.; Yang, H.; Zhang, J.; Zhang, P.; Wang, G.; Zhuang, X.; Cuniberti, G.; Feng, X. A Dual-Stimuli-Responsive Sodium-Bromine Battery with Ultrahigh Energy Density. *Adv. Mater*. **2018**, *30*, 1800028.
6. Ducati, T. R. D.; Simões, L. H.; Galembeck, F. Charge Partitioning at Gas−Solid Interfaces: Humidity Causes Electricity Buildup on Metals. *Langmuir* **2010**, *26*, 13763-13766.
7. Gouveia, R. F.; Galembeck, F. Electrostatic Charging of Hydrophilic Particles Due to Water Adsorption. *J. Am. Chem. Soc*. **2009**, *131*, 11381-11386.
8. Santos, L. P.; Ducati, T. R. D.; Balestrin, L. B. S.; Galembeck, F. Water with Excess Electric Charge. *J. Phys. Chem. C* **2011**, *115*, 11226-11232.
9. Burgo, T. A. L.; Galembeck, F. Electrified Water: Liquid, Vapor and Aerosol. *J. Braz. Chem. Soc*. **2016**, *27*, 229-238.
10. Bai, J.; Huang, Y.; Cheng, H.; Qu, L. Moist-electric generation. *Nanoscale* **2019**, *11*, 23083-23091.

TH-2654_156122042

11. Zhao, F.; Cheng, H.; Zhang, Z.; Jiang, L.; Qu, L. Direct Power Generation from a Graphene Oxide Film under Moisture. *Adv. Mater*. **2015** , *27*, 4351-4357.
12. Zhao, F.; Liang, Y.; Cheng, H.; Jiang, L.; Qu, L. Highly efficient moisture-enabled electricity generation from graphene oxide frameworks. *Energy. Environ. Sci*. **2016**, *9*, 912-916.
13. Huang, Y.; Cheng, H.; Yang, C.; Zhang, P.; Liao, Q.; Yao, H.; Shi, G.; Qu, L. Interface-mediated hygroelectric generator with an output voltage approaching 1.5 volts. *Nat. Commun*. **2018**, *9*, 4166.
14. Shen, D.; Xiao, M.; Zou, G.; Liu, L.; Duley, W. W.; Zhou, Y. N. Self-Powered Wearable Electronics Based on Moisture Enabled Electricity Generation. *Adv. Mater*. **2018**, *30*, 1705925.
15. Liu, X.; Gao, H.; Ward, J. E.; Liu, X.; Yin, B.; Fu, T.; Chen, J.; Lovley, D. R.; Yao, J. Power generation from ambient humidity using protein nanowires. *Nature* **2020**, *578*, 550-554.
16. Bae, J.; Yun, T. G.; Suh, B. L.; Kim, J.; Kim, I.-D. Self-operating transpiration-driven electrokinetic power generator with an artificial hydrological cycle. *Energy. Environ. Sci*. **2020**, *13*, 527-534.
17. Li, L.; Hao, M.; Yang, X.; Sun, F.; Bai, Y.; Ding, H.; Wang, S.; Zhang, T. Sustainable and Flexible Hydrovoltaic Power Generator for Wearable Sensing Electronics. *Nano Energy* **2020**, *72*, 104663.
18. Xie, P.; Rong, M. Z.; Zhang, M. Q. Moisture Battery Formed by Direct Contact of Magnesium with Foamed Polyaniline. *Angew. Chem*. **2015**, *128*, 1837-1841.
19. Ye, M.; Cheng, H.; Gao, J.; Li, C.; Qu, L. A respiration-detective graphene oxide/lithium battery. *J. Mater. Chem. A* **2016**, *4*, 19154-19159.

TH-2654_156122042

20. Fang, Z.; Feng, J.; Fu, X.; Li, J.; Hu, X.; Xie, X.; Yu, D. Humidity and Pressure Dual-Responsive Metal–Water Batteries Enabled by Three-In-One All-Polymer Cathodes for Smart Self-Powered Systems. *ACS Appl. Mater. Interfaces* **2020**, *12*, 23853-23859.
21. Raidongia, K.; Huang, J. Nanofluidic Ion Transport through Reconstructed Layered Materials. *J. Am. Chem. Soc*. **2012**, *124*, 16528-16531.
22. Deka, J.; Saha, K.; Konch, T. J.; Gogoi, R. K.; Saikia, S.; Saikia, P. P.; Dutta, G. K.; Raidongia, K. Reconstruction of Soil Components into Multifunctional Freestanding Membranes. *ACS Omega* **2019**, *4*, 1292-1299.
23. Gogoi, R. K.; Raidongia, K. Intercalating cation specific self-repairing of vermiculite nanofluidic membrane. *J. Mater. Chem. A* **2018**, *6*, 21990-21998.
24. Huang, K.; Rowe, P.; Chi, C.; Sreepal, V.; Bohn, T.; Zhou, K. G.; Su, Y.; Prestat, E.; Pillai, P. B.; Cherian, C. T.; Michaelides, A.; Nair, R. R. Cation-controlled wetting properties of vermiculite membranes and its promise for fouling resistant oil–water separation. *Nat. Commun*. **2020**, *11*, 1097.
25. Gogoi, R. K.; Saha, K.; Deka, J.; Brahma, D.; Raidongia, K. Solvent-driven responsive bilayer membranes of clay and graphene oxide. *J. Mater. Chem. A* **2017**, *5*, 3523-3533.
26. Saha, K.; Deka, J.; Hens, S.; Saikia, S.; Raidongia, K. Chemical reactions under the nanofluidic confinement of reconstructed lamellar membranes. *J. Mater. Chem. A* **2018**, *6*, 22931-22939.
27. Gogoi, R.K.; Raidongia, K. Strategic Shuffling of Clay Layers to Imbue Them with Responsiveness. *Adv. Mater*. **2017**, *29*, 1701164.

TH-2654_156122042

28. Janica, I.; Buffa, S. D.; Mikołajczak, A.; Eredia, M.; Pakulski, D.; Ciesielski, A.; Samorì, P. Thermal insulation with 2D materials: liquid phase exfoliated vermiculite functional nanosheets. *Nanoscale* **2018**, *10*, 23182.
29. Zhang, C.; Tjiu, W. W.; Fan, W.; Yang, Z.; Huang, S.; Liu, T. Aqueous stabilization of graphene sheets using exfoliated montmorillonite nanoplatelets for multifunctional free-standing hybrid films via vacuum-assisted self-assembly. *J. Mater. Chem*. **2011**, *21*, 18011.
30. Li, Y.-C.; Schulz, J.; Mannen, S.; Delhom, C.; Condon, B.; Chang, S.; Zammarano, M.; Grunlan, J. C. Flame Retardant Behavior of Polyelectrolyte Clay Thin Film Assemblies on Cotton Fabric. *ACS Nano* **2010**, *6*, 3325-3337.
31. Ming, P.; Song, Z.; Gong, S.; Zhang, Y.; Duan, J.; Zhang, Q.; Jiang, L.; Cheng, Q. Nacre-inspired integrated nanocomposites with fire retardant properties by graphene oxide and montmorillonite. *J. Mater. Chem. A* **2015**, *3*, 21194.
32. Chen, P.; Zhao, Y.; Wang, W.; Zhang, T.; Song, S. Correlation of Montmorillonite Sheet Thickness and Flame Retardant Behavior of a Chitosan–Montmorillonite Nanosheet Membrane Assembled on Flexible Polyurethane Foam. *Polymers* **2019**, *11*, 213.
33. Evangelou, V. P. *John Wiley & Sons, New York* **1998,** 120.

TH-2654_156122042

Chapter 5

Fabrication of Pressure Responsive Energy Device from Nanofluidic Vanadium Pentoxide and Polymeric Hydrogel

Summary*

In this chapter the principles of metal-water batteries were applied to develop a sustainable pressure-responsive energy delivery system. Application of a humble pressure of 56 kPa on agar and glycerol-based hydrogel membrane sandwiched between aluminum foil and nanofluidic V_2O_5 membrane (Al-gel-VO device) generate open-circuit voltage up to 1.3 V accompanied by an output current of 85 µA (power density = 0.45 Wm^{-2}). The output power of Al-gel-VO can be further improved by tuning parameters like lateral dimensions of the layers, applied pressure, and ionic conductivity of the gel membrane. Remarkably, under ambient conditions, the hydrogel and V_2O_5 based devices can provide a constant potential difference up to five conjugative days. Unlike typical humidity powered energy systems, the energy output of the current device is resistant towards the diurnal variations in environmental conditions. Remarkably, both gel and V_2O_5 membrane can be completely regenerated after damage caused by prolong use or accidents without any deterioration in the energy-efficiencies. Moreover, the Al-gel-VO devices can also be connected in series (or parallel) to add-up the voltage (or current) values of the individual devices.

---

* Paper based on these studies has appeared in *ACS Appl. Electron Mater.*, 2021, 3, 277

TH-2654_156122042

5.1: INTRODUCTION

The never-ending pursuit of perfection in making human life easier and satisfying led to an explosive growth in the electronic devices. The phenomenal growth of the electronic gadgets is powered by an equivalent development in the systems capable of harvesting, storing, and delivering electrical energy. Among these numerous power management devices, chemical potential based systems are considered to be the most reliable, convenient, and energy-efficient systems.[1-4] In order to cope with the ever-changing requirements, there is a continuous evolution in the structure and functionalities of the traditional energy delivery systems, which led to the fabrication of several types of compressible, stretchable and implantable super capacitors and batteries.[5-9] Similarly, multiple kinds of energy storage and power delivering devices capable of apperceiving and responding to environmental changes in a spontaneous, and timely manner has also been demonstrated.[10-11]

Even though lithium-ion batteries dominate the current market of electronic devices, it is not free from the shortcomings and challenges.[12-13] Therefore, a widespread search for alternative strategies are being pursued to meet the demands of future appliances. Among various perspective systems, metal-air and metal-water batteries have drawn a great deal of interest owing to their advantages like environmental compatibility, high energy density, and constant discharge voltage.[14-16] In typical metal-air batteries, an alkaline electrolyte is sandwiched between the metal anode and air-breathing cathode. While ubiquitous oxygen molecules diffuse through the air-breathing cathode is exploited as the cathode reagent, metal atoms of the anode are consumed as the anode reagent.[17-19] In the metal-water (or moisture) batteries also metal atoms are consumed at the anode, but instead of oxygen here water molecules are utilized as the cathode reagent.[11,20-22] Therefore, less expensive metals such as Mg and Al are the most attractive options of anode for these kind of batteries. These

TH-2654_156122042

inexpensive and abundant metals exhibiting large energy density, high theoretical voltage, and safe working environments possess large potential of application in the future technology.

5.2: SCOPE OF THE PRESENT INVESTIGATION

On its journey towards commercial applications, metal air/water (or moisture) battery needs to overcome several hurdles like high self-discharge rate, sluggish discharge kinetics, lack of rechargeability, and short self-life.[23-25] For example, metal-water batteries that exploit liquid water as cathode material require appropriate gas-tight assemblies to prevent leaking or evaporation of water molecules. In typical metal-moisture batteries, assemblies of pre-polished metals (like Li, Mg, or Zn) and polymeric sponges are enclosed into a coin-type cell, where cell walls are punched to facilitate the entrance of water molecules from the atmosphere. These set-ups need to be stored in an inert atmosphere while not in use to avoid self-discharge. Moreover, the functioning of these devices is highly sensitive to environmental conditions. Any drops in the humidity levels, drastically downgrade the output power values. For example, when the RH level was decreased below 40 %, the open circuit potential of moisture battery formed by direct contact of magnesium with foamed polyaniline reduced drastically and became negligible at RH levels ~ 20%.[26] Similarly, the self-powered battery fabricated via the assembly of Li foil and a graphene oxide film displayed a gradual decrease of both the open-circuit voltage and output current values in the decreasing RH values from 90% to 20%.[27] The open-circuit potential of smart metal−water battery prepared through direct contact of Mg or Zn anode with an all-polymer moisture electrode became negligible when RH levels were reduced to below 40%.[11]

While researchers working in this area are making significant progress towards overcoming these hurdles, here, we report fabrication of a responsive and robust energy delivering system based on the principles of metal-water batteries. The pressure responsive power

TH-2654_156122042

delivery system described here exploit the hygroscopic nature of agar and glycerol based hydrogel and outstanding nanofluidic conductivity of freestanding V_2O_5 membrane as the solid state electrolyte and spacer. In a clear contrast to the existing moisture-driven energy systems, the V_2O_5 and hydrogel based devices can provide energy under extreme low humidity conditions, making it an ideal candidate for challenging applications like powering of autonomous undersea vehicles (AUV).

One of the most critical components of the primary battery is the spacer.[28-29] Ionic conductivity of the spacer was found to be critically important for the performance of batteries and supercapacitors. In order to attain the required levels of ionic conductivity various corrosive/inflammable liquid (or solid) based electrolytes are used as electrolytes, however, these reactive electrolytes drastically reduce lifetime of the devices.[20-32] Moreover, in most of the supercapacitors or batteries the spacer/electrolyte is the most vulnerable component of the devices, lifetime of which dictate the overall durability of the devices. In the recent years, efforts were made to overcome these trade-offs by employing advanced nano- or biomaterials based membranes that exhibit high nanofluidic ionic conductivity, thermal robustness, and chemical stability.[33-39] The percolated network of the molecularly sized nanochannels formed by the interlayer spaces of reconstructed V_2O_5 membrane is known to exhibit high stability and proton conductivity,[40] and hence provide an ideal platform to fabricate chemically robust, thermally stable, and environment friendly power delivering systems.

5.3: EXPERIMENTAL SECTION

Materials and Chemicals: Vanadium pentoxide, hydrogen peroxide, agar, glycerol, sodium chloride, potassium chloride and lithium chloride were purchased from Merck. Aluminium sheets were purchased from local vendor.

TH-2654_156122042

Preparation of V_2O_5 membrane: V_2O_5 nanosheets were prepared from V_2O_5 powder upon H_2O_2 treatment in an ice cold condition. 2.38 g of V_2O_5 was dissolved in 25 mL of deionised water to yield a brown coloured clear solution. The entire experimental apparatus was placed in an ice bath and 25 mL of 50 % H_2O_2 was added to the reaction mixture. Addition of H_2O_2 resulted in vigorous bubbling with formation of dark brown precipitate which gradually turned into a thick gel. The as prepared gel was diluted with 100 mL water and bath sonicated for half an hour. 6 mL of 6 mg/mL dispersion of V_2O_5 nanosheet was vacuum filtered through a PTFE filter paper and air dried to obtain free standing V_2O_5 membrane.

Preparation of gel membrane: The gel membranes of agar and glycerol were prepared by mixing agar powder and glycerol (50 % w/w ratio) in deionised water followed by microwave-assisted heating of the aqueous solution for two minutes. The resultant gelatinous solution was casted in a Petri dish and dried for 24 hours at 50 ˚C to obtain a transparent free standing gel membrane.

Fabrication of Al-gel-VO device: A V_2O_5 strip of dimension ~ 1.5 cm ×1.5 cm × 0.006 cm was cut-out from a free standing V_2O_5 membrane and connected to a Cu wire by employing conductive silver paste. The surface of V_2O_5 strip connected to the Cu wire was pasted to an insulating board with the help of a doubled sided sticky tape. An Al film of similar dimension was pasted to the other end of the board with the help of doubled sided tape. A gel membrane of dimension 1.5 cm × 1.5 cm was sandwiched between the V_2O_5 and aluminium. The board was flapped such a way that the open surface of Al film can make a homogeneous contact with that of the gel strip attached to a V_2O_5 membrane. In order to apply pressure on Al-gel-VO devices, pre-calibrated weights were placed on the Al side of the cardboard.

TH-2654_156122042

Self-healing of vanadium pentoxide membranes: A V_2O_5 strip of 1.5 cm × 1.5 cm was cut into two halves with the help of scissors and gently placed upon one another with edges overlapping each other. A water droplet of 20 µL is spread over the overlapping edges and was allowed to dry under ambient conditions. The water droplet evaporates from the surface within 2 hours, thereby assisting water-induced self-repairing of the V_2O_5 strips into a single strip.

Recycling of agar gel membranes: The used pieces of agar gel membranes were easily recycled by simply re-melting and re-casting. For example, broken agar membranes are placed on a Petri dish and microwaved for 2-3 minutes. The microwave assisted heating melts the agar membranes and form a gelatinous solution which is allowed to dry at 50 ° C in a vacuum oven for several hours to obtain free standing gel membranes.

Characterisation: The structural morphology of the V_2O_5 and gel samples was characterized by field emission scanning electron microscope (FESEM) (Zeiss, Model: Sigma). Interlayer spacing between the V_2O_5 nanochannels was characterised by X-ray diffractometer (XRD) (Rigaku, Model: Micromax- 007HF). All electrochemical measurements were carried out by using a source meter instrument (Keithley 2450). The stress-strain curves of the V_2O_5 and gel membranes were recorded by a 5kN Universal Testing Machine (UTM) (Zwick Roell, Model: Z005TN).The EIS data were collected by using Multi Autolab/M204 potentiostat/galvanostat equipped with a FRA32M module in the frequency range of 1 MHz to 1 Hz, in open circuit potential with a perturbation voltage amplitude of 5 mv.

5.4: RESULTS AND DISCUSSION

In order to fabricate the pressure responsive energy delivering systems, a gel membrane was prepared by dissolving appropriate amount of agar and glycerol under warm conditions. Details of the fabrication process are described in the experimental section.

TH-2654_156122042

Agar itself is a highly abundant natural polysaccharide with slight negative charges on its backbone.[41-42] With three hydroxyl groups on its backbone, the hygroscopic glycerol is known for its antimicrobial and antiviral properties. The warm mixture of the aqueous agar and glycerol can be casted on different casting molds to prepare hydrogels of desired shapes. Here, it was placed on glass petri dishes to prepare uniform 2D films. Digital photograph of a representative film of aqueous agar and glycerol (gel) is shown in Figure 5.1a. Field Emission Scanning Electron Microscopic (FESEM) examination revealed that the air drying process shrinks the gel surface and creates wrinkles and shallow trances, a

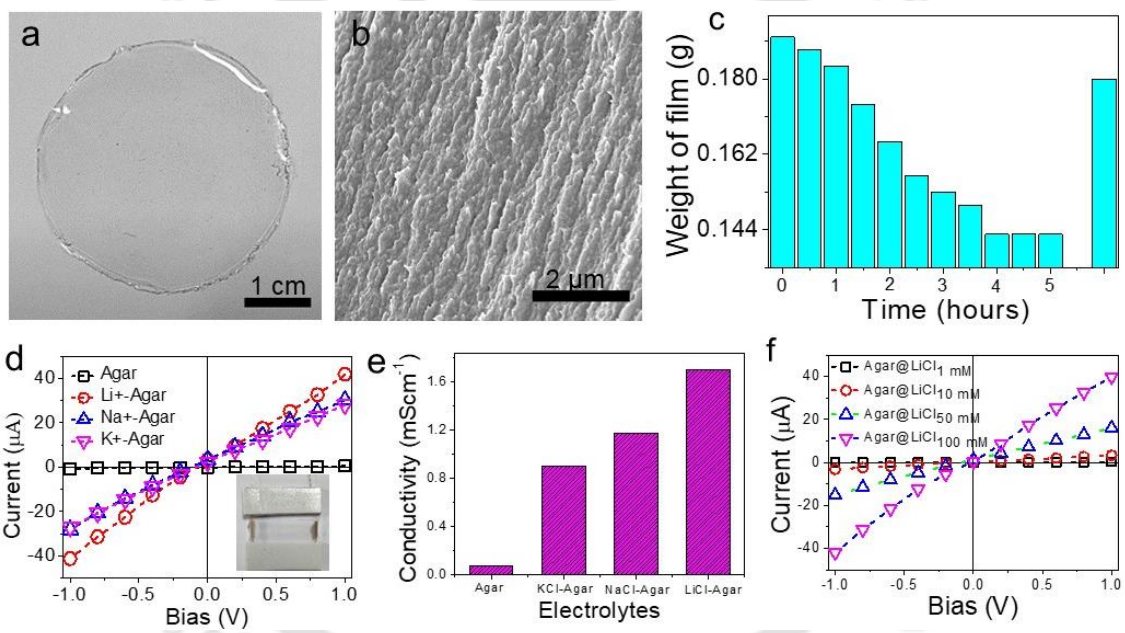

Figure 5.1: Characterisation of Agar gel membrane: (a) Digital photograph and (b) FESEM image of agar gel membrane, (c) Weight loss of agar membrane at a low humidity of 12 % RH as a function of time followed by recovery at environmental humidity of RH 65 % (a) (d) characteristics I-V curves of agar gel membranes intercalated with different electrolytes, inset showing digital photograph of device fabricated to measure the ionic conductivity of agar gel membranes, (e) bar diagram showing conductivity of different agar gel electrolytic membranes, and (f) characteristics I-V curves of agar gel membranes intercalated with electrolytes of different concentration.

representative image is shown in Figure 5.1b. The gel membrane of agar and glycerol exhibits extraordinary water holding capacity. Even under low humid conditions, it can hold up a large amount of water molecules on its pores. As shown in Figure 5.1c, at RH = 15 %, it took around 4 hours to completely dehydrate a gel membrane of dimension 2 cm

TH-2654_156122042

× 2 cm. Remarkably, the dehydrated gel re-gained 1.3 times of its weight just in 5 minutes by absorbing water molecules from the atmosphere at RH = 65 %. The water molecules trapped inside the gel membrane also support fast transport of ionic species. For example, at RH of 65 % (23 °C), it exhibits an ionic conductivity of 0.072 $mScm^{-1}$, which was increased to 0.9 $mScm^{-1}$, 1.17 $mScm^{-1}$, and 1.7 $mScm^{-1}$ upon addition of electrolytes such as KCl, NaCl, and LiCl (10 mM each), respectively. Electrolytes were added to the warm water during the fabrication process of the gel membrane. The enhancement in the ionic conductivity value of the electrolyte containing gel was found to be directly proportional to the decreasing radius of the cations, suggesting cations to be the dominant charge carrier species. The conductivity of gel membranes was measured by connecting two ends of a rectangular strips of dimension 3 cm × 0.4 cm × 100 µm to copper wires with the help of conductive silver paste. The photograph of a device is shown in the inset of Figure 5.1d. The current-voltage (*I*-*V*) curves are shown in Figure 5.1d. Figure 5.1e shows the bar diagram depicting the conductivity values of the gel membranes intercalated with various electrolytes. The conductivity of gel membranes were also found to increase with the increasing concentration of the intercalated electrolyte as evident from the *I*-*V* curves in Figure 5.1f.

The reconstructed membranes of exfoliated V_2O_5 nanoflakes are known to exhibit excellent nanofluidic conductivity.[40] A digital photo of the V_2O_5 membrane prepared by following a procedure reported earlier is shown in Figure 5.2a. The uniform lamellar stacking of the membrane is revealed by the cross-sectional FESEM image (Figure 5.2b), and confirmed by the presence of a sharp peak at X-ray diffraction pattern (XRD) shown in Figure 5.2c. The XRD peak at $2\theta = 6.8°$ (d =1.28 nm) resembles to the interlayer spacing of (001) plane of V_2O_5 crystal. The presence of ultra-thin 2D nanofluidic channels in V_2O_5 membrane is evident from the characteristic surface charge governed ionic conductivity of V_2O_5

TH-2654_156122042

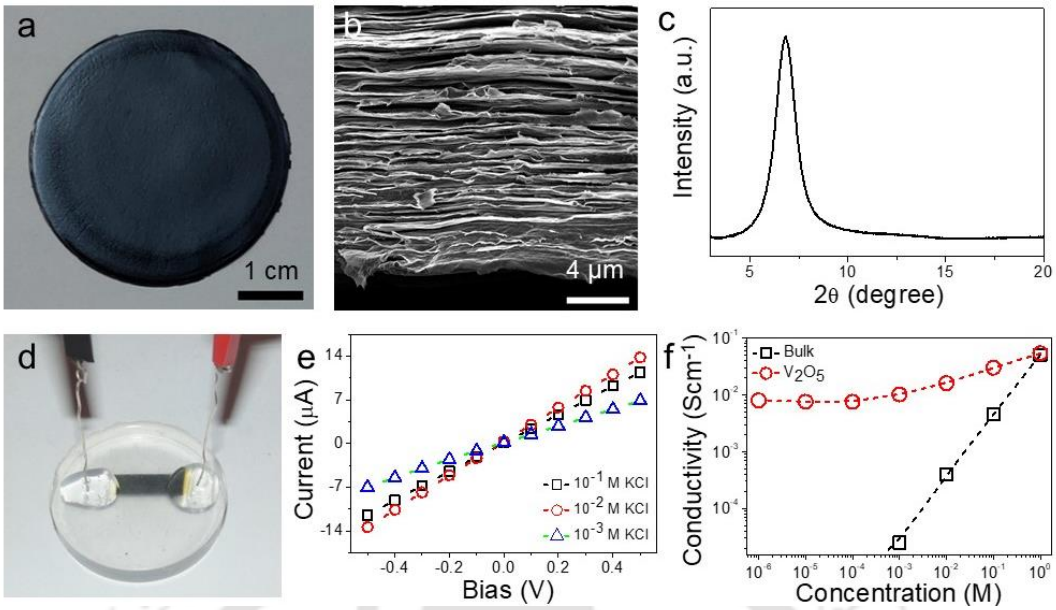

Figure 5.2: Characterisation of V_2O_5 membrane: (a) Digital photograph and (b) cross-sectional FESEM image of V_2O_5 membrane, (c) XRD pattern of reconstructed V_2O_5 membrane, (d) Digital photograph of device, (e) Representative I-V curves recorded with nanofluidic V_2O_5 at different electrolyte concentration. and (f) Ionic conductivity versus concentration plot of V_2O_5 nanochannels (red curve) is compared with that of the bulk (black curve) solutions.

nanofluidic device shown in Figure 5.2f. Nanofluidic device was prepared by encapsulating a rectangular strip of V_2O_5 film into a PDMS (polydimethylsiloxane) elastomer and carving out the edges to form electrolyte chambers. The photo of a nanfluidic V_2O_5 device is shown in Figure 5.2d. The linear I-V curves (Figure 5.2e) recorded for different electrolytes confirm the formation of percolated nanofluidic channels of V_2O_5. Conductivity values at different electrolyte concentration was determined by multiplying the slope of the I-V curves with respective cell constant of the device.

In order to fabricate pressure responsive energy delivering systems, a 2D film of gel (thickness =160 µm) was sandwiched between a pair of aluminium (Al) (thickness = 11µm) and reconstructed V_2O_5 membrane (thickness = 35 µm) of lateral dimension ~ 1.5 cm × 1.5 cm. A schematic illustration of the device is presented in Figure 5.3a. Both V_2O_5 membrane and Al-foil were connected to a copper wire through conducting silver paste. When the exposed surface of the agar film was pressed (~ 56 kPa) on to an Al foil of similar size, it

TH-2654_156122042

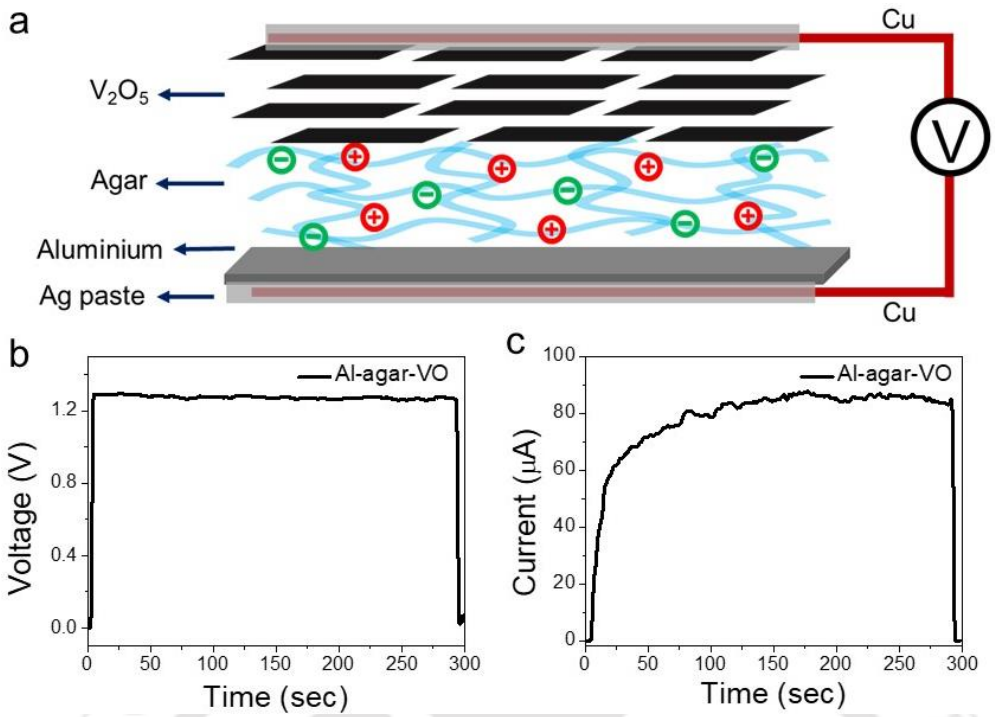

Figure 5.3: Electrical energy from Al-gel-VO devices: (a) Schematic representation of an Al-gel-VO device fabricated to harvest electrical energy. (b) Open-circuit-potential and (c) short-circuit current developed on an Al-gel-VO device of dimension 1.5 cm × 1.5 cm upon application of a humble pressure of 56 kPa.

generated an open circuit potential of 1.3 V (Figure 5.3b), which was measured by a source meter instrument (Keithley 2450) connected through copper wires by using conducting silver paste. The open-circuit-voltage generated by the Al-agar-VO device was also accompanied by a short circuit current of 85 μA (Figure 5.3c), yielding a power density of 0.45 Wm^{-2}.

As shown in the Figure 5.4a, the output current of Al-agar-VO devices is directly proportional to the lateral dimensions of the devices, however, the output potential did not change with the increasing lateral dimension. The output current of the Al-agar-VO device was also found to be dependent on the ionic conductivity of the gel membrane. Al-gel-VO devices were also prepared by using gel film containing different electrolytes (LiCl, NaCl, KCl, and HCl). As shown in Figure 5.4b, the output current values of the devices increases with the decreasing radius of the cations (or increasing ionic conductivity values). The high output-current for the HCl containing (Al-gel@H^+-VO) device is attributed to the high

TH-2654_156122042

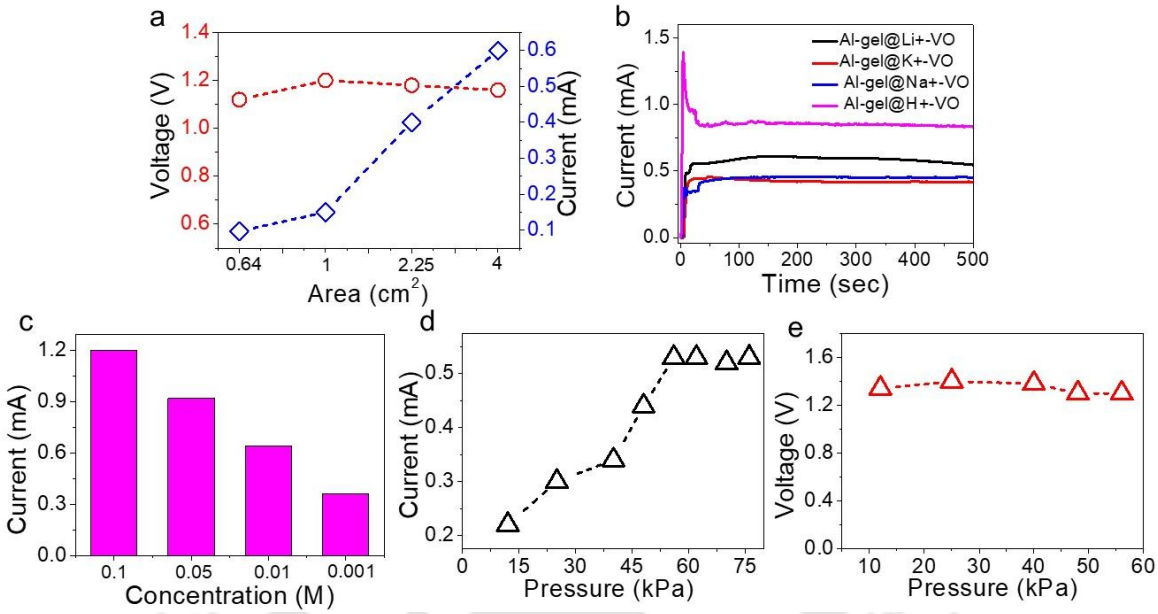

Figure 5.4: Tuning of power-output of the pressure responsive electrical devices: (a) Open-circuit potential and output-current of Al-gel@Li+-VO devices of different lateral dimensions. Output-current of Al-gel@Li+-VO devices with gel membrane containing (b) different electrolytes, and (c) LiCl of different concentrations. (d) Output-current, and (e) open-circuit potential as a function of applied pressure of an Al-gel@Li+-VO device. Unless otherwise mentioned typical device dimension (= 1.5 cm × 1.5 cm), electrolyte concentration (= 10 mM), and pressure (= 56 kPa) were kept constant.

ionic mobility of the protons. Similarly, the output-current values were also found to be proportional to the concentration of the electrolytes present in the gel membrane (Figure 5.4c).

The output current of the Al-agar-VO devices was found to be dependent on the applied pressure between films, it increases with the increasing magnitude of the applied pressure (Figure 5.4d). Here again, the output potential remains constant with the varying applied pressure (Figure 5.4e). As shown in the FESEM image of Figure 5.1b, the surface of gel is not uniform, but comprised of various sallow trenches. The increasing pressure can flatten the rough surface of gel to induce better contact between the layers, which is attributed for the improved current values at higher applied pressure. In order to confirm this hypothesis Electrochemical Impedance Spectra (EIS) was recorded at different applied pressure on the Al-agar-VO device, Figure 5.5. The experimental and simulated EIS data with the possible equivalent circuit are shown in Figure 5.5a. Rs represents the electrodes and electrolyte's

TH-2654_156122042

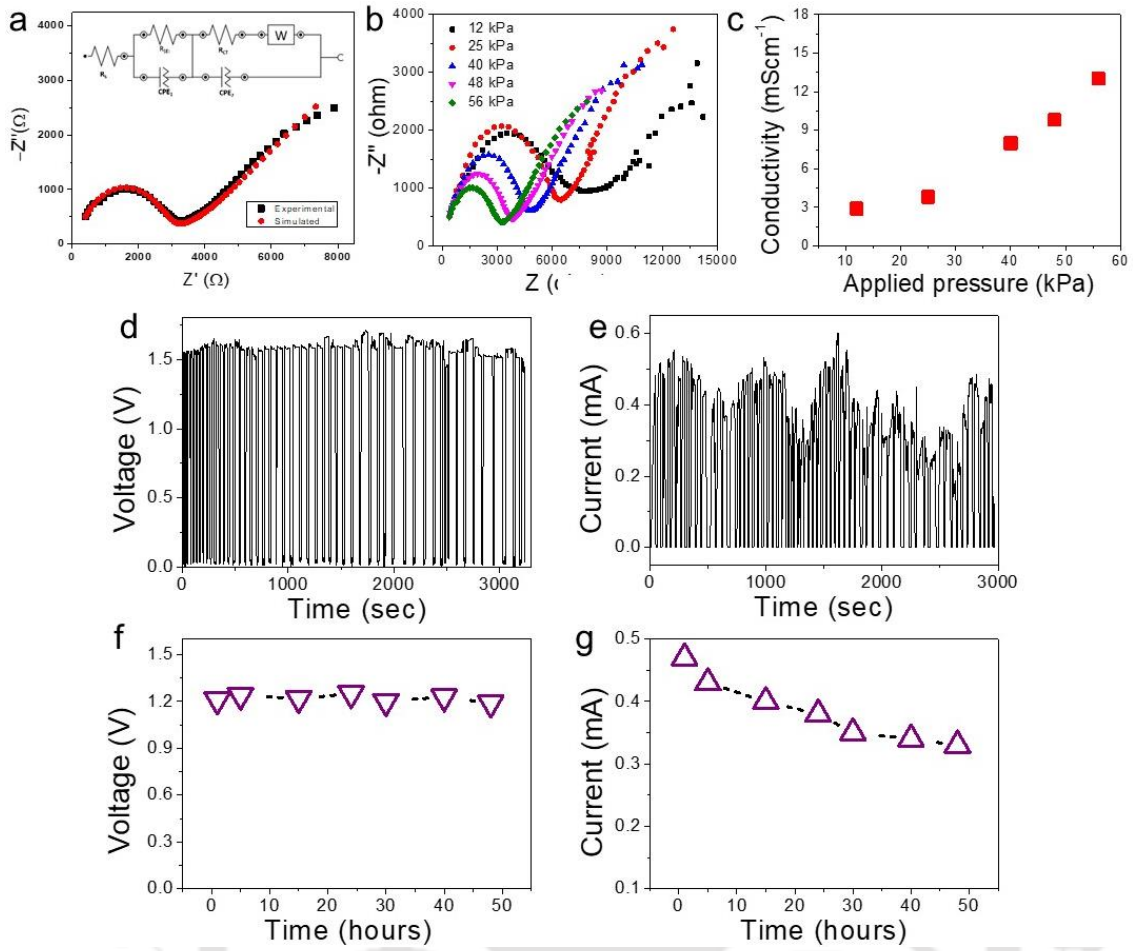

Figure 5.5: Extraction of energy from a wider range of mechanical manoeuvres: (a) Experimental and simulated EIS of Al-gel@Li+-VO device with the equivalent circuit (inset), (b) Nyquist plot for Al-gel@Li^+-VO device recorded at different applied pressure (c) Conductivity of Al-gel@Li^+-VO device as a function of applied pressure. (d) Open-circuit potential and (e) short-circuit-current developed by an Al-gel@Li+-VO device upon application of 56 kPa pressure for short cycles of 0.05 Hz frequency, (f) Open-circuit potential and (g) short-circuit-current developed by an Al-gel@Li+-VO device upon application of 56 kPa pressure an extended period of 48 hours.

ohmic resistance, and Rsei is the resistance of ion migration through the solid electrolyte interphase (SEI). The charge transfer resistance (Rct) is due to ion diffusion into the electrode and the electrolyte. The constant phase elements (CPE) can be correlated to the capacitance contribution by the active material's surface. The Warburg impedance (W) at the low-frequency region results from the diffusion of ions to the electrode interface from the bulk electrolyte. The Rct values decrease with the increase of pressure indicating the ions can be easily transferred to the electrode.[43-44] (Figure 5.5b). Moreover, the conductivity value across the films of V_2O_5 and gel, calculated from the I-V curves recorded at different

TH-2654_156122042

pressure, were found to be increasing with the increasing pressure(Figure 5.5c). The Al-agar-VO devices can also be exploited as a pressure sensor. As shown in Figure 5.5d and Figure 5.5e the voltage and current generated by an Al-agar-VO device during a high frequency (0.05 Hz) mechanical pressure on the aluminium side of an Al-agar-VO device as a function of time. The study performed for about 60 cycles did not show any drop in the potential values. The slight variation in the current values is attributed to uneven contact between layers (Al/agar and agar/V_2O_5) during the high-frequency manual pressing. Similarly, when a stable pressure is applied the Al-agar-VO based device yields stable power for around 50 hours. As shown in Figure 5.5f, upon continuous pressing (56 kPa), an Al-agar@Li^+-VO device yielded uninterrupted potential for more than 48 hours. The potential was also associated with an output current of ~ 0.33 mA, Figure 5.5g.

In order to verify the requirement of atmospheric water molecules in the energy generating process, experiments with Al-gel-VO devices were also performed under low atmospheric humidity conditions. The low humidity condition was achieved by placing the required amount of desiccants in a gas-tight sealed container (Figure 5.6a). The output current values of Al-gel-VO devices placed inside the desiccator (RH = 15 %), and was monitored as function of time. As shown in Figure 5.6b, even inside the desiccator, the current values displayed no significant drop up to 2.5 hours. This resilience of Al-gel-VO devices against the decreasing humidity levels is attributed to the extraordinary water holding capacity of gel membrane. After 2.5 hours, the output current started declining steadily and reached saturation after 10 hours, with an output current of ~ 8 µA. No further decline in the current values at RH = 15 % indicate establishment of a dynamic equilibrium between the rate of consumption of water molecules as cathode reagent and the rate of absorption from the atmosphere. In order to rule out the possibility of atmospheric-oxygen consumption as the cathode reagent under low humidity conditions, the surrounding atmosphere was replaced

TH-2654_156122042

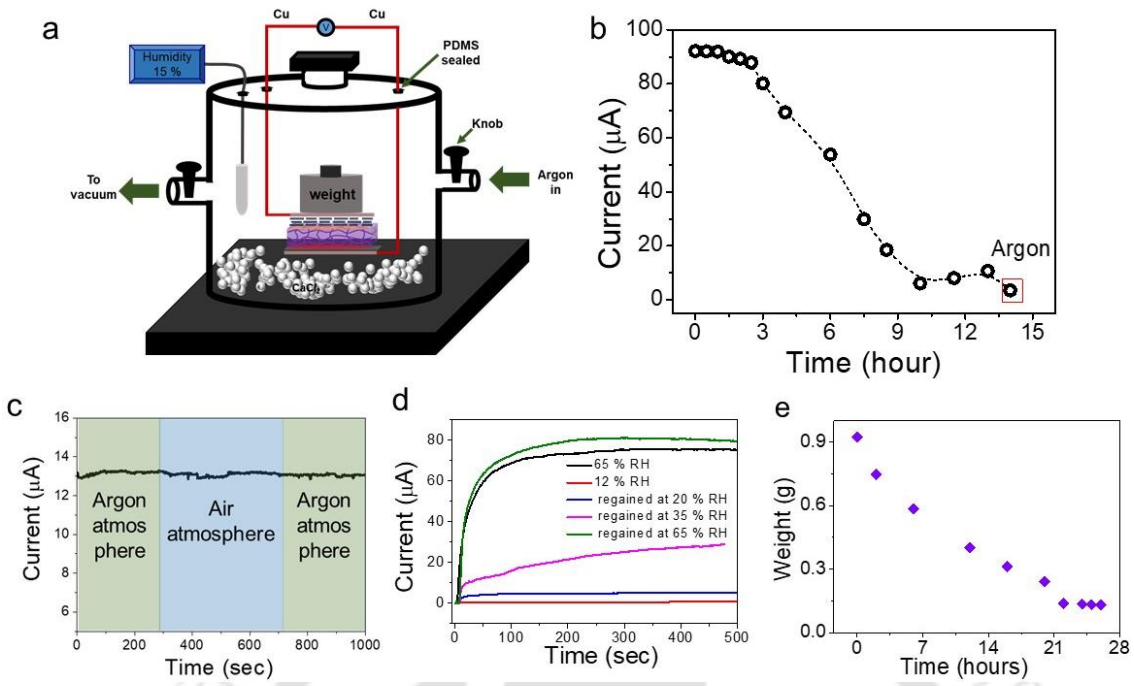

Figure 5.6: Role of atmospheric moisture: (a) Schematic representation of controlled humidity chamber, (b) Short-circuit-current of an Al-gel-VO device recorded at low humidity (RH = 15 %) as a function of time. (c) Output-current of an Al-gel-VO device in alternating argon and air atmosphere at 15 % relative humidity, (d) A plot comparing the output-current of an Al-gel-VO devices recorded at different humidity levels. (e) Weight loss of agar membrane wrapped in V_2O_5 membrane and Al foil at a low humidity of 12 % RH as a function of time.

with ultrapure argon gas. Even after 40 minutes of purging of Ar gas, the Al-gel-VO device did not show any drastic drop in the output current values (the point encircled with a red circle in Figure 5.6b). The hypothesis was further confirmed by periodically exchanging the surrounding atmosphere of an Al-gel-VO device between air and argon, Figure 5.6c. Remarkably, the output current of dehydrated Al-gel-VO device can be re-gained within 10 minutes of exposure to humid air (RH= 65 %) as shown in Figure 5.6d. The dependence of the output current on the atmospheric humidity levels confirms the consumption of atmospheric water molecules as the cathode reagent. As discussed in Figure 5.6e, when all sides are open it takes around 4 hours for complete dehydration of a gel membrane. In Al-gel-VO devices, both sides of the gel membranes are covered with Al foil and V_2O_5 membrane, so it took longer time for the dehydration. During the recovery time, all sides of gel membrane were exposed to humid atmosphere (RH = 65 %). Moreover, when

TH-2654_156122042

recovered at different atmospheric conditions, the output current values were found to be dependent on the atmospheric humidity levels, as shown in Figure 5.6d.

In order to gain further insight into the energy delivering process, devices were also prepared by systematically excluding V_2O_5 and gel membrane from Al-gel-VO devices. As can be seen from the Figure 5.7a, the device of Al foil and gel (excluding V_2O_5 membrane)

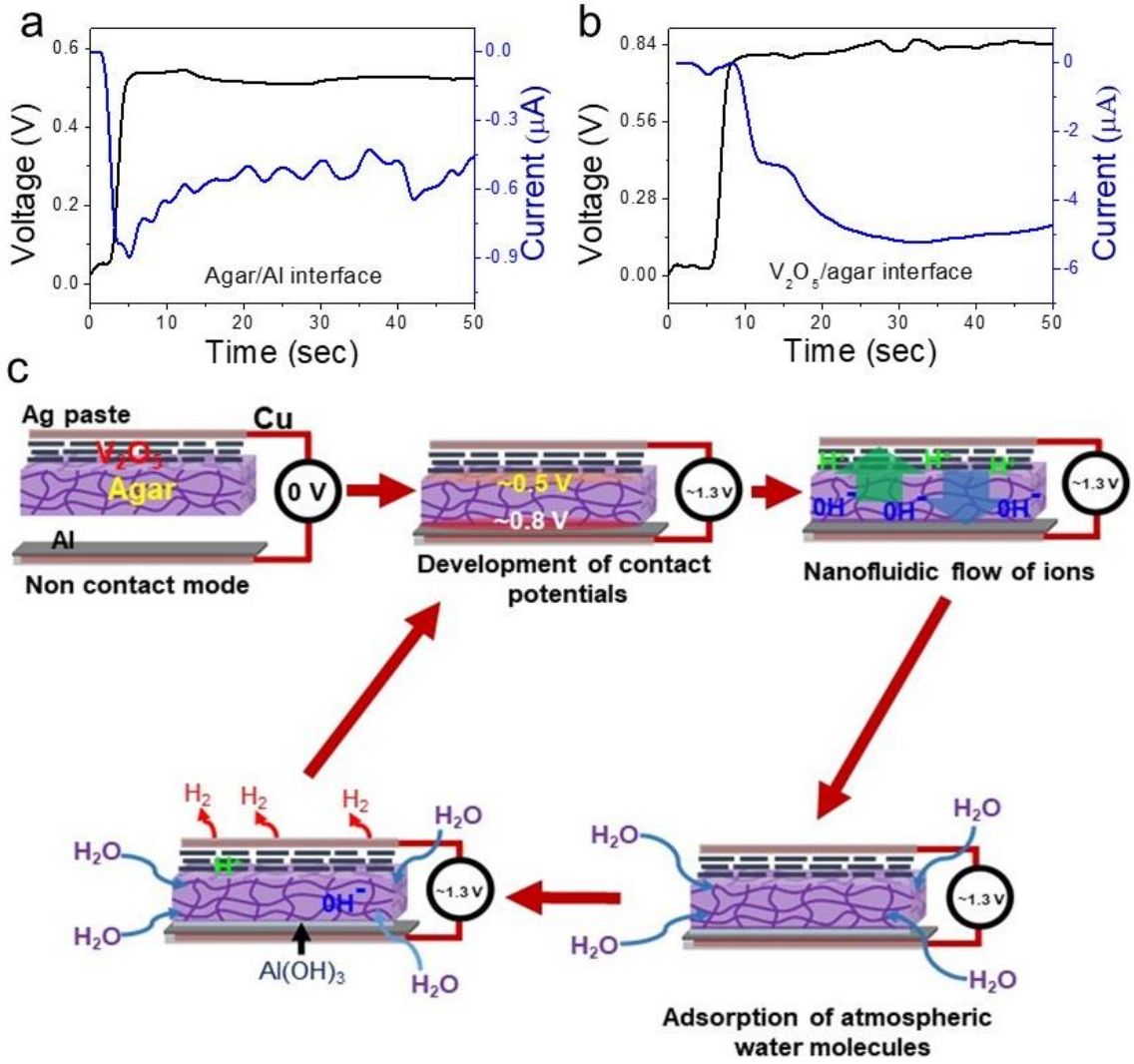

Figure 5.7: Mechanism for pressure responsive power generation: Open circuit voltage and short circuit current generated at the interface of (a) agar and aluminium and (b) V_2O_5 and agar. (c) Schematic representation of the working mechanism of interfacial potentials based mechanical energy harnessing devices.

developed a potential of 0.5 V, which was accompanied by tiny current values of ~ 0.6 µA. Similarly, the interface of gel and V_2O_5 (excluding Al membrane) generated a potential of 0.8 V (Figure 5.7b), accompanied by an output current of 6 µA. Therefore, overall potential

TH-2654_156122042

of the Al-gel-VO devices can be considered as the combination of Al/gel and gel/ V_2O_5 interfacial potential. Based on these experimental findings and the existing literature the possible mechanism of the long-lasting power delivery can be explained as follows (Figure 5.7c). Due to the influence of negative surface charges of agar molecules some of the water molecules absorbed by the gel film get dissociated into H^+, and OH^--ions. Under the influence of interfacial potential, the H^+-ions moves towards the atomically thin cation-selective channels of V_2O_5, and the OH^--ions are attracted by the Al-electrode. While, OH^--ions oxidize Al atoms of the Al-anode releasing $Al(OH)_3$ and three electrons, the H^+-ions get reduced to H_2 gas at the Cu-electrode. In addition, an Al-gel-VO device was pressed continuously for five days. A gradually decline in the output-potential was

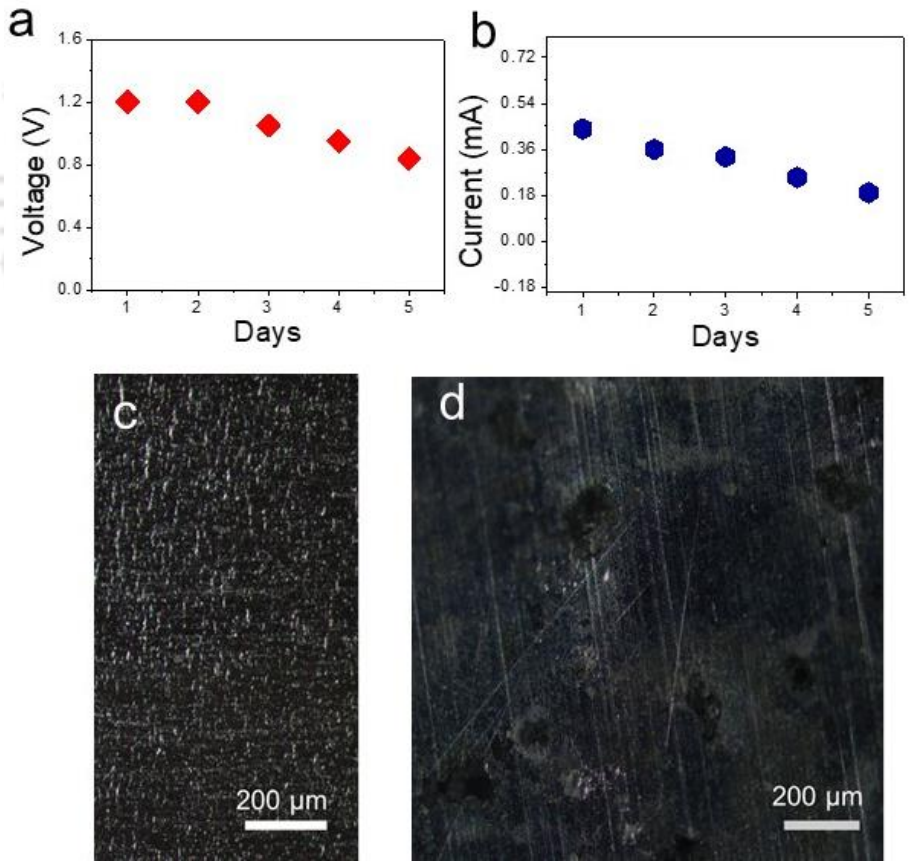

Figure 5.8: Device stability: (a) Open circuit voltage and (b) short circuit current of Al-agar@Li+-VO device recorded for 5 continuous days in contact mode. Optical microscopic images of Al surface (c) before and (d) after the generation of electrical energy for 7 days.

observed after 48 hours, Figure 5.8a. A simultaneous decline in the current values are also evident in Figure 5.8b. After five days, Al-electrode was observed under optical

TH-2654_156122042

microscope, corrosion of the Al-surface by the OH^- ions was clearly visible from the images of Figure 5.8c and 5.8d. In order to gain further insight, the surface of the aluminium foil before and after the discharge process was studied by examining the surface under X-ray photoelectron spectroscopy (XPS). The XPS survey scan on Al foil after five

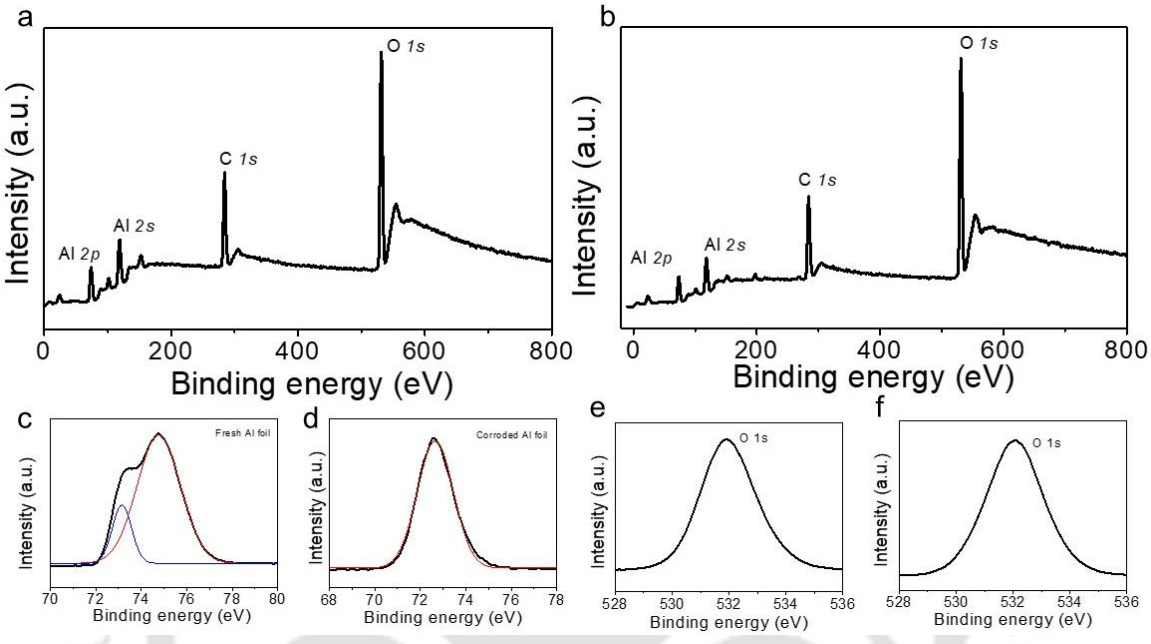

Figure 5.9: XPS survey scan of Al electrode recorded (a) before and (b) after 5 days of continuous power generation, the presence of carbon along with Al and O is attributed to the absorption of carbon dioxide on the surface. Moreover, the sample was attached the XPS stub with the help of a conductive carbon tape. XPS Al 2p peaks of (c) fresh Al foil and (d) corroded Al foil, XPS peaks of O1s of (e) fresh Al foil and (f) corroded Al foil.

continuous days of application is compared with that of pristine foil in Figure 5.9. The Al to O ratio of pristine aluminium foil was found to decrease from 0.48 to 0.3 in the corroded foil, supporting the hypothesis of Al atom consumption in the anodic reaction. The Al 2p spectra of fresh Al foil (Figure 5.9c) are comprised of two maximus, which were deconvoluted into two peaks centred at 74.7 eV and 73.1 eV corresponding to the presence of Al_2O_3 and $Al(OH)_3$ species, respectively. The Al 2p spectra of corroded Al foil displayed a single peak centred at 72.6 eV, corresponding to the $Al(OH)_3$ species (Figure 5.9d).

One of the remarkable characteristics of Al-gel-VO device is that both gel and V_2O_5 membrane can be completely regenerated after damage caused by prolong use or accidents.

TH-2654_156122042

For example, Figure 5.10a shows pieces of V_2O_5 membrane manually disintegrated after applying in the energy generation experiments for ~160 hours. These pieces of disintegrated membrane were readily fused into a single piece just by applying a drop of water. For the fusion process separate strips were connected together by placing their edges on top of each other and a tiny droplet of water placed at the junction. Once the droplet of

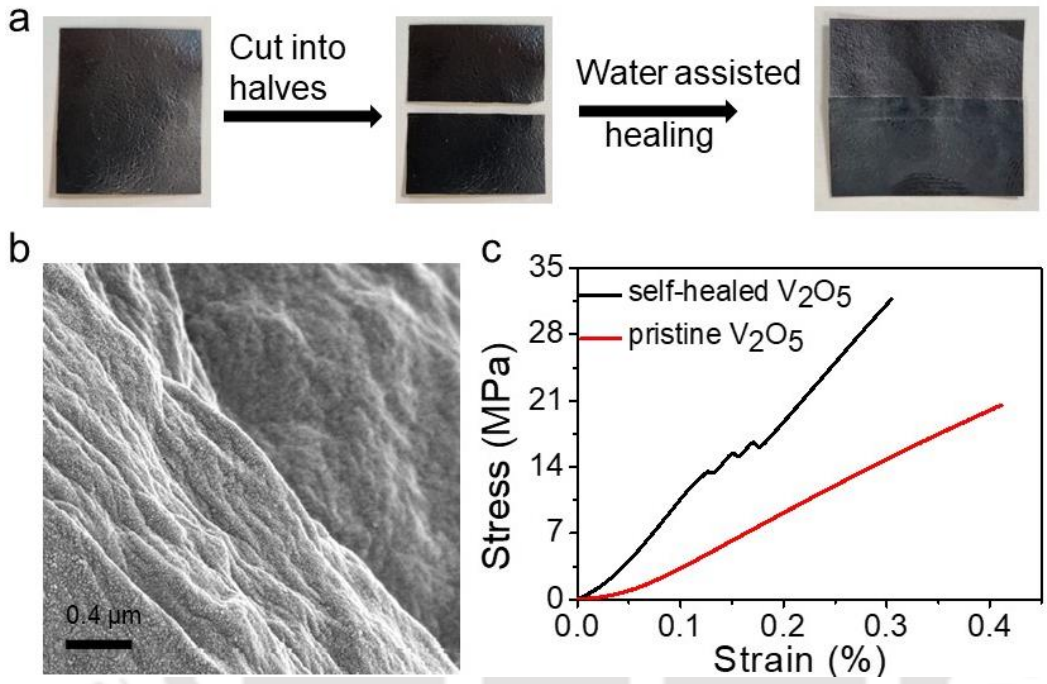

Figure 5.10: Regeneration energy harvesting devices: (a) Photographs showing water assisted healing of V_2O_5 membrane, (b) Surface FESEM image of self-healed V_2O_5 membrane, (c) comparison of stress-strain curve of self-healed and pristine V_2O_5 membrane**.**

water evaporated under ambient conditions, the strips fused into a single piece, as demonstrated in Figure 5.10a. While, under FESEM the surface morphology of the healed membrane is indistinguishable from that of a pristine membrane (Figure 5.10b), the stress-stain curve suggests an improvement in the mechanical robustness of the healed membrane, shown in Figure 5.10c. The improved mechanical strength of the healed membrane is attributed to increased thickness in the healed area. In freestanding V_2O_5 membranes, individual V_2O_5 flakes are held together by various inter-sheet interactions like van der Waals forces, hydrogen bonding, and cross-linking of the nanosheets by the trace amount of cations V^{2+}, V^{3+} and VO^{2+} etched out during the exfoliation process. When two pieces

TH-2654_156122042

of V_2O_5 strips are put together in the presence of liquid water, these interactions extend between the surfaces of the strips leading to the fusion of the strips. Similarly, a gel

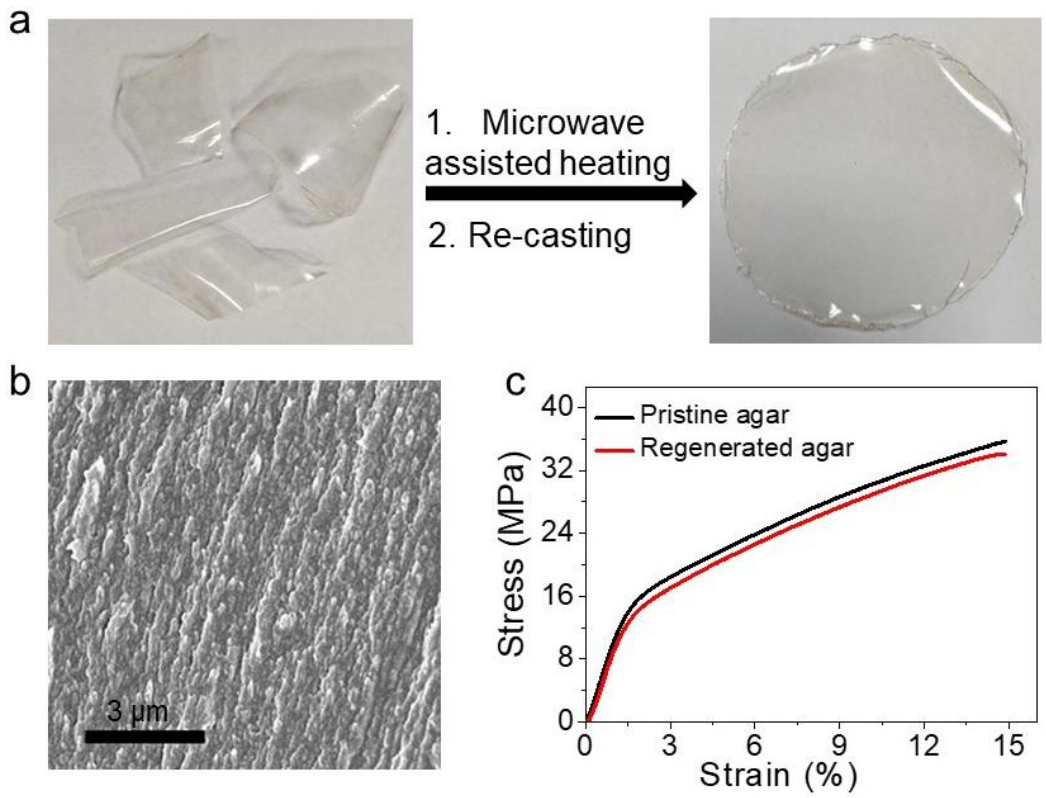

Figure 5.11: Regeneration energy harvesting devices: (a) Photographs showing recycling of gel membranes, (b) Surface FESEM image of regenerated gel membrane, and (c) comparison of stress-strain curve of regenerated and pristine gel membrane.

membrane was broken into pieces after its application on an Al-gel-VO device, shown in Figure 5.11a. The broken pieces of gel were collected in a glass-petri-dish and subjected to microwave assisted heating for two minutes and allowed to cool down at room temperature. As can be seen from Figure 5.11a, after the heat treatment process the broken pieces of gel yielded a membrane as good as the fresh membrane. The surface morphology and mechanical properties of the regenerated membrane remain unaltered as evident from the FESEM image and stress-strain curves shown in Figure 5.11b and Figure 5.11c, respectively. Figure 5.12a and 5.12b, shows that not only the morphology of the V_2O_5 and gel membrane can be recovered after the damage but also the output current and potential

TH-2654_156122042

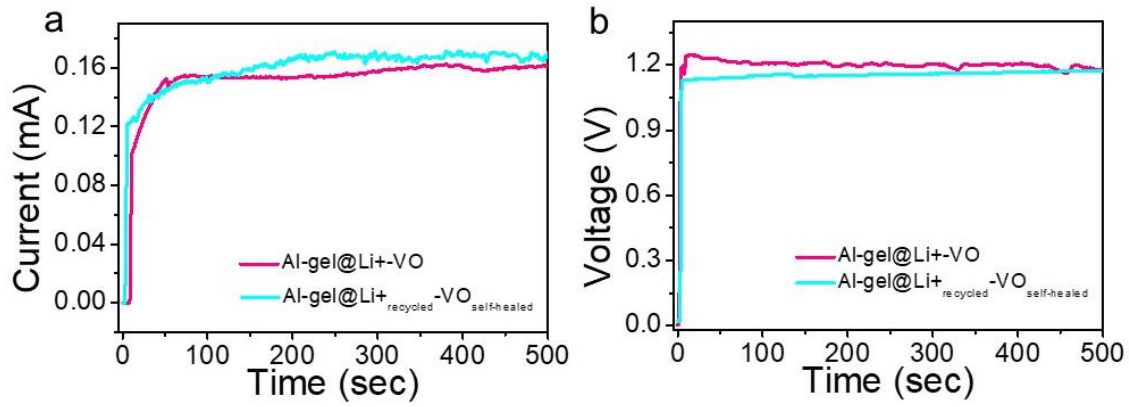

Figure 5.12: Energy extraction from re-generated devices: (f) Output current and (g) open circuit potential of Al-gel@$Li^{+}_{recycled}$-$VO_{self\text{-}healed}$ device compared to that of pristine device.

can be recovered by the regeneration process. The regeneration ability of the gel membrane is attributed to its low melting point (~85 °C). When heated at a temperature above its melting point, the broken pieces of gel membrane transforms into liquid without affecting its molecular structure. As a result, it can be re-casted into any desired shape and size by pouring into appropriate casting molds.

Moreover, the Al-gel-VO devices can also be connected in series (or parallel) to add-up the voltage (or current) values of the individual devices. Figure 5.13a shows that the series connection of 4 devices yielded a potential values of 5.2 V. Similarly, parallel connections of four devices yielded a total current value of 2.4 mA (Figure 5.13b). The power obtained from a single Al-gel-VO device were found to be sufficient to power small electronic devices such as calculator, humidity sensor and LED light. (Figure 5.13c, 5.13d and 5.13e). Figure 5.13f shows lighting of a LED continuously for 3 days simply by pressing a gel membrane between Al foil and V_2O_5 membrane with two paper clips. Pressure responsive energy devices like Al-gel-VO could support the advancements in remote sensing technologies. There is an increasing demand for self-triggered equipment like camera traps for tracking wild animals, security systems installed in remote areas. In such systems, the sensors that trigger the equipment need to be continuously powered for prolongs periods, and hence discharge-time of the battery is one of the bottlenecks in such operations. The

TH-2654_156122042

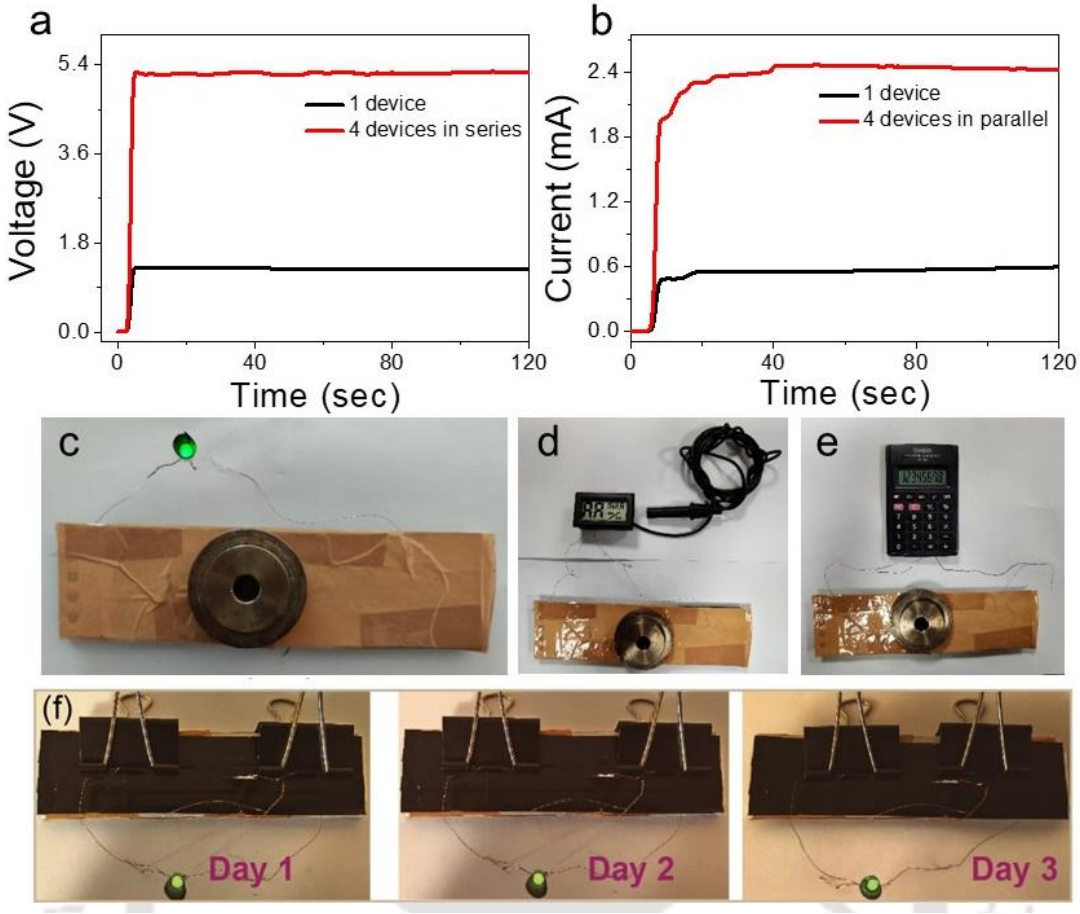

Figure 5.13: Application of energy harvesting device: Plots comparing the (a) open-circuit-potential and (b) output-current of single Al-gel@Li^+-VO device to that of four Al-gel@Li^+-VO devices assembled in series and parallel connections, respectively. Digital photographs showing powering of a (c) LED, (d) humidity sensor, and (e) calculator. (f) Digital photographs showing powering of a LED for three consecutive days.

pressure responsive energy devices like Al-gel-VO that discharge only in the presence of certain pressure could drastically enhance the operation time of such devices. As a proof of concept, a device panel capable of generating a voltage of ~ 6V was prepared by connecting four pressure-responsive devices in series. In idle condition, these devices did not generate any potential difference, however, upon application of a gentle pressure (56 kPa) on the panel developed the potentials difference (~ 6V) and started releasing the power, shown in Figure 5.14. These kinds of energy devices could enhance the ability of remote sensing systems.

TH-2654_156122042

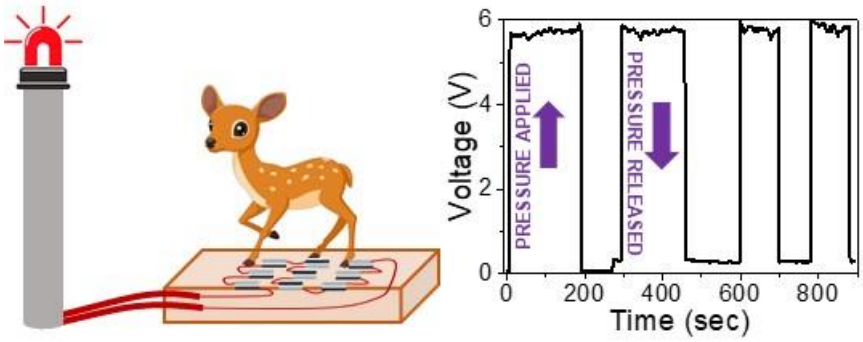

Figure 5.14: Application of pressure responsive device: A proof of concept demonstrating an animal sensor

Sl. No.	Materials used	OCP (V)	Current density	Ideal Humidity (RH%)	Voltage at lowest humidity(V)	Reference
1	PANI foam/Mg	1.84 V	--	50 - 90 %	~0.23 V at 20 % RH	22
2	Li foil and graphene oxide film	2.7 V	360 µA cm^{-2}	90 %	1 V at 20 % RH	27
3	Mg/Zn anode and PANI coated polyurethane sponge	1.7 V	--	60-100 %	~0.1 V at 20 % RH	
4	PDDA-VM/Al	0.8 V	40 µA cm^{-2}	80 %	0.65 V at 12 % RH	Chapter 4
5	Al-Agar gel-V_2O_5	1.3 V	35 µA cm^{-2}	65 %	1 V at 15 % RH	Chapter 5

5.5: CONCLUSION

In conclusion, the principles of metal water batteries were exploited here to develop a moisture powered pressure responsive energy delivery system. Due to the hygroscopic nature of the gel membrane, the Al-gel-VO devices can hold the water molecules even under extreme low humidity conditions, making it an ideal candidate for challenging applications. The power output of Al-gel-VO can be further improved through enhancement in the lateral dimensions of the layers, increased applied pressure, and doping

TH-2654_156122042

of the gel membrane with electrolytes. For practical applications multiple Al-gel-VO devices can be connected in series (or parallel) connection to add-up the voltage (or current) values of the individual devices. Additionally, the Al-gel-VO device open up new possibilities for environmentally friendly routes of hydrogen production and electrochemical batteries. A table comparing the electrochemical performance of this work with other metal moisture batteries is presented here (Table 5.1). While the electrochemical performance of the current system is inferior to recently published metal moisture batteries, it has additional advantages like reusability of the constituents and superior tolerance to the changing environmental conditions.

TH-2654_156122042

5.6: REFERENCES

1. Winter, M.; Brodd, R. J. What Are Batteries, Fuel Cells, and Supercapacitors? *Chem. Rev*. **2004**, *104*, 4245-4269.
2. Tie, S. F.; Tan, C. W.A review of energy sources and energy management system in electric vehicles. *Renew. Sustain. Energy Rev*. **2013**, *20*, 82-102.
3. Gur, T. M. Review of electrical energy storage technologies, materials and systems: challenges and prospects for large-scale grid storage. *Energy Environ. Sci*. **2018**, *11*, 2696-2767.
4. Yang, Z.; Zhang, J.; Meyer, M. C. W. K.; Lu, X.; Choi, D.; Lemmon, J. P.; Liu, J. Electrochemical Energy Storage for Green Grid. *Chem. Rev*. **2011**, *111*, 3577-3613.
5. Niu, Z.; Dong, H.; Zhu, B.; Li, J.; Hng, H. H.; Zhou, W.; Chen, X.; Xie, S. Highly Stretchable, Integrated Supercapacitors Based on Single-Walled Carbon Nanotube Films with Continuous Reticulate Architecture. *Adv. Mater*. **2013**, *25*, 1058-1064.
6. Xu, C.; Li, Z.; Yang, C.; Zou, P.; Xie, B.; Lin, Z.; Zhang, Z.; Li, B.; Kang, F.; Wong, C. P. An Ultralong, Highly Oriented Nickel-Nanowire-Array Electrode Scaffold for High-Performance Compressible Pseudocapacitors. *Adv. Mater*. **2016**, *28*, 4105-4110.
7. Zhao, Y.; Liu, J.; Hu, Y.; Cheng, H.; Hu, C.; Jiang, C.; Jiang, L.; Cao, A.; Qu, L. Highly Compression-Tolerant Supercapacitor Based on Polypyrrole-mediated Graphene Foam Electrodes. *Adv. Mater.* **2013**, *25*, 591-595.
8. Liu, W.; Chen, Z.; Zhou, G.; Sun, Y.; Lee, H. R.; Liu, C.; Yao, H.; Bao, Z.; Cui, Y. 3D Porous Sponge-Inspired Electrode for Stretchable Lithium-Ion Batteries. *Adv. Mater*. **2016**, *28*, 3578-3583.

TH-2654_156122042

9. Albano, F.; Chung, M.; Blaauw, D.; Sylvester, D.; Wise, K.; Sastry, A. Design of an implantable power supply for an intraocular sensor, using POWER (power optimization for wireless energy requirements). *J. Power Sources* **2007**, *170*, 216-224.
10. Wang, X.; Gao, J.; Cheng, Z.; Chen, N.; Qu, L. A Responsive Battery with Controlled Energy Release. *Angew. Chem. Int. Ed*. **2016**, *55*, 14643-14647.
11. Fang, Z.; Feng, J.; Fu, X.; Li, J.; Hu, X.; Xie, X.; Yu, D. Humidity and Pressure Dual-Responsive Metal−Water Batteries Enabled by Three-In-One All-Polymer Cathodes for Smart Self-Powered Systems. *ACS Appl. Mater. Interfaces* **2020**, *12*, 23853-23859.
12. Bruce, P. G.; Freunberger, S. A.; Hardwick, L. J.; Tarascon, J.-M. Li–O2 and Li–S batteries with high energy storage. *Nat. Mater*.**2012**, *11*, 19-30.
13. Pellow, M. A.; Emmott, C. J. M.; Barnhart, C. J.; Benson, S. M. Hydrogen or batteries for grid storage?A net energy analysis. *Energy Environ. Sci*. **2015**, *8*, 1938-1952.
14. Blueton, K. F.; Sammells, A.F. Metal/air batteries: their status and potential – a review. *J. Power Sources* **1979**, *4*, 263-279.
15. Lee, J.-S.; Kim, S. T.; Cao, R.; Choi, N. -S.; Liu, M.; Lee, K.T.; Cho, J. Metal–Air Batteries with High Energy Density: Li–Air versus Zn–Air. *Adv. Energy Mater*. **2011**, *1*, 34-50.
16. Kraytsberg, A.; Ein-Eli, Y. The impact of nano-scaled materials on advanced metal–air battery systems. *Nano Energy* **2013**, *2*, 468-480.
17. Wang, C.; Yu, Y.; Niu, J.; Liu, Y.; Bridges, D.; Liu, X.; Pooran, J.; Zhang, Y.; Hu, A. Recent Progress of Metal–Air Batteries—A Mini Review. *Appl. Sci.* **2019**, *9*, 2787.

TH-2654_156122042

18. Liu, Y.; Sun, Q.; Li, W.; Adair, K. R.; Li, J.; Sun, X. A comprehensive review on recent progress in aluminum–air batteries. *Green Energy & Environ*. **2017**, *2*, 246-277.

19. Egan, D.R.; León, C. P.; Wood, R.J.K.; Jones, R.L.; Stokes, K.R.; Walsh, F.C. Developments in electrode materials and electrolytes for aluminium-air batteries. *J. Power Sources*, **2013**, *236*, 293-310.

20. Katoh, T.; Inda, Y.; Nakajima, K.; Ye, R.; Baba, M. Lithium/water battery with lithium ion conducting glass–ceramics electrolyte. *J. Power Sources* **2011**, *196*, 6877-6880.

21. Liu, Q.; Yan, Z.; Wang, E.; Wang, S.; Sun, G. A high-specific-energy magnesium/water battery for full-depth ocean application. *Int. J. Hydrog. Energy* **2017**, *42*, 23045-23053.

22. Xie, P.; Rong, M. Z.; Zhang, M. Q. Moisture Battery Formed by Direct Contact of Magnesium with Foamed Polyaniline. *Angew. Chem. Int. Ed*., **2016**, *55*, 1805-1809.

23. Rahman, M.A., Wang, X.; Wen, C. High Energy Density Metal-Air Batteries: A Review. *J. Electrochem. Soc*. **2013**, *160*, 1759.

24. Kar, M.; Simons, T.J.; Forsyth, M.; MacFarlane, D.R. Ionic liquid electrolytes as a platform for rechargeable metal–air batteries: a perspective. *Phys. Chem. Chem. Phys*. **2014**, *16*, 18658-18674.

25. Wang, Z. L.; Xu, D.; Xu, J.J.; Zhang, X.B. Oxygen electrocatalysts in metal–air batteries: from aqueous to nonaqueous electrolytes. *Chem. Soc. Rev*. **2014**, *43*, 7746-7786.

TH-2654_156122042

26. Xie, P.; Rong, M. Z.; Zhang, M. Q. Moisture battery formed by direct contact of magnesium with foamed polyaniline. *Angew. Chem., Int. Ed*. **2016**, *55*, 1805−1809.
27. Ye, M.; Cheng, H.; Gao, J.; Li, C.; Qu, L. A respiration-detective graphene oxide/lithium battery. *J. Mater. Chem. A* **2016**, *4*, 19154-19159.
28. Xu, M.; Ivey, D.G.; Xie, Z.; Qu, W. Rechargeable Zn-air batteries: Progress in electrolyte development and cell configuration advancement. *J. Power Sources*, **2015**, *283*, 358-371.
29. Mokhtar, M.; Talib, M. Z. M.; Majlan, E. H.; Tasirin, S. M.; Ramli, W. M. F. W.; Daud, W. R. W.; Sahar, J. Recent developments in materials for aluminum–air batteries: A review. *J. Ind. Eng. Chem*. **2015**, *32*, 1-20.
30. Liu, Y.; Sun, Q.; Li, W.; Adair, K. R.; Li, J.; Sun, X. A comprehensive review on recent progress in aluminium-air batteries. *Green Energy & Environ*. **2017**, *2*, 246-277.
31. Panda, P. K.; Grigoriev, A.; Mishra, Y. K.; Ahuja, R. Progress in supercapacitors: roles of two dimensional nanotubular materials. *Nanoscale Adv*. **2020**, *2*, 70-108.
32. Tan, D. H. S.; Banerjee, A.; Chen, Z.; Meng, Y. S. From nanoscale interface characterization to sustainable energy storage using all-solid-state batteries. *Nat. Nanotechnol*. **2020**, *15*, 170-180.
33. Cao, L.; Wu, H.; Yang, P.; He, X.; Li, J.; Li, Y.; Xu, M.; Qiu, M.; Jiang, Z. Graphene Oxide-Based Solid Electrolytes with 3D Prepercolating Pathways for Effcient Proton Transport. *Adv. Funct. Mater*. **2018**, *28*, 1804944.
34. He, G.; Xu, M.; Zhao, J.; Jiang, S.; Wang, S.; Li, Z.; He, X.; Huang, T.; Cao, M.; Wu, H.; Guiver, M. D.; Jiang, Z. Bioinspired Ultrastrong Solid Electrolytes with Fast Proton Conduction along 2D Channels. *Adv. Mater*. **2017**, *29*, 1605898.

TH-2654_156122042

35. Kim, Y.; Kwon, S. J.; Jang, H.-K.; Jung, B. M.; Lee, S. B.; Choi, U H. High Ion Conducting Nanohybrid Solid Polymer Electrolytes via Single-Ion Conducting Mesoporous Organo silica in Poly(ethyleneoxide). *Chem. Mater*. **2017**, *29*, 4401-4410.

36. Jia, W.; Wu, P. Stable functionalized graphene oxide–cellulose nanofiber solid electrolytes with long-range 1D/2D ionic nanochannels. *J. Mater. Chem. A* **2019**, *7*, 20871-20877.

37. Park, H.; Lee, K. H.; Kim, Y. B.; Ambade, S. B.; Noh, S. H.; Eom, W.; Hwang, J. Y.; Lee, W. J.; Huang, J.; Han, T. H. Dynamic assembly of liquid crystalline graphene oxide gel fibers for ion transport. *Sci. Adv*. **2018**, *4*, eaau2104.

38. Wu, Z.; Ji, P.; Wang, B.; Sheng, N.; Zhang, M.; Chen, S.; Wang, H. Oppositely charged aligned bacterial cellulose biofilm with nanofluidic channels for osmotic energy harvesting. *Nano Energy* **2020**, 80, 105554-105564.

39. Deka, J.; Saha, K.; Konch, T. J.; Gogoi, R. K. Saikia, S.; Saikia, P. P.; Dutta, G. K.; Raidongia, K. Reconstruction of Soil Components into Multifunctional Freestanding Membranes. *ACS Omega* **2019**, *4*, 1292−1299.

40. Gogoi, R. K.; Neog, A. B.; Konch, T. J.; Sarmah, N.; Raidongia, K. A two-dimensional ion-pump of a vanadium pentoxide nanofluidic membrane. *J. Mater. Chem. A* **2019**, *7*, 10552-10560.

41. Raphael, E.; Avellaneda, C. O.; Manzolli, B.; Pawlicka, A. Agar-based films for application as polymer electrolytes. *Electrochim. Acta* **2010**, *55*, 1455-1459.

42. Menzel, J.; Frackowiak, E.; Fic, K. Agar-based aqueous electrolytes for electrochemical capacitors with reduced self-discharge. *Electrochim. Acta* **2020**, *332*, 135435.

TH-2654_156122042

43. Su, F. Y.; You, C.; He, Y. B.; Lv, W.; Cui, W. Jin, F.; Li, B.; Yang, Q.H.; Kang, F. Flexible and planar graphene conductive additives for lithium-ion batteries. *J. Mater. Chem*. **2010**, *20*, 9644-9650.

44. Li, J.; Zhang, X.; Peng, R.; Huang, Y.; Guo, L.; Qia Y. LiMn2O4/graphene composites as cathodes with enhanced electrochemical performance for lithium-ion capacitors. *RSC Adv*. **2016**, *6*, 54866-54873.

TH-2654_156122042

Chapter 6

Conclusions and Future perspective

6.1. Conclusions

In summary, we have demonstrated various examples of reconstructed membrane systems of two-dimensional layered materials with a broad goal of developing energy devices capable of harvesting energy from ambient atmosphere.

Multifunctional nanofluidic membranes were fabricated with components of soil such as exfoliated nanoflakes of vermiculite clay and purified humic acids. Cross-linking of VM and HA incorporates under water stability in vermiculite membranes for various nanofluidic phenomena such as selective ionic and molecular transport and energy harvesting under salinity gradient. Heating the soil membranes under inert atmosphere induces electrical conductivity in otherwise insulating soil membranes without affecting its ionic conductivity. Mixed conducting membranes were utilised for gas sensing applications for sensing traces of NH_3 vapors in the atmosphere.

Harvesting energy from serene water sources have been demonstrated by both theoretical and experimental studies on complimentary charge transfer activities of boron- and nitrogen-doped reduced graphene oxide membranes with water molecules. Having understood the role of B-r-GO with stronger charge transfer ability and higher stability, we have achieved remarkable stability and consistency of the energy devices up to 7 repetitive cycles of power generation. Potential application of energy devices in wearable electronics has been demonstrated as a proof of concept.

Fabrication and design of sustainable pressure-responsive energy harvesting devices working on the principle of metal-moisture batteries has been demonstrated to

TH-2654_156122042

continuously power small electronic devices for several days. Firstly, natural clay based nanofluidic membrane with inherent chemical and thermal stability are coated with a hygroscopic polymer PDDA to fabricate pressure-responsive energy device with extraordinary robustness and flame retardant properties.

Hygroscopic nature of agar- and glycerol-based hydrogel and outstanding nanofluidic conductivity of the free-standing V_2O_5 membrane as the solid-state electrolyte and spacer has been utilised to fabricate pressure-responsive energy device to harness energy from atmospheric water in a wide range of humidity. Re-generation of entire energy device has been achieved after damage caused by prolonged use with similar performance with that of the pristine device.

6.2. Future scope

The advancement in 2-D materials in transition step towards sustainable energy has been remarkable in last decade. While 2-D materials have led to emergence of many unique phenomenon for energy harvesting, multiple challenges need to be overcome by the scientific community in order to attain extensive application in daily lives. For example cost effective and energy efficient exfoliation of 2-D materials to achieve large-scale production of 2-D sheets is a foremost challenge. The ongoing techniques are lacking in scaling up (viz., low yield and random flake dimensions). Thus, challenge is to discover novel material technology to achieve scalable production of 2-D materials for design of efficient and high-performance energy devices. Reconstructed nanofluidic membranes possess enormous potentials for applications in areas like nanofluidic transport, fabrication of responsive materials, durable touch panels, and environmental energy harvesting. The quality that separates them from other materials such as porous membranes and electrophoresis gels is their well-defined and deterministic network of nanochannels. Researchers around the globe have explored the reconstructed membranes of 2-D materials

TH-2654_156122042

for energy generation and storage. However, having a better understanding of mechanism of energy generation and charge transfer phenomena will ease the optimization of output performance of the energy devices thus bringing them a step closer to our daily lives. Achieving stability and adaptability of the energy devices to a wide variety of environmental conditions is yet another challenge to researchers. Thus material properties and device engineering techniques need to be optimized to achieve reliability of the energy devices under harsh environmental conditions. Thus, there are abundant research and development opportunities for novel and advanced technologies to shift 2-D energy materials for real-world applications in our daily lives.

TH-2654_156122042

List of works performed during Ph.D. tenure:

Included in thesis

1. Reconstruction of Soil Components into Multifunctional Freestanding Membranes, **Jumi Deka**, Kundan Saha, Tukhar Jyoti Konch, Raj Kumar Gogoi, Subhasmita Saikia, Partha Pratim Saikia, Gitish K Dutta, Kalyan Raidongia. *ACS Omega* **2019***, 4,* 1292–1299
2. Electrical power Generation from the Contrasting Interfacial Activities of Boron- and Nitrogen-Doped Reduced Oxide Membranes, **Jumi Deka**, Kundan Saha, Suresh Kumar, Hemant Kumar Srivastava, Kalyan Raidongia. *ACS Appl. Nano Mater.* 2019*, 2,* 7997–8004
3. Fabrication of Pressure-Responsive Energy Device from Nanofluidic Vanadium Pentoxide and Polymeric Hydrogel, **Jumi Deka**, Kundan Saha, Raktim Gogoi, Gitish K. Dutta, and Kalyan Raidongia. *ACS Appl. Electron. Mater*. 2021, *3*, 277–284
4. Clay-Based Nanofluidic Membrane Derived from Vermiculite Nanoflakes for Pressure-Responsive Power Generation, **Jumi Deka**, Kundan Saha, Anish Yadav, Kalyan Raidongia. *ACS Appl. Nano Mater*. 2021, *4*, 4872–4880

Excluded from thesis

5. Chemical reactions under the nanofluidic confinement of reconstructed lamellar membranes, Kundan Saha, **Jumi Deka**, Sushovan Hens, Sourav Saikia, Kalyan Raidongia. *J. Mater. Chem. A,* **2018***, 6,* 22931-22939
6. Energy from the Nanofluidic Transport of Water through Nanochannels between Packed Silica Spheres, Kundan Saha, **Jumi Deka**, Kalyan Raidongia. *ACS Appl. Nano Mater.* **2019***, 2,* 5850–5856
7. Extraction of Evaporation-driven Electrokinetic Streaming Potential from V2O5 Nanochannels through Secondary Sources, Kundan Saha, **Jumi Deka**, Kalyan Raidongia. *ACS Appl. Energy Mater*.(Just accepted)
8. Solvent-driven responsive bilayer membranes of clay and graphene oxide, Raj Kumar Gogoi, Kundan Saha, **Jumi Deka**, Dulu Brahma, Kalyan Raidongia. *J. Mater. Chem. A,* **2017***, 5,* 3523-3533

TH-2654_156122042

9. Nanofluidic transport through humic acid modified graphene oxide nanochannels, Tukhar Jyoti Konch, Raj Kumar Gogoi, Abhijit Gogoi, Kundan Saha, **Jumi Deka**, K Anki Reddy, Kalyan Raidongia. *Mater. Chem. Front.,* **2018***, 2,* 1647-1654
10. Robust and self-healable bulk-superhydrophobic polymeric coating, Avijit Das, **Jumi Deka**, Kalyan Raidongia, Uttam Manna. *Chem. Mater.* **2017***, 29,* 8720–8728
11. Strategic formulation of graphene oxide sheets for flexible monoliths and robust polymeric coatings embedded with durable bioinspired wettability, Avijit Das, **Jumi Deka**, Adil M Rather, Bibhas K Bhunia, Partha Pratim Saikia, Biman B Mandal, Kalyan Raidongia, Uttam Manna. *ACS Appl. Mater. Interfaces* ***2017****, 9,* 42354–42365
12. Synthesis of fish scale and lotus leaf mimicking, stretchable and durable multilayers, Avijit Das, Shreyasi Sengupta, **Jumi Deka**, Adil Majeed Rather, Kalyan Raidongia, Uttam Manna. *J. Mater. Chem. A,* **2018***, 6,* 15993-16002
13. Microporous Organic Polymer-Derived Nitrogen-Doped Porous Carbon Spheres for Efficient Capacitive Energy Storage, Namrata Deka, Jayshree Barman, Jumi Deka, Kalyan Raidongia, Gitish K Dutta. *Chem. Electro. Chem.,* **2019***, 6,* 3327-3336
14. Nitrogen-Doped Porous Carbon Derived from Carbazole-Substituted Tetraphenylethylene-Based Hypercrosslinked Polymer for High-Performance Supercapacitor, Namrata Deka, **Jumi Deka**, Gitish K Dutta. *Chemistry Select,* **2018***, 3,* 8483-8490
15. Enhanced catalytic activity and near room temperature gas sensing properties of SnO_2 nanoclusters@mesoporous Sn (iv) organophosphonate composite, Suchibrata Borah, Bagmita Bhattacharyya, **Jumi Deka**, Aditya Borah, Anuchaya Devi, Dhanapati Deka, Shashank Mishra, Kalyan Raidongia, Nayanmoni Gogoi. *Dalton Trans.,* **2017***, 46,* 8664-8672

TH-2654_156122042

List of Conferences/Seminars attended during the Ph.D tenure:

1. Presented poster entitled ***Reconstruction of Soil Components into Multifunctional Freestanding Membranes*"** 20th CRSI National Symposium in Chemistry organized by Department of Chemistry, Gauhati University, Guwahati.
2. Presented poster entitled "***Reconstruction of Soil Components into Multifunctional Freestanding Membranes*"** in *Research Conclave 18* organized by Students' Academic Board (SAB), IIT Guwahati.
3. Presented poster entitled "***Reconstruction of Soil Components into Multifunctional Freestanding Membranes*"** in *International conference on Nanoscience and Technology, ICONSAT 2018* organized by Centre for Nano and Soft Matter Sciences.
4. Presented poster entitled "***Electrical power Generation from the Contrasting Interfacial Activities of Boron- and Nitrogen-Doped Reduced Graphene Oxide Membranes***" *in Frontier in Chemical Sciences (FICS-2018)* organized by Department of Chemistry, IIT Guwahati**.**
5. Presented model entitled "***Harvesting electrical energy from ambiedent pressure using clay membranes*"** in *Research Conclave 19* organized by Students' Academic Board (SAB), IIT Guwahati.
6. Presented poster entitled "***Application of Clay-Based Nanofluidic Membrane to Fabricate Robust and Responsive Electrical Power Delivery System*"** in *National Conference on recent Advances in Chemistry (RAC 2019)* organized by NIT Meghalaya.

TH-2654_156122042